Tampere University

IINA KORKKA

Ionic Signaling in Retinal Pigment Epithelium

From physiological characterization to stem cell applications

Tampere University Dissertations 637

Tampere University Dissertations 637

IINA KORKKA

Ionic Signaling in Retinal Pigment Epithelium

From physiological characterization to stem cell applications

ACADEMIC DISSERTATION
To be presented, with the permission of
the Faculty of Medicine and Health Technology
of Tampere University,
for public discussion in the auditorium F115
of the Arvo building, Arvo Ylpön katu 34, Tampere,
on 2 September, at 12 o'clock.

ACADEMIC DISSERTATION
Tampere University, Faculty of Medicine and Health Technology
Finland

Responsible supervisor and Custos	Docent Soile Nymark Tampere University Finland	
Supervisor	Professor Jari Hyttinen Tampere University Finland	
Pre-examiners	Associate Professor Bikash Pattnaik University of Wisconsin-Madison USA	Docent Sari Lauri University of Helsinki Finland
Opponent	Professor Olaf Strauss Charité Universitätsmedizin Berlin Germany	

The originality of this thesis has been checked using the Turnitin OriginalityCheck service.

Cover design: Roihu Inc.

ISBN 978-952-03-2487-2 (print)
ISBN 978-952-03-2488-9 (pdf)
ISSN 2489-9860 (print)
ISSN 2490-0028 (pdf)
http://urn.fi/URN:ISBN:978-952-03-2488-9

Carbon dioxide emissions from printing Tampere University dissertations have been compensated.

PunaMusta Oy – Yliopistopaino
Joensuu 2022

ACKNOWLEDGEMENTS

The research for this dissertation was started in the Computational Biophysics and Imaging Group but was primarily carried out in the Biophysics of the Eye Group, both currently at the Faculty of Medicine and Health Technology, Tampere University, Finland. First of all, for funding and for making this dissertation possible, I would like to thank the Academy of Finland, TEKES (Human Spare Part Project), the Doctoral Programme of the President of the Tampere University of Technology, the Finnish Cultural Foundation, the Emil Aaltonen Foundation, and the Finnish Foundation for Technology Promotion.

I would like to thank two of the most important people throughout this journey, my supervisors Soile Nymark and Jari Hyttinen. You gave me interesting projects and the freedom to work independently, yet always being available for discussion and guidance. Soile, your immense knowledge, the attitude to get things done, and the vision to point out the right direction at the most challenging points never ceased to amaze me. Jari, you are one of the most innovative persons I have ever met. Your ideas always gave an interesting and fresh perspective to the subject at hand. I also want to thank the pre-examiners of my thesis, Professor Bikash Pattnaik, and Docent Sari Lauri, for your valuable comments that remarkably improved this thesis.

The past and present personnel of the Biophysics of the Eye Group, the Computational Biophysics and Imaging Group, and the Eye Group deserve my gratitude for the projects we carried out together, especially Viivi Jokinen, Julia Johansson, Aapo Tervonen, Taina Viheriälä, Heli Skottman, and Kati Juuti-Uusitalo. Our laboratory technician and my good friend Outi Heikkilä, without your support I would have never finished this dissertation.

In addition, I would like to thank the personnel from the Tampere Imaging Facility, especially Outi Paloheimo, and the personnel from the Tampere Facility of Electrophysiological Measurements, especially Juha Heikkilä and Dmitry Fayuk, for your help with high technical expertise.

Virpi Alarautalahti, Heidi Halonen, Amna Abu Khamidakh, and Antti Ahola, thank you for your friendship during all these years at the university. Ilmari Tamminen and Markus Hannula, thank you for me always being welcome to the μCT room.

My parents, mummi, parents-in-laws, and friends, I want to express my gratitude for all the support. With love, I thank my husband Henkka for walking by my side the past 19 years and for being a great father to our children Anni, Eevi, and Otso. You have taught me more about life than I could have ever imagined.

Iina Korkka
Nurmijärvi, June 15, 2022

ABSTRACT

Retinal pigment epithelium (RPE) is crucial for our visual ability performing important functions for the maintenance of photoreceptor viability. Correct physiological functionality is a prerequisite for RPE to execute all its retinal maintenance tasks, several of which are dependent on the various ion channels it expresses. Malfunctions in RPE physiology often cause vision-threatening retinal diseases that can eventually lead to blindness. Stem cell-derived RPE provides a potential model system to investigate RPE physiology and pathophysiology while serving as a cell source for cell transplantation therapies to replace the diseased RPE.

The aim of this dissertation was to investigate the physiology of human embryonic stem cell (hESC)-derived RPE concentrating on ionic signaling and to evaluate these features compared to the native counterpart. This aim was approached by determining the distribution of different ion channels with immunostainings and confocal microscopy in the hESC- and native mouse RPE. The functionality of the ion channels in these cells was studied with patch clamp electrophysiology by recording ionic currents across the cell membrane. The physiological role of ion channels was evaluated for two key processes in the RPE: 1) the phagocytosis of the photoreceptor outer segments (POS) by performing phagocytosis assays and 2) the secretion of the vascular endothelial growth factor (VEGF) using ELISA. These assays were combined with manipulation of ion channel activity with pharmacological compounds. Computational modeling was used to investigate the intra- and intercellular Ca^{2+} signaling in the RPE monolayer.

In this thesis, a diverse pattern of Ca^{2+}, K^+, and Cl^- channels were detected at the protein level from the hESC-RPE cell membrane, and generally, the ion channel localization profile was comparable to the native mouse RPE. The basolateral localization of inwardly rectifying K^+ channel Kir7.1 and the apical localization of L-type voltage-gated Ca^{2+} channel $Ca_V1.3$ were found here as novel observations in the RPE. Furthermore, the work revealed a link between $Ca_V1.3$ and RPE development as the $Ca_V1.3$ channel localization changed remarkably during RPE maturation. Considering physiological relevance, the L-type Ca^{2+} channels participated in the regulation of phagocytosis and VEGF secretion. The features of L-type Ca^{2+} currents recorded from the hESC-RPE resembled those measured from

the native mouse RPE in this study as well as the native RPE reported in the literature. However, differences appeared between K^+ currents in the hESC-RPE compared to the literature from the native RPE, especially with the Kir currents. This may indicate a compromised functionality of Kir channels in the hESC-RPE.

In conclusion, ion channels are highly sensitive to the external cell culture conditions as well as the maturation level of the RPE. Thus, assessing the functional phenotype of the stem cell-derived RPE is extremely important when evaluating the physiological maturity of the cells and their capability to perform the crucial tasks of the native RPE. All in all, the presence of functional machinery of ion channels in the hESC-RPE indicates great potential for their use as cell models and in transplantation therapies.

TIIVISTELMÄ

Silmän verkkokalvon pigmenttiepiteeli (retinal pigment epithelium; RPE) on erityisen tärkeä näköaistinsolujen toiminnan ja siten myös koko näköaistin kannalta. Ionikanavien oikealainen toiminta puolestaan on edellytys sille, että RPE suoriutuu kaikista tehtävistään. RPE:n fysiologiaan liittyvät toimintahäiriöt johtavat usein näkökykyä heikentäviin sairauksiin, jotka saattavat edetä aina sokeuteen asti. Kantasoluista erilaistetut RPE-solut ovat hyvä solumalli RPE:n perustoimintojen ja sairauksien tutkimiseen. Toisaalta niitä voidaan potentiaalisesti käyttää myös vahingoittuneen RPE-kudoksen korvaamiseen solusiirrehoidoissa näkökykyä uhkaavien sairauksien parantamiseksi.

Tämän väitöskirjatyön tavoitteena oli tutkia ihmisen alkion kantasoluista erilaistetun RPE:n fysiologiaa ja ioneihin liittyvää signalointia sekä verrata saatuja tuloksia natiiviin kudokseen. Ionikanavien lokalisoitumista solukalvolla kantasoluista erilaistetussa RPE:ssä ja natiivissa hiiren RPE:ssä selvitettiin immunovärjäysten ja konfokaalimikroskopian avulla. Ionikanavien toiminnallisuutta tutkittiin patch clamp – menetelmällä, jolla mitataan solukalvon läpi kulkevia ionivirtoja. Ionikanavien roolia RPE:n fysiologiassa arvioitiin käyttämällä farmakologisia yhdisteitä ja mittaamalla RPE:n kykyä fagosytoida näköaistinsolujen ulkojäseniä. Vastaavaa farmakologiaa sekä ELISA-menetelmää käytettiin verisuonen endoteelin kasvutekijän (vascular endothelial growth factor; VEGF) erityksen mittaamiseen. Lisäksi laskennallisella mallinnuksella tutkittiin solun sisäistä ja solujen välistä Ca^{2+} signalointia.

Tässä työssä löydettiin monipuolinen koneisto Ca^{2+}, K^+ ja Cl^- -kanavia kantasoluista erilaistetusta RPE:stä. Näiden kanavien lokalisoituminen solukalvoilla vastasi suurelta osin hiirestä saatuja tuloksia. K^+-kanava Kir7.1:n basolateraalinen sijainti ja Ca^{2+}-kanava $Ca_V1.3$:n apikaalinen sijainti RPE:ssä havaittiin tässä työssä ensimmäistä kertaa. $Ca_V1.3$:n ja RPE:n kehityksen välillä huomattiin yhteys, sillä $Ca_V1.3$:n lokalisaatio muuttui merkittävästi kudoksen kypsymisen myötä. L-tyypin Ca^{2+}-kanavat osallistuivat myös fagosytoosin ja VEGF:n erityksen säätelyyn kantasoluista erilaistetussa RPE:ssä. Lisäksi L-tyypin Ca^{2+}-kanavista mitatut virrat muistuttivat tässä työssä natiivista hiiren RPE:stä mitattuja virtoja sekä kirjallisuudessa esitettyjä tuloksia. Kantasoluista erilaistetusta RPE:stä mitatut K^+-

virrat kuitenkin vastasivat vain osittain kirjallisuudessa esitettyjä natiivin aikuisen RPE-kudoksen ominaispiirteitä, mutta osoittivat samankaltaisuutta primääriviljelmistä tai natiivista sikiön RPE:stä saatuihin tuloksiin. Tästä johtuen näihin kanaviin liittyvät toiminnot voivat olla natiivia kudosta heikompia kantasoluista erilaistetussa RPE:ssä.

Johtopäätöksenä todettakoon, että ionikanavat ovat erityisen herkkiä solujen kypsyysasteelle ja viljelyolosuhteille. Tästä syystä kantasoluista erilaistetun RPE:n toiminnallisen fenotyypin määrittäminen on tärkeää solujen kypsyyden ja toimintakyvyn arvioimisessa. Ennen kaikkea tässä työssä selvitetty laaja ja funktionaalinen ionikanavien koneisto kertoo kuitenkin kantasoluista erilaistetun RPE:n käytön hyvistä mahdollisuuksista solumalleissa ja solusiirrehoidoissa.

CONTENTS

ABBREVIATIONS

AMD	Age-related macular degeneration
Ano	Anoctamin channel
ATP	Adenosine triphosphate
Best-1	Bestrophin-1
$[Ca^{2+}]_i$	Intracellular Ca^{2+} concentration
Ca^{2+}	Calcium ion
CaCC	Ca^{2+}-activated Cl^- channel
Ca_V	Voltage-gated Ca^{2+} channel
CFTR	Cystic fibrosis transmembrane conductance regulator
Cl^-	Chloride ion
ClC-2	Chloride channel 2
ELISA	Enzyme-linked immunosorbent assay
ER	Endoplasmic reticulum
FGF	Fibroblast growth factor
GA	α-glycyrrhetinic acid
GJs	Gap junctions
HCO_3^-	Bicarbonate
hESC	Human embryonic stem cell
hfRPE	Human fetal RPE
hiPSC	Human induced pluripotent stem cell
IP_3	Inositol 1, 4, 5 - trisphosphate
IP_3R_3	IP_3 receptor type 3
K^+	Potassium ion
Kir	Inwardly rectifying K^+ channel
K_V	Voltage-gated K^+ channel
L	Ligand
MERTK	Mer tyrosine kinase
MS	Mechanically stimulated
Na^+	Sodium ion
NB	Neighboring cell (layer)

NF	Normalized fluorescence
PCNT	Pericentrin
PEDF	Pigment epithelium-derived factor
PIP_2	Phosphatidylinositol 4,5-bisphosphate
PLC	Phospholipase C
PMCA	Plasma membrane Ca^{2+}-ATPase
POS	Photoreceptor outer segment
RPE	Retinal pigment epithelium
RT	Room temperature
RyR	Ryanodine receptor
SERCA	Sarco/endoplasmic reticulum Ca^{2+}-ATPase
SSCC	Stretch-sensitive Ca^{2+} channel
TEP	Transepithelial potential
TER	Transepithelial resistance
TRP	Transient receptor potential
UTP	Uridine triphosphate
VEGF	Vascular endothelial growth factor
ZO-1	Zonula occludens 1

ORIGINAL PUBLICATIONS

Publication I Korkka I, Viheriälä T, Juuti-Uusitalo K, Uusitalo-Järvinen H, Skottman H, Hyttinen J, Nymark S. Functional voltage-gated calcium channels are present in human embryonic stem cell-derived retinal pigment epithelium. Stem Cells Transl Med. 2019, 8(2):179-193.

Publication II Korkka I, Skottman H, Nymark S. Heterogeneity of potassium channels in human embryonic stem cell-derived retinal pigment epithelium. Manuscript. Accepted for publication in Stem Cells Transl Med.

Publication III Korkka I*, Johansson JK*, Skottman H, Hyttinen J, Nymark S. Characterization of chloride channels in human embryonic stem cell derived retinal pigment epithelium. EMBEC & NBC 2017. IFMBE Proceedings, 2017, 65:454-457.

Publication IV Vainio I, Abu Khamidakh A, Paci M, Skottman H, Juuti-Uusitalo K, Hyttinen J, Nymark S. Computational model of Ca^{2+} wave propagation in human retinal pigment epithelial ARPE-19 cells. PLoS One. 2015, 10(6):e0128434.**

*Authors contributed equally.

**Publication was included in the doctoral dissertation "Assessment of Ca^{2+} Dynamics in Human Retinal Pigment Epithelial Cell Cultures" by Amna Abu Khamidakh at the Faculty of Medicine and Health Technology, Tampere University, Finland, in 2019.

AUTHOR'S CONTRIBUTION

Publication I The study was designed by Korkka and Nymark with Viheriälä contributing to the maturation studies. The experimental work and data analysis were performed primarily by Korkka with Viheriälä executing the research related to maturation. The results were interpreted by Korkka, Viheriälä, and Nymark, who wrote the manuscript with contributions from all co-authors.

Publication II Korkka and Nymark designed the study, interpreted the results, and wrote the manuscript. Korkka performed the experimental work and data analysis. Skottman provided stem cell expertise and contributed to the writing of the manuscript.

Publication III Korkka and Johansson designed the study, performed the experiments and data analysis, interpreted the results, and wrote the manuscript with equal contributions. Nymark contributed to the writing of the manuscript.

Publication IV Vainio created the computational model and wrote the manuscript with the help of Hyttinen and Nymark. The experimental data for modeling was generated by Abu Khamidakh. All co-authors contributed to the writing of the manuscript.

1 INTRODUCTION

Retinal pigment epithelium (RPE) is vital for retinal welfare and thus highly important for our vision. RPE consists of a monolayer of polarized and pigmented epithelial cells positioned next to the retina between the photoreceptors and the choroid. RPE serves as the outer blood-retina barrier transporting ions, water, nutrients, oxygen, and waste products, secreting growth factors, controlling the ionic homeostasis of the subretinal space, retaining photoreceptor light sensitivity, and maintaining their viability by the phagocytosis of the photoreceptor outer segments (POS) [1, 2]. RPE has an essential role in the pathogenesis of degenerative eye diseases, from which age-related macular degeneration (AMD) is the primary reason of impaired vision among the elderly worldwide [3]. Currently, in Europe alone, 67 million people have been diagnosed with AMD [4]. Devastatingly, there is no significant cure for retinal degenerative diseases with the present treatment strategies.

Stem cell technology with human embryonic stem cell (hESC) and human induced pluripotent stem cell (hiPSC) derived RPE has improved the possibility to develop model systems to investigate RPE functionality and RPE-related diseases that can eventually lead to blindness [5-19]. Stem cell-derived RPE also provides great potential for transplantation therapies that aim to replace the diseased RPE with healthy stem cell-derived tissue [20-28]. Stem cell-derived RPE resembles the native RPE in many respects, for example, in its capacity to secrete growth factors [29-32] and phagocytose POS particles [10, 29, 32, 33]. However, there is only limited information about the ionic signaling in stem cell-derived RPE [29, 30, 33]. Still, transplantation therapies based on these cells have already proceeded to clinical trials [20-28] without a detailed characterization of their electrophysiological properties. The important ionic signaling mechanisms set the basis for RPE functionality via the action of ion transporters and ion channels that regulate or execute the RPE-specific functions. On the other hand, malfunctions in the ionic machinery may lead to suppressed activity of the RPE so that it is unable to perform its important tasks predisposing the retina to the pathogenesis of vision-threatening diseases.

The aim of this dissertation was to investigate the RPE physiology focusing on the ionic signaling mechanisms of the RPE. This aim was driven by an overarching

hypothesis that the stem cell-derived RPE expresses diverse machinery of functional ion channels relevant to RPE physiology. Characterization of the ion channels benefits the evaluation of stem cell-derived RPE for transplantation therapies and its use as an RPE cell model in fundamental cell biology research as well as in the studies of the pathogenesis of RPE-related diseases.

2 LITERATURE REVIEW

2.1 The retina and the retinal pigment epithelium (RPE)

The human eye is an organ giving us visual ability. It can be divided into three regions (Figure 1A): The outer region consisting of the cornea and the sclera, the middle region including the iris, the ciliary body, and the choroid, and the inner region consisting of the retina and the retinal pigment epithelium (RPE). The neural retina is further organized in parallel layers (Figure 1B), with ganglion cells forming the innermost layer followed by a layer consisting of bipolar cells, amacrine cells, and horizontal cells, and the outermost layer formed by rod and cone photoreceptors. Müller cells extend throughout the retina from the ganglion cell level to the photoreceptors. RPE underlines the neural retina, and these two tissues are in intimate physical and functional interaction. [34]

The cornea is the most anterior part of the eye, and together with the lens, it transmits light to the inner sections. The amount of light reaching the retina is regulated by the iris that controls the size of the pupil. The cornea connected to the sclera protects the eye against external and internal forces. Light travels to the back of the eye, reaching the retina, where it is captured and conversed into an electrical signal by the photoreceptors. [34] The photoreceptors have optimized their functionality so that the cones dominate the bright light vision and are responsible for detecting color and fine details, whereas rods with their high sensitivity are responsible for the dim-light vision. The fovea is a specialized center for the sharp vision that is devoid of rods and where the cones are densely packed. [35] The signal from the photoreceptors is processed in bipolar, amacrine, horizontal, and ganglion cells, with Müller cells supporting the retina structurally and functionally. The electrical signal is translated into nerve impulses by ganglion cells whose axons form the optic nerve that sends the signal to the brain for further processing and visual sensation. [34]

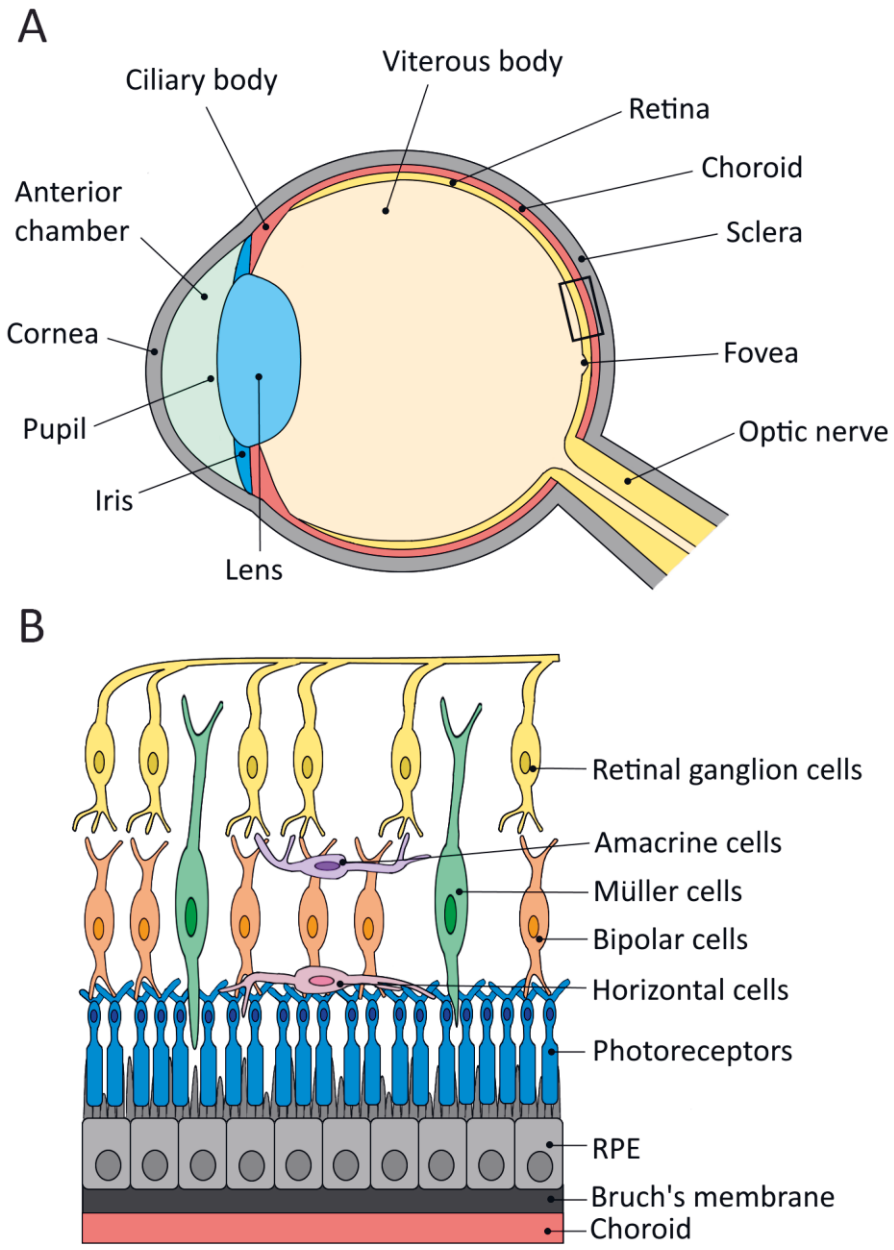

Figure 1. Anatomy of (A) the eye and (B) the retina with the retinal pigment epithelium (RPE). The black rectangle in the back of the eye highlights the retina, the RPE, and the choroid. The image is re-drawn with modifications from Willoughby et al 2010 [34], Fu et al. 2020 [36], and Keeling et al. 2018 [37].

RPE is a monolayer of hexagonal and pigmented cells located between the photoreceptors and the choroid, forming an epithelial barrier [1]. Tight junctions have an essential role in this barrier since they connect the membranes of neighboring cells with apical cell-cell junctions that prevent free paracellular diffusion. The major proteins the tight junctions are composed of include claudins with a regulatory function, occludins responsible for selectivity to different ions and molecules, and zonula occludens (e.g., ZO-1), forming structural connections with the actin cytoskeleton. [38] As a polarized epithelium, the apical and basolateral membranes of the RPE differ in structure and membrane protein distribution [1], for example, Na^+/K^+-ATPase localizes on the apical cell membrane [39-45]. Melanin pigment granules appear in the apical cytoplasm of the RPE, and the apical microvilli face the photoreceptor outer segments. The basolateral membrane of the RPE forms deep folds and contacts the Bruch's membrane, which locates above the fenestrated choriocapillaris. [34]

The barrier structure, together with the ion transporters and ion channels, defines the electrical properties of the RPE at the monolayer level. Transepithelial resistance (TER) is often used to measure epithelial integrity that is usually over 200 $\Omega \cdot cm^2$ in RPE [31, 45-51]. Transepithelial potential (TEP) describes the voltage difference between the apical and the basolateral cell membranes ranging from 1 to 6 mV so that the basolateral membrane is depolarized compared to the apical membrane [31, 47-49, 51-53].

2.1.1 Functions of the RPE

RPE has many critical functions related to the maintenance of the photoreceptors and our vision (Figure 2). The main RPE functions reviewed e.g., by Strauss 2005 [1] are transepithelial transport between the subretinal space and the choroid, phagocytosis of photoreceptor outer segments, secretion of growth factors, protection against photo-oxidation by the absorption of light, spatial buffering of the ions in the subretinal space, and supporting the visual cycle. It is essential for the visual ability that RPE performs its tasks properly since RPE dysfunctions often lead to visual disorders and even blindness. [1]

RPE transports ions and water from the subretinal space to the bloodstream benefiting the structural integrity of the retina by creating adhesion forces. Intraocular pressure and the large metabolic activity of the neurons and the photoreceptors produce water in the retina. The transport of water is mostly driven

by changes in potassium (K^+) and chloride (Cl^-) concentrations that are tightly coupled to the function of active transporters. [1] RPE also maintains the viability of the photoreceptors by eliminating their metabolic end products, such as lactate [54, 55]. In addition, RPE transports glucose [56, 57], vitamin A [58, 59], O_2 [60, 61], and docosahexaenoic acid [62, 63] from the bloodstream to the photoreceptors.

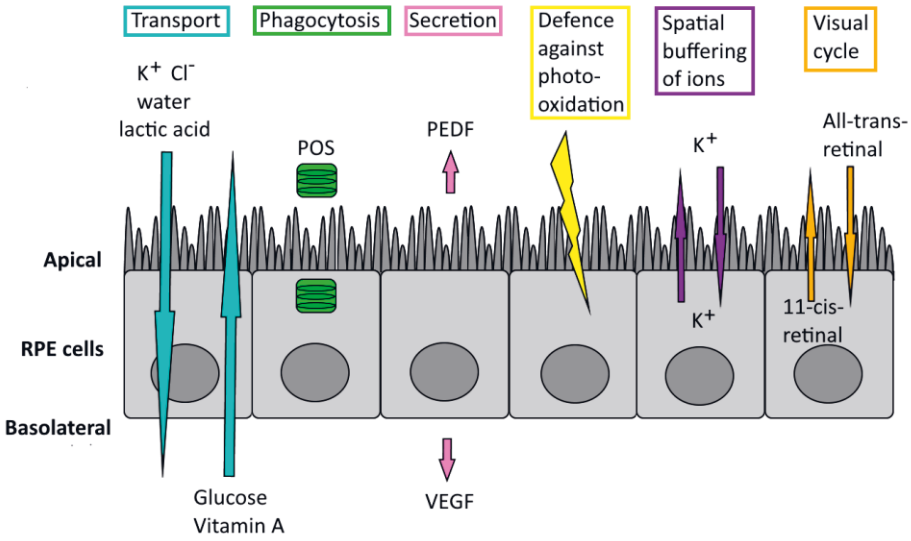

Figure 2. The main functions of the RPE: transepithelial transport, phagocytosis, secretion, defense against photo-oxidation, spatial buffering of ions, and visual cycle. The image is re-drawn with modifications from Strauss 2005 [1].

The present knowledge highlights the metabolic relationship between the RPE and the retina as a metabolic ecosystem that promotes the survival of this ensemble [60, 64]. The photoreceptors take up high amounts of glucose and convert it to lactate, which further acts as a fuel for the neighboring retinal cells. Using lactate, the photoreceptors also suppress the glycolysis in RPE, protecting the glucose so that more of it reaches the retina. [64] Another important process of the metabolic ecosystem is the malate-succinate shuttle that delivers unused reducing power, i.e., electrons, from the hypoxic retina to the oxygen-rich RPE-choroid complex. The hypoxic environment in the retina drives the cells to use fumarate as an electron acceptor instead of O_2. The reverse succinate dehydrogenase reaction uses fumarate to produce succinate, which is exported to the RPE-choroid complex and oxidized to malate. Malate is then transferred back into the retina and converted to fumarate. [60]

The photoreceptors are exposed to high levels of light that cause the accumulation of photo-oxidative radicals and photo-damaged molecules in the cell. Therefore, the photoreceptors are renewed constantly, and the damaged tips of POS are phagocytosed by the RPE. [65, 66] The apical membrane contains receptors, of which αvβ5 integrin facilitates POS binding and Mer tyrosine kinase (MERTK) POS ingestion [65-68]. In digestion, the phagosomes mature during migration from the apical to the basolateral direction. The final degradation occurs when a mature phagosome unites with a lysosome forming a phagolysosome. [65, 66] POS phagocytosis follows a circadian rhythm, and at least in rod-dominant species, the highest activity takes place soon after the light onset [69-71].

RPE secretes several different growth factors to support the choriocapillaris and the photoreceptors, including fibroblast growth factor (FGF), pigment epithelium-derived factor (PEDF), and vascular endothelial growth factor (VEGF). [1] The secretion of PEDF and VEGF is polarized so that PEDF is mainly secreted to the apical side [46, 47, 72] and VEGF to the basolateral side [46, 47, 73, 74]. VEGF stabilizes the endothelium of the choriocapillaris [75]. PEDF is a neuroprotective factor and angiogenesis inhibitor, thus, it maintains the structure of the retina, promoting the survival of the photoreceptors [76-78].

The combination of light focused on the retina and an oxygen-rich environment with high blood flow of the choriocapillaris predisposes the retina to light and oxygen-induced damage. To defend against these threats, RPE contains melanin pigments in melanosomes that absorb and filter light. RPE also contains antioxidants, including superoxide bismutase, catalase, and carotenoids that protect RPE against photo-oxidation. [1, 79]

Following light detection in the photoreceptors, the K^+ concentration in the subretinal space decreases from 5 mM to 2 mM [80]. RPE compensates for these fast changes in the subretinal ion composition by a process called spatial buffering of ions which is important for the maintenance of photoreceptor excitability [1]. The mild inwardly rectifying K^+ channels are inversely dependent on the extracellular K^+ concentration, and therefore, a decrease in subretinal K^+ concentration increases the conductance of these channels on the apical membrane [81-83]. This leads to the recycling of K^+ ions across the apical cell membrane between the RPE and the subretinal space. [1]

All-trans retinal is formed from 11-cis-retinal in the photoreceptors during photon absorption, but the photoreceptors lack the ability to re-isomerize this molecule. Therefore, in the visual cycle RPE re-isomerizes all-trans-retinal back into

11-cis-retinal that is transported to the photoreceptors to maintain their light sensitivity. [1]

2.1.2 RPE-associated eye diseases cause a loss of vision

Several RPE-related disorders, including age-related macular degeneration (AMD), Stargardt disease, and bestrophinopathies, cause loss of vision and can eventually lead to blindness. These diseases are inheritable or caused by daily environmental stress in the eye. A common feature for them is the malfunctioning of the RPE which leads to the destruction of the photoreceptors.

AMD is the primary cause of vision loss and blindness in Europe, especially among the elderly. Currently, 67 million European people are influenced by any form of AMD, and this number is predicted to increase to 77 million by 2050. [4] The pathogenesis of AMD is a complex process. It involves the accumulation of lipofuscin due to dysfunction of the RPE phagocytic and metabolic activity as well as the formation of drusen between the RPE and the Bruch's membrane. This further activates chronic inflammation and choroidal or subretinal neovascularization linked to unbalanced angiogenic signaling of VEGF and PEDF. The new leaky vessels often bleed and form dense macular scars that are the main reason for the final vision loss in AMD. The disease is called dry-AMD until it proceeds to neovascularization, and after that, it is called wet-AMD. The traditional therapies for the treatment of AMD include photodynamic therapy, transpupillary thermotherapy, thermal laser photocoagulation, and injection of anti-angiogenic agents. [84] These therapies only prevent the progression of dry-AMD to wet-AMD, and no therapy is approved for the late form of dry-AMD since the restoration of the damaged RPE cells or the photoreceptors is not currently possible. However, several treatment strategies are under investigation considering nutritional supplements, anti-inflammatory therapy, neuroprotective therapy, lipofuscin and visual cycle inhibitors, and choroidal blood flow restoration agents. [85]

Stargardt disease is another common form of macular dystrophy, but unlike AMD, it is common among children and young adults with a prevalence of 1:8000-10000 [86]. This inherited eye disease is most often caused by mutations in ABCA4 gene. The development of visual disorders and blindness in Stargardt disease is associated with the dysfunction of RPE that leads to the degeneration of the photoreceptors. [87, 88]

Bestrophinopathies are inherited retinal dystrophies disturbing the vision. These disorders are caused by over 250 different mutations in bestrophin-1 gene that codes a Ca^{2+}-activated Cl^- channel in the RPE. The most common bestrophinopathy is the Best disease, whose onset occurs during childhood or early adulthood with a prevalence of 1:5000-1:67000. [89]

Currently, there is no cure to the retinal disorders originating in the RPE that cause loss of vision and blindness. Gene therapy is under investigation, and it is a potential treatment for visual disorders targeting specific genetic mutations in the eye [90-92]. On the other hand, stem cell transplantation therapies aim to replace the damaged RPE and restore the vision, and these treatments have already proceeded on clinical trials [20-28]. In addition, the new disease-specific human RPE cell models derived from stem cells provide a way to investigate the pathogenesis of RPE-based diseases [5-19].

2.1.3 Stem cell-derived RPE in transplantation therapies and human cell models

Stem cells are unique cells that have the ability to self-renew and produce specialized progeny. Human embryonic stem cells (hESC) are pluripotent cells produced from blastocysts. Human induced pluripotent stem cells (hiPSC) are derived from adult somatic cells, such as fibroblasts, that are reprogrammed into a pluripotent state. Both stem cell types can be differentiated into any cell type of the body. After various cell cultivation steps that include differentiation and maturation, the cells develop into hESC-RPE or hiPSC-RPE that are presently tested in clinical trials for cell transplantation therapies and used as human cell models in health and disease, as illustrated in Figure 3. [93]

Cell transplantation is a procedure where the cells, such as stem cell-derived RPE, are delivered to the target site of the human body. The administration of the RPE cells to the human retina can be performed either with cell sheets or cell suspension. A subretinal cannula is used to inject the RPE cell suspension, while the transplantation of the cell sheet requires a more invasive surgical procedure. Therefore, the risk for surgical complications is higher with the cell sheet compared to the cell suspension. [94]

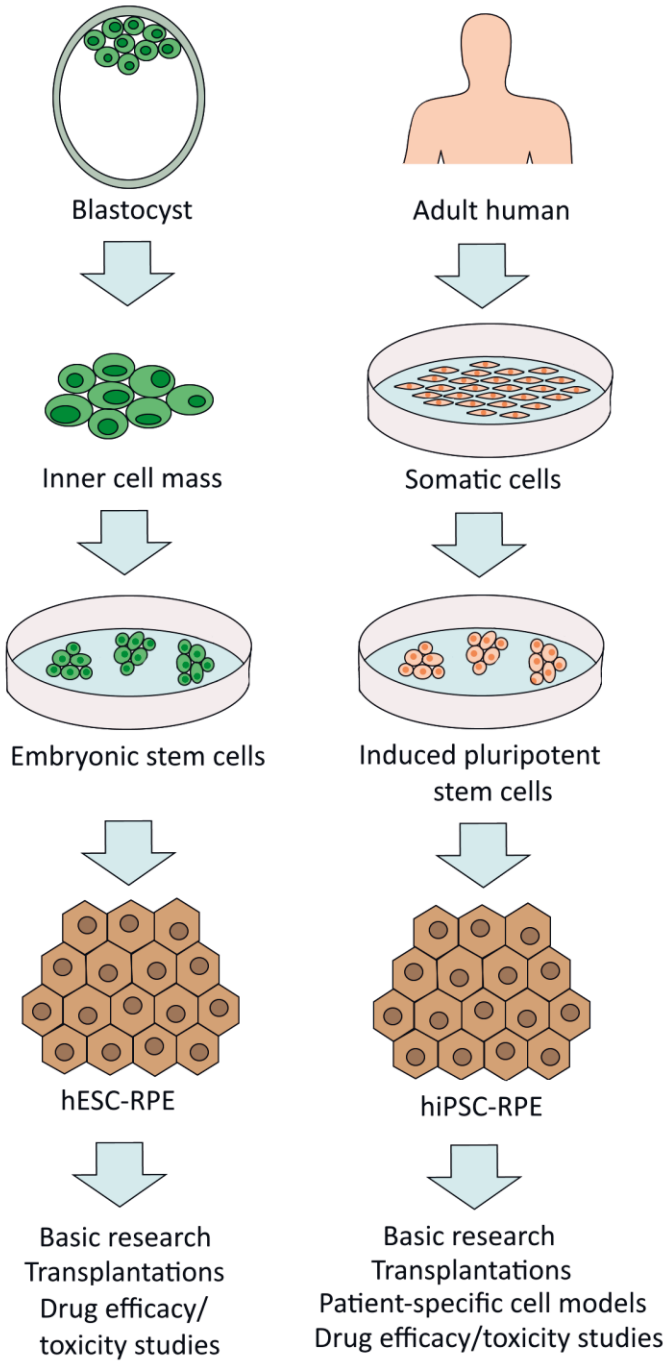

Figure 3. The origin and development of human embryonic stem cell (hESC)-RPE and human induced pluripotent stem cell (hiPSC)-RPE. The image is re-drawn with modifications from Lutolf et al. 2009 [93].

The stem cell-derived RPE transplantation therapies are already investigated in clinical trials for patients with AMD [20-26] and Stargardt disease [20, 22, 26-28], aiming to improve the visual ability and evaluate the safety of the treatment. So far, the clinical trials have mainly utilized the hESC-RPE cells [20, 22-28]. In most of these studies, the visual ability was improved to some extent during the follow-up period [20, 22, 23, 25, 26] showing signs of anatomic stability of the hESC-RPE or integration of the transplant to the host [22-24, 26, 28]. No serious safety issues resulting from the transplanted cells were reported, such as hyperproliferation, tumorigenicity, or rejection-related inflammatory responses [20, 22, 23, 26-28].

The hiPSC-RPE provides an alternative to use patient-specific cell lines reprogrammed from adult somatic cells. These cells can also be applied to targeted gene therapy for transplantation that aims to correct the genetic defects using healthy autologous hiPSC-RPE [95]. Mandai et al. presented an autologous hiPSC-RPE sheet generated from skin fibroblasts that was transplanted under the retina in one patient with neovascular AMD. After a one-year follow-up, the implanted hiPSC-RPE sheet was intact, and the procedure did not affect the visual ability. [21]

The hiPSC-RPE is also a well-warranted human RPE cell model to investigate the physiology of the RPE. In addition, the patient-specific or disease-specific hiPCS-RPE is a useful tool to study the pathogenesis of RPE-derived retinal diseases. The specific hiPSC-RPE cell lines are presently used to study physiological processes such as phagocytosis [6, 7, 10, 15, 19], and diseases such as Bestrophinopathies [5, 8-12, 17], AMD [16], and Batten disease [13].

2.2 Ion channels in the RPE function

The electrophysiological properties of the RPE are key determinants of cellular and epithelial functionality and enable RPE to perform its functions that are critical for retaining vision. Ionic signaling in the RPE combines the following aspects into a functional entity: 1) Ion gradients are created and maintained by active ion transporters across the cell membranes and membranes of the intracellular organelles. 2) The work done by the ion transporters enables the ion channels to conduct ions down the electrochemical gradients. 3) Ion transporters and ion channels respond to external and intracellular conditions and specific stimuli mediating cellular functions with either regulatory or direct roles. 4) The ionic signaling mechanisms participate in numerous signaling cascades that control, for

instance, transepithelial transport of ions and water, secretion, phagocytosis, and ionic homeostasis of the RPE and the subretinal space.

2.2.1 Ion transporters

Differences in ion concentration and charge between the inside and outside of the cell generate an electrochemical gradient for an ion across the cell membrane. This gradient drives the movement of ions down the electrochemical gradient, and at the reversal potential of each ion type, the net movement of the ion ceases. In the RPE, the extracellular ion concentrations are higher than the cytosolic ion concentrations for Na^+, Cl^- and Ca^{2+}, and at the resting membrane potential their driving force is oriented inward of the cell. For K^+ ions, the electrochemical gradient is the opposite since the extracellular ion concentration is lower than the cytosolic. [2, 96] Ion channels are membrane proteins that form pores to permit rapid, highly selective, and tightly regulated ion movement down the electrochemical gradient. On the contrary, active transporters move ions against the electrochemical gradient either by hydrolyzing ATP (ATPases) or using the movement of an ion down its electrochemical gradient to transport the other ion against its electrochemical gradient (cotransporters and exchangers). The transporters have a critical role in creating and maintaining the ionic gradients across the cell membrane enabling complex ionic signaling and homeostatic regulation via ion channels. [97, 98]

Na^+/K^+-ATPase and $Na^+/K^+/2Cl^-$ cotransporter

Na^+/K^+-ATPase maintains a steep Na^+ gradient between the extracellular space and the cytosol. This gradient supports the transport of various ions, molecules, and metabolic endproducts from the subretinal space into the RPE. [2] Several studies have shown the presence of Na^+/K^+-ATPase in the native and cultured RPE predominantly on the apical membrane [39-45]. The unique apical localization of Na^+/K^+-ATPase is based on the opposite polarity of the entire membrane-cytoskeleton complex [99] and the expression of the β subunit [100]. Misfunctions in these mechanisms may cause Na^+/K^+-ATPase distribution also on the basolateral cell membrane in the cultured RPE [41, 42, 45]. Modifications in Na^+/K^+-ATPase activity were found to alter the tight junction structure and permeability [45]. In addition, hyperglycemia impairs Na^+/K^+-ATPase function in the RPE cells, which may contribute to the pathogenesis of diabetic retinopathy [101]. Apical Na^+/K^+-ATPase together with apical $Na^+/K^+/2Cl^-$ cotransporter continuously transport K^+

into the RPE [2] and account for the transepithelial transport of ions and water [102-106] that is controlled by the changes in extracellular K^+ and Cl^- levels [45, 104]. To support the function of Na^+/K^+-ATPase, inwardly rectifying K^+ (Kir) channel Kir7.1 recycles the redundant K^+ over the apical membrane [107, 108].

pH regulation by Na^+/H^+ exchanger, Na^+/HCO_3^- cotransporter, and Cl^-/HCO_3^- exchanger

The oxygen consumption of the photoreceptors increases in the dark which produces CO_2 and water to the subretinal space. These metabolic byproducts are transported to the choroidal blood supply by the RPE, which maintains the pH and volume homeostasis of the subretinal space. [109] Apical Na^+/H^+ exchanger [110-112], apical Na^+/HCO_3^- cotransporter [112, 113], and basolateral Cl^-/HCO_3^- exchanger [112, 113] are involved in the regulation of pH in the RPE and the subretinal space. These functions are related to the transepithelial transport of HCO_3^-. The stimulation of Cl^-/HCO_3^- exchanger is dependent on intracellular pH so that it is activated by increased intracellular HCO_3^- concentration due to alkalinization of the cytosol [112, 114]. This results in the acidification of the cytosol that stimulates Cl^- and water absorption across the RPE [109, 114]. In addition, Na^+/H^+ exchanger is involved in the control of the balance between autophagy and apoptosis [115], and its function is downregulated by sustained elevation of extracellular glucose [116].

Ca^{2+} transport by Na^+/Ca^{2+} exchanger and Ca^{2+}-ATPase

A Na^+/Ca^{2+} exchanger eliminates Ca^{2+} efficiently from the cytoplasm. This way, RPE can handle the large amounts of Ca^{2+} that it contains. [2] The Na^+/Ca^{2+} exchanger in the RPE was identified as the cardiac type [117, 118] locating in the apical membrane [119]. The Na^+/Ca^{2+} exchanger participates in the regulation of thrombin-induced glutamate release from the RPE [120]. The removal of Ca^{2+} from the cytoplasm is supported by the Ca^{2+}-ATPase on the plasma membrane, and this transport is powered by the hydrolysis of ATP [121].

2.2.2 Potassium (K^+) channels

Potassium (K^+) channels form a prominent family of ion channels in the RPE. These channels include voltage-gated K^+ (K_V) channels, inwardly rectifying K^+ (Kir) channels, and Ca^{2+} activated K^+ channels, which are all constructed from four pore-

forming subunits [2]. In this chapter, we focus on the beforementioned K^+ channels, yet there exists also two-pore K^+ channels in the RPE that are known to protect RPE against oxidative stress [122]. In general, K^+ channels participate in several RPE functions such as control of cell volume [123, 124], phagocytosis [125, 126], and growth factor secretion [29], generation of the membrane potential [127], transport of ions and water [2], and response to changes in illumination [80]. The main K^+ channel subtypes in the RPE are summarized in Figure 4, and they are introduced in detail in this chapter. K_V channels and Kir channels are investigated in the hESC-RPE in this dissertation and will be covered in the results and discussion chapters (**Study II**).

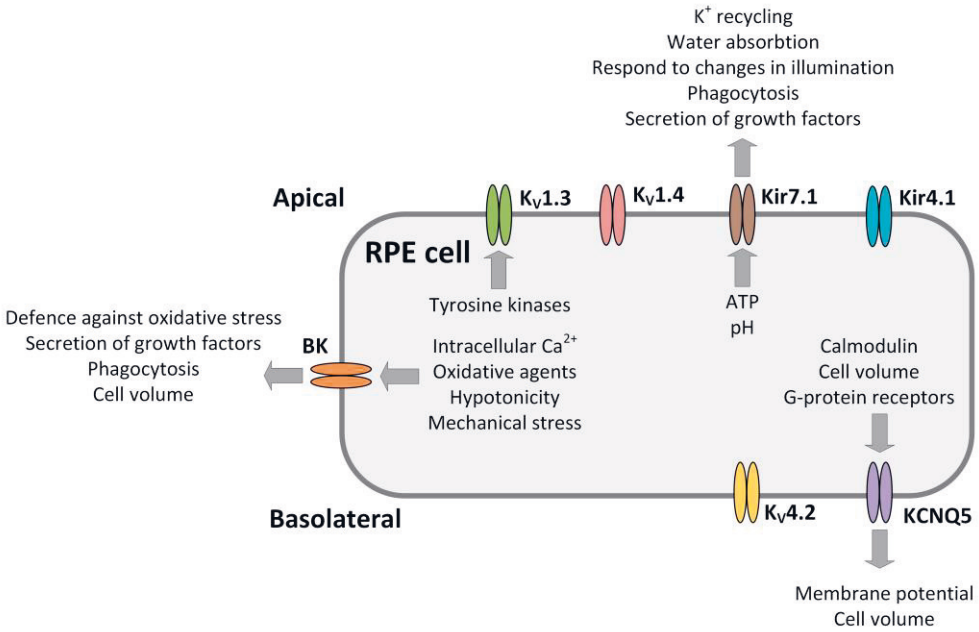

Figure 4. Schematic diagram of the localization, regulation, and function of K^+ channels in the RPE including voltage-gated K^+ (K_V) channels, inwardly rectifying K^+ (Kir) channels, and Ca^{2+}-activated BK channels. Each K^+ channel type is presented with a different color. The regulatory mechanisms of each ion channel are listed next to the arrows pointing towards the ion channel, while the arrows pointing outwards the ion channel indicate the cellular functions that the channel regulates.

Voltage-gated K^+ (K_V) channels

A heterogeneous class of K_V channels conducts outward K^+ currents during depolarization. This class is further divided into delayed rectifier K^+ channels, KCNQ channels, and A-type K^+ channels, and they differ in their activation and

inactivation kinetics, voltage sensitivity, and selectivity to different pharmacological modulators.

Delayed rectifier K^+ currents have been measured from the native and cultured RPE from different species [128-136], including human [133] with nearly 100 % incidence [131-136], meaning that this conductance is present in almost every recorded cell. The currents have been reported to activate at around -30 mV [128-136] and to be sensitive to extracellular Ba^{2+} [128, 131, 134], TEA [131-135] and Agitoxin-2 [130, 136]. The sensitivity to Agitoxin-2 identifies the contribution of $K_V1.3$ channel subtype to the delayed rectifier currents. The presence of $K_V1.3$ has been verified by immunolabeling [136, 137] with localization to the apical membrane of the RPE [137]. Tyrosine kinases regulate $K_V1.3$ by shifting their activation threshold without changing the membrane potential [130].

KCNQ channels (KCNQ1-KCNQ5), also called $K_V7.1$-$K_V7.5$ channels, have an essential role in RPE functionality as they participate in the generation of the membrane potential [127] and control of the cell volume [123]. These functions further promote the epithelial transport of ions and water [2]. Calmodulin [138], cell volume [123], and G-protein coupled receptors [2] in turn control the KCNQ channels. These channels conduct large and sustained M-currents that activate approximately at -70 mV [127, 135, 139], and are sensitive to Ba^{2+} [127, 135], linopirdine [139] and XE991 [140], but are relatively insensitive to TEA [127, 131, 135, 139]. M-currents have been measured in the cultured and native RPE from several species [81, 127, 131, 135, 139, 140]. The expression of KCNQ1, KCNQ4, and KCNQ5 has been reported in the native bovine [141] and monkey [140] RPE. From these subtypes, only KCNQ5 has been found at the protein level [140, 141], localizing to the basolateral membrane in the native monkey [140] and rat [138] RPE. Furthermore, KCNQ4 and KCNQ5 were the main contributors to the M-currents in the monkey RPE [139] which further highlights the significance of KCNQ5 in the RPE.

In the mouse RPE, $K_V1.4$ localizes in the apical microvilli and $K_V4.2$ on the basolateral membrane [137]. These channels conduct fast activating and transient A-type currents, but functional currents have never been reported in the fresh native adult RPE. Instead, A-type currents have been measured in the cultured primary rabbit [134] and human [81, 133] RPE as well as in the fresh native human fetal RPE (hfRPE) [133].

Inwardly rectifying K^+ (Kir) channels

Despite the name, inwardly rectifying K^+ (Kir) channels conduct both inward and outward currents. They shift the membrane potential towards the K^+ equilibrium potential that is negative to the typical resting potential of the epithelial cell. [2] The property of inward rectification is caused by an internal Mg^{2+} or polyamine block of the channel pore [142].

Kir7.1 currents have been measured in the native and cultured RPE from several species [80-83, 128, 129, 131-134, 136, 143, 144], including humans [7, 81, 133], being the most prominent inward rectifier subtype in these cells. Typical features of Kir7.1 currents are mild inward rectification [7, 80-83, 128, 129, 131-134, 136, 143, 144], higher conductance with decreased extracellular K^+ concentration [81-83], activation caused by hyperpolarization at around -70 mV [81-83, 128, 129, 131-134, 136, 144], sensitivity to Rb^+ activation [7, 82, 145], as well as Ba^{2+} and Cs^+ inhibition [81-83, 128, 129, 132-134, 143]. Furthermore, Kir7.1 is regulated by intracellular ATP [143, 144] and pH [145, 146].

Kir7.1 localizes to the apical cell membrane in several RPE cell types [6, 7, 29, 80, 107, 108, 141], and the apical localization is important for RPE functionality. The co-localization with Na^+/K^+-ATPase supports the K^+ recycling across the apical membrane [107, 108]. This is critical upon illumination when the K^+ concentration in the subretinal space decreases from 5 mM to 2 mM [80]. Kir7.1 also promotes the absorption of water across the RPE, which helps to prevent retinal detachment by attaching the retina to the proximity of RPE [2]. In addition, Kir7.1 participates in the regulation of phagocytosis [6, 29] and secretion of growth factors [29]. In fact, the loss of Kir7.1 function impairs phagocytosis and cell alignment [6], and therefore recently, the possibilities of readthrough therapy and gene augmentation of Kir7.1 have been studied in Leber congenital amaurosis [7].

Contrary to the dominating channel type Kir7.1, strong inwardly rectifying Kir4.1 currents have been measured only from the native rat RPE [147] and the cultured human RPE [81]. Immunolabeling has revealed channel localization in the apical processes [29, 107, 147]. However, the Kir4.1 transcript has been absent in the native bovine [108] and human [148] RPE. It has been suggested that Kir4.1 most likely carries only a minor contribution to the macroscopic whole cell current in the RPE when compared to Kir7.1 [82].

Ca^{2+}-activated K^+ channels

Ca^{2+}-activated K^+ channels are divided by their conductance and pharmacological properties into small conductance SK channels, intermediate conductance IK channels, and large conductance BK or maxi K^+ channels. All these channels are gated by intracellular free Ca^{2+}, and BK channels also by voltage. [2] In addition, BK channels are regulated by oxidative agents [149], cell swelling induced by hypotonic stress [124], membrane stretch [150], and Ca^{2+} inflow through voltage-gated L-type Ca^{2+} channels [151]. The BK channels may further provide a negative feedback mechanism to control the L-type Ca^{2+} channels [151].

BK currents have been measured from the ARPE-19 cells [151, 152], the hiPSC-RPE [29], as well as from the cultured human [124] and rabbit [153] RPE, and these currents are blocked by iberiotoxin [124, 151, 153, 154]. RT-PCR revealed the BK channel expression also in the freshly isolated human RPE [151], and the lateral membrane localization was found by immunolabeling [29, 125]. In the RPE, BK channels regulate cell volume [124], secretion of VEGF and PEDF [29], and phagocytosis [125, 126] as well as its circadian rhythmicity [125]. They also participate in the protection against oxidative stress [126, 154].

2.2.3 Chloride (Cl^-) channels

Among chloride (Cl^-) channels, RPE expresses Ca^{2+}-activated Cl^- channels (CaCCs), ClC channels, and cystic fibrosis transmembrane conductance regulator (CFTR) channels (Figure 5). A diverse pattern of Cl^- currents has been measured in the RPE [155-158], participating in fluid transport, cell volume control, and pH regulation [2]. Below, the abovementioned Cl^- channels will be introduced in detail. In addition, these Cl^- channels are studied in the hESC-RPE as part of this dissertation and will be covered in the results and discussion chapters (**Study III**).

Ca^{2+}-activated Cl^- channels (CaCCs)

Two types of Ca^{2+}-activated Cl^- channels (CaCCs) have been identified in the RPE: Bestrophin (Best) and Anoctamin (Ano) channels. They are anion, mainly Cl^-, conducting channels activated by elevations in intracellular Ca^{2+}. [2] Best-1 localizes near the basolateral membrane of the RPE [159-161], and it is modulated by direct interaction of ATP [162]. Best-1 activity regulates transepithelial electrical properties [163], Ca^{2+} signaling [163], L-type Ca^{2+} channels [164, 165], and phagocytosis [125,

166]. Best-1 has also been found with subcellular localization in the fresh porcine RPE mainly in the ER, where it most likely assists Ca^{2+} uptake into Ca^{2+} stores using Cl^- as a counter ion [159]. Indeed, Best-1 plays a role in intracellular Ca^{2+} signaling, since in primary cultures of wild-type mice, ATP stimulation led to increased intracellular Ca^{2+} concentration via its release from the ER, whereas in bestrophin-1-deficient mice, the release of Ca^{2+} from the ER was reduced and, instead, also the early endosomes were involved [159]. As stated earlier, mutations in the gene coding Best-1 are associated with the pathogenesis of bestrophinopathies [167]. In addition, Ano1 [168] and Ano2 [156] were found in the basolateral membrane of the RPE, where they participate in the Ca^{2+}-dependent Cl^- conductance.

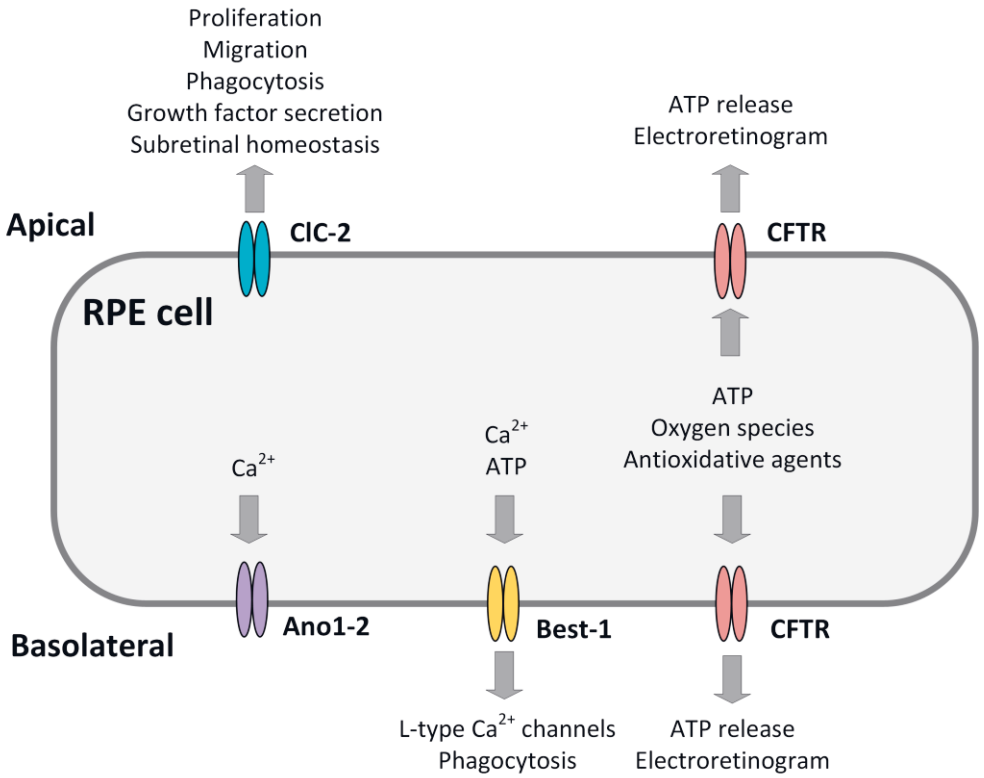

Figure 5. Schematic diagram of the localization, regulation, and function of Cl^- channels in the RPE including voltage-gated Cl^- channels (ClC), cystic fibrosis transmembrane conductance regulator (CFTR), Anoctamin (Ano) channels, and Bestrophin-1 (Best-1). Each Cl^- channel type is presented with a different color. The regulatory mechanisms of each ion channel are listed next to the arrows pointing towards the ion channel, while the arrows pointing outwards the ion channel indicate the cellular functions that the channel regulates.

ClC channels

ClCs are voltage-gated Cl^- channels, which conduct inwardly rectifying currents after activation by hyperpolarization [2]. RT-PCR and Western blot studies have revealed the presence of ClC-2 in the RPE [158, 169], and immunolabeling has shown its localization to the apical membrane [29, 170]. ClCs contribute to RPE cell proliferation [171], migration [171], phagocytosis [29], growth factor secretion [29], and maintenance of the subretinal homeostasis [170].

Cystic fibrosis transmembrane conductance regulator (CFTR)

Cystic fibrosis transmembrane conductance regulator (CFTR) channels are ABC transporters that open by conformational changes after ATP binding [2]. The gene and protein level expression of CFTR channels has been reported in the RPE [158, 169, 172], where CFTR localizes to the apical and basolateral cell membranes [172]. CFTR channels are modulated by reactive oxygen species and antioxidative agents [158], and they are involved in ATP release [173], and in the generation of electroretinogram c-wave [174].

2.2.4 Sodium (Na^+) channels

Two main sodium (Na^+) channel families exist: voltage-gated Na^+ channels ($Na_V1.1$–$Na_V1.9$) and epithelial Na^+ channels (ENaCα, β, γ, and δ) [2]. Generally, Na_V channels are responsible for action potential generation and propagation in excitable cells [175], while ENaCs maintain the Na^+ homeostasis in epithelial cells [176]. Na_V channel subtypes $Na_V1.4$, $Na_V1.6$, and $Na_V1.8$ have recently been identified from the hESC- and mouse RPE, where these channels were shown to play an essential role in phagocytosis [33]. Na_V currents have been measured in the hESC-RPE [33] and the sub-confluent RPE cultures [177-179], but not in their freshly isolated counterparts. ENaC subunits β and γ were detected at the protein level in the human RPE [180], but there is no evidence of functional ENaCs conducting currents in the RPE.

2.2.5 Calcium (Ca^{2+}) channels

Ca^{2+} channels on the RPE cell membrane enable the extracellular Ca^{2+} influx into the cell down its electrochemical gradient. These inward Ca^{2+} currents increase the intracellular free Ca^{2+} concentration that further controls the critical RPE functions, such as phagocytosis and secretion, to support the functionality and viability of the retina and the photoreceptors. Voltage-gated Ca^{2+} (Ca_V) channels, transient receptor potential (TRP) channels, and ligand-activated Ca^{2+} channels have been reported in the RPE (Figure 6) and will be covered next. [2] In addition to these channels, RPE expresses store-operated Orai channels [181, 182].

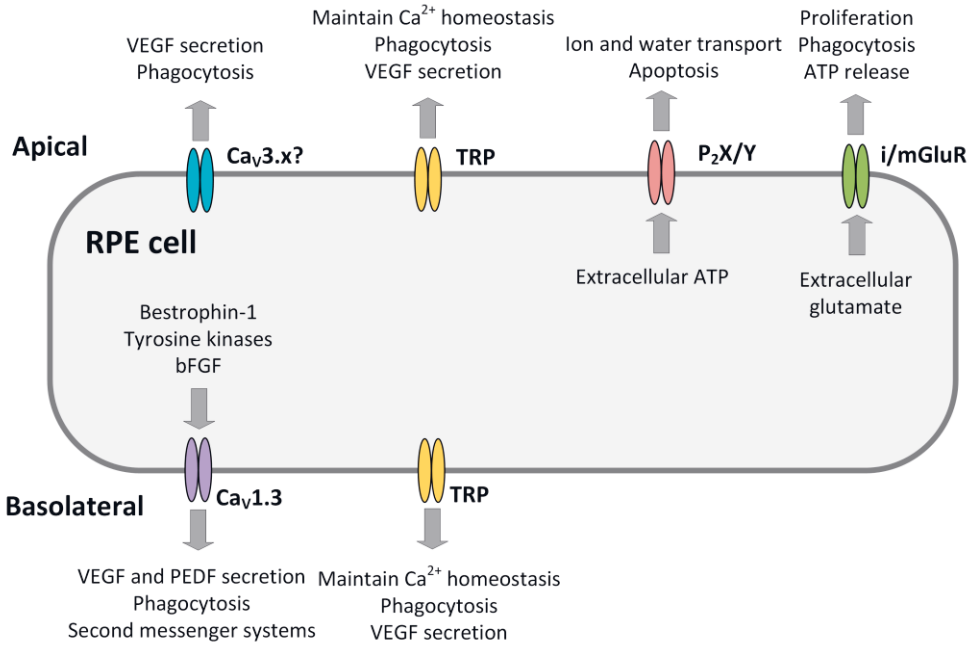

Figure 6. Schematic diagram of the localization, regulation, and function of Ca^{2+} channels in the RPE including voltage-gated Ca^{2+} (Ca_V) channels, transient receptor potential (TRP) channels, and ligand-activated Ca^{2+} channels. Each Ca^{2+} channel type is presented with a different color. The regulatory mechanisms of each ion channel are listed next to the arrows pointing towards the ion channel, while the arrows pointing outwards the ion channel indicate the cellular functions that the channel regulates.

Voltage-gated Ca^{2+} channels

Voltage-gated Ca^{2+} channels (Ca_Vs) are divided into L-type channels ($Ca_V1.1$–1.4), N, P/Q and R-type channels ($Ca_V2.1$–2.3), and T-type channels ($Ca_V3.1$–3.3). α-subunits of these ion channels form the functional channel pore, and β-subunits modify the channel activity. [2]

In patch clamp measurements, Ba^{2+} is often used as a charge carrier since L-type Ca^{2+} channels are more permeable to Ba^{2+} than Ca^{2+} [2]. These channels are opened at negative potentials by depolarization [183], and they conduct fast activating and slowly inactivating currents [2]. L-type Ca^{2+} channels are sensitive to dihydropyridine derivatives nifedipine and (-)BayK8644 with inhibitory and stimulative effects, respectively [164, 184-192].

L-type Ca^{2+} channels are present in the cultured and native RPE [29, 125, 136, 151, 164, 165, 184-194]. Even though subtypes $Ca_V1.1$-$Ca_V1.3$ are expressed in the RPE [184], $Ca_V1.3$ is considered as the main subtype [125, 136, 164, 165, 184, 185, 191-193]. $Ca_V1.3$ has been detected on the basolateral membrane in the murine [193] and porcine [165] RPE. L-type Ca^{2+} channels participate in the regulation of VEGF [29, 185] and PEDF secretion [29], as well as the phagocytic activity [29, 125, 195]. They are also involved in the initiation of the inositol 1, 4, 5 - trisphosphate (IP_3) second messenger system [196]. Bestrophin-1 [194] and tyrosine kinases [190, 191, 196] are reported to regulate the L-type Ca^{2+} channel activity, and bFGF stimulates the L-type Ca^{2+} channels by sifting their voltage-dependent activation towards more negative potentials [2, 187, 192].

The expression of $Ca_V2.x$ subtypes is not reported in the RPE [184]. Still, transient T-type Ca^{2+} currents have been measured from the RPE [184] carried likely by subtypes $Ca_V3.1$ and $Ca_V3.3$ [29, 184]. T-type Ca^{2+} channels have been found to contribute to RPE physiology by the regulation of phagocytosis and VEGF secretion [29].

In addition, this dissertation introduces new information related to Ca_V channels in the hESC- and native mouse RPE that will be covered in the results and discussion (**Study I**).

Transient receptor potential (TRP) channels

Transient receptor potential (TRP) channels form a superfamily of channels with six transmembrane segments. The channel subtypes vary in sequence homology, selectivity to different cations, and activation mechanism. [197] From channel

subtypes, Ca^{2+}-selective vallinoid receptor (TRPV) channels, divalent cations conducting melastatin (TRPM) channels, and non-selective canonical (TRPC) cation channels have been found from the RPE. Indeed, several studies have presented that the native and cultured RPE express TRPV1-TRPV6 channels [198-201]. TRPV4 localizes to the apical microvilli in the native hfRPE [201], and TRPV5 and TRPV6 to the apical and basolateral membranes in the native human RPE [198]. TRPV channels participate in the regulation of phagocytosis [125, 198] and VEGF secretion [199], maintain the Ca^{2+} homeostasis [198], and likely participate in the Ca^{2+} and water movement [200]. In addition, RPE expresses TRPC1 [202, 203] and TRPC4 [201, 203] channels as well as TRPM1 [201], TRPM3 [201, 204], and TRPM7 [201] channels, from which TRPC4 and TRMP3 are located on the apical side at tight junctions and TRPM3 at the base of primary cilia [201].

Ligand-activated Ca^{2+} channels

Adenosine triphosphate (ATP) and glutamate are possibly the most well-known extracellular ligands binding to the ligand-activated Ca^{2+} channels in the RPE. ATP acts as an autocrine and paracrine extracellular messenger. It can bind to apical purinergic P_2X and P_2Y receptors, from which P_2X are ligand-activated Ca^{2+} conducting ion channels, and P_2Y are G-protein-coupled receptors initiating an intracellular second messenger cascade. [2] RPE can secrete ATP into the subretinal space for autocrine stimulation of the ATP-receptors [173, 205, 206]. This secretion is controlled by several factors, including growth factors [205], pyrimidines [205], changes in tonicity [205], CFTR channels [173], and vesicular transport pathways [173]. P_2X [207, 208] and P_2Y [206, 207, 209-211] receptors are both present in the RPE. P_2Y receptors participate in the regulation of ion and water transport [211], and P_2X receptors contribute to apoptosis [208]. Dysfunctions in P_2 receptors could underlie the pathogenesis and progression of the AMD [208, 212, 213].

RPE also expresses ligand-gated ionotropic glutamate receptors (iGluRs) [214-218], and G-protein-coupled metabotropic glutamate receptors (mGluRs) [217, 218]. Both receptor types are activated by the extracellular neurotransmitter glutamate. This leads to Ca^{2+} elevations in the cytoplasm either directly by the opening of the ion channel or via the G-protein cascade, respectively. Glutamate receptors may be involved in the regulation of phagocytotic activity [215, 219] and cell proliferation in the RPE [216]. Glutamate has been also found to trigger the release of ATP via ionotropic N-methyl D-aspartate (NMDA)-receptors on the apical membrane that may further amplify the glutaminergic signal by increasing the intracellular Ca^{2+}. The

interaction of glutaminergic and purinergic systems may control the light-induced changes between the photoreceptors and the RPE. [214]

Stretch-sensitive Ca^{2+} channels

Mechanical stimulation opens stretch-sensitive Ca^{2+} channels (SSCCs) on the cell membrane, and their closure is followed by relaxation or adaption to that mechanical force. SSCCs are involved in the regulation of cell volume, shape, and motility in different tissues [220], and they are also found in the RPE [221, 222].

2.3 Ca^{2+} signaling in the RPE

Ca^{2+} is a cellular signaling molecule that directly modifies protein function and acts as a second messenger. RPE cells maintain low intracellular free Ca^{2+} concentration by actively pumping Ca^{2+} to the extracellular space and the endoplasmic reticulum (ER). [2, 223] Specific for RPE, it also stores high amounts of Ca^{2+} in the melanosomes locating in the apical side of the cytosol giving RPE cells their typical pigmentation [224, 225]. Ca^{2+}-induced changes in cell function require controlling the intracellular Ca^{2+} level and the spatial- and time-dependent Ca^{2+} distribution [2, 223]. In the RPE, Ca^{2+} signals modify an array of processes, including phagocytosis [29, 125, 195, 198], secretion [29, 185, 199], ion and water transport [200, 211], apoptosis [208], and cell proliferation [216].

Several organelles, Ca^{2+} channels, and Ca^{2+} transporters need to collaborate to generate the Ca^{2+} signals. Na^+/Ca^{2+} exchanger and Ca^{2+}-ATPase on the cell membrane efficiently remove Ca^{2+} from the cytosol and keep the Ca^{2+} concentration low at rest (Chapter 2.2.1). Ca^{2+} channels, including Ca_Vs and TRP channels, conduct Ca^{2+} from the extracellular space to the cytosol down the electrochemical gradient (Chapter 2.2.5). In addition, ligand-activated Ca^{2+} channels, such as glutamate receptors as well as P_2X and P_2Y_2 receptors, contribute to Ca^{2+} signaling (Chapter 2.2.5). Next, we focus on the intra- and intercellular Ca^{2+} signaling mechanisms following the activation of the P_2Y_2 receptor and G-protein cascade. These mechanisms include Ca^{2+} release from the ER via IP_3 receptors (IP_3Rs) and ryanodine receptors (RyRs), as well as Ca^{2+} and IP_3 diffusion between the adjacent RPE cells via gap junctions (GJs).

ATP or uridine triphosphate (UTP) binding to G-protein coupled P_2Y_2 receptors leads to phospholipase C (PLC) activation. At the cell membrane, PLC hydrolyses phosphatidylinositol 4,5-bisphosphate (PIP_2) to IP_3 and diacylglycerol. [226] IP_3 is a powerful signaling molecule that diffuses fast in the cytosol interacting with the Ca^{2+} channels on the ER [227]. IP_3Rs locate on the membrane of the ER conducting Ca^{2+} from the ER to the cytosol. The IP_3R opening requires the binding of IP_3 which increases the sensitivity of the receptor to Ca^{2+}. At low Ca^{2+} concentration, Ca^{2+} activates the IP_3R, but at high Ca^{2+} concentration, the effect changes to inhibitory. [223] The IP_3R subtype in the RPE is still unknown, however, subtype 3 (IP_3R_3) is found in other epithelia [228-230]. Ryanodine receptors (RyRs) are also involved in the Ca^{2+} signaling in the RPE [151, 152, 221]. They contribute to Ca^{2+} release from the ER, and the elevation of the intracellular Ca^{2+} level triggers the opening of RyRs. Therefore, RyRs amplify the Ca^{2+} signal via Ca^{2+}-induced Ca^{2+} release. The continued rising of the Ca^{2+} level eventually closes RyRs. [231] Ca^{2+} is removed from the intracellular space to the ER by the sarcoendoplasmic reticulum Ca^{2+}-ATPase (SERCA). There is indirect evidence of SERCA in the RPE obtained by depleting the ER Ca^{2+} stores using SERCA-specific blocker thapsigargin [222, 232].

Only a small proportion of Ca^{2+} that enters the cytosol ends up as free intracellular Ca^{2+} since Ca^{2+} is strongly buffered in the cytosol by Ca^{2+}-binding proteins such as calbindin and calretinin. The buffers modulate the amplitude and the recovery time of the Ca^{2+} signals as well as their spatial and temporal features. [223]

RPE cells form intercellular connections via GJs, enabling the Ca^{2+} or IP_3 signals to propagate between the adjacent cells [2]. Several studies have shown that in the RPE, GJs are involved in the intercellular signaling after mechanical stimulation [221, 232, 233]. GJs are composed of two connexons located at the membranes of two neighboring cells, and together they construct a gap between them. Six connexin proteins form each connexon. [234] Connexin 43 (Cx43) is the primary connexin expressed in the RPE GJs [235, 236], and its expression is modulated e.g., by extracellular glucose level and protein kinase C activity [221, 237]. In addition to gap junction formation, Cx43 is involved in the regulation of VEGF secretion [238] and the RPE differentiation via cyclic adenosine monophosphate (cAMP) signaling [239].

2.3.1 Computational Ca^{2+} signaling models

A computational model approximates a real system with mathematical equations that are simulated with computers. The model simplifies the real system, including only the components that are considered the most relevant based on the previous knowledge. Still, the models are well suited to interpret experimental data and predict system behavior.

Several computational models are developed to describe the features of certain receptors and cascades involved in Ca^{2+} signaling. These include the ligand binding to the metabotropic P_2Y_2 receptor following the G-protein cascade and the production of IP_3 to the cytosol [226, 240], which leads to the activation of IP_3R [241-245] and RyR [246]. In addition, the influence of Ca^{2+} buffers [244, 247], SERCA pump [248], and Ca^{2+} diffusion though GJs [244, 249] has been modeled to describe Ca^{2+} signaling.

Epithelial cell-type-specific models combine the knowledge of Ca^{2+} signaling to represent the epithelial tissue with characteristic properties using equations and parameters. For example, in mouse mesothelial cells, Ca^{2+} oscillations depend on IP_3 concentration, while the frequency of oscillations is modified by Ca^{2+} influx through the plasma membrane and activity of the SERCA pumps [250]. Ca^{2+} signaling is also closely related to the modeling of wound healing [251, 252] and the epidermis [253], as well as the urothelial cell functionality [254].

Several studies have investigated the role of Ca^{2+} in the airway epithelium, providing new knowledge about the system itself [255-257]. Warren et al. developed a computational Ca^{2+} signaling model of human airway epithelium that described the interactions of ATP, Ca^{2+}, and IP_3 in mechanically initiated Ca^{2+} waves. A single cell model was combined with a spatial model of a cell culture so that the extracellular ligand and diffusion via GJs mediated the Ca^{2+} signal. With this modeling approach, they found evidence of regenerative ATP release downstream of the stimulated cell. [255] They also modeled intracellular Ca^{2+} oscillations that modified the fluid secretion in the airway epithelium [256].

So far, to my knowledge, Ca^{2+} signaling in the RPE is computationally modeled for the first time in this dissertation and will be introduced in the materials and methods, results, and discussion paragraphs **(Study IV).**

3 AIMS

The overarching objective of this dissertation was to investigate the physiology of the RPE with a focus on RPE ionic signaling. The general research hypothesis was that diverse machinery of ion channels is present and functional in the stem cell-derived RPE with high physiological relevance. The specific aims of this dissertation are outlined below.

1. Characterize the electrophysiological properties of the hESC-derived RPE (**Study I, II, III**) focusing on voltage-gated Ca^{2+} channels (**Study I**), K^+ channels (**Study II**), and Cl^- channels (**Study III**).

2. Compare the physiology of the hESC-derived RPE to its native counterpart considering the ion channels described above (**Study I, II**).

3. Determine the role of voltage-gated Ca^{2+} channels in the regulation of phagocytosis, growth factor secretion, and RPE maturation (**Study I**).

4. Resolve Ca^{2+} signaling mechanisms in the RPE by computational modeling of Ca^{2+} wave propagation induced by mechanical stimulation (**Study IV**).

4 MATERIALS AND METHODS

4.1 Ethical view

The National Authority for Medicolegal Affairs, Finland (Dnro 1426/32/300/05) approved the research with human surplus embryos, and a supportive statement was obtained from The Local Ethics Committee of the Pirkanmaa Hospital District, Finland (R05116). No new cell lines were derived in this study. The research with hfRPE cells was in accordance with the Declaration of Helsinki and the NIH institutional review board. Studies on C57BL/6 mice followed the Finnish Animal Welfare Act 1986 and ARVO Statement for the Use of Animals in Ophthalmic and Vision Research.

4.2 RPE cells

Human embryonic stem cell (hESC)-derived RPE, isolated mouse RPE, cultured human fetal RPE (hfRPE), and ARPE-19 cells were used in this study.

4.2.1 Human embryonic stem cell (hESC)-derived RPE (Study I, II, III)

The hESC lines Regea08/023, Regea08/017, and Regea11/013 were cultured and spontaneously differentiated in floating cell clusters as previously described [258, 259] (**Study I, II, III**). Pigmented areas of the floating aggregates were dissociated after manual separation with TrypLE Select (Invitrogen, UK), and the isolated cells were seeded (5.5×10^5 cells/cm^2) onto Collagen IV (5 μg/cm^2, Sigma-Aldrich, St. Louis, MO) coated 24-well cell culture plates (Corning CellBIND; Corning, Inc., Corning, NY). This was followed by cryopreservation for the cell line Regea11/013 [260]. The pigmented cells were passaged for maturation (2.5×10^5 cells/cm^2) on hanging culture inserts (polyethylene terephthalate, pore size 1 μm, Merck Millipore) coated with Collagen IV (10 μg/cm^2, Sigma-Aldrich) or with Collagen IV and laminin (1.8 μg/cm^2, LN521, Biolamina, Sweden). The cells were further cultured in

the hESC-RPE culture medium until mature monolayers were obtained. The hESC-RPE culture medium consisted of KnockOut™ D-MEM (500ml) supplemented with KnockOut™ Serum Replacement (90ml), GlutaMAX™ (6ml), Penicillin-Streptomycin (3ml), and β-mercaptoethanol (1.2ml) (all from ThermoFisher Scientific) and Minimum Essential Medium nonessential amino acid solution (6ml, BioNordika Oy). For the patch clamp experiments with single cells, the mature monolayers were dissociated with TrypLE Select, and the cells attached on coverslips coated with poly-l-lysine (Sigma-Aldrich). For the monolayer patch clamp measurements and for immunolabeling, the hESC-RPE monolayer on the insert membrane was removed from the insert and cut into several pieces.

TER values were measured during cell culturing to investigate the integrity of the hESC-RPE, and the experiments of this thesis were performed on monolayers with TER values over 200 $\Omega \cdot cm^2$. In addition, strong pigmentation and cobblestone morphology were used as other indicators of the hESC-RPE maturity. A set of immunostainings was routinely performed on the hESC-RPE covering at minimum F-actin staining with phalloidin, ZO-1, claudin-3, CRALBP, Na^+/K^+-ATPase, and bestrophin-1 (primary antibodies listed in Table A1) that together give information about the maturity and polarization of the tissue.

4.2.2 Native mouse RPE (Study I, II)

C57BL/6 mice (**Study I, II**) at the age of 8–12 weeks were euthanized by CO_2 inhalation and cervical dislocation. After this, the eyes were enucleated and bisected along the equator. In Ames' solution (Sigma-Aldrich) supplemented with 10 mM HEPES (pH ~7.4), the retina was carefully removed, leaving the RPE firmly attached to the eyecup. The mouse RPE cells were isolated from the eyecup preparations for patch clamp experiments either using TrypLE Select (15 minutes) or 25 U/ml activated papain (Sigma-Aldrich, 30 minutes) and measured within 6 hours. The detailed protocol is presented in **Study I** and **Study II**.

4.2.3 Cultured human fetal RPE (hfRPE) (Study II)

The human fetal RPE (hfRPE) cells **(Study II)** were received as a generous gift from National Eye Institute, NIH (NEI), and the cells were cultured to confluent and mature monolayers as described before [47]. The cells (10^6 cells/cm^2) were seeded on human extracellular matrix (ECM)-coated (3 μg/cm^2, Corning, UK) inserts (pore

size 1 μm, Merc Millipore, Germany). For the patch clamp recordings, the cells were isolated from the inserts with Trypsin (Lonza, Walkersville, MD).

4.2.4 ARPE-19 cell line (Study IV)

ARPE-19 is an immortalized human RPE cell line (**Study IV**), and the ARPE-19 cells were cultured as previously described [232] on coverslips or glass-bottomed dishes at a density of 1.5 x 10^5 cells/cm^2.

4.3 Patch clamp recordings and data analysis (Study I, II, III)

Patch clamp measurements (Figure 7) were performed at room temperature (RT) in whole cell configuration and voltage clamp mode by recording individual cells in the hESC-RPE monolayer (**Study III**) or dissociated single hESC-RPE (**Study I, II**), mouse RPE (**Study I**) and hfRPE (**Study II**) cells. Patch pipettes (resistance 4–8 MΩ) were filled with internal solution (Table 1). The pH was adjusted to ~7.2 (CsOH or KOH), and osmolarity was adjusted to ~290 mOsm (sucrose). In test conditions, the content of $CaCl_2$ in Cl^- internal solution (**Study III**) was decreased to 0 mM.

Table 1. Internal solutions for patch clamp measurements used for the indicated ion channels.

Component	Ca^{2+} channel internal solution (in mM) (Study I)	K^+ channel internal solution (in mM) (Study II)	Cl^- channel internal solution (in mM) (Study III)
ATP-Mg	4	4	4
$CaCl_2$	0.5	0.5	0.5
$CsCH_3SO_3$	83	-	-
CsCl	25	-	130
EGTA	5.5	5.5	5.5
GTP-Na	0.1	0.1	0.1
HEPES	10	10	10
KCl	-	25	-
K-gluconate	-	83	-
Lidocaine N-ethyl chloride	2	2	-
NaCl	5	5	5
TeaCl	-	-	5

RPE cells were perfused with external solutions presented in Table 2. The pH was adjusted to ~7.4 (NaOH) and osmolarity to ~305 mOsm (sucrose). In certain experiments, $BaCl_2$ concentration in Ca_V external solution was decreased from 10 mM to 1 mM (**Study I**). In addition, voltage-gated K^+ channels were also investigated using Ames' solution (Sigma-Aldrich) supplemented with 10 mM HEPES and 10 mM NaCl (**Study II**).

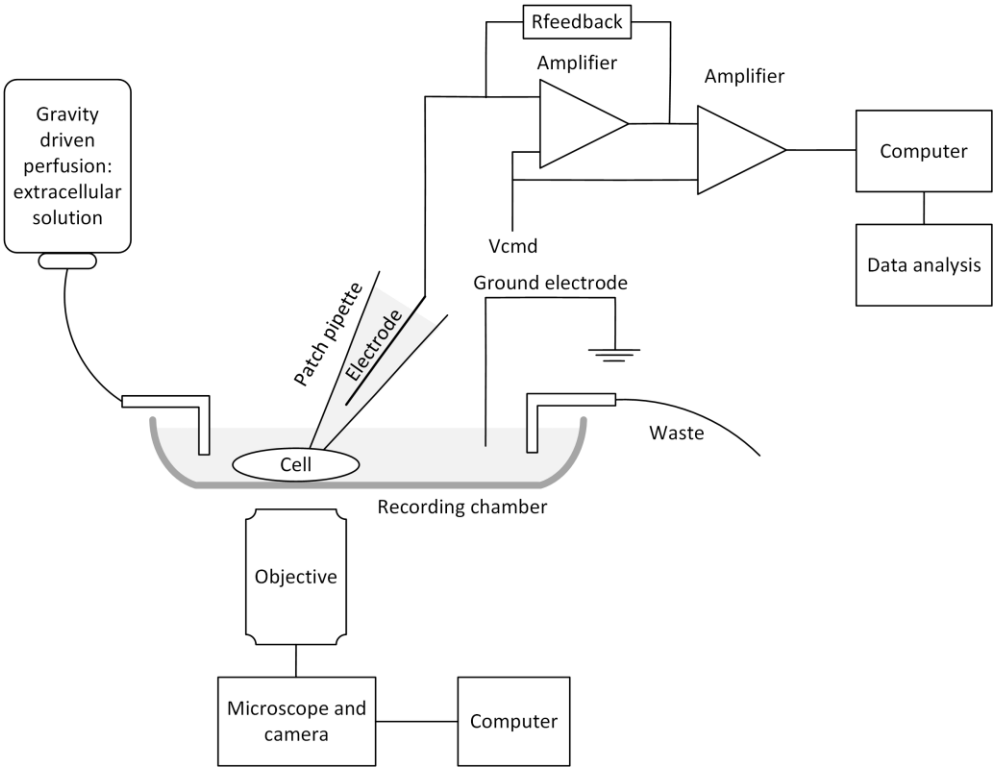

Figure 7. Schematics of the patch clamp method. The extracellular solution from a gravity-driven reservoir perfuses the cell in the recording chamber. The cell is visualized by a microscope that is connected to a camera and a computer. In whole cell configuration, the glass micropipette containing the intracellular solution and the electrode wire form a gigaseal with the cell membrane, and once this is obtained, the cell membrane facing the interior of the glass pipette is ruptured by suction. In voltage clamp mode the membrane potential is controlled by the user, and the membrane current is measured. Voltage clamp operation is based on an electronic feedback system where the measured potential is compared with the command voltage (Vcmd). The output is connected to a computer, and the recorded current is later processed in the data analysis. The image is re-drawn with modifications from Okada 2012 [261].

An L-type Ca^{2+} channel activator 10 μM (-)BayK8644 (Sigma-Aldrich) and an inhibitor 10 μM nifedipine (Sigma-Aldrich) were used to characterize the voltage-gated Ca^{2+} channels in the hESC-RPE (**Study I**). Different K^+ channel blockers were used to study the voltage-gated K^+ channels in detail, including 5 mM $BaCl_2$, 20 mM TeaCl, 10 nM Agitoxin-2 (Alomone), and 300 nM linopirdine (Sigma-Aldrich) (**Study II**). For the enhancement of the Kir currents, the K^+ external solution was modified so that NaCl was replaced by an equivalent amount of RbCl (**Study II**).

Table 2. External solutions for patch clamp measurements used for the indicated ion channels.

Component	Ca^{2+} channel external solution (in mM) (Study I)	K^+ channel external solution (in mM) (Study II)	Cl^- channel external solution (in mM) (Study III)
$BaCl_2$	10	-	-
$CaCl_2$	1.1	1.1	1.1
Glucose	5	6	5
HEPES	10	10	10
KCl	-	3	-
$MgCl_2$	1.2	1.2	1.2
NaCl	120	120	130
TeaCl	5	-	5

The Axopatch200B patch clamp amplifier was connected to an acquisition computer via AD/DA Digidata1440 (Molecular Devices, CA). Access resistances were below 30 MΩ and membrane resistances were above 200 MΩ. Significant liquid junction potentials were corrected in the data analysis. The peak value of the current was plotted against applied voltages to obtain the current-voltage (IV)-curve using either Clampfit 10.5 or an earlier version or Python 3.8 and the pyABF module [262]. The averaging, normalization, and statistical analysis were performed with Excel or with Python 3.8. pandas, numpy, sklearn, and scipy modules.

4.4 Immunofluorescence and confocal microscopy (Study I, II, III, IV)

Immunofluorescence labeling was used to localize the ion channels of interest from the RPE. hESC-RPE monolayers, mouse RPE eyecup whole-mount preparations, and ARPE-19 cells were processed as described in **Study I, II, III, IV**. The staining protocol for paraffin-embedded vertical sections of the hESC-RPE monolayers and

the mouse eyecups is described in **Study I** and **Study II**. All samples were fixed with 4 % paraformaldehyde (Sigma-Aldrich) for 15 minutes at RT. The primary antibodies used in this dissertation are listed in Appendix 1, Table A1, and the secondary antibodies in Appendix 1, Table A2. The samples were imaged by Zeiss LSM780 confocal microscope (Zeiss, Jena, Germany) using Plan-Apochromat ×63/1.4 oil immersion objective setting the image size to 1024 × 1024 pixels. The images were saved in czi-format for further processing with ImageJ [263].

4.5 Phagocytosis assay (Study I)

Pulse-chase phagocytosis assay was used to investigate the role of voltage-gated Ca^{2+} channels in the regulation of POS phagocytosis in the RPE (**Study I**). POS particles were obtained from fresh porcine eyes as described before [259, 264]. In the pulse phase, POS containing control medium or medium with a drug (10 μM (-)BayK8644, 10 μM nifedipine, or 5 μM T-type Ca^{2+} channel inhibitor ML218 (Sigma-Aldrich)) were incubated on the apical sides of the hESC-RPE inserts (30 minutes at 37 °C). In the chase phase, the cells were further incubated after washing out the unbound POS particles (2 hours at 37 °C). Then, the samples were fixed and immunolabeled as described in **Study I** using the primary antibodies opsin and ZO-1. Large random fields were imaged using the Zeiss LSM780 to count the POS particles with n = 15–16 images (3 inserts, 5-6 images per insert).

4.6 VEGF-ELISA (Study I)

VEGF Quantikine enzyme-linked immunosorbent assay (ELISA) kit (R&D Systems, MN) was used to assess VEGF secretion in the hESC-RPE following the manufacturer's instructions (**Study I**). In the control condition, the hESC-RPE culture medium samples were collected separately from the apical and basolateral sides of the insert after 24 hours of incubation to investigate the polarized VEGF secretion. Combined samples of the apical and basal hESC-RPE culture medium were collected to study the effect of Ca_V channel modulators (10 μM (-)BayK8644, 10 μM nifedipine, or 5 μM ML218) on the total VEGF concentration. The VEGF

concentration was normalized to the number of cells counted from images obtained with Zeiss LSM780.

4.7 Statistical analysis (Study I, II, III)

The data is stated as mean ± SEM (n, p), where n refers to the number of samples and p refers to the statistical significance. Some of the data sets did not meet the normality criteria tested with the Shapiro-Wilk normality test, and therefore the p-values were calculated using the Mann-Whitney U test.

4.8 Ca^{2+} imaging (Study IV)

Ca^{2+} imaging was done as previously described [232] to study the Ca^{2+} wave propagation induced by mechanical stimulation in the RPE monolayer. Briefly, the ARPE-19 cells were loaded with fura-2-acetoxymethyl ester (fura-2 AM; Invitrogen, Molecular Probes), a Ca^{2+}-sensitive fluorescent dye with emission at 505 nm and excitation changing from 340 nm to 380 nm following calcium binding. Single cell mechanical stimulation was performed using a glass micropipette that perforated the mechanically stimulated (MS) cell to initiate a Ca^{2+} wave. The Ca^{2+} wave propagation was measured with an Olympus IX51 fluorescence microscope and ANDOR iXion 885 camera. The emitted fluorescence intensity ratio (F_{340}/F_{380}) was obtained by the excitation at 340 and 380 nm with Polychrome V and determined for each cell after background correction. Normalized fluorescence (NF) was calculated so that the fluorescence was divided by the mean fluorescence before the mechanical stimulation. This value reflects the relative changes in intracellular Ca^{2+} concentration.

For the construction of the computational model of Ca^{2+} signaling after mechanical stimulation (**Study IV**), the experimental data of Abu Khamidakh et al. [232] was used and supplemented with new data forming three data sets: control data set, α-glycyrrhetinic acid (GA) – treated data set (GJs blocked), and GA-suramin-treated data set (GJs and P_2-receptors blocked), $n \geq 3$ for each set. For the GA-treated data set, the cells were incubated in a solution containing 30 μM GA (SigmaAldrich) for 30 minutes [232], and for the GA-suramin-treated data set, the solution also contained 50 μM suramin (SigmaAldrich).

4.9 Computational modeling (Study IV)

After the mechanical injury in the MS cell, the Ca^{2+} wave traveled over the ARPE-19 monolayer. The Ca^{2+} wave spread from the MS cell to the immediately surrounding neighboring (NB) cells defined as the first NB layer (NB_1), following the cells surrounding the NB_1 cells defined as the second NB layer (NB_2) and so forth (**Study IV, Figure 1**).

To gain the new understanding of Ca^{2+} signaling in the RPE, a computational model was constructed based on the literature evidence of the ion channels, pumps, and cell organelles that are most relevant for the process. The six model components that were combined in this study were (Figure 8): (I) stretch-sensitive Ca^{2+} channel (SSCC) (model component designed in this study), (II) P_2Y_2 receptor [226], (III) IP_3 receptor type 3 (IP_3R_3) [245], (IV) ryanodine receptor (RyR) [246], (V) the commonly known model for sarco/endoplasmic reticulum Ca^{2+}-ATPase (SERCA) and plasma membrane Ca^{2+}-ATPase (PMCA), and (VI) gap junctions (GJs) connecting the neighboring cells. The model assumes that these components participate in the Ca^{2+} signaling as follows (**Study IV, Table 1**):

(I) The MS cell and the closest neighboring cell layers experience stretch that leads to the opening of SSCCs. This allows Ca^{2+} inflow into the cell.

(II) The stimulated ARPE-19 cells secrete ligand (ATP or UTP) to the extracellular space, where it binds to the G-protein coupled P_2Y_2 receptor leading to the production of IP_3 to the cytoplasm.

(III) IP_3 interacts with IP_3R_3 releasing Ca^{2+} from the ER to the cytoplasm.

(IV) The increasing cytoplasmic Ca^{2+} concentration activates RyRs which leads to an additional Ca^{2+} outflow from the ER.

(V) SERCA and PMCA pump Ca^{2+} to the ER and extracellular space, respectively. IP_3 degrades in the cytoplasm.

(VI) Ca^{2+} and IP_3 diffuse between the NB layers through GJs.

These actions related to the model components (I-VI) are mathematically presented as a collection of Ca^{2+} fluxes that cause the time-dependent changes in intracellular Ca^{2+} concentration $[Ca^{2+}]_i$ as follows

$$\frac{d[Ca^{2+}]_i}{dt} = J_{SSCC} + J_{IP_3R_3} + J_{RyR} - J_{Pump} + J_{Leak} + J_{GJ,Ca^{2+}}$$

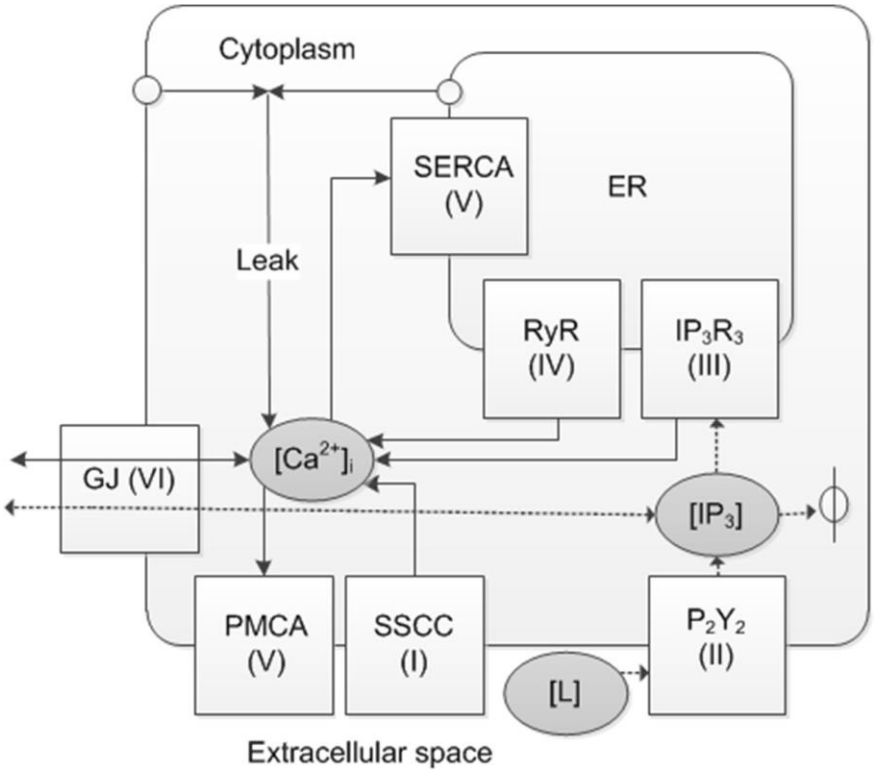

Figure 8. Schematics for the Ca^{2+} signaling in the RPE, where $[Ca^{2+}]_i$ presents the cytoplasmic Ca^{2+} concentration, $[IP_3]$ cytoplasmic inositol 1, 4, 5 - trisphosphate concentration, [L] the extracellular ligand concentration, and Φ the degradation of IP_3. Roman numerals I-VI designate the model components (I) stretch-sensitive Ca^{2+} channels (SSCC), (II) purinergic receptor P_2Y_2, (III) IP_3 receptor type 3 (IP_3R_3), (IV) ryanodine receptor (RyR), (V) sarco/endoplasmic reticulum Ca^{2+}-ATPase (SERCA) and plasma membrane Ca^{2+}-ATPase (PMCA), as well as (VI) gap junctions (GJs). Leak refers to a combinatory Ca^{2+} leak from the extracellular space and the endoplasmic reticulum (ER) to the cytoplasm. The image is reproduced under the terms of the Creative Commons Attribution License from **Study IV**.

where subscripts describe the source of the flux according to the nomination presented above. The detailed model equations are presented in **Study IV** for each component. The abovementioned three data sets (control, GA-treated, and GA-suramin-treated) were simulated with the model. First, the model without GJs was created, and parameters were optimized using the GA-treated data set. Then, the model was revised with the control data set, where the GJ model component was included. Finally, the model was applied to predict the influence of GA and suramin on Ca^{2+} signals. The experimental work produced Ca^{2+} data in relative NF units lacking the absolute concentration reference. The computational model presents

absolute Ca^{2+} concentrations, and thus, the model predictions are considered only relative.

The parameters are presented in **Study IV Table 2**. Most parameters and initial values were reused from the models of Lemon et al. 2003 [226], LeBeau et al. 1999 [245], and Keizer & Levine 1996 [246] or fitted with Matlab SimBiology (R2012a, The MathWorks, Natick, MA) using the Parameter Fit Task. The solver type was set to ode45 (Dormand-Prince), the maximum iterations to 100, the error model to constant error model, and the simulation time step to 0.1 seconds. First, the parameter values were fitted with GA-treated data set in the NB_5 layer having the largest Ca^{2+} response from those NB layers that exclude (I) SSCC and (VI) GJ model components. Then, the SSCC model component was included in NB_1 layer, experiencing the largest stretch using the same GA-treated data set. The parameters for the GJs were fitted in the control data set in the NB_1 layer. Three parameters were assumed to vary based on their distance to the MS cell: stretch (θ) activating the SSCCs, the extracellular ligand concentration ([L]), and the phosphorylation rate of IP_3R_3 (α_4) (**Study IV, Table 3**).

The uncertainty of selected parameters was assessed with sensitivity analysis: Ca^{2+} wave peak amplitude, time to peak, Ca^{2+} wave width at half maximum, and Ca^{2+} concentration at the end of the Ca^{2+} wave. In addition, the model was used to investigate the mechanism by which suramin modulates the Ca^{2+} signaling in the ARPE-19 cells by comparing the selected parameters of the P_2Y_2 receptor and G-protein cascade between the GA-treated data set and the GA-suramin-treated data set. Finally, the model was tuned to the GA-suramin-treated data set by refitting the parameters that changed the Ca^{2+} curve towards suramin modulation.

5 RESULTS

5.1 Ca^{2+}, K^+, and Cl^- channels in the hESC-RPE (Study I, II, III)

Different ion channels were studied in the hESC-RPE using immunostainings, confocal microscopy, patch clamp, phagocytosis assay, and ELISA. Several functional ion channel types were found, including voltage-gated Ca^{2+} channels, K^+ channels, and Cl^- channels. These ion channels are highly important for RPE functionality and for maintaining the visual ability in the eye. The L-type Ca^{2+} channels in the hESC-RPE were comparable to studies from the fresh native RPE, and they were linked to the regulation of phagocytosis, VEGF secretion, and maturation. However, when the amplitude and the incidence of the K^+ currents were compared to the literature, hESC-RPE did not cover all the features of the fresh native adult RPE but resembled more the fresh native hfRPE or the primary RPE cultures.

5.1.1 Localization of the ion channels in the hESC- RPE and comparison to the native mouse RPE (Study I, II, III)

Localization of Ca^{2+}, K^+, and Cl^- channels were investigated in the hESC-RPE by immunolabeling and confocal microscopy. Figure 9 demonstrates the distribution of ion channels on the apical and basolateral membranes in the hESC-RPE. Typical for the RPE, K^+ channels $K_V1.4$, Kir4.1, and Kir7.1 were observed at the apical membrane, and Best-1, $Ca_V1.2$, $Ca_V1.3$, $K_V4.2$, and KCNQ5 at the basolateral membrane. In addition to these, channel subtypes $Ca_V1.3$, $Ca_V3.1$, $K_V4.2$, and KCNQ2-3 were found at the apical membrane, and $Ca_V3.2$, Kir7.1, and KCNQ2-4 at the basolateral membrane. KCNQ1, $K_V1.3$, ClC-2, and CFTR were detected by immunolabelling, yet, with uncertainties in the exact localization.

The localization of Ca^{2+} and K^+ channels in the hESC-RPE was compared to the native mouse RPE, and the original confocal images can be found in the publications according to Table 3. The localization pattern in the hESC-RPE was closely similar to the mouse RPE with some exceptions: First, $Ca_V3.1$ stained the apical membrane

in the hESC-RPE, while in the mouse RPE, it was observed in both apical and basolateral membranes. Second, Kir7.1 was detected at the apical and basolateral membranes in the hESC-RPE and additionally at the lateral membrane in the mouse RPE. Third, K_V4.2 was detected only at the basolateral membrane in the mouse RPE while appearing both at the apical and basolateral membranes in the hESC-RPE. Fourth, the junctional localization of K_V1.4 and KCNQ3 was not observed in the mouse RPE even though it was present in the hESC-RPE. Fifth, KCNQ1 localized clearly on the apical and basolateral membranes in the mouse RPE, but the localization in the hESC-RPE was uncertain.

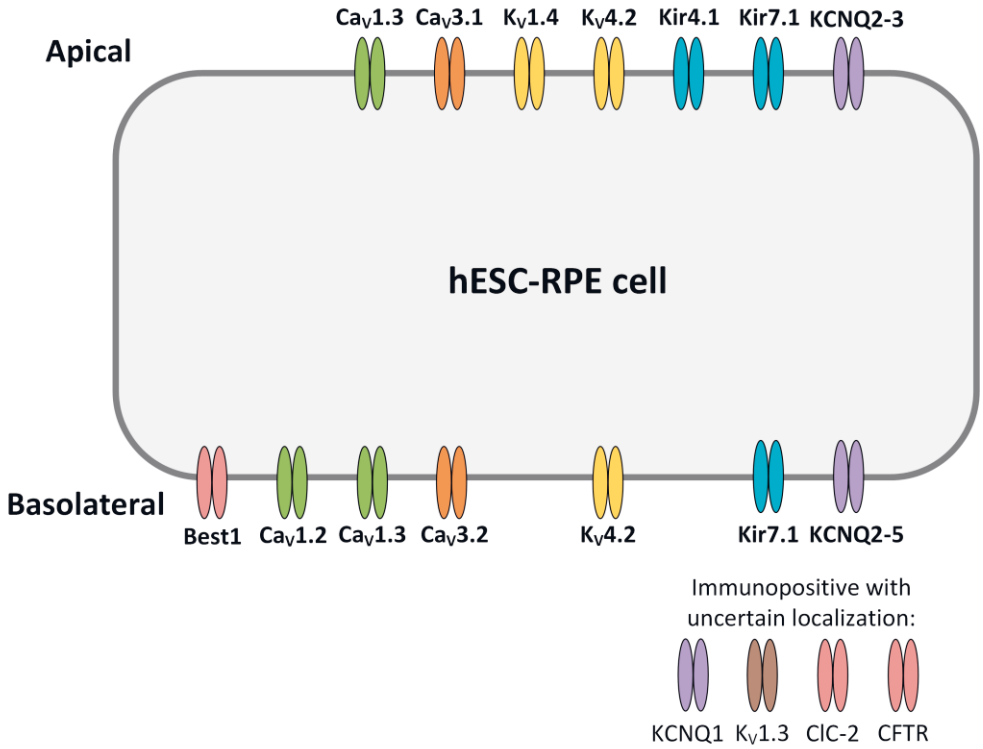

Figure 9. Localization of the ion channels in the hESC-RPE at the apical and basolateral membranes considering the following channels: Cl^- channels including Best-1, ClC-2, and CFTR (red), from which the localization of ClC-2 and CFTR were unclear, L-type Ca^{2+} channels $Ca_V1.2$ and $Ca_V1.3$ (green), T-type Ca^{2+} channels $Ca_V3.1$ and $Ca_V3.2$ (orange), A-type K^+ channels $K_V1.4$ and $K_V4.2$ (yellow), inwardly rectifying K^+ channels Kir4.1 and Kir7.1 (blue) as well as KCNQ channels KCNQ1-5 (purple). Delayed rectifier channel $K_V1.3$ (brown) was immunopositive with inconclusive localization.

Interestingly, $Ca_V1.3$ was found at the apical membrane in both hESC- and mouse RPE. According to our results (Chapter 5.1.3), $Ca_V1.3$ participates in the vital RPE functions such as phagocytosis, VEGF secretion, and maturation, where the newly detected apical localization may play a critical role. In addition, Kir7.1 typically localizes on the apical membrane as shown here for the hESC-RPE and the mouse RPE, however, this study clearly presented its basolateral localization as well in both cell types.

Table 3. Localization of ion channels in the hESC- and mouse RPE. The localization of each ion channel in the hESC-RPE is compared to the mouse RPE, and the original confocal images are listed in the table.

Ion channel	Localization in hESC-RPE	Compared to mouse RPE	Study	Figure
Best-1	Uniform, basolateral membrane	-	I-II-III	3F - 1G - 3A
$Ca_V1.2$	Basolateral membrane	Similar	I	3G, 4F
$Ca_V1.3$	Apical and basolateral membrane	Similar	I	3D, 3H, 4D, 4G
$Ca_V3.1$	Apical membrane	Both apical and basolateral membrane	I	3E, 3I, 4E, 4H
$Ca_V3.2$	Junctional and basolateral membrane	Similar	I	3J, 4I
CFTR	Annular structures	-	III	3B
ClC-2	Junctional, cell centers	-	III	3C
Kir4.1	Apical microvilli	Similar	II	5E, 6A
Kir7.1	Apical and basolateral membrane	In all membranes: apical, basolateral and lateral	II	5F, 5G, 6B, 6D
$K_V1.3$	Inconclusive	Similar	II	S1A, S1B
$K_V1.4$	Junctional, apical membrane	Only apical membrane	II	4C, 6C
$K_V4.2$	Apical and basolateral membrane	Only basolateral membrane	II	4D, 6E
KCNQ1	Inconclusive	Apical and basolateral membrane	II	3G, 6F, S2A, S2F
KCNQ2	Apical and basolateral membrane	Similar	II	3H, 6G, S2B, S2G
KCNQ3	Junctional, apical and basolateral membrane	Only apical and basolateral membrane	II	3I, 6H, S2C, S2H
KCNQ4	Basolateral membrane	Similar	II	3J, 6I, S2D, S2I
KCNQ5	Basolateral membrane	Similar	II	3K, 6J, S2E, S2J

As an example of the immunostainings and confocal images, the localization pattern of L-type Ca^{2+} channel $Ca_V1.3$ is presented in Figure 10 for the hESC-RPE monolayer (Figure 10A) and vertical section (Figure 10C) as well as for the mouse RPE whole-mount preparation (Figure 10B) and vertical section (Figure 10D).

$Ca_V1.3$ appears as continuous apical staining in the hESC- and mouse RPE monolayer, while its basolateral localization is revealed in the vertical sections of both cell types

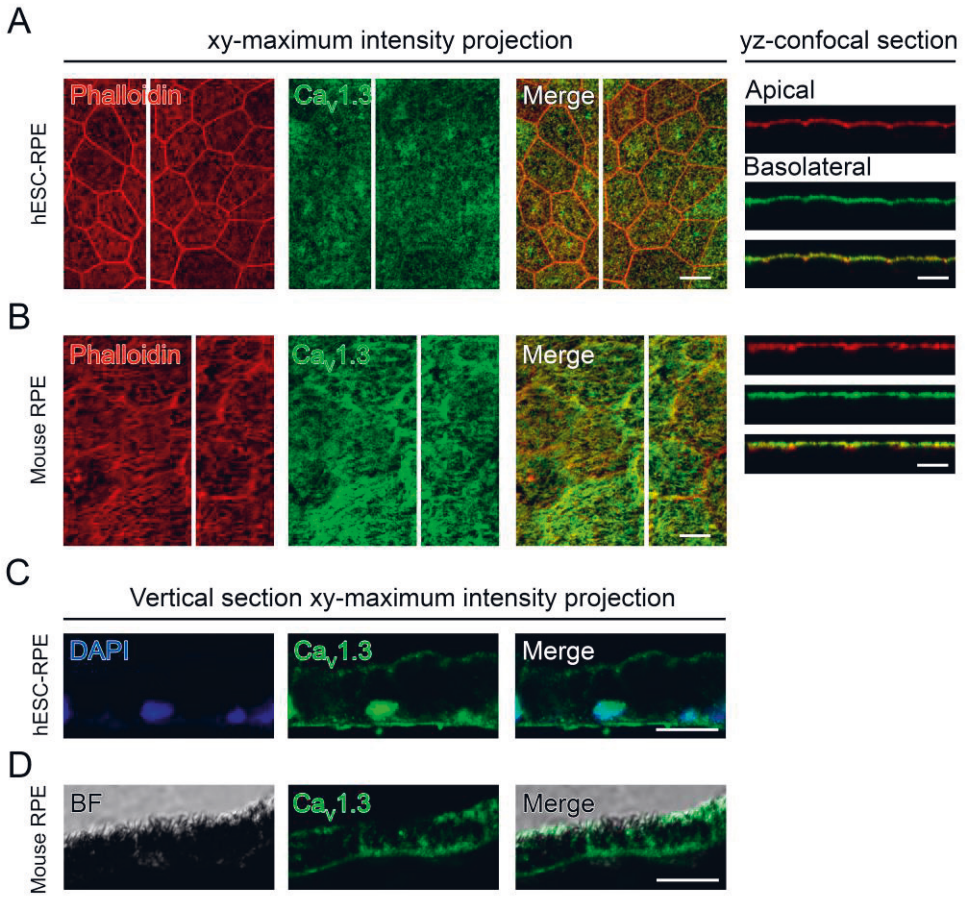

Figure 10. Immunostainings of L-type Ca^{2+} channel $Ca_V1.3$ in the hESC- and mouse RPE. Confocal images of (A) the hESC-RPE and (B) the mouse RPE monolayers illustrated with xy-maximum intensity projections and yz-confocal sections (white bar denotes the localization of the section) for actin cytoskeleton (phalloidin, red) and $Ca_V1.3$ (green). Confocal images of RPE vertical sections with xy-maximum intensity projections (apical side upwards): (C) the hESC-RPE, where nuclei (DAPI, blue) were stained together with $Ca_V1.3$ (green), and (D) the mouse RPE, where bright-field (BF) image was presented together with $Ca_V1.3$ (green). Scale bars 10 µm. The image is reproduced and modified under the terms of the Creative Commons license from **Study I**.

5.1.2 Characterization of the ion currents in the hESC-RPE (Study I, II, III)

Ion currents through Ca^{2+}, K^+, and Cl^- channels were measured using patch clamp method revealing L-type Ca^{2+} channels, delayed rectifier K^+ channels, KCNQ channels, A-type K^+ channels, inwardly rectifying Kir channels, and Cl^- channels in the hESC-RPE.

The L-type Ca^{2+} channels were activated at low potentials and reached the maximum at 10 mV according to the IV-curve (n = 9), when stimulated with a 50 ms voltage pulse from -80 mV to 60 mV in 10 mV increments (**Study I Figure 1C, 1D**). This slowly inactivating current was further studied by modulating the extracellular conditions. Decrease of the extracellular Ba^{2+} from 10 mM to 1 mM decreased the maximum current density from 2.4 ± 0.5 $pA{\cdot}pF^{-1}$ (n = 9) to 1.3 ± 0.3 $pA{\cdot}pF^{-1}$ (n = 7) characteristic to the L-type Ca^{2+} channels (Table 4, **Study I Figure 1F**). Furthermore, the currents were activated by 10 µM (-)BayK8644 (Table 4, **Study I Figure 2A, 2C, 2E**) and inhibited by 10 µM nifedipine (Table 4, **Study I Figure 2B, 2D, 2F**). The slowly inactivating current features resembled those measured from the native mouse RPE in this study (**Study I Figure 4A**). The currents in the mouse RPE activated at low potentials, and the maximum current occurred at 20 mV with the current density of 2.3 ± 0.6 $pA{\cdot}pF^{-1}$ (n = 4) (**Study I Figure 4B**). Fast transient currents resembling T-type Ca^{2+} channels were also recorded from three hESC-RPE cells, however, they were not further characterized (**Study I, Figure 1G**).

Table 4. The influence of ion channel modulators on the currents. The ion channel, modulation, resulting change, and original representations are listed below.

Ion channel	Modification	Change	Study	Figure
$Ca_V1.3$	10 µM (-)BayK8644	+80±9 % (n = 3) *	I	2A, 2C, 2E
$Ca_V1.3$	10 µM Nifedipine	-56±5 % (n = 4) *	I	2B, 2D, 2F
$Ca_V1.3$	10 mM Ba^{2+} → 1 mM Ba^{2+}	-46 % (n = 7-9) *	I	1F
Cl^- channels	intracellular 0.5 mM Ca^{2+} → 0 mM Ca^{2+}	~ -50 % (n = 3)	I	2
Kir7.1	120 mM NaCl → 120mM RbCl	+319±76 % (n = 8) *	II	5C, 5D
$K_V1.3$	10 nM Agitoxin-2	-51±9 % (n = 4) *	II	2G, 2H
KCNQ channels	300 nM linopirdine	-57±10 % (n = 3) *	II	3E, 3F
K^+ channels	5 mM Ba^{2+}	-79±3 % (n = 5) *	II	2C, 2D
K^+ channels	20 mM TEA	-56±9 % (n = 7) *	II	2E, 2F

*Statistically significant $p < 0.05$

A heterogeneous pattern of K^+ channels was found in the hESC-RPE, including delayed rectifier K^+ channels, KCNQ channels, A-type K^+ channels, and inwardly

rectifying Kir channels. The following features of the K^+ currents were analyzed: current response, IV-curve characteristics, current amplitude, and incidence of the current.

80 % of the hESC-RPE cells measured with a 50 ms voltage pulse from −45 mV to 45 mV in 10 mV steps expressed outward currents that activated at -30 mV with current amplitude 92 ± 11 pA (n = 47) at 45 mV (**Study II Figure 2A, 2B**). General K^+ channel blockers Ba^{2+} and TEA, as well as $K_V1.3$ channel inhibitor Agitoxin-2, all decreased the currents compared to the control (Table 4, **Study II Figure 2C-2H**), indicating the presence of delayed rectifier K^+ channel $K_V1.3$ in the hESC-RPE. Similar currents were also detected in 79 % (n = 11) of the cultured hfRPE cells in our measurements (**Study II, Supplementary Figure 3**).

Slowly activating and sustained outward K^+ currents were recorded from 22 % (n = 9) of the hESC-RPE cells with a prolonged pulse of 1000 ms from –70 mV to 40 mV in 10 mV increments (**Study II Figure 3A**). The currents activated at around -60 mV, and the current amplitude was 529 ± 164 pA (n = 9) at 40 mV (**Study II Figure 3B**). KCNQ channel inhibitor linopirdine decreased the current, indicating the presence of M-currents in the hESC-RPE (Table 4, **Study II Figure 3E, 3F**).

A-type currents have been previously measured only in the cultured RPE or the fresh native hfRPE [133, 134]. Transient currents resembling those in the literature were detected in 15 % (n = 6) of the hESC-RPE cells using the same prolonged protocol described above (**Study II Figure 4A, 4B**). The current amplitude was 108 ± 26 pA (n = 6) at 40 mV, and the currents inactivated completely during the pulse.

Inwardly rectifying currents were found in 14 % (n = 9) of the measured hESC-RPE cells by hyperpolarization from -45 mV to -145 mV in 10 mV steps by a 50 ms pulse (**Study II Figure 5A**). The inwardly rectifying currents activated at -70 mV reaching the maximum current amplitude of -43 ± 5 pA (n = 9) at -145 mV (**Study II Figure 5B**). The current amplitude tripled when the Na^+-based control solution was replaced with Rb^+-based test solution (Table 4, **Study II Figure 5C, 5D**) that typically enhances the inwardly rectifying currents. In addition, the cultured hfRPE cells were studied for the inwardly rectifying currents (n = 14), but none of the cells presented these currents (**Study II**).

After depolarization to 0 mV, 10 mV voltage steps of 400 ms duration were applied until potentials -150 mV and 150 mV were reached, revealing the presence of Cl^- currents in the hESC-RPE (**Study III, Figure 1A**). At the negative and positive potentials, the currents activated at around -90 mV and 40 mV, respectively (**Study III, Figure 1B**). A similar activation threshold at positive potentials was obtained with a protocol starting from -50 mV (**Study III, Figure 1C, 1D**). In

addition, we found currents that activated at around -50 mV due to hyperpolarization (**Study III, Figure 1E, 1F**). The depletion of intracellular Ca^{2+} from 0.5 mM to 0 mM decreased the currents at positive potentials (Table 4, **Study III Figure 2A, 2B**), possibly indicating the regulatory role of Ca^{2+} on CaCCs in the hESC-RPE.

5.1.3 L-type Ca^{2+} channels regulate phagocytosis, growth factor secretion, and maturation in the hESC-RPE (Study I)

The role of voltage-gated Ca^{2+} channels in VEGF secretion (Table 5, **Study I Figure 5**) and phagocytosis (Table 5, **Study I Figure 6**) was investigated in the hESC-RPE. In the phagocytosis assay, the number of bound and internalized POS particles was counted from the confocal images of the hESC-RPE monolayer. In Figure 11, the POS particles stained with opsin are presented together with the actin cytoskeleton.

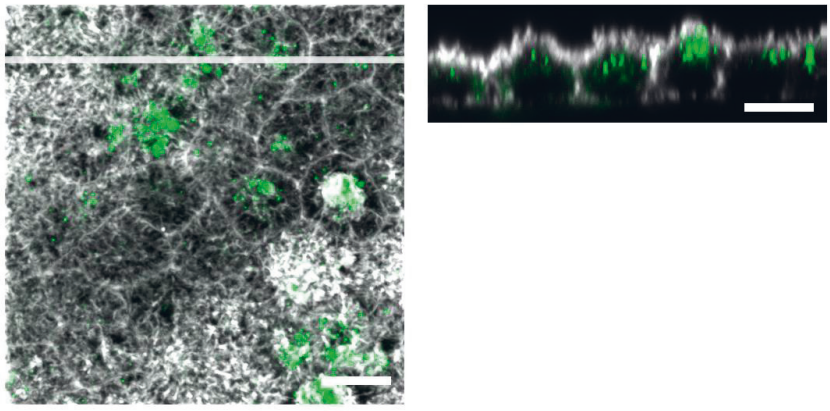

Figure 11. An example of photoreceptor outer segment (POS) phagocytosis in the hESC-RPE monolayer. Confocal image with xy-maximum intensity projection and yz-confocal section (apical side upwards, localization of the section highlighted with a white bar) illustrate POS particles stained with opsin (green) together with the actin cytoskeleton (phalloidin, gray). Scale bar 10 µm.

According to Table 5, L-type Ca^{2+} channel inhibitor nifedipine had a direct influence on VEGF secretion and phagocytosis since the application of nifedipine significantly decreased both functions. On the contrary, activation of the L-type Ca^{2+} channels by (-)BayK8644 increased VEGF secretion but decreased the number of phagocytosed POS particles. We also found that the T-type Ca^{2+} channel inhibitor

ML218 increased the phagocytosis of POS particles, however, its effect on VEGF secretion did not reach statistical significance.

Table 5. The influence of Ca^{2+} channel modulators on vascular endothelial growth factor (VEGF) secretion and phagocytosis in the hESC-RPE.

Modulator	Effect	VEGF secretion	Phagocytosis
(-)BayK8644	L-type Ca^{2+} channel activator	+24 ± 9 % (n = 9) *	-30 % (n = 16) **
Nifedipine	L-type Ca^{2+} channel inhibitor	-19 ± 9% (n = 8) *	-62 % (n = 15) **
ML2018	T-type Ca^{2+} channel inhibitor	+8 ± 14 % (n = 8)	+32 % (n = 16) *

*Statistically significant $p < 0.05$, **Statistically significant $p < 0.001$

The localization of the L-type Ca^{2+} channel subtype $Ca_V1.3$ during RPE maturation was addressed by immunolabeling $Ca_V1.3$ together with pericentrin (PCNT) that localizes to the centrosomes at the base of the primary cilia. Table 6 summarizes the change in the localization of these proteins during the hESC-RPE maturation (**Study I, Figure 7**).

Table 6. Changes in $Ca_V1.3$ localization during hESC-RPE maturation. Morphology, $Ca_V1.3$ localization, and bright apical $Ca_V1.3$ puncta co-localization with pericentrin (PCNT) are presented with respect to days of post-confluence.

Days post-confluence	Morphology	$Ca_V1.3$ localization	$Ca_V1.3$ puncta co-localization with PCNT	Illustration
1	Fusiform	Throughout the cell	No	Study II, Figure 7A, Figure S2A
6	Epitheloid	Towards apical and basolateral membranes	Yes	Study II, Figure 7B, Figure S2B
31	Cobblestone	Apical and basolateral membranes	One distinct cluster per cell	Study II, Figure 7C, Figure S2C
84	Cobblestone	Uniformly on apical and basolateral membranes	One distinct cluster per cell	Study II, Figure 7D, Figure S2D

During maturation, the hESC-RPE morphology developed from fusiform to epitheloid and finally to cobblestone. The apical staining of $Ca_V1.3$ became more prominent and homogeneous on the cell membrane, resembling the channel appearance in the native mouse RPE (**Study I, Figure 4D**). However, with increasing maturation, the basolateral staining appeared challenging to detect because of the pigmentation. The bright apical puncta of $Ca_V1.3$ co-localizing with PCNT also became visible during maturation.

5.1.4 K^+ current features in the hESC-RPE compared to the primary RPE cultures and the fresh native RPE (Study II)

The amplitude and the incidence of K^+ currents are compared in Table 7 between the hESC-RPE investigated in this dissertation and the literature on the primary RPE cultures or the freshly isolated native RPE from different species.

Table 7. Comparison of the amplitudes and the incidences of different K^+ currents in the hESC-RPE to the primary RPE cultures and the freshly isolated native RPE of various cell types. The values for the cultured and native RPE are approximations collected and pooled together from the literature.

Ion channel	hESC-RPE	Primary RPE cultures	Freshly isolated native RPE
Delayed rectifier			
Amplitude	~90 pA	~100-1000 pA [128-130, 133, 134, 136]	~100-1000 pA [131, 133, 135]
Incidence	80 %	40-90 % [133, 134, 136]	80-100 % [131, 133, 135]
KCNQ			
Amplitude	~530 pA	? pA	~100-5000 pA [127, 131, 135, 139]
Incidence	22 %	6 % (human RPE) [81]	26 % (hfRPE) [133] 80 % (adult human) [127]
A-type			
Amplitude	~110 pA	~500 pA [134]	~500 pA [133]
Incidence	15 %	10-30 % [81, 133, 134]	Only in hfRPE 90-100% [133], never in adult RPE
Kir			
Amplitude	~40 pA	~200-500 pA [128, 129, 134, 136]	~300-1500 pA [81-83, 131-133, 144]
Incidence	14 %	5-40 % [128, 129, 133, 134, 136]	80-100 % [81, 133]

The features of the delayed rectifier currents and M-currents conducted by the KCNQ channels in the hESC-RPE resembled those previously studied in the primary RPE cultures and the fresh native RPE. However, the incidence of M-currents was closer to the cultured RPE or the fresh native hfRPE than the native adult counterpart. A-type currents have previously been detected only in the cultured RPE or the fresh native hfRPE but never in the fresh native adult RPE. The A-type currents were measured here in the hESC-RPE which may indicate immaturity related to K^+ channel machinery and physiology of the tissue. Notably, the amplitude and the incidence of the Kir currents in the hESC-RPE were both found to be lower than typically in the RPE, and therefore, their function in the stem cell-derived RPE may be compromised. All in all, the features of A-type and Kir currents in the hESC-RPE resembled the primary RPE cultures or the fresh native hfRPE in several

aspects, whereas the delayed rectifier and M-currents were in line with the literature from the fresh native adult RPE.

5.2 Computational simulation of Ca^{2+} signaling in the RPE following mechanical stimulation

In this study, a computational Ca^{2+} signaling model was developed to simulate the experimental data following mechanical stimulation in the RPE monolayer. The model explained Ca^{2+} signaling in the ARPE-19 cells as follows:

1) Near the stimulation site, cells conduct Ca^{2+} through plasma membrane SSCCs.

2) GJs conduct Ca^{2+} and IP_3 farther from the MS cell, and these fluxes decrease with distance to the stimulation site.

3) The MS cell, together with the surrounding cells, secrete ligand to the extracellular space, where it mediates the Ca^{2+} signal with decaying ligand concentration.

4) The phosphorylation rate of the IP_3 receptor determines the sensitivity of the cell to the extracellular ligand, and the cells become less sensitive towards the distant NB layers.

The simulations of the computational Ca^{2+} model based on the experimental data are presented in Figure 12A for the GA-treated data set, in Figure 12B for the control data set, and in Figure 12C for the GA-suramin-treated data set. The simulations matched to the features of the experimental data so that 90 % of the fits resulted in $R^2 > 0.8$ (**Study IV, Table 4**).

The sensitivity analysis of certain Ca^{2+} wave features for NB1, NB5, and NB10 revealed that:

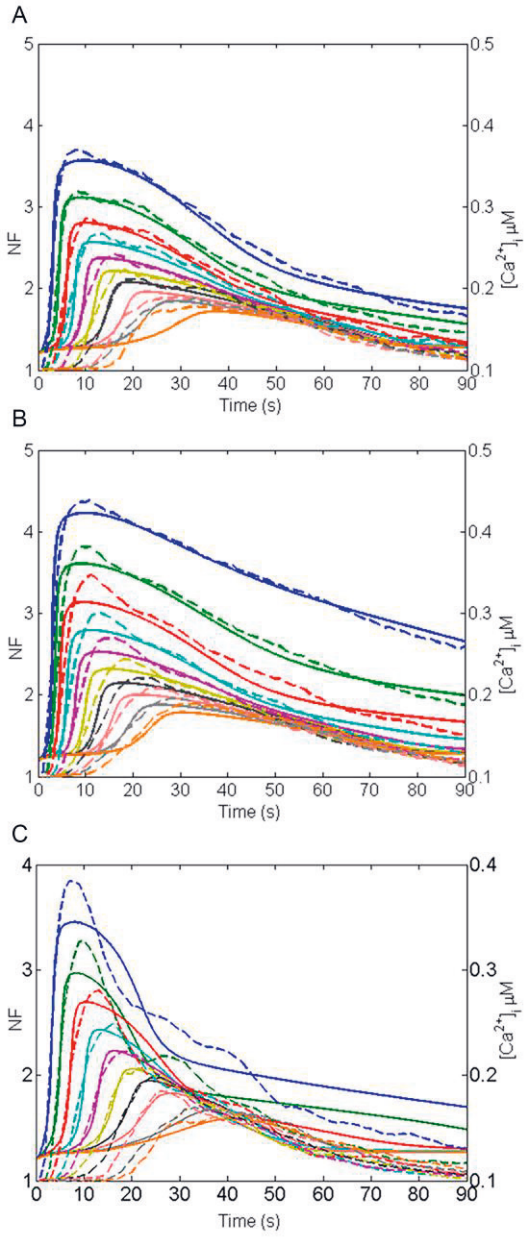

Figure 12. Model simulations compared to the experimental data in: (A) α-glycyrrhetinic acid (GA)-treated, (B) control, and (C) GA-suramin-treated data sets (dashed lines - dimensionless NF units, solid lines - arbitrary Ca^{2+} concentrations in μM) for the NB layers NB1 (blue), NB2 (green), NB3 (red), NB4 (light blue), NB5 (purple), NB6 (yellow), NB7 (black), NB8 (light red), NB9 (gray), and NB10 (orange). The image is reproduced under the terms of the Creative Commons Attribution License from **Study IV**.

1) Decreasing the stretch (θ) parameter in NB1 (**Study IV, Figure 6B**) decreased time to peak of the Ca^{2+} wave.

2) Increasing IP_3 input to NB1 via GJs (In_{IP3}) increased the Ca^{2+} wave width at half maximum (**Study IV, Figure 6C**) and resulted in higher Ca^{2+} concentration at the end of the wave (**Study IV, Figure 6D**). The influence was stronger in the NB layers near the stimulus site compared to the distant NB layers.

3) Time to peak decreased (**Study IV, Figure 6B**) and the Ca^{2+} wave width at half maximum increased (**Study IV, Figure 6C**) with higher extracellular ligand concentration (L).

4) Decreasing the IP_3 receptor phosphorylation rate (α_4) increased the Ca^{2+} wave peak amplitude (**Study IV, Figure 6A**) and decreased the time to peak (**Study IV, Figure 6B**). Ca^{2+} wave width at half maximum was either increased or decreased depending on the NB layer (**Study IV, Figure 6C**), while the Ca^{2+} wave end concentration was increased (**Study IV, Figure 6D**).

The experimental GA-treated and GA-suramin-treated data sets were compared to investigate the effect of suramin on P_2Y_2 receptor and G-protein cascade (**Study IV, Figure 7A**). The sensitivity analysis showed that increasing P_2Y_2 unphosphorylated receptor dissociation constant (K_1) modified the time to peak (**Study IV, Figure 7B**), and increasing P_2Y_2 receptor phosphorylation rate (k_p) narrowed the Ca^{2+} wave width at half maximum (**Study IV, Figure 7C**) similarly to the experimental observations. The simulations using the corrected parameter values for K_1 and k_p are illustrated in Figure 12C.

6 DISCUSSION

6.1 Localization of the ion channels in the hESC-RPE and the native mouse RPE

Immunostainings revealed a diverse set of Ca^{2+}, K^+, and Cl^- channels on the apical and basolateral membranes of the hESC-RPE, indicating the presence of a complex ion channel machinery (**Study I, II, III**). The main features of this set were similar to the native mouse RPE with few exceptions. We also found ion channels with new localizations in the RPE compared to the previous knowledge from the literature.

RPE expresses L-type Ca^{2+} channel subtypes $Ca_V1.1$-$Ca_V1.3$ [184], from which $Ca_V1.3$ stands as the main contributor to ionic signaling [125, 136, 164, 165, 184, 185, 191-193]. So far, $Ca_V1.3$ has been observed to localize only to the basolateral cell membrane in the murine [193] and porcine [165] RPE. We found that in addition to the basolateral membrane, $Ca_V1.3$ localizes to the apical membrane in the hESC- and mouse RPE, providing an apical route for the Ca^{2+} influx (**Study I**). The apical localization may be important in the control of growth factor secretion as well as in the regulation of phagocytosis (**Study I**), as POS binding and ingestion take place at the apical membrane [65-68], and the primary growth factors are secreted both apically and basolaterally [46, 47, 72-74]. Our immunostainings also revealed the basolateral localization of $Ca_V1.2$ in the hESC- and mouse RPE (**Study I**), thus its involvement in the RPE functionality cannot be excluded.

T-type Ca^{2+} channel subtypes $Ca_V3.1$ and $Ca_V3.3$ have previously been reported in the RPE [29, 184]. We also found $Ca_V3.1$ on the cell membranes of the hESC- and mouse RPE, but instead of $Ca_V3.3$, our immunostainings revealed $Ca_V3.2$ expression at the protein level in these cells (**Study I**). Therefore, it is still controversial which T-type Ca^{2+} channels contribute to the RPE physiology.

Immunostainings of the hESC- and mouse RPE showed the presence of KCNQ1 as well as the apical localization of KCNQ2-3 and the basolateral localization of KCNQ2-5 (**Study II**). The basolateral localization of KCNQ5 is in accordance with the literature [138, 140], and it is most likely the main subunit responsible for the basolateral K^+ conductivity [139]. KCNQ1 and KCNQ4 gene expression is reported in the native bovine [141] and monkey [140] RPE, but their

contribution, as well as the contribution of KCNQ2-3, in RPE functionality remain unresolved.

Pinto & Klumpp showed that $K_V1.4$ localizes on the apical microvilli and $K_V4.2$ on the basolateral membrane in the mouse RPE [137]. Our results with the hESC- and mouse RPE agreed with this study, except that $K_V4.2$ localized additionally to the apical membrane in the hESC-RPE (**Study II**). Whether these channels have a role in RPE functionality is still unknown since no currents have been measured from the fresh native adult RPE despite their protein level expression.

To date, Kir7.1 localization has been reported only at the apical membrane in the RPE [6, 7, 29, 80, 107, 108, 141], where its co-localization with Na^+/K^+-ATPase supports K^+ recycling across the apical cell membrane [107, 108]. Interestingly, we found Kir7.1 both at the apical and basolateral membranes in the hESC- and mouse RPE (**Study II**). The choroidal K^+ concentration varies approximately in the same range as the subretinal K^+ concentration [265]. Kir7.1 on the basolateral membrane may respond to the changes in the choroidal K^+ concentration and fine-tune it.

Kir4.1 has been found from the apical processes of the RPE [29, 107, 147], even though other studies report the absence of its gene product in the native bovine [108] and human [148] RPE. We also found Kir4.1 protein from the apical microvilli in the hESC- and mouse RPE (**Study II**). However, the contribution of Kir4.1 to the RPE functionality is still contradictory based on this study and the literature.

We found Cl^- channels Best-1, ClC-2, and CFTR from the hESC-RPE with immunolabeling (**Study III**). Best-1 localized to the basolateral membrane in the hESC-RPE (**Study I-III**) which is in agreement with the literature [159-161]. In addition, recent studies have revealed the localization of ClC-2 to the apical membrane [29, 170].

6.2 Electrophysiological properties of the hESC-RPE

Ca^{2+} (**Study I**), K^+ (**Study II**), and Cl^- currents (**Study III**) were measured with patch clamp recordings from the hESC-RPE. hESC-RPE expresses a heterogeneous pattern of ion channels, and in such a system, several ion channels may contribute to the conductivity stimulated by the same voltage protocol. The ion currents can still be characterized by carefully selecting the intra- and extracellular solutions, designing specific voltage protocols for stimulation, and applying ion channel-specific drugs.

Slowly inactivating Ca^{2+} currents were considered as L-type Ca^{2+} currents (**Study I**) based on the current features and IV-curve that resembled those of the fresh native RPE in previous studies [184, 185, 188, 189]. In addition, typical for L-type Ca^{2+} channels, the currents were inhibited by nifedipine [164, 185, 186, 188, 189], and activated by (-)BayK8644 [184, 187-192] as well as by increase in extracellular Ba^{2+} concentration [188, 189]. The main subtype carrying the current is likely $Ca_V1.3$ due to activation of the current at negative potentials [183], features of the IV-curve [165, 184, 185], and slow inactivation time. In general, $Ca_V1.3$ is considered as the primary L-type Ca^{2+} channel in the RPE [125, 136, 164, 165, 184, 185, 191-193]. Furthermore, we observed fast transient currents often appearing in combination with the slowly inactivating currents (**Study I**). These currents closely resembled the T-type currents previously measured from the cultured human RPE [184].

Different types of voltage-gated outward K^+ currents were recorded from the hESC-RPE cells (**Study II**). The most frequent current activating at -30 mV resembled the delayed rectifier current measured in the RPE in several studies [128-136]. The sensitivity of the current to Agitoxin-2 in the hESC-RPE identifies the delayed rectifier channel subtype $K_V1.3$ as a main carrier of the current [130, 136]. Furthermore, slowly activating, large amplitude, and sustained K^+ currents were measured from the hESC-RPE (**Study II**). These currents were inhibited by the application of linopirdine which is a blocker of KCNQ channels. Similar M-currents have previously been measured in the RPE [81, 127, 131, 135, 139, 140] with sensitivity to linopirdine [139]. Subtypes KCNQ4 and KCNQ5 were considered to conduct the M-current in the monkey RPE [139]. However, the hESC-RPE expressed subtypes KCNQ1-KCNQ5 at the protein level in the immunostainings, and the contribution of specific channel subtypes to the macroscopic current stays unsolved. We also found fast-activating and transient outward currents in the hESC-RPE (**Study II**) that resembled A-type currents reported in the cultured rabbit [134] and human [81, 133] RPE and in the native hfRPE [133]. Despite the presence of $K_V1.4$ and $K_V4.2$ at the protein level in the native RPE [137], A-type currents have never been recorded from the native adult RPE. This may indicate changes or immaturity in the cultured RPE phenotype.

Kir7.1 is generally considered the dominating Kir channel subtype in the RPE, and several studies report mild inwardly rectifying currents in the RPE of a variety of species [80-83, 128, 129, 131-134, 136, 143, 144], including human [7, 81, 133]. We recorded small but detectable inwardly rectifying currents in 15 % of the hESC-RPE cells (**Study II**). Typically for Kir7.1 current in the RPE, they activated at around -70 mV [81-83, 128, 129, 131-134, 136, 144] and the current amplitude

increased by Rb^+ application [7, 82, 145]. Kir7.1 currents with a rather small amplitude (on the average of 144 pA) have also been measured from the hiPSC-RPE [7]. Together the results from the hiPSC-RPE [7] and our results from the hESC-RPE may indicate an attenuated Kir channel machinery in the stem cell-derived RPE overall compared to the fresh native adult RPE. Contrary to the widely studied Kir7.1 channel subtype, Kir4.1 currents have been detected only in two studies in the native rat [147] and the cultured human RPE [81]. The contribution of Kir4.1 to the measured Kir conductance in the hESC-RPE cannot be omitted due to the positive immunolabeling of Kir4.1. However, our results support the idea that the contribution of Kir4.1 to the whole-cell Kir conductance is minor compared to Kir7.1 [82].

We also found slowly inactivating voltage-dependent Cl^- currents from the hESC-RPE (**Study III**) that resembled ClC currents previously measured from the RPE [155]. In addition, Ca^{2+}-sensitive Cl^- conductance was present in the hESC-RPE consistent with the results from the *Xenopus* RPE [155]. These currents could be mediated by Best-1 [159-161] or anoctamin [156, 168] channels. However, further studies are required to identify the Cl^- channel subtypes.

6.3 The role of ion channels in VEGF secretion and phagocytosis

The fine balance between VEGF and PEDF secretion in the RPE influences the welfare of the choriocapillaris and the photoreceptors. The secretion of growth factors in the healthy RPE is polarized so that VEGF secretion is more pronounced at the basal side [46, 47, 73, 74] as we observed in the hESC-RPE (**Study I**), and PEDF at the apical side [47, 72]. PEDF works as an angiogenesis inhibitor stabilizing the endothelium of the choriocapillaris [78] and as a neuroprotective factor promoting the survival of the photoreceptors [76, 77]. VEGF maintains the endothelium of the choriocapillaris [75].

The VEGF secretion is controlled, for example, by hyperosmolarity [266], hyperthermia [267], and oxidative stress [268]. On the other hand, these factors can further influence or be the consequence of ion channel functionality. Indeed, VEGF secretion is coupled to the activity of several ion channels found in the RPE including L-type Ca^{2+} channels [29, 185], T-type Ca^{2+} channels [29], TRPV channels [199], ClC-2 channels [29], and BK channels [29].

Ion channels work together to trigger and regulate the secretion process by controlling the cell membrane potential, interacting directly with different proteins, and creating an osmotically favorable environment for the secretory granule formation and changes in the cell volume. For example, in pancreatic acinar cells, secretory granules contain specific sets of ion channels, such as ClC-2 and KCNQ1, that control the exocytosis and prevent the granules from collapsing [269]. Secondly, the physical interaction between SNARE (soluble N-ethylmaleimide-sensitive factor attachment protein receptor) proteins and K^+ channels drives the final stages of vesicle fusion in secretion [270].

Our ELISA results showed the involvement of L-type and T-type Ca^{2+} channels in VEGF secretion in the hESC-RPE (**Study I**). These results were recently confirmed by Mamaeva et al. in the hiPSC-RPE [29]. L-type Ca^{2+} channels mediate Ca^{2+} entry into the RPE [29, 125, 136, 151, 164, 165, 184-194] as well as the initiation of the IP_3 second messenger cascade [196]. The activity of L-type Ca^{2+} channels can be regulated by shifting their voltage-dependency instead of a change in the membrane potential [2, 187, 192]. It has been proposed that the influx of Ca^{2+} via L-type Ca^{2+} channels is controlled by outwardly rectifying K^+ channels that eventually terminate the Ca^{2+} inflow by hyperpolarizing the cell membrane [1, 130]. The L-type Ca^{2+} channels have been reported to regulate the secretion also in other cell types. Interestingly, L-type Ca^{2+} channels form clusters on the cell membrane near the secretion area that increases local intracellular Ca^{2+} concentration triggering catecholamine release from chromaffin cells [271] and insulin secretion from pancreatic β-cells [272]. Taken together, the L-type Ca^{2+} channels in the hESC-RPE most likely control the VEGF secretion in concert with the other ion channels, possibly including the K^+ and Cl^- channels characterized in the hESC-RPE (**Study II, III**), with each channel type playing its interactive role in the process.

Phagocytosis in the RPE also involves the collaboration of several ion channels, including glutamate receptors [215, 219], TRP channels [125, 198], T-type Ca^{2+} channels [29], L-type Ca^{2+} channels [29, 125, 195], Best-1 [125, 166], ClCs [29], Kir7.1 channels [6, 29], BK channels [125, 126], and Na_Vs [33]. They mediate ion fluxes across the membranes to meet the changes in osmotic conditions and surface-to-volume ratio to maintain the ion homeostasis [273, 274]. Imbalance in the ion channel co-operation can lead to abnormal lysosome morphology or defective vesicle trafficking [274]. It is proposed that Best-1 controls phagocytosis via modulation of the L-type Ca^{2+} channel activity [125], while TRP channels are a likely interaction partner for BK channels [125, 275]. Furthermore, L-type Ca^{2+} channels can directly activate BK channels that in turn control the L-type Ca^{2+} channels via

negative feedback [151]. It is also possible that the regulatory role of Na_V channels in POS phagocytosis [33] is coupled to the functioning of the L-type Ca^{2+} channels, as Na_V and Ca_V channels typically form signaling complexes, especially in excitable tissues [276].

We found that L-type Ca^{2+} channel inhibition by nifedipine directly decreased the phagocytotic activity in the hESC-RPE. The slight inhibitive effect of L-type Ca^{2+} channel activator (-)BayK8644 may depend on the interactions with other ion channels involved in the process. We also revealed the contribution of T-type Ca^{2+} channels to phagocytosis so that the channel inhibition increased the amount of detected POS particles. (**Study I**) On the contrary, inhibition of the T-type Ca^{2+} channels in the hiPSC-RPE directly reduced the phagocytotic activity [29]. Thus, the role of T-type Ca^{2+} channels in phagocytosis is still controversial and requires more studies in RPE and in its stem cell-derived counterpart.

6.4 Comparison of the hESC-RPE physiology to the native counterpart

L-type Ca^{2+} currents were measured from the native mouse RPE to enable a comparison of the hESC-RPE to the native tissue (**Study I**). The current characteristics in the hESC-RPE were similar to the mouse RPE based on the current waveform, IV-curve, and current density. In addition, the L-type Ca^{2+} current features in the hESC-RPE resembled those of various fresh native RPE cell types described in the literature [184, 185, 188, 189]. However, they differed from the primary RPE cultures [185, 187, 190-192] by the more negative activation threshold as well as the gradual activation slope of the IV-curve that we observed in the hESC-RPE. This could be explained by possible differences in splicing variants, phosphorylation, or the composition of the accessory subunits between the hESC-RPE and the primary RPE cultures [277, 278]. However, the conclusive reason for the detected differences remains unresolved in this study.

We found that during the hESC-RPE maturation, $Ca_V1.3$ localization became more homogeneous, starting to resemble the native mouse RPE (**Study I**). This implicates high sensitivity of $Ca_V1.3$ expression and localization to RPE maturity, as previously suggested for Best-1 [32, 161]. In maturing hESC-RPE, punctuated staining of $Ca_V1.3$ co-localized with PCNT to the base of the primary cilia, where $Ca_V1.3$ may play a role in ciliogenesis or primary cilia function. Interestingly, TRPM3

in the hfRPE shows a comparable punctuated appearance [201], possibly indicating the collaboration between different ion channels in these processes.

The amplitude and incidence of the delayed rectifier K^+ currents in the hESC-RPE were compared to the literature on the primary RPE cultures [128-130, 133, 134, 136] and the freshly isolated native RPE [131, 133, 135] (**Study II**). These features of delayed rectifier currents in the hESC-RPE matched with the literature. The M-current amplitudes measured in the hESC-RPE resembled the native counterparts [127, 131, 135, 139], but the M-current incidence was closer to the cultured human RPE [81] or the native hfRPE [133] instead of the native adult human RPE [127]. The recorded M-currents may include conductivities through other ion channels, such as BK channels [149, 151] or voltage-gated Cl^- channels [29, 158, 169, 170] since the slope of the conductance curve was less steep than previously presented [127, 139].

Despite the appearance of $K_V1.4$ and $K_V4.2$ channels in the immunostainings of the native adult RPE [137], the transient A-type currents have been measured only in the cultured RPE [81, 133, 134] or in the native hfRPE [133], but never in the native adult tissue. Characteristic to this, Wen et al. observed A-type currents in 33 % of the cultured human RPE cells and almost in every native hfRPE cell, but they did not find these currents in the native adult RPE [133]. In this study, A-type currents were recorded in 15 % of the hESC-RPE cells that expressed the typical RPE maturity markers (**Study II**). Together these results may indicate that the membrane channel phenotype changes during maturation with the disappearance of A-type currents [133] and that the mature hESC-RPE resembles the hfRPE [279-281].

Small but detectable Kir currents were measured in 15 % of the hESC-RPE cells (**Study II**). Similar to our results, low amplitude Kir7.1 currents were recently measured from the hiPSC-RPE [7]. In addition, Rb increased the current in the hESC-RPE only 3-fold compared to the typical 10-fold increase [82, 146]. Based on these three observations, it is possible that Kir channel machinery is attenuated in the stem cell-derived RPE compared to the fresh native adult RPE, where the majority of the measured cells conduct high amplitude Kir7.1 currents [81-83, 131-133, 144]. In general, Kir7.1 current amplitudes and incidences are lower in the primary RPE cultures than in the fresh native RPE [128, 129, 133, 134, 136], still they are higher compared to the stem cell-derived RPE.

In summary, the K^+ ionic mechanisms in the hESC-RPE resembled the fresh native adult RPE regarding delayed rectifier and M-currents, and the primary RPE cultures or the fresh native hfRPE regarding A-type and Kir currents. Ion channels

in the RPE are sensitive markers of the maturation stage [32, 161] and functionality [6, 33] and this most likely considers K^+ channels as well. There is a reason to speculate that K^+ channels and especially Kir channels in the RPE cell cultures are affected by the cell culturing conditions. For instance, in rabbit Müller cells, the native expression of Kir4.1 disappears during cell culture and reappears when the cells are cultured on laminin-coated dishes in a medium containing insulin [282]. Furthermore, KCNQ1 localization has been reported to change in response to extracellular calcium level [283]. Attention should also be paid to physiological ion gradients and their natural changes that do not occur across the epithelium in culture conditions. Importantly, stem cell-derived RPE requires a long cultivation time to mature compared to the primary cell cultures. Cultured cells also lack their functional environment as they are not challenged to perform the typical RPE tasks in which the ion channels are involved. This might be reflected in the lower level of functional channel expression in the cultured RPE and is likely to be extremely critical for stem cell-derived RPE with no previous exposure to the proper physiological environment. One possible approach to partially overcome this deficiency could be challenging the RPE cells daily during their maturation by POS particle feeding to enhance channel expression and functionality. Taken together, there is a need to carefully consider the present cell culturing methods to develop environments that mimic the physiological conditions also from the ion gradient and functional point of view to further improve the cultured and stem cell-derived epithelial cell models.

6.5 Mechanisms of Ca^{2+} signaling in the ARPE-19 monolayer

The computational model developed in this dissertation unites the most relevant Ca^{2+} signaling mechanisms in the ARPE-19 cells evoked by mechanical stimulation **Study IV**). The model showed that in a monolayer, the mechanical force is sensed by SSCCs near the stimulus site, and IP_3 and Ca^{2+} spread the signal via GJs between the connected cells. Most likely, the MS cell and the closest neighboring cells secrete ligand to the extracellular space, where it delivers the signal so that the ligand concentration decays with distance to the stimulation site. Phosphorylation of the IP_3 receptor determines the sensitivity of the cell to the extracellular ligand, and this sensitivity decreases with distance to the MS cell.

In the model, the high ligand concentration resulted in fast responding and high amplitude Ca^{2+} waves. Similar behavior has previously been observed both experimentally [209, 284] and mathematically [255]. In the RPE, the ligand is most

likely ATP that is secreted under different stimuli [173, 205, 206]. In addition, the modulation of IP_3 phosphorylation (described with parameter α_4) near the stimulus site enables fast and high Ca^{2+} waves, representing an important regulatory mechanism for Ca^{2+} release [285-287]. Parameter α_4 may also reflect other signaling mechanisms that the model does not cover.

The model was also utilized to predict the effect of suramin on Ca^{2+} signaling. We found two possible mechanisms targeting P_2Y_2 receptors in an inhibitory manner: first, suramin may disrupt ligand binding to the receptors, or second, it may enhance the receptor desensitization (**Study IV**). On the other hand, suramin has been shown to disrupt the cell membrane receptor and G-protein coupling by inhibiting the association of G-protein α and $\beta\gamma$ subunits [288]. The P_2Y_2 receptor blockage by suramin has clinical relevance as the functioning of P_2 receptors has been linked to the development of AMD [212, 213].

Similar to the airway epithelial Ca^{2+} signaling models, our model combined previously designed model components of different receptors and signaling cascades to present a tissue-specific model. Additional model components were designed and parameterized to describe the stimulation conditions and to investigate the biological phenomena of interest. [255, 256] In other words, epithelial cell-type-specific models combine the knowledge of Ca^{2+} signaling linked to epithelial functionality.

6.6 Future perspectives and limitations

The proteome of the stem cell-derived RPE resembles the native RPE in many aspects [289], and the stem cell-derived RPE can perform several RPE functions, such as phagocytosis [10, 29, 32, 33, 290-292], VEGF secretion [29-32], and visual cycle [293, 294]. Important differences include a lower efficiency in the phagocytosis [66] and growth factor secretion [295], as well as differences in the expression of adhesion junction and membrane transport genes [296]. This dissertation also showed similarities and differences in the ion channel machinery between the hESC-RPE and the native counterpart that are essential for stem cell applications.

The presence of a diverse pattern of functional ion channels in the hESC-RPE is promising for the success of stem cell-based transplantation therapies and the use of stem cell models in eye research. However, the functionality of K^+ channel machinery may be compromised in the cultured RPE, particularly those derived from pluripotent stem cells requiring long culture time. This indicates a need to further develop the present cell culturing methods considering ionic gradients and

their natural changes. This is important since ion channels, in general, are highly sensitive indicators of cell maturity [32, 161] and functionality [6, 33], and reflect changes in the cell culture conditions [282, 283].

Currently, the evaluation of maturity and functionality in the stem cell-derived RPE mainly relies on the identification of gene and protein level markers. This approach characterizes the RPE genotype well but excludes the functional phenotype that may differ from the genetic background. Based on the results of this dissertation, especially related to the Ca^{2+} and K^{+} channels, the functional evaluation is critical to define the sufficient maturity and correct physiology of the stem cell-derived RPE. However, traditional patch clamp measurements are time-consuming and require intense training to perform successfully. For systematic testing of the stem cell-derived RPE for clinical applications, fast and comprehensive patch clamp measurements with a high success rate would be a prerequisite. Approaches utilizing the automated patch clamp technique have been attempted to overcome these issues in epithelial and RPE cells [297, 298], yet further development is required to improve the yield. Especially in small-sized and polarized epithelial cells, the positioning of the measurement electrode is critical to obtain a large number of comparable recordings. Furthermore, such comprehensive testing requires the determination of a reliable electrophysiological gold standard corresponding human RPE with warranted maturity.

There are certain limitations in stem cell research worth noting. First, there is variation between stem cell lines as well as between the individual batches. Second, the poor availability of the native human RPE cells raises a need to find an appropriate control for the experimental work. Primary cell cultures provide a widely used cell model, and the freshly isolated mouse RPE can be utilized in most institutions. We used both freshly isolated mouse RPE and cultured hfRPE. Even though they are well-characterized and comprehensive RPE cell models, neither one of these corresponds precisely to the native human RPE. For example, the gene and protein expression profiles between human and mouse resemble each other [299, 300], yet there are anatomical differences between the species. The control issue remains to be overcome in the stem cell field.

The lack of experimental data is a general challenge in computational modeling. Usually, the experimental data is first produced in the laboratory by a different person than the modeler, who later uses this data to build the model. This makes performing the important iterations between the experimental work and the computational work challenging. Due to the lack of resources, this was also the case in this dissertation and should be paid more attention to in the design of future

projects. It is also worth noting that the ARPE-19 cell line used in our experimental setup for the computational modeling is not presently considered an optimal RPE cell model, and these cells lose their RPE-like phenotype after multiple passages. Furthermore, ARPE-19 forms a leaky epithelium with a relatively low TER value and weak barrier properties [301]. Relevant to this study, the ARPE-19 cells lack the melanosomes that may participate in Ca^{2+} signaling in the RPE as they contain high levels of Ca^{2+} [224, 225]. Furthermore, the experimental data was produced only as relative Ca^{2+} concentrations instead of absolute values [232].

7 CONCLUSIONS

Ion channels are central determinants of the RPE physiology, and therefore, their expression, functionality, and roles in RPE are crucial to investigate. This concerns especially the stem cell-derived RPE that are increasingly used as RPE cell models and in clinical therapy development, often without a thorough evaluation of their physiological properties. This dissertation provided new insight into this highly relevant and topical issue focusing on the functionality of voltage-gated Ca^{2+} channels, K^+ channels, and Cl^- channels in the hESC-RPE combined with computational modeling of Ca^{2+} signaling in a human RPE cell model. The main findings and conclusions are:

1. An extensive pattern of ion channels was found from the hESC-RPE at the protein level, and in most cases, the membrane localization was comparable to the native mouse RPE. Furthermore, this dissertation revealed the apical and cilial localization of $Ca_V1.3$ in the RPE. Previously Kir7.1 has been shown to localize only on the apical membrane, but we found its basolateral localization as well in the hESC- and native mouse RPE.

2. Both similarities and differences were observed when the ion current features were compared between the hESC-derived and the freshly isolated native RPE. The L-type Ca^{2+} channel characteristics of the hESC-RPE resembled the native mouse RPE investigated here and the native RPE in general, according to the literature. However, the hESC-RPE cells expressed heterogeneous K^+ channel machinery that did not cover all the features of the native adult RPE when compared to previous studies by other research groups. Instead, it possessed features from the native hfRPE or the cultured primary RPE from different species.

3. A central finding in this dissertation was that the ion channels are highly sensitive to RPE maturation and external conditions. Indeed, the cell culturing environment appears to be critical for the maturation of the stem cell-derived RPE functional phenotype, especially regarding the K^+

channels. It is also worth noting that $Ca_V1.3$ membrane localization developed during RPE maturation, and the co-localization of $Ca_V1.3$ near the primary cilia may be essential in this process.

4. This dissertation demonstrated that in the hESC-RPE, voltage-gated Ca^{2+} channels have a regulatory role in VEGF secretion and phagocytosis that are essential for retinal development and welfare, including photoreceptor renewal. This finding highlights the importance of ion channels for RPE functionality and thus for our visual ability.

5. Maturity and functionality of the stem cell-derived RPE are routinely evaluated based on gene or protein level expression of markers that characterize the typical RPE genotype. However, the results of this dissertation suggest that the assessment of the functional phenotype is of utmost importance for verifying the sufficient physiological maturity of the stem cell-derived RPE. Introduction of this approach to clinical applications would require the determination of the electrophysiological gold standard of human RPE as well as further improvement of the automated patch clamp method. Overall, the presence and functionality of the different ion channels in the hESC-RPE, as shown in this thesis work, are promising for the use of stem cell-derived RPE as cell models and in transplantation therapies.

6. The computational Ca^{2+} model developed in this study enabled the simulation of the experimental data of Ca^{2+} signaling in the RPE after mechanical injury. The model provided mechanistic insight into Ca^{2+} signaling mechanisms in different experimental conditions and predicted drug responses.

8 REFERENCES

1 Strauss O. The retinal pigment epithelium in visual function. Physiol Rev 2005;85:845-881.

2 Wimmers S, Karl MO, Strauss O. Ion channels in the RPE. Prog Retin Eye Res 2007;26:263-301.

3 Wong WL, Su X, Li X et al. Global prevalence of age-related macular degeneration and disease burden projection for 2020 and 2040: a systematic review and meta-analysis. Lancet Glob Health 2014;2:e106-e116.

4 Li JQ, Welchowski T, Schmid M et al. Prevalence and incidence of age-related macular degeneration in Europe: a systematic review and meta-analysis. Br J Ophthalmol 2020;104:1077-1084.

5 Moshfegh Y, Velez G, Li Y et al. BESTROPHIN1 mutations cause defective chloride conductance in patient stem cell-derived RPE. Hum Mol Genet 2016;25:2672–2680.

6 Kanzaki Y, Fujita H, Sato K et al. KCNJ13 gene deletion impairs cell alignment and phagocytosis in retinal pigment epithelium derived from human-induced pluripotent stem cells. Invest Ophthalmol Vis Sci 2020;61:38.

7 Shahi PK, Hermans D, Sinha D et al. Gene augmentation and readthrough rescue channelopathy in an iPSC-RPE model of congenital blindness. Am J Hum Genet 2019;104:310-318.

8 Lin T, Lin Y, Hsu C et al. Nanomedicine-based curcumin approach improved ROS damage in Best dystrophy-specific induced pluripotent stem cells. Cell Transplant 2019;28:1345-1357.

9 Marmorstein AD, Johnson AA, Bachman LA et al. Mutant Best1 expression and impaired phagocytosis in an iPSC model of autosomal recessive Bestrophinopathy. Sci Rep 2018;8:4487.

10 Singh R, Shen W, Kuai D et al. iPS cell modeling of Best disease: insights into the pathophysiology of an inherited macular degeneration. Hum Mol Genet 2013;22:593–607.

11 Liu J, Taylor RL, Baines RA et al. Small molecules restore Bestrophin 1 expression and function of both dominant and recessive Bestrophinopathies in patient-derived retinal pigment epithelium. Invest Ophthalmol Vis Sci 2020;61:28.

12 Ji C, Li Y, Kittredge A et al. Investigation and restoration of BEST1 activity in patient-derived RPEs with dominant mutations. Sci Rep 2019;9:19026.

13 Tang C, Han J, Dalvi S et al. A human model of Batten disease shows role of CLN3 in phagocytosis at the photoreceptor–RPE interface. Commun Biol 2021;4:161.

14 Sinha D, Steyer B, Shahi PK et al. Human iPSC modeling reveals mutation-specific responses to gene therapy in a genotypically diverse dominant maculopathy. Am J Hum Genet 2020;107:278-292.

15 Biswas P, Borooah S, Matsui H et al. Detection and validation of novel mutations in MERTK in a simplex case of retinal degeneration using WGS and hiPSC–RPEs model. Hum Mutat 2021;42:189-199.

16 Gong J, Cai H, NYSCF Global Stem Cell Array Team et al. Stem cell-derived retinal pigment epithelium from patients with age-related macular degeneration exhibit reduced metabolism and matrix interactions. Stem Cells Transl Med 2020;9:364-376.
17 Li Y, Zhang Y, Xu Y. Patient-specific mutations impair BESTROPHIN1's essential role in mediating Ca2+-dependent Cl- currents in human RPE. ELife 2017;6:e29914.
18 Galloway CA, Dalvi S, Shadforth AMA et al. Characterization of human iPSC-RPE on a prosthetic Bruch's membrane manufactured from silk fibroin. Invest Ophthalmol Vis Sci 2018;59:2792-2800.
19 Almedawar S, Vafia K, Schreiter S et al. MERTK-dependent ensheathment of photoreceptor outer segments by human pluripotent stem cell-derived retinal pigment epithelium. Stem Cell Reports 2020;14:374-389.
20 Song WK, Park K, Kim H et al. Treatment of macular degeneration using embryonic stem cell-derived retinal pigment epithelium: Preliminary results in Asian patients. Stem Cell Reports 2015;4:860-872.
21 Mandai M, Watanabe A, Kurimoto Y et al. Autologous induced stem-cell–derived retinal cells for macular degeneration. N Engl J Med 2017;376:1038-1046.
22 Schwartz SD, Tan G, Hosseini H et al. Subretinal transplantation of embryonic stem cell–derived retinal pigment epithelium for the treatment of macular degeneration: an assessment at 4 years. Invest Ophthalmol Vis Sci 2016;57:ORSFc1-ORSFc9.
23 Liu Y, Xu HW, Wang L et al. Human embryonic stem cell-derived retinal pigment epithelium transplants as a potential treatment for wet age-related macular degeneration. Cell Discov 2018;4:50.
24 Kashani AH, Lebkowski JS, Rahhal FM et al. A bioengineered retinal pigment epithelial monolayer for advanced, dry age-related macular degeneration. Sci Transl Med 2018;10:eaao4097.
25 da Cruz L, Fynes K, Georgiadis O et al. Phase 1 clinical study of an embryonic stem cell–derived retinal pigment epithelium patch in age-related macular degeneration. Nat Biotechnol 2018;36:328–337.
26 Schwartz SD, Regillo CD, Lam BL et al. Human embryonic stem cell-derived retinal pigment epithelium in patients with age-related macular degeneration and Stargardt's macular dystrophy: follow-up of two open-label phase 1/2 studies. Lancet 2015;385:509-516.
27 Mehat MS, Sundaram V, Ripamonti C et al. Transplantation of human embryonic stem cell-derived retinal pigment epithelial cells in macular degeneration. Ophthalmology 2018;125:1765-1775.
28 Sung Y, Lee MJ, Choi J et al. Long-term safety and tolerability of subretinal transplantation of embryonic stem cell-derived retinal pigment epithelium in Asian Stargardt disease patients. Br J Ophthalmol 2021;105:829-837.
29 Mamaeva D, Jazouli Z, DiFrancesco ML et al. Novel roles for voltage-gated T-type Ca2+ and ClC-2 channels in phagocytosis and angiogenic factor balance identified in human iPSC-derived RPE. FASEB J 2021;35:e21406.
30 Kokkinaki M, Sahibzada N, Golestaneh N. Human induced pluripotent stem-derived retinal pigment epithelium (RPE) cells exhibit ion transport, membrane potential, polarized vascular endothelial growth factor secretion, and gene expression pattern similar to native RPE. Stem Cells 2011;29:825-835.
31 Blenkinsop TA, Saini JS, Maminishkis A et al. Human adult retinal pigment epithelial stem cell–derived RPE monolayers exhibit key physiological characteristics of native tissue. Invest Ophthalmol Vis Sci 2015;56:7085-7099.

32 Brandl C, Zimmermann SJ, Milenkovic VM et al. In-depth characterisation of retinal pigment epithelium (RPE) cells derived from human induced pluripotent stem cells (hiPSC). Neuromolecular Med 2014;16:551–564.
33 Johansson JK, Karema-Jokinen VI, Hakanen S et al. Sodium channels enable fast electrical signaling and regulate phagocytosis in the retinal pigment epithelium. BMC Biol 2019;17:63.
34 Willoughby CE, Ponzin D, Ferrari S et al. Anatomy and physiology of the human eye: effects of mucopolysaccharidoses disease on structure and function – a review. Clin Experiment Ophthalmol 2010;38:2-11.
35 Hoon M, Okawa H, Della Santina L et al. Functional architecture of the retina: development and disease. Prog Retin Eye Res 2014;42:44-84.
36 Fu Z, Sun Y, Cakir B et al. Targeting neurovascular interaction in retinal disorders. Int J Mol Sci 2020;21:1503.
37 Keeling E, Lotery AJ, Tumbarello DA et al. Impaired cargo clearance in the retinal pigment epithelium (RPE) underlies irreversible blinding diseases. Cells 2018;7(2):16.
38 Naylor A, Hopkins A, Hudson N et al. Tight junctions of the outer blood retina barrier. Int J Mol Sci 2019;21:211.
39 Okami T, Yamamoto A, Omori K et al. Immunocytochemical localization of Na+,K(+)-ATPase in rat retinal pigment epithelial cells. J Histochem Cytochem 1990;38:1267-1275.
40 Korte GE, Wanderman MC. Distribution of Na+ K+-ATPase in regenerating retinal pigment epithelium in the rabbit. A study by electron microscopic cytochemistry. Exp Eye Res 1993;56:219-229.
41 Rizzolo LJ. The distribution of Na+,K+-ATPase in the retinal pigmented epithelium from chicken embryo is polarized in vivo but not in primary cell culture. Exp Eye Res 1990;51:435-446.
42 Hu JG, Gallemore RP, Bok D et al. Localization of NaK ATPase on cultured human retinal pigment epithelium. Invest Ophthalmol Vis Sci 1994;35:3582-3588.
43 Sugasawa K, Deguchi J, Okami T et al. Immunocytochemical analyses of distributions of Na, K-ATPase and GLUT1, insulin and transferrin receptors in the developing retinal pigment epithelial cells. Cell Struct Funct 1994;19:21-28.
44 Defoe DM, Ahmad A, Chen W et al. Membrane polarity of the Na+-K+ pump in primary cultures of Xenopus retinal pigment epithelium. Exp Eye Res 1994;59:587-596.
45 Rajasekaran SA, Hu J, Gopal J et al. Na,K-ATPase inhibition alters tight junction structure and permeability in human retinal pigment epithelial cells. Am J Physiol Cell Physiol 2003;284:C1497-C1507.
46 Ablonczy Z, Dahrouj M, Tang PH et al. Human retinal pigment epithelium cells as functional models for the RPE in vivo. Invest Ophthalmol Vis Sci 2011;52:8614-8620.
47 Maminishkis A, Chen S, Jalickee S et al. Confluent monolayers of cultured human fetal retinal pigment epithelium exhibit morphology and physiology of native tissue. Invest Ophthalmol Vis Sci 2006;47:3612-3624.
48 Quinn RH, Miller SS. Ion transport mechanisms in native human retinal pigment epithelium. Invest Ophthalmol Vis Sci 1992;33:3513-3527.
49 Frambach DA, Fain GL, Farber DB et al. Beta adrenergic receptors on cultured human retinal pigment epithelium. Invest Ophthalmol Vis Sci 1990;31:1767-1772.
50 Peng S, Rao VS, Adelman RA et al. Claudin-19 and the barrier properties of the human retinal pigment epithelium. Invest Ophthalmol Vis Sci 2011;52:1392-1403.

51 Hernandez EV, Hu JG, Frambach DA et al. Potassium conductances in cultured bovine and human retinal pigment epithelium. Invest Ophthalmol Vis Sci 1995;36:113-122.
52 Gallemore RP, Hernandez E, Tayyanipour R et al. Basolateral membrane Cl- and K+ conductances of the dark-adapted chick retinal pigment epithelium. J Neurophysiol 1993;70:1656-1668.
53 Joseph DP, Miller SS. Apical and basal membrane ion transport mechanisms in bovine retinal pigment epithelium. J Physiol 1991;435:439-463.
54 Hamann S, Kiilgaard JF, la Cour M et al. Cotransport of H+, lactate, and H2O in porcine retinal pigment epithelial cells. Exp Eye Res 2003;76:493-504.
55 Lin H, la Cour M, Andersen MV et al. Proton-lactate cotransport in the apical membrane of frog retinal pigment epithelium. Exp Eye Res 1994;59:679-688.
56 To CH, Hodson SA. The glucose transport in retinal pigment epithelium is via passive facilitated diffusion. Comp Biochem Physiol A Mol Integr Physiol 1998;121:441-444.
57 Swarup A, Samuels IS, Bell BA et al. Modulating GLUT1 expression in retinal pigment epithelium decreases glucose levels in the retina: impact on photoreceptors and Müller glial cells. Am J Physiol Cell Physiol 2019;316:C121-C133.
58 Chan T, Zhu L, Madigan MC et al. Human organic anion transporting polypeptide 1A2 (OATP1A2) mediates cellular uptake of all-trans-retinol in human retinal pigmented epithelial cells. Br J Pharmacol 2015;172:2343-2353.
59 Harrison EH. Mechanisms of transport and delivery of vitamin A and carotenoids to the retinal pigment epithelium. Mol Nutr Food Res 2019;63:1801046.
60 Bisbach CM, Hass DT, Robbings BM et al. Succinate can shuttle reducing power from the hypoxic retina to the O2-rich pigment epithelium. Cell Rep 2020;31:107606.
61 Nash RW, McKay BS, Burke JM. The response of cultured human retinal pigment epithelium to hypoxia: a comparison to other cell types. Invest Ophthalmol Vis Sci 1994;35:2850-2856.
62 Tachikawa M, Akanuma S, Imai T et al. Multiple cellular transport and binding processes of unesterified docosahexaenoic acid in outer blood–retinal barrier retinal pigment epithelial cells. Biol Pharm Bull 2018;41:1384-1392.
63 Bazan NG, Gordon WC, Rodriguez de Turco, E B. Docosahexaenoic acid uptake and metabolism in photoreceptors: retinal conservation by an efficient retinal pigment epithelial cell-mediated recycling process. Adv Exp Med Biol 1992;318:295-306.
64 Kanow MA, Giarmarco MM, Jankowski CS et al. Biochemical adaptations of the retina and retinal pigment epithelium support a metabolic ecosystem in the vertebrate eye. ELife 2017;6:e28899.
65 Lakkaraju A, Umapathy A, Tan LX et al. The cell biology of the retinal pigment epithelium. Prog Retin Eye Res 2020;78:100846.
66 Mazzoni F, Safa H, Finnemann SC. Understanding photoreceptor outer segment phagocytosis: Use and utility of RPE cells in culture. Exp Eye Res 2014;126:51-60.
67 Finnemann SC, Nandrot EF. MerTK activation during RPE phagocytosis in vivo requires alphaVbeta5 integrin. Adv Exp Med Biol 2006;572:499-503.
68 Nandrot EF, Kim Y, Brodie SE et al. Loss of synchronized retinal phagocytosis and age-related blindness in mice lacking alphavbeta5 integrin. J Exp Med 2004;200:1539-1545.
69 Yao J, Jia L, Shelby SJ et al. Circadian and noncircadian modulation of autophagy in photoreceptors and retinal pigment epithelium. Invest Ophthalmol Vis Sci 2014;55:3237-3246.

70 Laurent V, Sengupta A, Sánchez-Bretaño A et al. Melatonin signaling affects the timing in the daily rhythm of phagocytic activity by the retinal pigment epithelium. Exp Eye Res 2017;165:90-95.
71 Goyal V, DeVera C, Laurent V et al. Dopamine 2 receptor signaling controls the daily burst in phagocytic activity in the mouse retinal pigment epithelium. Invest Ophthalmol Vis Sci 2020;61.
72 Patricia Becerra S, Fariss RN, Wu YQ et al. Pigment epithelium-derived factor in the monkey retinal pigment epithelium and interphotoreceptor matrix: apical secretion and distribution. Exp Eye Res 2004;78:223-234.
73 Klettner A, Kaya L, Flach J et al. Basal and apical regulation of VEGF-A and placenta growth factor in the RPE/choroid and primary RPE. Mol Vis 2015;21:736-748.
74 Blaauwgeers HG, Holtkamp GM, Rutten H et al. Polarized vascular endothelial growth factor secretion by human retinal pigment epithelium and localization of vascular endothelial growth factor receptors on the inner choriocapillaris. Evidence for a trophic paracrine relation. Am J Pathol 1999;155:421-428.
75 Saint-Geniez M, Kurihara T, Sekiyama E et al. An essential role for RPE-derived soluble VEGF in the maintenance of the choriocapillaris. Proc Natl Acad Sci U S A 2009;106:18751-18756.
76 Cayouette M, Smith SB, Becerra SP et al. Pigment epithelium-derived factor delays the death of photoreceptors in mouse models of inherited retinal degenerations. Neurobiol Dis 1999;6:523-532.
77 Cao W, Tombran-Tink J, Elias R et al. In vivo protection of photoreceptors from light damage by pigment epithelium-derived factor. Invest Ophthalmol Vis Sci 2001;42:1646-1652.
78 Dawson DW, Volpert OV, Gillis P et al. Pigment epithelium-derived factor: a potent inhibitor of angiogenesis. Science 1999;285:245-248.
79 Boulton M, Dayhaw-Barker P. The role of the retinal pigment epithelium: Topographical variation and ageing changes. Eye 2001;15:384–389.
80 Shahi PK, Liu X, Aul B et al. Abnormal electroretinogram after Kir7.1 channel suppression suggests role in retinal electrophysiology. Sci Rep 2017;7:10651.
81 Hughes BA, Takahira M. Inwardly rectifying K+ currents in isolated human retinal pigment epithelial cells. Invest Ophthalmol Vis Sci 1996;37:1125-1139.
82 Shimura M, Yuan Y, Chang JT et al. Expression and permeation properties of the K+ channel Kir7.1 in the retinal pigment epithelium. J Physiol 2001;531:329-346.
83 Segawa Y, Hughes BA. Properties of the inwardly rectifying K+ conductance in the toad retinal pigment epithelium. J Physiol 1994;476:41-53.
84 Nowak JZ. Age-related macular degeneration (AMD): pathogenesis and therapy. Pharmacol Rep 2006;58:353-363.
85 Bandello F, Sacconi R, Querques L et al. Recent advances in the management of dry age-related macular degeneration: A review. F1000Res 2017;6:245.
86 Tsang SH, Sharma T. Atlas of inherited retinal diseases. Springer 2018:139-151.
87 Cideciyan AV, Aleman TS, Swider M et al. Mutations in ABCA4 result in accumulation of lipofuscin before slowing of the retinoid cycle: a reappraisal of the human disease sequence. Hum Mol Genet 2004;13:525–534.
88 Lenis TL, Hu J, Ng SY et al. Expression of ABCA4 in the retinal pigment epithelium and its implications for Stargardt macular degeneration. Proc Natl Acad Sci U S A 2018;115:E11120-E11127.

89 Grewal SS, Smith JJ, Carr AF. Bestrophinopathies: perspectives on clinical disease, Bestrophin-1 function and developing therapies. Ther Adv Ophthalmol 2021;13:1-16.
90 DiCarlo JE, Mahajan VB, Tsang SH. Gene therapy and genome surgery in the retina. J Clin Invest 2018;128:2177-2188.
91 Ammar MJ, Hsu J, Chiang A et al. Age-related macular degeneration therapy: a review. Curr Opin Ophthalmol 2020;31:215-221.
92 Yang T, Justus S, Li Y et al. BEST1: the best target for gene and cell therapies. Mol Ther 2015;23:1805-1809.
93 Lutolf MP, Gilbert PM, Blau HM. Designing materials to direct stem-cell fate. Nature 2009;462:433–441.
94 Maeda T, Sugita S, Kurimoto Y et al. Trends of stem cell therapies in age-related macular degeneration. J Clin Med 2021;10(8):1785.
95 Nguyen HV, Li Y, Tsang SH. Patient-specific iPSC-derived RPE for modeling of retinal diseases. J Clin Med 2015;4:567-578.
96 Dvoriashyna M, Foss AJE, Gaffney EA et al. Fluid and solute transport across the retinal pigment epithelium: a theoretical model. J R Soc Interface 2020;17:20190735.
97 Dubyak GR. Ion homeostasis, channels, and transporters: an update on cellular mechanisms. Adv Physiol Educ 2004;28:143-154.
98 Neverisky DL, Abbott GW. Ion channel-transporter interactions. Crit Rev Biochem Mol Biol 2015;51:257-267.
99 Gundersen D, Orlowski J, Rodriguez-Boulan E. Apical polarity of Na,K-ATPase in retinal pigment epithelium is linked to a reversal of the ankyrin-fodrin submembrane cytoskeleton. J Cell Biol 1991;112:863-872.
100 Lobato-Álvarez JA, Roldán ML, López-Murillo TD et al. The apical localization of Na+, K+-ATPase in cultured human retinal pigment epithelial cells depends on expression of the β2 subunit. Front Physiol 2016;7:450.
101 Crider JY, Yorio T, Sharif NA et al. The effects of elevated glucose on Na+/K(+)-ATPase of cultured bovine retinal pigment epithelial cells measured by a new nonradioactive rubidium uptake assay. J Ocul Pharmacol Ther 1997;13:337-352.
102 Edelman JL, Miller SS. Epinephrine stimulates fluid absorption across bovine retinal pigment epithelium. Invest Ophthalmol Vis Sci 1991;32:3033-3040.
103 Skarphedinsdottir SB, Eysteinsson T, Árnason SS. Mechanisms of ion transport across the mouse retinal pigment epithelium measured in vitro. Invest Ophthalmol Vis Sci 2020;61:31.
104 Bialek S, Joseph DP, Miller SS. The delayed basolateral membrane hyperpolarization of the bovine retinal pigment epithelium: mechanism of generation. J Physiol 1995;484:53-67.
105 Hu JG, Gallemore RP, Bok D et al. Chloride transport in cultured fetal human retinal pigment epithelium. Exp Eye Res 1996;62:443-448.
106 Mikami Y, Hara M, Yasukura T et al. Atrial natriuretic peptide stimulates Cl- transport in retinal pigment epithelial cells. Curr Eye Res 1995;14:391-397.
107 Kusaka S, Inanobe A, Fujita A et al. Functional Kir7.1 channels localized at the root of apical processes in rat retinal pigment epithelium. J Physiol 2001;531:27-36.
108 Yang D, Pan A, Swaminathan A et al. Expression and localization of the inwardly rectifying potassium channel Kir7.1 in native bovine retinal pigment epithelium. Invest Ophthalmol Vis Sci 2003;44:3178-3185.

109 Adijanto J, Banzon T, Jalickee S et al. CO2-induced ion and fluid transport in human retinal pigment epithelium. J Gen Physiol 2009;133:603-622.
110 Zadunaisky JA, Kinne-Saffran E, Kinne R. A Na/H exchange mechanism in apical membrane vesicles of the retinal pigment epithelium. Invest Ophthalmol Vis Sci 1989;30:2332-2340.
111 Lin H, Kenyon E, Miller SS. Na-dependent pHi regulatory mechanisms in native human retinal pigment epithelium. Invest Ophthalmol Vis Sci 1992;33:3528-3538.
112 Kenyon E, Maminishkis A, Joseph DP et al. Apical and basolateral membrane mechanisms that regulate pHi in bovine retinal pigment epithelium. Am J Physiol 1997;273:456-472.
113 Lin H, Miller SS. pHi-dependent Cl-HCO3 exchange at the basolateral membrane of frog retinal pigment epithelium. Am J Physiol 1994;266:C935-C945.
114 Edelman JL, Lin H, Miller SS. Acidification stimulates chloride and fluid absorption across frog retinal pigment epithelium. Am J Physiol 1994;266:C946-C956.
115 Giansanti V, Rodriguez GE, Savoldelli M et al. Characterization of stress response in human retinal epithelial cells. J Cell Mol Med 2013;17:103-115.
116 Civan MM, Marano CW, Matschinsky FW et al. Prolonged incubation with elevated glucose inhibits the regulatory response to shrinkage of cultured human retinal pigment epithelial cells. J Membr Biol 1994;139:1-13.
117 Loeffler KU, Mangini NJ. Immunohistochemical localization of Na+/Ca2+ exchanger in human retina and retinal pigment epithelium. Graefes Arch Clin Exp Ophthalmol 1998;236:929-933.
118 Mangini NJ, Haugh-Scheidt L, Valle JE et al. Sodium-calcium exchanger in cultured human retinal pigment epithelium. Exp Eye Res 1997;65:821-834.
119 Fijisawa K, Ye J, Zadunaisky JA. A Na+/Ca2- exchange mechanism in apical membrane vesicles of the retinal pigment epithelium. Curr Eye Res 1993;12:261-270.
120 López E, Lee-Rivera I, Alvarez-Arce A et al. Thrombin induces Ca2+-dependent glutamate release from RPE cells mediated by PLC/PKC and reverse Na+/Ca2+ exchange. Mol Vis 2019;25:546-558.
121 Kennedy BG, Mangini NJ. Plasma membrane calcium-ATPase in cultured human retinal pigment epithelium. Exp Eye Res 1996;63:547-556.
122 Huang H, Li H, Shi K et al. REK-TRAAK two-pore domain potassium channels protect human retinal pigment epithelium cells from oxidative stress. Int J Mol Med 2018;42:2584-2594.
123 Grunnet M, Jespersen T, MacAulay N et al. KCNQ1 channels sense small changes in cell volume. J Physiol 2003;549:419-427.
124 Sheu S, Wu S, Hu D et al. The influence of hypotonicity on large-conductance calcium-activated potassium channels in human retinal pigment epithelial cells. J Ocul Pharmacol Ther 2004;20:563-575.
125 Müller C, Más Gómez N, Ruth P et al. CaV1.3 L-type channels, maxiK Ca2+-dependent K+ channels and bestrophin-1 regulate rhythmic photoreceptor outer segment phagocytosis by retinal pigment epithelial cells. Cell Signal 2014;26:968-978.
126 Sheu S, Bee Y, Chen C. Resveratrol and large-conductance calcium-activated potassium channels in the protection of human retinal pigment epithelial cells. J Ocul Pharmacol Ther 2008;24:551-556.
127 Hughes BA, Takahira M, Segawa Y. An outwardly rectifying K+ current active near resting potential in human retinal pigment epithelial cells. Am J Physiol 1995;269:C179-C187.

128 Strauss O, Wienrich M. Cultured retinal pigment epithelial cells from RCS rats express an increased calcium conductance compared with cells from non-dystrophic rats. Pflugers Arch 1993;425:68–76.
129 Strauss O, Weiser T, Wienrich M. Potassium currents in cultured cells of the rat retinal pigment epithelium. Comp Biochem Physiol A Physiol 1994;109:975-983.
130 Strauss O, Rosenthal R, Dey D et al. Effects of protein kinase C on delayed rectifier K+ channel regulation by tyrosine kinase in rat retinal pigment epithelial cells. Invest Ophthalmol Vis Sci 2002;43:1645-1654.
131 Fox JA, Steinberg RH. Voltage-dependent currents in isolated cells of the turtle retinal pigment epithelium. Pflugers Arch 1992;420:451–460.
132 Hughes BA, Steinberg RH. Voltage-dependent currents in isolated cells of the frog retinal pigment epithelium. J Physiol 1990;428:273-297.
133 Wen R, Lui GM, Steinberg RH. Whole-cell K+ currents in fresh and cultured cells of the human and monkey retinal pigment epithelium. J Physiol 1993;465:121-147.
134 Tao Q, Rafuse PE, Kelly ME. Potassium currents in cultured rabbit retinal pigment epithelial cells. J Membr Biol 1994;141:123-138.
135 Takahira M, Hughes BA. Isolated bovine retinal pigment epithelial cells express delayed rectifier type and M-type K+ currents. Am J Physiol 1997;273:C790-C803.
136 Wollmann G, Lenzner S, Berger W et al. Voltage-dependent ion channels in the mouse RPE: comparison with Norrie disease mice. Vision Res 2006;46:688-698.
137 Pinto LH, Klumpp DJ. Localization of potassium channels in the retina. Prog Retin Eye Res 1998;17:207-230.
138 Caminos E, Vaquero CF, Martinez-Galan JR. Relationship between rat retinal degeneration and potassium channel KCNQ5 expression. Exp Eye Res 2015;131:1-11.
139 Pattnaik BR, Hughes BA. Effects of KCNQ channel modulators on the M-type potassium current in primate retinal pigment epithelium. Am J Physiol Cell Physiol 2012;302:C821-C833.
140 Zhang X, Yang D, Hughes BA. KCNQ5/K_v7.5 potassium channel expression and subcellular localization in primate retinal pigment epithelium and neural retina. Am J Physiol Cell Physiol 2011;301:C1017-C1026.
141 Zhang X, Hughes BA. KCNQ and KCNE potassium channel subunit expression in bovine retinal pigment epithelium. Exp Eye Res 2013;116:424-432.
142 Lu Z. Mechanism of rectification in inward-rectifier K+ channels. Annu Rev Physiol 2004;66:103-129.
143 Hughes BA, Takahira M. ATP-dependent regulation of inwardly rectifying K^+ current in bovine retinal pigment epithelial cells. Am J Physiol 1998;275:C1372-C1383.
144 Pattnaik BR, Hughes BA. Regulation of Kir channels in bovine retinal pigment epithelial cells by phosphatidylinositol 4,5-bisphosphate. Am J Physiol Cell Physiol 2009;297:C1001-C1011.
145 Yuan Y, Shimura M, Hughes BA. Regulation of inwardly rectifying K+ channels in retinal pigment epithelial cells by intracellular pH. J Physiol 2003;549:429-438.
146 Hughes BA, Swaminathan A. Modulation of the Kir7.1 potassium channel by extracellular and intracellular pH. Am J Physiol Cell Physiol 2008;294:C423-C431.
147 Kusaka S, Horio Y, Fujita A et al. Expression and polarized distribution of an inwardly rectifying K+ channel, Kir4.1, in rat retinal pigment epithelium. J Physiol 1999;520:373-381.

148 Yang D, Zhang X, Hughes BA. Expression of inwardly rectifying potassium channel subunits in native human retinal pigment epithelium. Exp Eye Res 2008;87:176-183.
149 Sheu S, Wu S. Mechanism of inhibitory actions of oxidizing agents on calcium-activated potassium current in cultured pigment epithelial cells of the human retina. Invest Ophthalmol Vis Sci 2003;44:1237-1244.
150 Sheu S, Wu S, Hu D. Stretch-stimulated activity of large conductance calcium-activated potassium channels in human retinal pigment epithelial cells. J Ocul Pharmacol Ther 2005;21:429-435.
151 Wimmers S, Halsband C, Seyler S et al. Voltage-dependent Ca2+ channels, not ryanodine receptors, activate Ca2+-dependent BK potassium channels in human retinal pigment epithelial cells. Mol Vis 2008;14:2340-2348.
152 Genewsky A, Jost I, Busch C et al. Activation of endogenously expressed ion channels by active complement in the retinal pigment epithelium. Pflugers Arch 2015;467:2179–2191.
153 Tao Q, Kelly ME. Calcium-activated potassium current in cultured rabbit retinal pigment epithelial cells. Curr Eye Res 1996;15:237-246.
154 Tsuruma K, Tanaka Y, Shimazawa M et al. Unoprostone reduces oxidative stress- and light-induced retinal cell death, and phagocytotic dysfunction, by activating BK channels. Mol Vis 2011;17:3556-3565.
155 Hartzell HC, Qu Z. Chloride currents in acutely isolated Xenopus retinal pigment epithelial cells. J Physiol 2003;549(Pt 2):453-469.
156 Keckeis S, Reichhart N, Roubeix C et al. Anoctamin2 (TMEM16B) forms the Ca2+-activated Cl− channel in the retinal pigment epithelium. Exp Eye Res 2017;154:139-150.
157 Botchkin LM, Matthews G. Chloride current activated by swelling in retinal pigment epithelium cells. Am J Physiol 1993;265:C1037-C1045.
158 Weng TX, Godley BF, Jin GF et al. Oxidant and antioxidant modulation of chloride channels expressed in human retinal pigment epithelium. Am J Physiol Cell Physiol 2002;283:C839-C849.
159 Neussert R, Müller C, Milenkovic VM et al. The presence of bestrophin-1 modulates the Ca2+ recruitment from Ca2+ stores in the ER. Pflugers Arch 2010;460:163-175.
160 Marmorstein AD, Marmorstein LY, Rayborn M et al. Bestrophin, the product of the Best vitelliform macular dystrophy gene (VMD2), localizes to the basolateral plasma membrane of the retinal pigment epithelium. Proc Natl Acad Sci U S A 2000;97:12758-12763.
161 Bakall B, Marmorstein LY, Hoppe G et al. Expression and localization of bestrophin during normal mouse development. Invest Ophthalmol Vis Sci 2003;44:3622-3628.
162 Zhang Y, Kittredge A, Ward N et al. ATP activates bestrophin ion channels through direct interaction. Nat Commun 2018;9:3126.
163 Marmorstein AD, Kinnick TR, Stanton JB et al. Bestrophin-1 influences transepithelial electrical properties and Ca2+ signaling in human retinal pigment epithelium. Mol Vis 2015;21:347-359.
164 Rosenthal R, Bakall B, Kinnick T et al. Expression of bestrophin-1, the product of the VMD2 gene, modulates voltage-dependent Ca2+ channels in retinal pigment epithelial cells. FASEB J 2006;20:178-180.
165 Reichhart N, Milenkovic VM, Halsband C et al. Effect of bestrophin-1 on L-type Ca2+ channel activity depends on the Ca2+ channel beta-subunit. Exp Eye Res 2010;91:630-639.

166 Strauß O, Reichhart N, Gomez NM et al. Contribution of ion channels in calcium signaling regulating phagocytosis: maxiK, Cav1.3 and bestrophin-1. Adv Exp Med Biol 2016;854:739-744.
167 Johnson AA, Guziewicz KE, Lee CJ et al. Bestrophin 1 and retinal disease. Prog Retin Eye Res 2017;58:45-69.
168 Schreiber R, Kunzelmann K. Expression of anoctamins in retinal pigment epithelium (RPE). Pflugers Arch 2016;468:1921-1929.
169 Zhang H, Wong CL, Shan SW et al. Characterisation of Cl- transporter and channels in experimentally induced myopic chick eyes. Clin Exp Optom 2011;94:528-535.
170 Hanke-Gogokhia C, Lehmann GL, Benedicto I et al. Apical CLC-2 in retinal pigment epithelium is crucial for survival of the outer retina. FASEB J 2021;35:e21689.
171 Zhao J, Zhong W, Sun L et al. Effect of chloride channel activity on retinal pigment cell proliferation and migration. Mol Med Rep 2017;15:1771-1776.
172 Blaug S, Quinn R, Quong J et al. Retinal pigment epithelial function: a role for CFTR?. Doc Ophthalmol 2003;106:43-50.
173 Reigada D, Mitchell CH. Release of ATP from retinal pigment epithelial cells involves both CFTR and vesicular transport. Am J Physiol Cell Physiol 2005;288:C132-C140.
174 Wu J, Marmorstein AD, Peachey NS. Functional abnormalities in the retinal pigment epithelium of CFTR mutant mice. Exp Eye Res 2006;83:424-428.
175 Bagal SK, Marron BE, Owen RM et al. Voltage gated sodium channels as drug discovery targets. Channels (Austin) 2015;9:360-366.
176 Hanukoglu I, Hanukoglu A. Epithelial sodium channel (ENaC) family: Phylogeny, structure–function, tissue distribution, and associated inherited diseases. Gene 2016;579:95-132.
177 Wen R, Lui GM, Steinberg RH. Expression of a tetrodotoxin-sensitive Na+ current in cultured human retinal pigment epithelial cells. J Physiol 1994;476:187-196.
178 Sakai H, Saito T. Na+ and Ca2+ channel expression in cultured newt retinal pigment epithelial cells: comparison with neuronal types of ion channels. J Neurobiol 1997;32:377-390.
179 Botchkin LM, Matthews G. Voltage-dependent sodium channels develop in rat retinal pigment epithelium cells in culture. Proc Natl Acad Sci U S A 1994;91:4564-4568.
180 Krueger B, Schlötzer-Schrehardt U, Haerteis S et al. Four subunits (αβγδ) of the epithelial sodium channel (ENaC) are expressed in the human eye in various locations. Invest Ophthalmol Vis Sci 2012;53:596-604.
181 Cordeiro S, Strauss O. Expression of Orai genes and I(CRAC) activation in the human retinal pigment epithelium. Graefes Arch Clin Exp Ophthalmol 2011;249:47-54.
182 Gómez NM, Tamm ER, Strauβ O. Role of bestrophin-1 in store-operated calcium entry in retinal pigment epithelium. Pflugers Arch 2013;465:481-495.
183 Koschak A, Reimer D, Huber I et al. α1D (Cav1.3) subunits can form L-type Ca2+ channels activating at negative voltages. J Biol Chem 2001;276:22100-22106.
184 Wimmers S, Coeppicus L, Rosenthal R et al. Expression profile of voltage-dependent Ca2+ channel subunits in the human retinal pigment epithelium. Graefes Arch Clin Exp Ophthalmol 2008;246:685-692.
185 Rosenthal R, Heimann H, Agostini H et al. Ca2+ channels in retinal pigment epithelial cells regulate vascular endothelial growth factor secretion rates in health and disease. Mol Vis 2007;13:443-456.

186 Rosenthal R, Malek G, Salomon N et al. The fibroblast growth factor receptors, FGFR-1 and FGFR-2, mediate two independent signalling pathways in human retinal pigment epithelial cells. Biochem Biophys Res Commun 2005;337:241-247.
187 Mergler S, Steinhausen K, Wiederholt M et al. Altered regulation of L-type channels by protein kinase C and protein tyrosine kinases as a pathophysiologic effect in retinal degeneration. FASEB J 1998;12:1125-1134.
188 Ueda Y, Steinberg RH. Voltage-operated calcium channels in fresh and cultured rat retinal pigment epithelial cells. Invest Ophthalmol Vis Sci 1993;34:3408-3418.
189 Ueda Y, Steinberg RH. Dihydropyridine-sensitive calcium currents in freshly isolated human and monkey retinal pigment epithelial cells. Invest Ophthalmol Vis Sci 1995;36:373-380.
190 Strauss O, Mergler S, Wiederholt M. Regulation of L-type calcium channels by protein tyrosine kinase and protein kinase C in cultured rat and human retinal pigment epithelial cells. FASEB J 1997;11:859-867.
191 Strauss O, Buss F, Rosenthal R et al. Activation of neuroendocrine L-type channels (α1D subunits) in retinal pigment epithelial cells and brain neurons by pp60c-src. Biochem Biophys Res Commun 2000;270:806-810.
192 Rosenthal R, Thieme H, Strauss O. Fibroblast growth factor receptor 2 (FGFR2) in brain neurons and retinal pigment epithelial cells act via stimulation of neuroendocrine L-type channels (Ca(v)1.3). FASEB J 2001;15:970-977.
193 Reichhart N, Markowski M, Ishiyama S et al. Rab27a GTPase modulates L-type Ca2+ channel function via interaction with the II–III linker of CaV1.3 subunit. Cell Signal 2015;27:2231-2240.
194 Cordes M, Bucichowski P, Alfaar AS et al. Inhibition of Ca2+ channel surface expression by mutant bestrophin-1 in RPE cells. FASEB J 2020;34:4055-4071.
195 Karl MO, Kroeger W, Wimmers S et al. Endogenous Gas6 and Ca2+-channel activation modulate phagocytosis by retinal pigment epithelium. Cell Signal 2008;20:1159-1168.
196 Mergler S, Strauß O. Stimulation of L-type Ca2+channels by increase of intracellular InsP3 in rat retinal pigment epithelial cells. Exp Eye Res 2002;74:29-40.
197 Venkatachalam K, Montell C. TRP channels. Annu Rev Biochem 2007;76:387-417.
198 Kennedy BG, Torabi AJ, Kurzawa R et al. Expression of transient receptor potential vanilloid channels TRPV5 and TRPV6 in retinal pigment epithelium. Mol Vis 2010;16:665-675.
199 Cordeiro S, Seyler S, Stindl J et al. Heat-sensitive TRPV channels in retinal pigment epithelial cells: regulation of VEGF-A secretion. Invest Ophthalmol Vis Sci 2010;51:6001-6008.
200 Martínez-García MC, Martínez T, Pañeda C et al. Differential expression and localization of transient receptor potential vanilloid 1 in rabbit and human eyes. Histol Histopathol 2013;28:1507-1516.
201 Zhao PY, Gan G, Peng S et al. TRP channels localize to subdomains of the apical plasma membrane in human fetal retinal pigment epithelium. Invest Ophthalmol Vis Sci 2015;56:1916-1923.
202 Bollimuntha S, Cornatzer E, Singh BB. Plasma membrane localization and function of TRPC1 is dependent on its interaction with β-tubulin in retinal epithelium cells. Vis Neurosci 2005;22:163-170.
203 Wimmers S, Strauss O. Basal calcium entry in retinal pigment epithelial cells is mediated by TRPC channels. Invest Ophthalmol Vis Sci 2007;48:5767-5772.

204 Gilliam JC, Wensel TG. TRP channel gene expression in the mouse retina. Vision Res 2011;51:2440-2452.
205 Mitchell CH. Release of ATP by a human retinal pigment epithelial cell line: potential for autocrine stimulation through subretinal space. J Physiol 2001;534:193-202.
206 Reigada D, Lu W, Zhang X et al. Degradation of extracellular ATP by the retinal pigment epithelium. Am J Physiol Cell Physiol 2005;289:C617-C624.
207 Ryan JS, Baldridge WH, Kelly ME. Purinergic regulation of cation conductances and intracellular Ca2+ in cultured rat retinal pigment epithelial cells. J Physiol 1999;520:745-759.
208 Yang D, Elner SG, Clark AJ et al. Activation of P2X receptors induces apoptosis in human retinal pigment epithelium. Invest Ophthalmol Vis Sci 2011;52:1522-1530.
209 Sullivan DM, Erb L, Anglade E et al. Identification and characterization of P2Y2 nucleotide receptors in human retinal pigment epithelial cells. J Neurosci Res 1997;49:43-52.
210 Collison DJ, Tovell VE, Coombes LJ et al. Potentiation of ATP-induced Ca2+ mobilisation in human retinal pigment epithelial cells. Exp Eye Res 2005;80:465-475.
211 Peterson WM, Meggyesy C, Yu K et al. Extracellular ATP activates calcium signaling, ion, and fluid transport in retinal pigment epithelium. J Neurosci 1997;17:2324-2337.
212 Doktor F, Prager P, Wiedemann P et al. Hypoxic expression of NLRP3 and VEGF in cultured retinal pigment epithelial cells: contribution of P2Y2 receptor signaling. Purinergic Signal 2018;14:471-484.
213 Lu W, Gómez NM, Lim JC et al. The P2Y12 receptor antagonist ticagrelor reduces lysosomal pH and autofluorescence in retinal pigmented epithelial cells from the ABCA4-/- mouse model of retinal degeneration. Front Pharmacol 2018;19:242.
214 Reigada D, Lu W, Mitchell CH. Glutamate acts at NMDA receptors on fresh bovine and on cultured human retinal pigment epithelial cells to trigger release of ATP. J Physiol 2006;575:707-720.
215 López-Colomé AM, Fragoso G, Wright CE et al. Excitatory amino acid receptors in membranes from cultured human retinal pigment epithelium. Curr Eye Res 1994;13:553-560.
216 Uchida N, Kiuchi Y, Miyamoto K et al. Glutamate-stimulated proliferation of rat retinal pigment epithelial cells. Eur J Pharmacol 1998;343:265-273.
217 López-Colomé AM, Salceda R, Fragoso G. Specific interaction of glutamate with membranes from cultured retinal pigment epithelium. J Neurosci Res 1993;34:454-461.
218 Fragoso G, López-Colomé A. Excitatory amino acid-induced inositol phosphate formation in cultured retinal pigment epithelium. Vis Neurosci 1999;16:263-269.
219 Greenberger LM, Besharse JC. Stimulation of photoreceptor disc shedding and pigment epithelial phagocytosis by glutamate, aspartate, and other amino acids. J Comp Neurol 1985;239:361-372.
220 Hamill OP. Twenty odd years of stretch-sensitive channels. Pflugers Arch 2006;453:333-351.
221 Himpens B, Stalmans P, Gomez P et al. Intra- and intercellular Ca2+ signaling in retinal pigment epithelial cells during mechanical stimulation. FASEB J 1999;13:S63-S68.
222 Stalmans P, Himpens B. A decreased Ca2+-wave propagation is found among cultured RPE cells from dystrophic RCS rats. Invest Ophthalmol Vis Sci 1998;39:1493-1502.
223 Berridge M, Bootman M, Roderick H. Calcium signalling: dynamics, homeostasis and remodelling. Nat Rev Mol Cell Biol 2003;4:517–529.

224 Salceda R, Sánchez-Chávez G. Calcium uptake, release and ryanodine binding in melanosomes from retinal pigment epithelium. Cell Calcium 2000;27:223-229.
225 Jiang M, Paniagua AE, Volland S et al. Microtubule motor transport in the delivery of melanosomes to the actin-rich apical domain of the retinal pigment epithelium. J Cell Sci 2020;133:jcs242214.
226 Lemon G, Gibson WG, Bennett MR. Metabotropic receptor activation, desensitization and sequestration—I: modelling calcium and inositol 1,4,5-trisphosphate dynamics following receptor activation. J Theor Biol 2003;223:93-111.
227 Decrock E, De Bock M, Wang N et al. IP3, a small molecule with a powerful message. Biochim Biophys Acta 2013;1833:1772-1786.
228 Siefjediers A, Hardt M, Prinz G et al. Characterization of inositol 1,4,5-trisphosphate (IP3) receptor subtypes at rat colonic epithelium. Cell Calcium 2007;41:303-315.
229 Sugiyama T, Yamamoto-Hino M, Wasano K et al. Subtype-specific expression patterns of inositol 1,4,5-trisphosphate receptors in rat airway epithelial cells. J Histochem Cytochem 1996;44:1237-1242.
230 Maranto AR. Primary structure, ligand binding, and localization of the human type 3 inositol 1,4,5-trisphosphate receptor expressed in intestinal epithelium. J Biol Chem 1994;269:1222-1230.
231 Van Petegem F. Ryanodine receptors: structure and function. J Biol Chem 2012;287:31624-31632.
232 Abu Khamidakh AE, Juuti-Uusitalo K, Larsson K et al. Intercellular Ca2+ wave propagation in human retinal pigment epithelium cells induced by mechanical stimulation. Exp Eye Res 2013;108:129-139.
233 Stalmans P, Himpens B. Confocal imaging of Ca2+ signaling in cultured rat retinal pigment epithelial cells during mechanical and pharmacologic stimulation. Invest Ophthalmol Vis Sci 1997;38:176-187.
234 Nielsen MS, Axelsen LN, Sorgen PL et al. Gap junctions. Compr Physiol 2012;2:1981-2035.
235 Akanuma S, Higashi H, Maruyama S et al. Expression and function of connexin 43 protein in mouse and human retinal pigment epithelial cells as hemichannels and gap junction proteins. Exp Eye Res 2018;168:128-137.
236 Kerr NM, Johnson CS, de Souza CF et al. Immunolocalization of gap junction protein connexin43 (GJA1) in the human retina and optic nerve. Invest Ophthalmol Vis Sci 2010;51:4028-4034.
237 Malfait M, Gomez P, van Veen TA et al. Effects of hyperglycemia and protein kinase C on connexin43 expression in cultured rat retinal pigment epithelial cells. J Membr Biol 2001;181:31-40.
238 Pocrnich CE, Shao Q, Liu H et al. The effect of connexin43 on the level of vascular endothelial growth factor in human retinal pigment epithelial cells. Graefes Arch Clin Exp Ophthalmol 2012;250:515-522.
239 Kojima A, Nakahama K, Ohno-Matsui K et al. Connexin 43 contributes to differentiation of retinal pigment epithelial cells via cyclic AMP signaling. Biochem Biophys Res Commun 2008;366:532-538.
240 Lemon G, Gibson WG, Bennett MR. Metabotropic receptor activation, desensitization and sequestration—II: modelling the dynamics of the pleckstrin homology domain. J Theor Biol 2003;223:113-129.

241 De Young GW, Keizer J. A single-pool inositol 1,4,5-trisphosphate-receptor-based model for agonist-stimulated oscillations in Ca2+ concentration. Proc Natl Acad Sci U S A 1992;89:9895-9899.
242 Sneyd J, Dufour JF. A dynamic model of the type-2 inositol trisphosphate receptor. Proc Natl Acad Sci U S A 2002;99:2398-2403.
243 Tang Y, Stephenson JL, Othmer HG. Simplification and analysis of models of calcium dynamics based on IP3-sensitive calcium channel kinetics. Biophys J 1996;70:246-263.
244 Jafri MS, Keizer J. On the roles of Ca2+ diffusion, Ca2+ buffers, and the endoplasmic reticulum in IP3-induced Ca2+ waves. Biophys J 1995;69:2139-2153.
245 LeBeau AP, Yule DI, Groblewski GE et al. Agonist-dependent phosphorylation of the inositol 1,4,5-trisphosphate receptor: a possible mechanism for agonist-specific calcium oscillations in pancreatic acinar cells. J Gen Physiol 1999;113:851–872.
246 Keizer J, Levine L. Ryanodine receptor adaptation and Ca2+(-)induced Ca2+ release-dependent Ca2+ oscillations. Biophys J 1996;71:3477-3487.
247 Wagner J, Keizer J. Effects of rapid buffers on Ca2+ diffusion and Ca2+ oscillations. Biophys J 1994;67:447-456.
248 Higgins ER, Cannell MB, Sneyd J. A buffering SERCA pump in models of calcium dynamics. Biophys J 2006;91:151-163.
249 Wu D, Jia Y, Zhan X et al. Effects of gap junction to Ca2+ and to IP3 on the synchronization of intercellular calcium oscillations in hepatocytes. Biophys Chem 2005;113:145-154.
250 Pecze L, Schwaller B. Characterization and modeling of Ca2+ oscillations in mouse primary mesothelial cells. Biochim Biophys Acta 2015;1853:632-645.
251 Walker DC, Hill G, Wood SM et al. Agent-based computational modeling of wounded epithelial cell monolayers. IEEE Trans Nanobioscience 2004;3:153-163.
252 Narciso C, Wu Q, Brodskiy P. Patterning of wound-induced intercellular Ca(2+) flashes in a developing epithelium. Phys Biol 2015;12:056005.
253 Grabe N, Neuber K. A multicellular systems biology model predicts epidermal morphology, kinetics and Ca2+ flow. Bioinformatics 2005;21:3541-3547.
254 Appleby PA, Shabir S, Southgate J et al. Cell-type-specific modelling of intracellular calcium signalling: a urothelial cell model. J R Soc Interface 2013;10:20130487.
255 Warren NJ, Tawhai MH, Crampin EJ. Mathematical modelling of calcium wave propagation in mammalian airway epithelium: evidence for regenerative ATP release. Exp Physiol 2010;95:232-249.
256 Warren NJ, Tawhai MH, Crampin EJ. The effect of intracellular calcium oscillations on fluid secretion in airway epithelium. J Theor Biol 2010;265:270-277.
257 Sneyd J, Wetton BT, Charles AC et al. Intercellular calcium waves mediated by diffusion of inositol trisphosphate: a two-dimensional model. Am J Physiol 1995;268:C1537-C1545.
258 Skottman H. Derivation and characterization of three new human embryonic stem cell lines in Finland. In Vitro Cell Dev Biol Anim 2010;46:206-209.
259 Vaajasaari H, Ilmarinen T, Juuti-Uusitalo K et al. Toward the defined and xeno-free differentiation of functional human pluripotent stem cell-derived retinal pigment epithelial cells. Mol Vis 2011;17:558–575.

260 Hongisto H, Ilmarinen T, Vattulainen M et al. Xeno- and feeder-free differentiation of human pluripotent stem cells to two distinct ocular epithelial cell types using simple modifications of one method. Stem Cell Res Ther 2017;8:291.
261 Okada Y. Patch clamp techniques. Springer 2012:22-23.
262 Harden SW. pyABF 2.2.3. [Online]. Available: https://pypi.org/project/pyabf 2020.
263 Schneider CA, Rasband WS, Eliceiri KW. NIH Image to ImageJ: 25 years of image analysis. Nat Methods 2012;9:671-675.
264 Mao Y, Finnemann SC. Analysis of photoreceptor outer segment phagocytosis by RPE cells in culture. Methods Mol Biol 2013;935:285-295.
265 Immel J, Steinberg RH. Spatial buffering of K+ by the retinal pigment epithelium in frog. J Neurosci 1986;6:3197-3204.
266 Hollborn M, Vogler S, Reichenbach A et al. Regulation of the hyperosmotic induction of aquaporin 5 and VEGF in retinal pigment epithelial cells: involvement of NFAT5. Mol Vis 2015;21:360-377.
267 Faby H, Hillenkamp J, Roider J et al. Hyperthermia-induced upregulation of vascular endothelial growth factor in retinal pigment epithelial cells is regulated by mitogen-activated protein kinases. Graefes Arch Clin Exp Ophthalmol 2014;252:1737-1745.
268 Kannan R, Zhang N, Sreekumar PG et al. Stimulation of apical and basolateral VEGF-A and VEGF-C secretion by oxidative stress in polarized retinal pigment epithelial cells. Mol Vis 2006;12:1649-1659.
269 Frank Thévenod. Ion channels in secretory granules of the pancreas and their role in exocytosis and release of secretory proteins. Am J Physiol Cell Physiol 2002;283:C651-C672.
270 Waghmare S, Lefoulon C, Zhang B et al. K+ Channel-SEC11 binding exchange regulates SNARE assembly for secretory traffic. Plant Physiol 2019;181:1096-1113.
271 López MG, Albillos A, de la Fuente, M T et al. Localized L-type calcium channels control exocytosis in cat chromaffin cells. Pflugers Arch 1994;427:348-354.
272 Bokvist K, Eliassonm L, Ammälä C et al. Co-localization of L-type Ca2+ channels and insulin-containing secretory granules and its significance for the initiation of exocytosis in mouse pancreatic B-cells. EMBO J 1995;14:50-57.
273 Freeman SA, Uderhardt S, Saric A et al. Lipid-gated monovalent ion fluxes regulate endocytic traffic and support immune surveillance. Science 2020;367:301-305.
274 Xiong J, Zhu MX. Regulation of lysosomal ion homeostasis by channels and transporters. Sci China Life Sci 2016;59:777-791.
275 Sun X, Xu M, Cao Q et al. A lysosomal K+ channel regulates large particle phagocytosis by facilitating lysosome Ca2+ release. Sci Rep 2020;10:1038.
276 Catterall WA. Signaling complexes of voltage-gated sodium and calcium channels. Neurosci Lett 2010;486:107-116.
277 Striessnig J, Pinggera A, Kaur G et al. L-type Ca2+ channels in heart and brain. Wiley Interdiscip Rev Membr Transp Signal 2014;3:15-38.
278 Singh A, Gebhart M, Fritsch R et al. Modulation of voltage- and Ca2+-dependent gating of CaV1.3 L-type calcium channels by alternative splicing of a C-terminal regulatory domain. J Biol Chem 2008;283:20733-20744.
279 Liao J, Yu J, Huang K et al. Molecular signature of primary retinal pigment epithelium and stem-cell-derived RPE cells. Hum Mol Genet 2010;19:4229–4238.

280 Miyagishima KJ, Wan Q, Corneo B et al. In pursuit of authenticity: induced pluripotent stem cell-derived retinal pigment epithelium for clinical applications. Stem Cells Transl Med 2016;5:1562-1574.
281 Lidgerwood GE, Senabouth A, Smith-Anttila CJA et al. Transcriptomic profiling of human pluripotent stem cell-derived retinal pigment epithelium over time. Genomics Proteomics Bioinformatics 2020;S1672-0229(20)30135-2.
282 Ishii M, Horio Y, Tada Y et al. Expression and clustered distribution of an inwardly rectifying potassium channel, KAB-2/Kir4.1, on mammalian retinal Müller cell membrane: their regulation by insulin and laminin signals. J Neurosci 1997;17:7725-7735.
283 Andersen MN, Olesen SP, Rasmussen HB. $K_v7.1$ surface expression is regulated by epithelial cell polarization. Am J Physiol Cell Physiol 2011;300:C814-C824.
284 Hansen M, Boitano S, Dirksen ER et al. Intercellular calcium signaling induced by extracellular adenosine 5'-triphosphate and mechanical stimulation in airway epithelial cells. J Cell Sci 1993;106 (Pt 4):995-1004.
285 Caron AZ, Chaloux B, Arguin G et al. Protein kinase C decreases the apparent affinity of the inositol 1,4,5-trisphosphate receptor type 3 in RINm5F cells. Cell Calcium 2007;42:323-331.
286 Betzenhauser MJ, Fike JL, Wagner II LE et al. Protein kinase A increases type-2 inositol 1,4,5-trisphosphate receptor activity by phosphorylation of serine 937. J Biol Chem 2009;284:25116-25125.
287 Chaloux B, Caron AZ, Guillemette G. Protein kinase A increases the binding affinity and the Ca2+ release activity of the inositol 1,4,5-trisphosphate receptor type 3 in RINm5F cells. Biol Cell 2007;99:379-388.
288 Chung WC, Kermode JC. Suramin disrupts receptor-G protein coupling by blocking association of G protein alpha and betagamma subunits. J Pharmacol Exp Ther 2005;313:191-198.
289 Hongisto H, Jylhä A, Nättinen J et al. Comparative proteomic analysis of human embryonic stem cell-derived and primary human retinal pigment epithelium. Sci Rep 2017;7:6016.
290 Carr AJ, Vugler AA, Hikita ST et al. Protective effects of human iPS-derived retinal pigment epithelium cell transplantation in the retinal dystrophic rat. PLoS One 2009;4:e8152.
291 Thomas BB, Zhu D, Zhang L et al. Survival and functionality of hESC-derived retinal pigment epithelium cells cultured as a monolayer on polymer substrates transplanted in RCS rats. Invest Ophthalmol Vis Sci 2016;57:2877-2887.
292 Subrizi A, Hiidenmaa H, Ilmarinen T et al. Generation of hESC-derived retinal pigment epithelium on biopolymer coated polyimide membranes. Biomaterials 2012;33:8047-8054.
293 Maeda T, Lee MJ, Palczewska G et al. Retinal pigmented epithelial cells obtained from human induced pluripotent stem cells possess functional visual cycle enzymes in vitro and in vivo. J Biol Chem 2013;288:34484-34493.
294 Muñiz A, Greene WA, Plamper ML et al. Retinoid uptake, processing, and secretion in human iPS-RPE support the visual cycle. Invest Ophthalmol Vis Sci 2014;55:198-209.
295 Sugino IK, Sun Q, Wang J et al. Comparison of FRPE and human embryonic stem cell-derived RPE behavior on aged human Bruch's membrane. Invest Ophthalmol Vis Sci 2011;52:4979-4997.

296 Peng S, Gan G, Qiu C et al. Engineering a blood-retinal barrier with human embryonic stem cell-derived retinal pigment epithelium: transcriptome and functional analysis. Stem Cells Transl Med 2013;2:534-544.
297 Billet A, Froux L, Hanrahan JW et al. Development of automated patch clamp technique to investigate CFTR chloride channel function. Front Pharmacol 2017;8:195.
298 Lewallen CF, Wan Q, Maminishkis A et al. High-yield, automated intracellular electrophysiology in retinal pigment epithelia. J Neurosci Methods 2019;328:108442.
299 Bennis A, Gorgels TG, Ten Brink JB et al. Comparison of mouse and human retinal pigment epithelium gene expression profiles: potential implications for age-related macular degeneration. PLoS One 2015;10:e0141597.
300 Yang X, Chung JY, Rai U et al. Cadherins in the retinal pigment epithelium (RPE) revisited: P-cadherin is the highly dominant cadherin expressed in human and mouse RPE in vivo. PLoS One 2018;13:e0191279.
301 Nevala H, Ylikomi T, Tähti H. Evaluation of the selected barrier properties of retinal pigment epithelial cell line ARPE-19 for an in-vitro blood-brain barrier model. Hum Exp Toxicol 2008;27:741-749.

APPENDIX 1: ANTIBODIES FOR IMMUNOSTAINING

The primary and secondary antibodies used in this dissertation are listed in Table A1 and Table A2, respectively. The antibody name is presented together with the company, catalog number and dilution ratio.

Table A1. Primary antibodies.

Antibody	Company	Catalog number	Dilution ratio	Study
α-tubulin	Sigma Aldrich	T6793	1:1000	I
Bestrophin-1	Lagen laboratories	016-Best1-01	1:100, 1:500	I, II, III
$Ca_V1.1$	Alomone Labs	ACC-314	1:100	I
$Ca_V1.2$	Alomone Labs	ACC-003	1:100	I
$Ca_V1.3$	Alomone Labs	ACC-005	1:100	I
$Ca_V3.1$	Alomone Labs	ACC-021	1:100	I
$Ca_V3.2$	Alomone Labs	ACC-025	1:100	I
$Ca_V3.3$	Alomone Labs	ACC-009	1:100	I
CFTR	ThermoFisher Scientific	MA1-935	1:50	III
ClC-2	Alomone Labs	ACL-002	1:200	III
Claudin-3	Invitrogen	34-1700	1:80	I, II
CRALBP	Abcam	ab15051	1:500	I, II
Ezrin	Abcam	ab4069	1:100	I
Na^+/K^+-ATPase	Abcam	ab7671	1:200	I, II
Kir4.1	Abcam	ab80959	1:100	II
Kir7.1	Abcam	ab170631	1:100	II
$K_V1.3$	Alomone Labs	APC-002	1:100	II
$K_V1.4$	Abcam	ab99332	1:50	II
$K_V4.2$	Abcam	ab46797	1:50	II
KCNQ1	Alomone Labs	APC-022	1:100	II
KCNQ2	Alomone Labs	APC-050	1:100	II
KCNQ3	Alomone Labs	APC-051	1:100	II
KCNQ4	Alomone Labs	APC-164	1:100	II
KCNQ5	Alomone Labs	APC-155	1:100	II
Opsin	Sigma Aldrich	O4886	1:200	I
PCNT	Abcam	ab28144	1:200	I
ZO-1	Life Technologies	339100	1:50	I, II, III, IV

Table A2. Secondary antibodies and phalloidins.

Antibody	Company	Catalog number	Dilution ratio
Donkey anti-goat Alexa Fluor 568	Thermo Fisher Scientific	A11057	1:200
Donkey anti-mouse Alexa Fluor 488	Thermo Fisher Scientific	A21202	1:200
Donkey anti-mouse Alexa Fluor 568	Thermo Fisher Scientific	A10037	1:200
Donkey anti-mouse Alexa Fluor 647	Thermo Fisher Scientific	A31571	1:200
Donkey anti-rabbit Alexa Fluor 488	Thermo Fisher Scientific	A21206	1:200
Donkey anti-rabbit Alexa Fluor 568	Thermo Fisher Scientific	A10042	1:200
Goat anti-mouse Alexa Fluor 488	Thermo Fisher Scientific	A11029	1:200
Goat anti-mouse Alexa Fluor 568	Thermo Fisher Scientific	A11031	1:200
Goat anti-mouse Alexa Fluor 647	Thermo Fisher Scientific	A21236	1:200
Goat anti-rabbit Alexa Fluor 488	Thermo Fisher Scientific	A11008	1:200
Goat anti-rabbit Alexa Fluor 568	Thermo Fisher Scientific	A11011	1:200
Phalloidin-Atto 633	Sigma-Aldrich	68825	1:100
Phalloidin tetramethylrhodamine B 568	Sigma-Aldrich	P1951	1:400
Alexa Fluor 647 phalloidin	Thermo Fisher Scientific	A22287	1:50

PUBLICATIONS

PUBLICATION I

Functional voltage-gated calcium channels are present in human embryonic stem cell-derived retinal pigment epithelium

Korkka I, Viheriälä T, Juuti-Uusitalo K, Uusitalo-Järvinen H, Skottman H, Hyttinen J, Nymark S

Stem Cells Transl Med. 2019, 8(2):179-193
https://doi.org/10.1002/sctm.18-0026

STEM CELLS TRANSLATIONAL MEDICINE

TISSUE ENGINEERING AND REGENERATIVE MEDICINE

Functional Voltage-Gated Calcium Channels Are Present in Human Embryonic Stem Cell-Derived Retinal Pigment Epithelium

IINA KORKKA,[a] TAINA VIHERIÄLÄ,[a,b] KATI JUUTI-UUSITALO,[b] HANNELE UUSITALO-JÄRVINEN,[c,d] HELI SKOTTMAN,[b] JARI HYTTINEN,[a] SOILE NYMARK[a]

[a]Faculty of Biomedical Sciences and Engineering, BioMediTech, Tampere University of Technology, Tampere, Finland; [b]Faculty of Medicine and Life Sciences, BioMediTech, University of Tampere, Tampere, Finland; [c]Eye Centre, Tampere University Hospital, Tampere, Finland; [d]Faculty of Medicine and Life Sciences, Department of Ophthalmology, University of Tampere, Tampere, Finland

Correspondence: Soile Nymark, Ph.D., Arvo Ylpön katu 34, 33520 Tampere, Finland. Telephone: 358 40 849 0009; e-mail: soile.nymark@tut.fi

Received February 5, 2018; accepted for publication September 7, 2018; first published November 4, 2018.

http://dx.doi.org/10.1002/sctm.18-0026

Key Words. Retinal pigment epithelium • Voltage-gated Ca^{2+} channels • Stem cells • Patch-clamp • Vascular endothelial growth factor • Phagocytosis

ABSTRACT

Retinal pigment epithelium (RPE) performs important functions for the maintenance of photoreceptors and vision. Malfunctions within the RPE are implicated in several retinal diseases for which transplantations of stem cell-derived RPE are promising treatment options. Their success, however, is largely dependent on the functionality of the transplanted cells. This requires correct cellular physiology, which is highly influenced by the various ion channels of RPE, including voltage-gated Ca^{2+} (Ca_V) channels. This study investigated the localization and functionality of Ca_V channels in human embryonic stem cell (hESC)-derived RPE. Whole-cell patch-clamp recordings from these cells revealed slowly inactivating L-type currents comparable to freshly isolated mouse RPE. Some hESC-RPE cells also carried fast transient T-type resembling currents. These findings were confirmed by immunostainings from both hESC- and mouse RPE that showed the presence of the L-type Ca^{2+} channels $Ca_V1.2$ and $Ca_V1.3$ as well as the T-type Ca^{2+} channels $Ca_V3.1$ and $Ca_V3.2$. The localization of the major subtype, $Ca_V1.3$, changed during hESC-RPE maturation co-localizing with pericentrin to the base of the primary cilium before reaching more homogeneous membrane localization comparable to mouse RPE. Based on functional assessment, the L-type Ca^{2+} channels participated in the regulation of vascular endothelial growth factor secretion as well as in the phagocytosis of photoreceptor outer segments in hESC-RPE. Overall, this study demonstrates that a functional machinery of voltage-gated Ca^{2+} channels is present in mature hESC-RPE, which is promising for the success of transplantation therapies.
STEM CELLS TRANSLATIONAL MEDICINE *2019;8:179–193*

SIGNIFICANCE STATEMENT

Human stem cells provide a promising cell source for the replacement of diseased retinal pigment epithelium (RPE) in the eye, and several clinical trials with cell transplantations are ongoing. The success of these therapies is largely dependent on the correct functionality of the transplanted cells. Still, cellular ion channels, vital for the proper RPE physiology, are inadequately characterized in stem cell-derived RPE. The results of this study demonstrate the presence and functionality of voltage-gated Ca^{2+} channels in mature human embryonic stem cell-derived RPE similar to native RPE, and provide insight into their physiological relevance. This work is a significant contribution toward a more detailed functionality confirmation of stem cell-derived RPE.

INTRODUCTION

Retinal pigment epithelium (RPE) is a monolayer of polarized cells located in the back of the eye between the photoreceptors and the choroid, and forms a part of the blood-retinal-barrier [1]. As a barrier, RPE regulates the transport of nutrients and ions between the bloodstream and the subretinal space. In addition, RPE performs essential functions for vision such as phagocytosis, secretion, visual cycle, and light absorption (reviewed in [2]). RPE also plays a critical role in the pathogenesis of several degenerative eye diseases such as age-related macular degeneration (AMD) [3] that is the leading cause of vision loss and blindness among the elderly worldwide [4]. Stem cells provide potential for the development of transplantation therapies producing a limitless source of RPE cells for the treatment of AMD and other RPE-originated retinal dystrophies [5]. Remarkably, such therapies are already being subjected to clinical trials for AMD and Stargardt's macular dystrophy [6–21]

as well as to several preclinical trials [5, 22–28]. Stem cell-derived RPE has been demonstrated to resemble native tissue in many respects: it has been shown to have a proteome closely similar to the native counterpart [29], phagocytose photoreceptor outer segment (POS) fragments [27, 28, 30–32], secrete vascular endothelial growth factor (VEGF) [32–34], and participate in the functional visual cycle [35, 36]. However, much is still not understood about the genetic characteristics of stem cell-derived RPE [37] or its behavior after transplantation [38]. Furthermore, there is only limited information about the functionality of ion channels [33] and Ca^{2+} signaling [31, 39, 40] in stem cell-derived RPE. In particular, studies about the voltage-gated Ca^{2+} (Ca_V) channels in these cells are lacking.

The correct operation of Ca_V channels is required in order for the stem cell-derived RPE to perform its critical functions in therapeutic use, since many of the important RPE functions are related to changes in intracellular Ca^{2+} concentration [2]. L-type Ca^{2+} channels have been identified in cultured and native RPE [41–55], where they participate in the transport of ions and water [42] as well as the regulation of POS phagocytosis [41], VEGF secretion [43], and RPE differentiation [2]. On the other hand, the malfunctioning of L-type Ca^{2+} channels in RPE has been linked to the pathogenesis of certain degenerative eye diseases [45, 56]. Of the L-type Ca^{2+} channels, RPE has been shown to express the subtypes $Ca_V1.1$–1.3 [46] with several studies suggesting that subtype $Ca_V1.3$ is the primary contributor to RPE physiology [41, 43, 46, 50–55]. Of the T-type Ca^{2+} channels, RPE has been reported to express the subtypes $Ca_V3.1$ and $Ca_V3.3$, and it has been speculated that these channels participate in the regulation of VEGF secretion [46]. To date, α subtypes of the third subfamily $Ca_V2.x$ have not been detected in RPE [46]. It is, however, unclear whether this impressive machinery of Ca^{2+} channels is present in stem cell-derived RPE, and raises a question about the resemblance of human embryonic stem cell (hESC)-derived RPE to native RPE.

To address this issue, we investigated the functionality and localization profile of Ca_V channels in hESC-RPE. Here, we present our patch-clamp recordings that reveal slowly inactivating L-type currents in hESC-RPE that are similar to native RPE. In some hESC-RPE cells, fast transient currents that resemble T-type currents were also recorded. When compared with mouse tissue, there were similarities, as well as certain differences, in the localization of Ca_V channels in hESC-RPE. With regard to physiology, we show that L-type Ca^{2+} channels participate in POS phagocytosis and the regulation of VEGF secretion in hESC-RPE. Overall, our results suggest that a functional machinery of voltage-gated Ca^{2+} channels is present in hESC-RPE, and thus strengthen the potential of stem cell-derived RPE in transplantation therapies.

Materials and Methods

Culture of hESC-RPE

In this study, we used the previously derived hESC lines Regea08/023, Regea08/017, and Regea11/013 [57]. The undifferentiated hESCs were maintained, cultured, and spontaneously differentiated as described before [58]. After approximately 72–124 days of differentiation in the suspension culture, the pigmented areas of the floating aggregates were manually separated. The pigmented cell clusters were dissociated with TrypLE Select (Invitrogen, UK) and seeded onto Collagen IV (5 μg/cm^2, Sigma-Aldrich, St. Louis, MO) coated 24-well cell culture plates (Corning CellBIND; Corning, Inc., Corning, NY) with a density of 5.5×10^5 cells/cm^2. The cells were cultured for approximately 22–73 days, and cells from several independent differentiation batches were used for the study.

The cells were passaged with a density of 2.5×10^5 cells/cm^2 onto polyethylene terephthalate coated hanging culture inserts (pore size 1 μm, Merck Millipore) treated with Collagen IV (10 μg/cm^2, Sigma-Aldrich) or with Collagen IV and laminin (1.8 μg/cm^2, LN521, Biolamina, Sweden). The cultures became confluent in 5 days on inserts, after which they were further cultured until mature monolayers were obtained (days post-confluence presented in each figure legend). For single cell patch-clamp experiments, the cells were detached from the inserts with TrypLE Select and let to adhere on cover slips treated with poly-L-lysine (Sigma-Aldrich).

Isolation of Mouse RPE

We used C57BL/6 mice at the age of 8–12 weeks where the development and maturation of RPE had been completed [59]. The mice were euthanized by CO_2 inhalation and cervical dislocation. The eyes were then enucleated and bisected along the equator. The eyecups were sectioned in Ames' solution (Sigma-Aldrich) with 10 mM HEPES and pH adjusted to 7.4, and the retina was gently removed leaving the RPE firmly attached to the eyecup. To isolate the RPE cells for patch-clamp recordings, the eyecup was incubated at 37°C in 5% CO_2 either in TrypLE Select for 15 minutes or in a solution containing (in mM) 135 TeaCl, 5 KCl, 10 HEPES, 3 EDTA-KOH, 10 glucose, and 25 U/ml activated papain (Sigma-Aldrich) for 30 minutes. After this, the eyecups were washed in the HEPES buffered Ames' solution supplemented with 1% bovine serum albumin (BSA; Sigma-Aldrich). The RPE was collected by gentle trituration, stored at 37°C in 5% CO_2 in the RPE culture medium and measured within 6 hours.

Ethical Issues

Approval for research with human embryos was given by the National Authority for Medicolegal Affairs, Finland (Dnro 1426/32/300/05). A supportive statement was received from the Local Ethics Committee of the Pirkanmaa Hospital District, Finland to derive and expand hESC lines from surplus embryos, and to use these cell lines for research purposes (R05116). No new cell lines were derived in this study. The procedures carried out with C57BL/6 mice were in accordance with the ARVO Statement for the Use of Animals in Ophthalmic and Vision Research and the Finnish Animal Welfare Act 1986.

Patch-Clamp Recordings

Patch-clamp recordings were performed at room temperature (RT) on single hESC-RPE and mouse RPE cells. Ionic currents were recorded using the standard patch-clamp technique in whole-cell configuration. To minimize potassium currents, patch pipettes (resistance 4–8 MΩ) were filled with a cesium based internal solution containing (in mM) 83 $CsCH_3SO_3$, 25 CsCl, 5.5 EGTA, 0.5 $CaCl_2$, 4 ATP-Mg, 0.1 GTP-Na, 10 HEPES, and 5 NaCl; pH was adjusted to ~7.2 with CsOH and osmolarity was adjusted to ~290 mOsm with sucrose. The internal solution contained 2 mM lidocaine *N*-ethyl chloride (Sigma-Aldrich) to exclude the possibility of the measured fast transient currents being carried

by sodium [60]. The tissue was perfused with a control external solution containing (in mM): 120 NaCl, 5 TeaCl, 1.1 $CaCl_2$, 1.2 $MgCl_2$, 10 HEPES, 5 glucose, and 10 $BaCl_2$. pH was adjusted to 7.4 with NaOH and the osmolarity was set to ~305 mOsm with sucrose. In some experiments, the $BaCl_2$ concentration was decreased to 1 mM, and this was compensated by increasing the NaCl concentration to 130 mM. In the experiments that used Ca^{2+} channel modulators, the control bath solution contained L-type Ca^{2+} channel activator 10 μM (-)BayK8644 (Sigma-Aldrich) or L-type Ca^{2+} channel inhibitor 10 μM nifedipine (Sigma-Aldrich). The recordings were made in voltage-clamp mode using the Axopatch200B patch-clamp amplifier connected to an acquisition computer via AD/DA Digidata1440 (Molecular Devices, CA). Potentials were corrected for a 10 mV liquid junction potential during data analysis. Access resistance was <25 MΩ and membrane resistance was >300 MΩ. The membrane capacitance was 33 ± 5 pF (mean ± SEM, n = 9) for hESC-RPE cells and 23 ± 3 pF (mean ± SEM, n = 3) for mouse RPE cells. The depletion of the currents in hESC-RPE cells in whole-cell configuration was −11 ± 3% during 19 ± 5 minutes (mean ± SEM, n = 3) measured using a 50 ms voltage step from −100 to 10 mV. The measurements lasted for a shorter time than that of depletion. Current–voltage (IV)-curves were obtained from the peak value of the current at given voltages. Conductance (G) was calculated as $G = I/(V–V_R)$, where V_R is the reversal potential.

Indirect Immunofluorescence Staining

For immunofluorescence staining, hESC-RPE monolayers and mouse RPE eyecups were fixed for 15 minutes with 4% paraformaldehyde. The hESC-RPE monolayers and mouse RPE eyecup whole mount preparations were permeabilized by 15 minutes incubation in 0.1% Triton X-100 (Sigma-Aldrich) at RT. This was followed by incubation with 3% BSA in phosphate-buffered saline (PBS) (Sigma-Aldrich) at RT for 1 hour. Primary antibodies for $Ca_V1.1$, $Ca_V1.2$, $Ca_V1.3$, $Ca_V3.1$, $Ca_V3.2$, $Ca_V3.3$ (1:100; Alomone Labs, Jerusalem, Israel), cellular retinaldehyde-binding protein (CRALBP; 1:500; Abcam, UK), zonula occludens (ZO-1; 1:50; Life Technologies), claudin-3 (1:80; Thermo Fisher Scientific), ezrin (1:100; Abcam, UK), acetylated α-tubulin (1:1,000; Sigma-Aldrich), and pericentrin (PCNT; 1:200; Abcam, UK) were diluted in 3% BSA-PBS and incubated for 1 hour at RT. The samples were then washed four times with PBS, followed by 1 hour incubation at RT with the secondary antibodies donkey anti-rabbit or anti-mouse Alexa Fluor 488 and donkey anti-rabbit or anti-mouse Alexa Fluor 568 (1:200; Life Technologies) as well as goat anti-rabbit or anti-mouse Alexa Fluor 488 and goat anti-mouse Alexa Fluor 568 (1:200; Thermo Fisher Scientific) diluted in 3% BSA-PBS. Phalloidin was visualized using Phalloidin-Atto 633 (1:100; Sigma-Aldrich), an Alexa Fluor 568 conjugate (1:400; Sigma-Aldrich) or an Alexa Fluor 647 conjugate (1:50; Life Technologies). The washes with PBS were repeated and the nuclei were stained with the 4′,6-diamidino-2-phenylidole included in the mounting medium (Life Technologies).

For paraffin embedded vertical sections, the hESC-RPE monolayers and mouse eyecups with retina attached were infused in paraffin blocks and cut into 7 μm vertical sections with a Leica SM2000 R or Leica SM2010 R sliding microtome (Leica Biosystems). The sections were then attached on glass coverslides by 1 hour incubation at 60°C. The samples were deparaffinized and hydrolyzed using xylene and ethanol series. Antigen retrieval was carried out by microwaving the samples in 10 mM sodium citrate in 0.05% Tween20 (Sigma Aldrich). The samples were blocked using 10% donkey serum and 5% BSA in tris-buffered saline (TBS) for 1 hour at 37°C. After this, they were washed twice in 0.02% Tween20-TBS. The Ca_V primary antibodies listed above, as well as Na^+/K^+-ATPase (1:200; Abcam) and Bestrophin-1 (1:500; Lagen laboratories) were diluted in 1% BSA-TBS and incubated overnight at 4°C. The samples were then washed twice with 0.02% Tween20-TBS. The secondary antibodies introduced above were diluted with 1% BSA-TBS and incubated for 1 hour at RT, followed by two washes and mounting as described above.

Confocal Microscopy and Image Processing

Confocal microscopy was performed with a Zeiss LSM780 or LSM700 laser scanning confocal microscope (LSCM) on an inverted Zeiss Cell Observer microscope (Zeiss, Jena, Germany) and Plan-Apochromat ×63/1.4 oil immersion objective. Voxel size was set to $x = y$ = 66 nm and z = 100–200 nm and image size to 512 × 512 or 1,024 × 1,024 pixels. Reflection imaging was conducted by collecting light from the 488 nm laser line by using 20/80 dichroic beam splitter and 480–492 nm emission window at the photomultiplier tube detector. The images were saved in czi-format and processed with ImageJ [61], adjusting only brightness and contrast, and panels were assembled using Adobe Photoshop CS6 (Adobe Systems, San Jose).

Pulse-Chase Phagocytosis Assay

Mature hESC-RPE monolayers on culture inserts were preincubated for 24 hours at 37°C in the control medium or in the presence of the L-type Ca_V modulators 10 μM (-)BayK8644, or 10 μM nifedipine, or T-type Ca_V inhibitor 5 μM ML218 (Sigma-Aldrich). For phagocytosis assay, POS fragments were isolated and purified from fresh porcine eyes obtained from a local slaughterhouse as described before [58, 62]. The POS particles were suspended to 10% fetal bovine serum (FBS) containing medium in control or in one of the drug containing conditions. In the pulse stage, equal amounts of POS containing media were added on the apical sides of the hESC-RPE inserts and incubated for 30 minutes at 37°C. For the chase stage, the media were changed back to 10% FBS medium with or without the drugs, and the hESC-RPE inserts were further incubated for 2 hours at 37°C. After this, the samples were fixed and stained as described above using the primary antibodies opsin (1:200; Sigma Aldrich) and ZO-1. The samples were imaged using the Zeiss LSM780 LSCM as described above but by imaging large random fields. The number of bound and internalized POS particles that were larger than 1 μm in diameter, were counted from maximum intensity projection images after performing Gaussian blur using ImageJ. The assay was performed with three inserts in each condition and data from 5 to 6 images from each of the three inserts was pooled together resulting in n = 15–16.

Enzyme-Linked Immunosorbent Assay for VEGF Secretion

Secretion of VEGF by mature hESC-RPE was assessed with a commercially available human VEGF Quantikine enzyme-linked immunosorbent assay (ELISA) kit (R&D Systems, MN) according to the manufacturer's instructions. Briefly, the polarized VEGF secretion in control conditions was studied by collecting medium samples separately from the apical and basolateral sides of the

insert after 24 hours incubation with three replicates. To test the effect of Ca_V channel modulators on VEGF secretion, we measured the total VEGF concentration secreted through both apical and basolateral cell membranes. The inserts were incubated 24 hours in different pharmacological conditions: in 1% FBS medium in control conditions, or in this medium together with 10 μM (-)BayK8644, 10 μM nifedipine or 5 μM ML218 with eight to nine replicates. The VEGF concentration from the collected medium samples was normalized to the number of cells based on cell counting under the Zeiss LSM780 LSCM using ×20 or ×63 objective.

Statistical Analysis

The data is stated as mean ± SEM (n, p), where n refers to the number of samples used to generate the data set and p refers to statistical significance. The data was tested for normality using the Shapiro–Wilk normality test. Some of the data sets did not meet the normality criteria. Thus, a pair-wise comparison of the test conditions to control condition was conducted using non-parametric Mann-Whitney U test to confirm the possible statistical significance between the experimental conditions.

Results

Currents Through Voltage-Gated Ca^{2+} Channels in hESC-RPE

In control conditions with 10 mM extracellular Ba^{2+}, whole-cell voltage clamp recordings revealed voltage-gated currents in single hESC-RPE cells (Fig. 1A) dissociated from a mature RPE monolayer (Fig. 1B). In response to a 50 ms voltage pulse from −80 to 60 mV in 10 mV steps, nine cells showed slowly or non-inactivating currents (Fig. 1C). Based on the normalized and averaged IV-curve (n = 9), the current activated at low potentials reaching maximum at 10 mV (Fig. 1D). The normalized and averaged GV-curve showed half maximum conductance at −7 ± 3 mV (n = 9) (Fig. 1E). Typical to L-type Ca^{2+} channels [47, 48], diminishing the Ba^{2+} content from 10 to 1 mM decreased the maximum current density from 2.4 ± 0.5 pA·pF^{-1} (n = 9) to 1.3 ± 0.3 pA·pF^{-1} (n = 7) (Fig. 1F). In addition, three cells showed fast transient currents (Fig. 1G) with inactivation time constant 6 ± 1 ms (n = 3). The current pattern indicated that hESC-RPE is likely to express both slowly inactivating L-type currents and fast inactivating T-type resembling currents. However, a detailed characterization of the fast inactivating currents was not possible as will be discussed later.

The Effects of L-Type Ca^{2+} Channel Activator and Inhibitor

The effects of (-)BayK8644 and nifedipine, well-characterized activator and inhibitor of the L-type Ca^{2+} channels, were tested for the slowly inactivating currents. These currents were increased by 10 μM (-)BayK8644 (Fig. 2A, 2C) and decreased by 10 μM nifedipine (Fig. 2B, 2D). Comparison with the control current at maximum amplitude revealed that the slowly inactivating current increased after (-)BayK8644 application by 80 ± 9% (n = 3, p < .05) (Fig. 2E) and decreased after nifedipine application by 56 ± 5% (n = 4, p < .05) (Fig. 2F). Both effects were statistically significant. These recordings confirm that the slowly inactivating currents were carried by the L-type Ca^{2+} channels.

Localization of Voltage-Gated Ca^{2+} Channels in hESC-RPE

To evaluate the localization of the Ca_V channels detected in the patch-clamp measurements in hESC-RPE, we performed antibody labeling against the L-type Ca^{2+} channels $Ca_V1.1$-$Ca_V1.3$ and the T-type Ca^{2+} channels $Ca_V3.1$-$Ca_V3.3$, together with markers for actin cytoskeleton, RPE maturity, and polarization. The hESC-RPE showed a typical expression of CRALBP (Fig. 3A) and Na^+/K^+-ATPase (Fig. 3F) on the apical side of the monolayer, as well as Bestrophin-1 primarily on the basolateral side (Fig. 3F). Zonula occludens (ZO-1) (Fig. 3B) and claudin-3 (Fig. 3C) co-localized on the cell–cell junctions with the circumferential bands of actin (phalloidin), characteristic to mature RPE [63]. This data, together with the TER value of over 200 Ω cm^2, strong pigmentation and cobblestone morphology (see Fig. 1B), indicate the maturity and polarization of our hESC-RPE.

The most prominent staining in hESC-RPE monolayers was detected for the subtypes $Ca_V1.3$ and $Ca_V3.1$, both localizing strongly at the apical membrane (Fig. 3D, 3E). Staining of these subtypes together with RPE microvilli marker ezrin revealed the localization of $Ca_V1.3$ right below the microvilli (Supporting Information Fig. S1A) and $Ca_V3.1$ at the microvilli (Supporting Information Fig. S1B). Since pigmentation hinders the visualization of the basolateral side (see yz confocal sections in Fig. 3), we performed immunostainings on paraffin embedded vertical sections of the hESC-RPE. This confirmed the apical localization of the subtypes $Ca_V1.3$ (Fig. 3H) and $Ca_V3.1$ (Fig. 3I) and revealed a pronounced basolateral localization of $Ca_V1.3$ (Fig. 3H). Furthermore, in hESC-RPE, we observed basolateral localization of $Ca_V1.2$ (Fig. 3G), and basolateral and junctional localization of $Ca_V3.2$ (Fig. 3J). The $Ca_V1.1$ and $Ca_V3.3$ subtypes were not detected (data not shown).

Voltage-Gated Ca^{2+} Channels in Mouse RPE

To compare the currents through voltage-gated Ca^{2+} channels in hESC-RPE with native tissue, patch-clamp recordings were performed from the cells of freshly isolated mouse RPE (Fig. 4). An investigation of currents in whole-cell configuration as a response to series of depolarizing voltage steps from −80 to +60 mV revealed slowly inactivating currents in the recordings (Fig. 4A). The currents activated at low potentials reaching the maximum at 20 mV in the normalized and averaged IV-curve (n = 4) (Fig. 4B). The half maximum conductance was reached at −6 ± 3 mV (n = 4) based on the normalized and averaged GV-curve (Fig. 4C). The maximum current density of the slowly inactivating current was 2.3 ± 0.6 pA·pF^{-1} (n = 4). Thus, the current characteristics of the voltage-gated Ca^{2+} channels in mouse RPE were comparable to those we identified in hESC-RPE.

Antibody labeling, similar to hESC-RPE, was performed on mouse RPE-eyecup whole mount preparations (Fig. 4D, 4E, Supporting Information Fig. S1C, S1D) and vertical sections of paraffin embedded eyecups (Fig. 4F–4I). The channel localization in mouse RPE followed similar characteristics as in hESC-RPE with the exception that the apically localized $Ca_V3.1$ was also detected at the basolateral side in mouse RPE (Fig. 4H). Furthermore, it is worth pointing out, that the uniform apical staining profile of $Ca_V1.3$ observed in hESC-RPE (Fig. 3D, 3H, Supporting Information Fig. S1A) was especially strongly detected in mouse RPE (Fig. 4D, 4G, Supporting Information Fig. S1C).

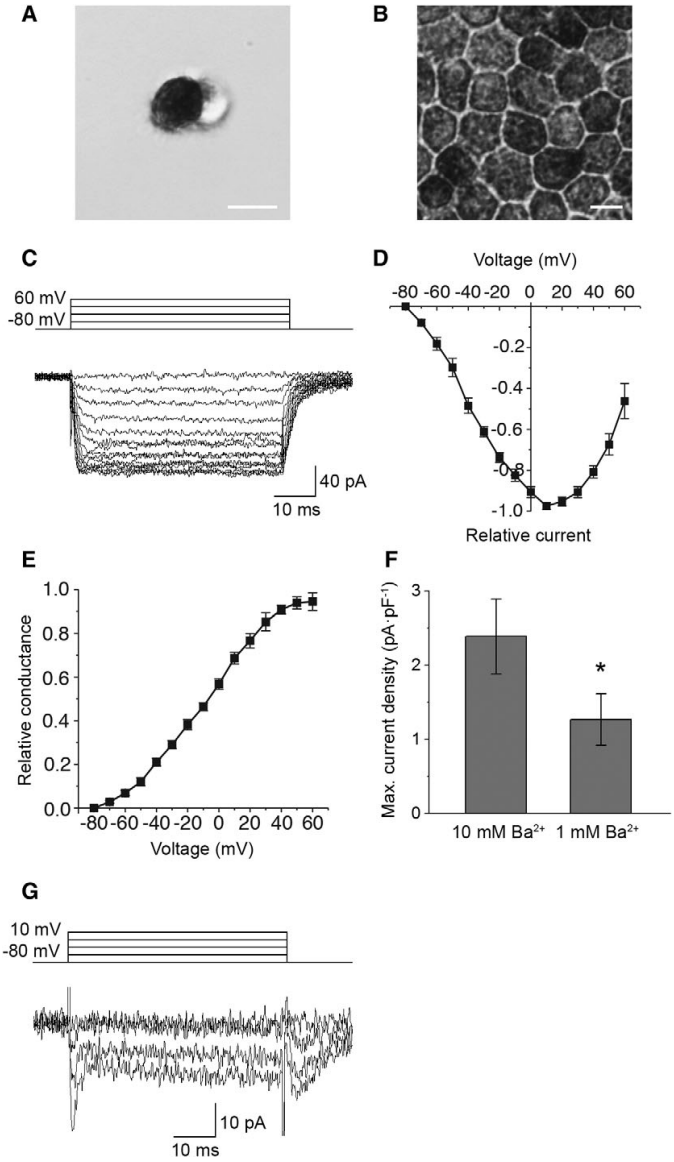

Figure 1. Voltage-gated currents in hESC-RPE. Examples of bright-field microscopy images of **(A)** a single hESC-RPE cell showing pigmented apical and non-pigmented basal sides and **(B)** a mature hESC-RPE monolayer with representative RPE morphology, scale bars 10 μm. Whole-cell voltage clamp recordings were carried out from single hESC-RPE cells. **(C):** A typical example of the slowly inactivating current elicited by 50 ms voltage steps from −80 to +60 mV in 10 mV increments. Normalized and averaged **(D)** IV-curve and **(E)** GV-curve of the slowly inactivating current (mean ± SEM, n = 9, cell lines 08/017 and 08/023, days post-confluence 73–128). **(F):** Averaged maximum current densities (obtained at 10 mV) of the slowly inactivating current in 10 mM Ba^{2+} (n = 9) and in 1 mM Ba^{2+} (n = 7, cell lines 08/017 and 08/023, days post-confluence 109–127). The difference in the current densities was statistically significant. **(G):** A typical example of the fast inactivating current elicited by 50 ms voltage steps from −80 to +10 mV in 10 mV increments (cell line 08/023, days post-confluence 109). *Statistically significant difference with $p < .05$.

VEGF Secretion in hESC-RPE

In hESC-RPE, characteristic to RPE physiology, VEGF secretion was polarized. Consistent with this, we found that the amount of VEGF secreted after a 24 hour incubation in control conditions was 588 ± 37 pg/10^5 cells to the apical side and 1,290 ± 38 pg/10^5 cells to the basolateral side (n = 3). Since the L-type Ca^{2+} channels have been reported to play an important role in VEGF secretion [43], we investigated the effect of their

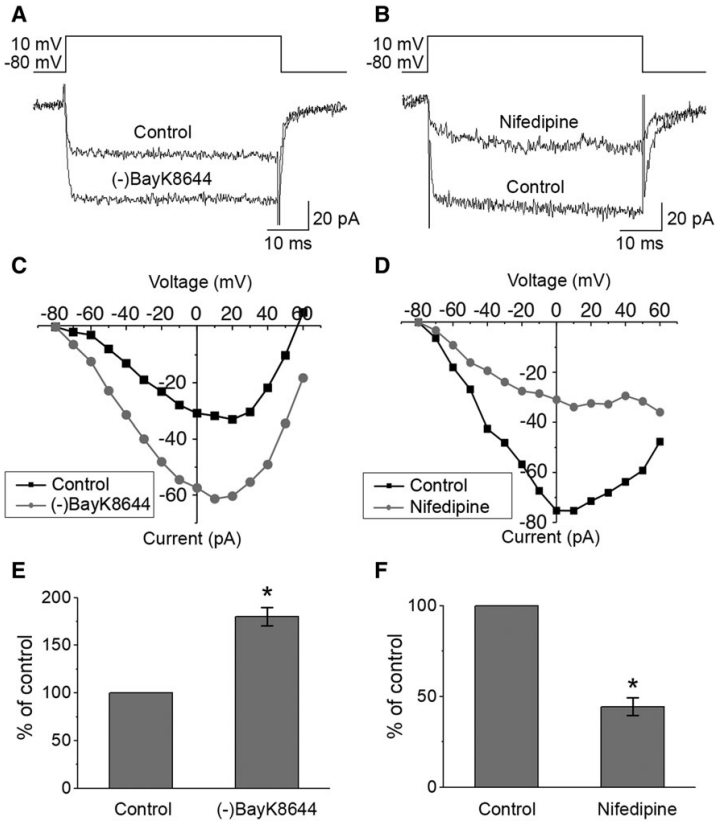

Figure 2. Responses of the currents to Ca^{2+} channel modulators. Whole-cell measurements of currents as responses to voltage pulses from −80 to +60 mV in 10 mV increments for 50 ms duration were performed before and after the application of the specific drugs. Examples of the effects of **(A)** L-type Ca^{2+} channel activator 10 μM (-)BayK8644 and **(B)** L-type Ca^{2+} channel inhibitor 10 μM nifedipine on Ba^{2+} currents in hESC-RPE and **(C, D)** the corresponding IV-curves, respectively. Changes in maximum current amplitudes presented as percentages from control conditions (mean ± SEM) show that both **(E)** activation with (-)BayK8644 (n = 3, cell line 08/017, days post-confluence 73–74) and **(F)** inhibition with nifedipine (n = 4, cell line 08/017, days post-confluence 73–99) resulted in statistically significant changes in the recorded currents. *Statistically significant difference with $p < .05$.

pharmacological modulation on the total amount of secreted VEGF in hESC-RPE. We followed the apical and basal secretion concurrently (Fig. 5) thus addressing the role of both apically and basally localized Ca^{2+} channels in the overall secretion. In control conditions, the total VEGF concentration in the medium after the 24 hour incubation was 1,950 ± 70 pg/10^5 cells (n = 9). Manipulation of the L-type Ca^{2+} channel activity directly affected the VEGF secretion as the activator (-) BayK8644 increased the secretion by 24 ± 9% (n = 9, $p < .05$) and the inhibitor nifedipine decreased the secretion by 19 ± 9% (n = 8, $p < .05$). Both effects were statistically significant. However, inhibition of the T-type channels by ML218 had little effect on the VEGF secretion (8 ± 14% increase, n = 8, $p > .05$).

Voltage-Gated Ca^{2+} Channels Regulate POS Phagocytosis in hESC-RPE

Previous studies indicate that L-type Ca^{2+} channels participate in the regulation of phagocytosis in RPE [41, 64]. Thus, we investigated the role of Ca_V channels in POS phagocytosis in hESC-RPE by pharmacologically modulating these channels during our phagocytosis assay. These experiments and subsequent labeling with opsin and ZO-1 showed a reduction in the total number of bound and internalized POS particles in the presence of either L-type channel activator or inhibitor, but an increase in the particle number in the presence of T-type channel inhibitor (Fig. 6). More specifically, the median value of POS particles in a randomly taken confocal image field decreased from the control conditions (n = 16, Fig. 6A, 6E) by 30% when the L-type channels were activated by (-)BayK8644 (n = 16, $p < .001$, Fig. 6B, 6E). A higher decrease of 62% occurred when the L-type Ca^{2+} channels were inhibited by nifedipine (n = 15, $p < .001$, Fig. 6C, 6E). Interestingly, we found that T-type Ca^{2+} channel inhibitor ML218 (Fig. 6D, 6E) increased the number of POS particles by 32% (n = 16, $p < .05$). All the effects were statistically significant.

Localization of $Ca_V1.3$ During hESC-RPE Maturation

It is well established that protein expression and localization change during RPE maturation [65]. We addressed this considering

the localization of the primary Ca_V channel subtype, $Ca_V1.3$, during hESC-RPE maturation. We immunolabeled $Ca_V1.3$ together with pericentrin (PCNT), a protein localized in the centrosomes at the base of the primary cilia, that have been recently shown to be important for RPE maturation [66, 67]. Figure 7 shows how the localization of these proteins changed remarkably during maturation. Fusiform hESC-RPE cells on the first day post-confluence (Supporting Information Fig. S2A) expressed $Ca_V1.3$ throughout the cell (Fig. 7A), and PCNT appeared as distinct puncta on the apical side. After 6 days post-confluence, the cells gained more epithelioid morphology (Supporting Information Fig. S2B) and $Ca_V1.3$ started to localize also to the apical and basal RPE cell membranes with brighter puncta forming on the apical side (Fig. 7B). Interestingly, these puncta showed co-localization with PCNT. The hESC-RPE cells obtained cobblestone morphology around 31 days post-confluence (Supporting Information Fig. S2C), and from this time point onwards, $Ca_V1.3$ was present more

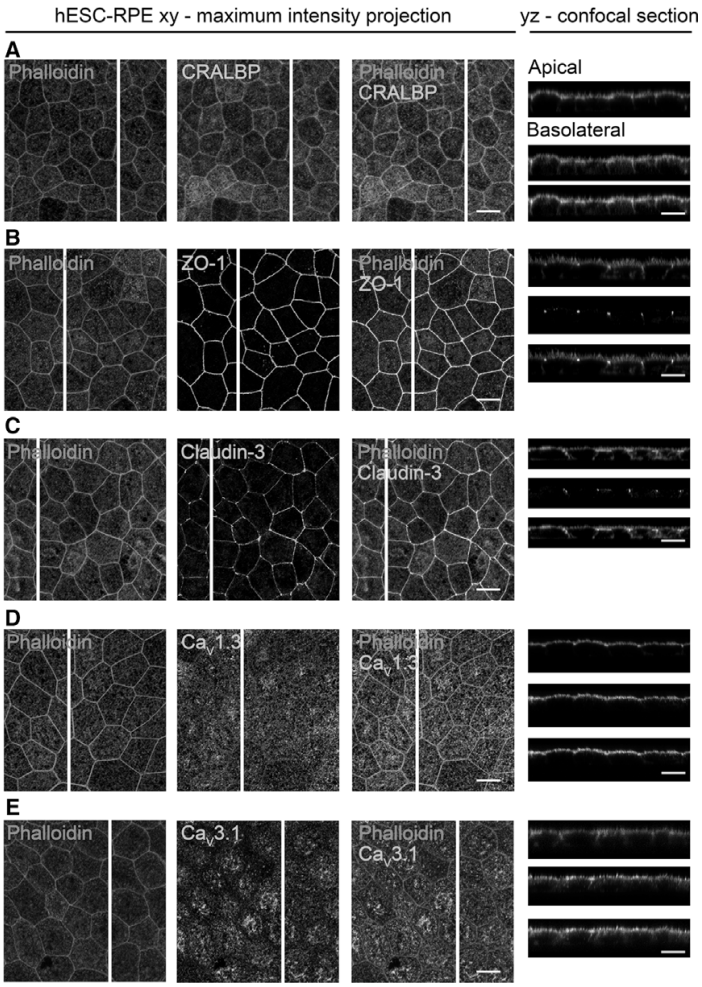

Figure 3. Localization of Ca_V channels in hESC-RPE. Immunostainings of RPE monolayers with xy-maximum intensity projections and yz-confocal sections (apical side upwards, localization of the section highlighted with a white bar). Actin cytoskeleton (phalloidin, red) labeled together with **(A)** RPE marker CRALBP (green, cell line 08/017, days post-confluence 91), **(B)** tight junction markers ZO-1, (green, cell line 08/017, days post-confluence 74) and **(C)** claudin-3 (green, cell line 08/017, days post-confluence 91), **(D)** L-type Ca^{2+} channel $Ca_V1.3$ (green, cell line 08/017, days post-confluence 109), and **(E)** T-type Ca^{2+} channel $Ca_V3.1$ (green, cell line 08/023, days post-confluence 66). Immunostainings of paraffin embedded hESC-RPE vertical sections with xy-maximum intensity projections (apical side upwards). **(F):** Cell polarization markers Na^+/K^+-ATPase (red) and Bestrophin-1 (green, cell line 08/023, days post-confluence 91). Cell nuclei (DAPI, blue) together with L-type Ca^{2+} channels **(G)** $Ca_V1.2$ (green, cell line 08/017, days post-confluence 84) and **(H)** $Ca_V1.3$ (green, cell line 08/023, days post-confluence 91), and T-type Ca^{2+} channels **(I)** $Ca_V3.1$ (green, cell line 08/017, days post-confluence 84) and **(J)** $Ca_V3.2$ (green, cell line 08/017, days post-confluence 84). Scale bars 10 μm. Abbreviations: Ca_V, voltage-gated Ca^{2+} channel; CRALBP, cellular retinaldehyde-binding protein; ZO-1, Zonula occludens; DAPI, 4′,6-diamidino-2-phenylidole; hESC, human embryonic stem cell; RPE, retinal pigment epithelium.

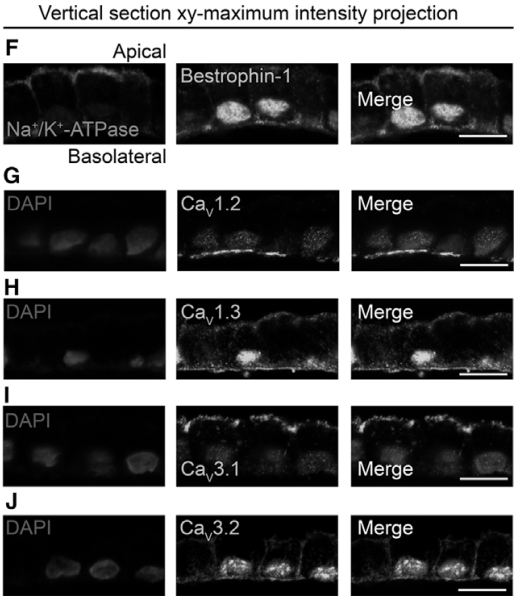

Figure 3. (Continued)

strongly on the apical and basolateral cell membranes (Fig. 7C). The apical side puncta were pronounced and appeared as one distinct cluster per cell co-localizing strongly with PCNT (Fig. 7C). Immunolabeling $Ca_V1.3$ with acetylated α-tubulin (Fig. 7E) showed the localization of $Ca_V1.3$ near the base of the primary cilia. With increasing maturation, the apical staining of $Ca_V1.3$ became more prominent and more homogeneous, while basolateral staining started to be difficult to detect due to increased pigmentation. At 84 days post-confluence (Fig. 7D), fairly uniform apical localization of $Ca_V1.3$ was present in hESC-RPE, although the puncta, co-localizing with PCNT, could still be distinguished. At this time point, PCNT localized near the apical centers of the cobblestone hESC-RPE cells (Fig. 7D, Supporting Information Fig. S2D), characteristic to mature RPE [67]. This data suggest that with increasing maturation, hESC-RPE started to gain the homogeneous apical localization of $Ca_V1.3$ detected in mouse RPE (Fig. 4D).

Discussion

Stem cell-derived RPE provides great potential for novel cell transplantation therapies and research has already proceeded to clinical trials [6–21]. Essential for the success of these therapies, stem cell-derived RPE has been shown to perform several key RPE functions [27–36]. However, the functionality of the ion channels and specifically the voltage-gated Ca^{2+} channels in these cells remain poorly known, even though many of the critical RPE functions are related to Ca^{2+} activity. This raises the question whether the stem cell-derived RPE destined for clinical purposes sufficiently resembles its native counterpart, and can thus replace the functions of lost cells. The present study addressed this issue by investigating the Ca_V channels in hESC-RPE. Using patch-clamp recordings and immunostainings, we showed the presence of functional L-type Ca^{2+} channels in hESC-RPE that are comparable to native mouse RPE.

In our study, two current types were detected, the slowly inactivating current and the fast inactivating current. We confirmed that the main current type, the slowly inactivating current, results from the activity of L-type Ca^{2+} channels since the current responses and IV-curves in this study resembled the previous recordings of L-type currents from various types of native RPE [43, 46–48]. Moreover, the sensitivity of the current to the L-type Ca^{2+} channel activator (-)BayK8644 [45–50, 53] and the inhibitor nifedipine [43, 44, 47, 48, 51] further indicated the presence of L-type currents in our measurements. The recorded current is likely to be carried primarily through $Ca_V1.3$ channels. This conclusion is based on the voltage-dependent activation of the currents at rather negative potentials [68], shape of the IV-curve characteristic to the $Ca_V1.3$ subtype [43, 46, 55], and slow inactivation of the current. It is still likely that $Ca_V1.2$ channels contribute to the recorded current as well, since our immunostainings confirmed the presence of both of the L-type Ca^{2+} channels, $Ca_V1.2$ and $Ca_V1.3$, in hESC-RPE. To date, $Ca_V1.3$ subtype has been reported to only localize basolaterally in murine [54] and porcine [55] RPE. Our data showed that both hESC- and mouse RPE express the $Ca_V1.3$ subtype also on the apical cell membrane, in addition to the basolateral membrane.

It is worth noting that patch-clamp recordings from primary RPE cultures show differences in L-type current characteristics when compared with our recordings from hESC-RPE [43, 45, 49, 50, 53], especially regarding the more negative activation threshold and the weaker slope of activation present in our study. The reason for this remains to be investigated, but it may be related to differences in phosphorylation, splicing variants, or the composition of the accessory subunits [69, 70]. Yet, the contribution of other Ca^{2+} conducting channels on the currents recorded in this study for hESC-RPE and native mouse RPE cannot be excluded. Several Ca^{2+}-conducting channels, such as store-operated Orai channels [71] and transient receptor potential (TRP) channels [41, 72–74], have important roles in the physiology of RPE. Relevant for this study, TRP channels are involved in the phagocytosis [41] and VEGF secretion [73]. In addition to these other Ca^{2+}-conductivities, the effect of cell dissociation to patch-clamp recordings needs to be taken into account. Cell–cell junctions break down in cell dissociation causing epithelial cells to lose their polarity, which compromises their normal ability to express and recycle proteins. This has a strong influence on the endocytotic processes that are important for the internalization of ion channels, regulating their numbers in the cell membrane [75]. Therefore, after cell dissociation, ion channels can be re-distributed to the intracellular compartments and those currents will thus be absent from the patch-clamp recordings.

In addition to L-type currents, our patch-clamp recordings revealed the presence of fast transient currents in hESC-RPE. The kinetics of these currents were comparable to those previously reported for the T-type Ca^{2+} channels in cultured human RPE [46], although faster than typically reported for other cell types (reviewed in [76]). Similar to the findings of the previous study [46], the fast transient currents were almost exclusively recorded in combination with the slowly inactivating current, which hindered their further analysis. In addition, TTX-sensitive currents can also contribute to the fast transient conductance

[60, 77] and make this current component extremely difficult to investigate. In immunostainings, we observed $Ca_V3.1$ and $Ca_V3.2$ in both hESC- and mouse RPE. $Ca_V3.1$ was localized apically at the microvilli in the both studied RPE cell types, while it was found also at the basolateral cell membrane in mouse RPE.

VEGF has a role in angiogenesis and vascular permeability, and therefore anti-VEGF agents are commonly used in the treatment of AMD [78]. In healthy RPE, VEGF secretion occurs in a polarized manner with significantly more pronounced secretion from the basal side [79, 80], as we showed here for hESC-RPE. This secretion is regulated by several factors including hyperosmolarity [81], hyperthermia [82], oxidative stress [83], and heat-sensitive TRPV channels [73]. Particularly relevant for this study, modulating the L-type Ca^{2+} channel activity has been shown to directly correlate with the VEGF secretion level [43]. Our ELISA results indicated similar behavior as the activator (-)BayK8644 increased the VEGF secretion and the inhibitor nifedipine decreased the VEGF secretion. This demonstrates that the L-type Ca^{2+} channels participate in the regulation of VEGF secretion in hESC-RPE. However, it is worth

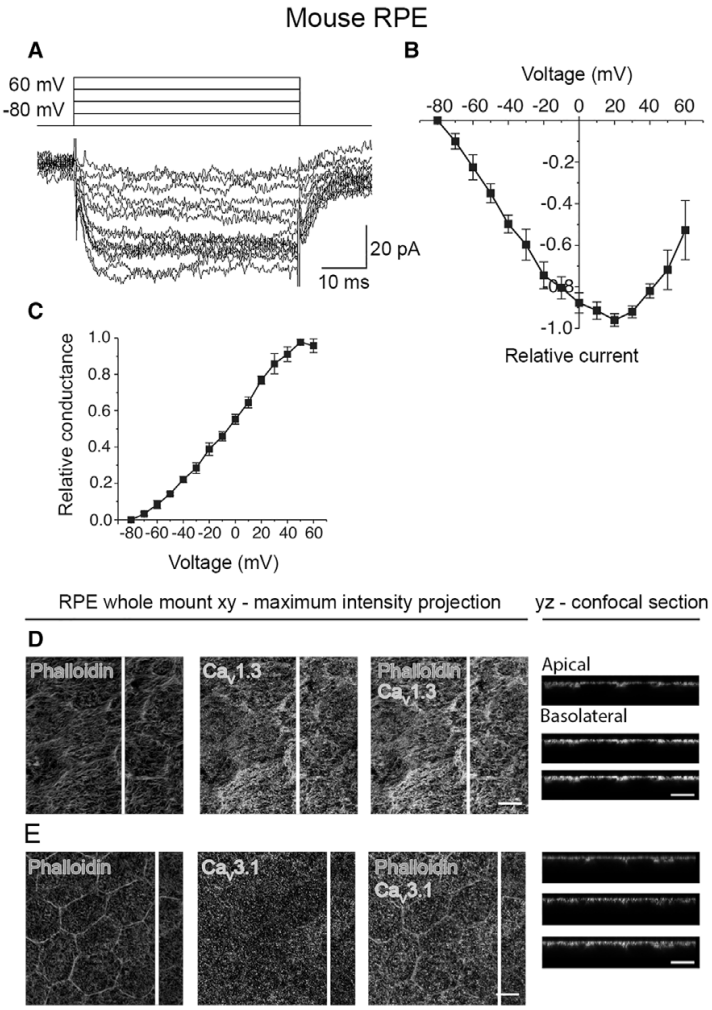

Figure 4. Ca_V channels in mouse RPE. **(A):** An example of the slowly inactivating L-type current measured in whole-cell configuration and elicited by 50 ms voltage steps from −80 to +60 mV in 10 mV increments. **(B):** Normalized and averaged IV-curve of the L-type current (mean ± SEM, n = 4). **(C):** Normalized and averaged GV-curve of the L-type current (mean ± SEM, n = 4). Localization of the Ca_V channels assessed by immunostainings of mouse RPE-eyecup whole mount preparations. Confocal images show the xy-maximum intensity projections and yz-confocal sections of the samples (apical side upwards, localization of the section highlighted with a white bar). Actin cytoskeleton (phalloidin, red) together with **(D)** L-type Ca^{2+} channel $Ca_V1.3$ (green), and **(E)** T-type Ca^{2+} channel $Ca_V3.1$ (green). Immunostainings of paraffin embedded vertical sections of mouse eyecups shown as xy-maximum intensity projections (apical side upwards). BF images together with L-type Ca^{2+} channels **(F)** $Ca_V1.2$ (green) and **(G)** $Ca_V1.3$ (green), and T-type Ca^{2+} channels **(H)** $Ca_V3.1$ (green) and **(I)** $Ca_V3.2$ (green). Scale bars 10 μm. Abbreviations: Ca_V, voltage-gated Ca^{2+} channel; BF, bright-field; RPE, retinal pigment epithelium.

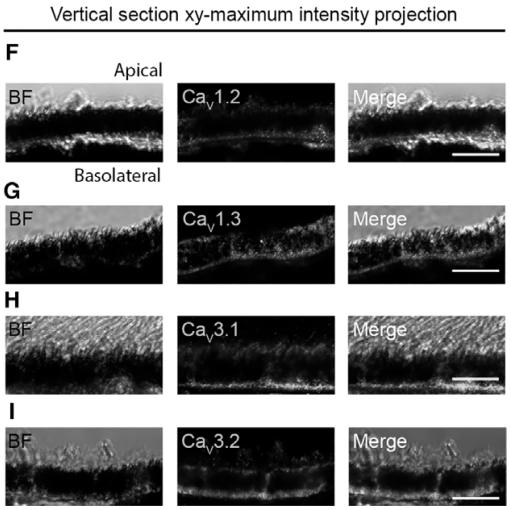

Figure 4. (Continued)

noting that the cell culture insert membrane with randomly spaced 1 μm holes may hinder both the diffusion of the drug to the basolateral cell membrane and the secretion of VEGF to the medium. Since the VEGF secretion is more pronounced in the basolateral side of the RPE, the structural constraints from the insert may lower the effect of pharmacological Ca^{2+} channel modulation on VEGF secretion.

Photoreceptor renewal is a critical task for RPE to maintain vision [2], and insufficient phagocytosis often leads to retinal diseases [84, 85]. Several ion channels, including the L-type Ca^{2+} channels, are known to have regulatory roles in phagocytosis in RPE [41, 64]. We found that in hESC-RPE, in line with the previous studies [64], inhibition of the L-type Ca^{2+} channels by nifedipine decreased the phagocytosis remarkably. On the other hand, activation of these channels by (-)BayK8644 also decreased the number of phagocytosed POS particles, although to a lesser extent. Interestingly, it was reported that in primary porcine RPE, the activation of L-type Ca^{2+} channels had no effect on phagocytosis, and this was suggested to be a consequence of the regulatory effect of bestrophin-1 setting a limit to L-type Ca^{2+} channel activity [41]. When comparing these results to our data, we want to point out that we used a pulse-chase POS phagocytosis assay, while Müller et al. [41] used an assay with continuous POS supply to the RPE cells that may lead to distinct outcomes. Moreover, it is possible that bestrophin-1 expression levels are much lower in hESC-RPE compared to primary porcine RPE [41] thus diminishing the regulatory effect of bestrophin-1 on L-type Ca^{2+} channels in our cells. Besides, the influence of Ca^{2+} in phagocytosis can also be inhibitory: increase in intracellular Ca^{2+} and subsequent activation of protein kinase C has been shown to reduce POS ingestion [86]. These observations indicate that the role for the L-type Ca^{2+} channels in the regulation of POS phagocytosis is a complex process (see also [41, 64]) and may include negative feedback mechanisms, especially after prolonged channel activation. Furthermore, it is known that these channels participate in the regulation of phagocytosis in concert with other ion channels including Ca^{2+}-dependent K^+ channels, bestrophin-1, TRPV [41], and most likely also the T-type Ca^{2+} channels. Our observation about the increased number of bound or ingested POS particles following T-type Ca^{2+} channel inhibition is similar to the effect of bestrophin-1 inhibition [41]. Analogous to bestrophin-1 [87], T-type Ca^{2+} channels are indicated to interact with the β subunits of the L-type Ca^{2+} channels [88]. This implies a possible role for the T-type channels to inhibit L-type channels through their interaction with β subunits. Taken together, these data demonstrate a need for further studies in elucidating the concerted functioning of Ca^{2+} conducting channels in the regulation of phagocytosis.

Regardless of the close resemblance between stem cell-derived and native RPE demonstrated for their proteome [29], capability of phagocytosis [27, 28, 30–32], VEGF secretion [32–34], and visual cycle [35, 36], many important differences have also been reported. These include a lower efficiency in the phagocytosis of POSs [89] as well as differences in growth factor secretion [90] and expression of adhesion junction and membrane transport genes [37]. We used mouse RPE as the native counterpart for hESC-RPE in our studies due to unavailability of live human RPE tissue. Previous work on gene and protein expression profiles of human and mouse RPE show high similarity regarding general biological functions, canonical pathways, and molecular networks [91, 92]. However, there are important species-specific differences between human and mouse RPE. These include immune regulation genes and genes related to the development of AMD and Usher syndrome [92] as well as the well-known anatomical differences such as the absence of macula in the mouse and differences in rod and cone types and distributions.

We studied the functionality of Ca_V channels in mature hESC-RPE where the localization of the primary Ca_V channel subtype, $Ca_V1.3$, started to resemble native RPE. During maturation, we observed significant changes in $Ca_V1.3$ localization in hESC-RPE implying that ion channels can be highly sensitive to the level of tissue maturity. This has been previously suggested at least for Bestrophin-1 in RPE [32, 93]. We

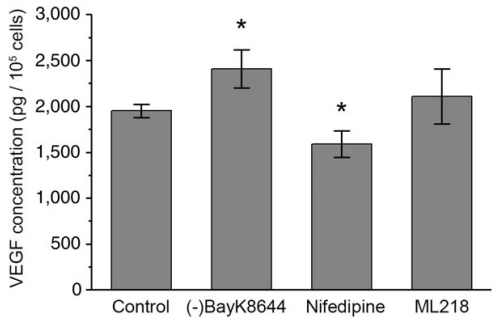

Figure 5. VEGF secretion from hESC-RPE. Total concentrations of VEGF secreted by the hESC-RPE after 24-hour incubation in control medium alone (n = 9) as well as in control medium with L-type Ca^{2+} channel activator 10 μM (-)BayK8644 (n = 9), L-type Ca^{2+} channel inhibitor 10 μM nifedipine (n = 8), or T-type channel inhibitor 5 μM ML218 (n = 8) (mean ± SEM, cell lines 08/023 and 11/013, days post-confluence 66–147). *Statistically significant difference with $p < .05$. Abbreviation: VEGF, vascular endothelial growth factor.

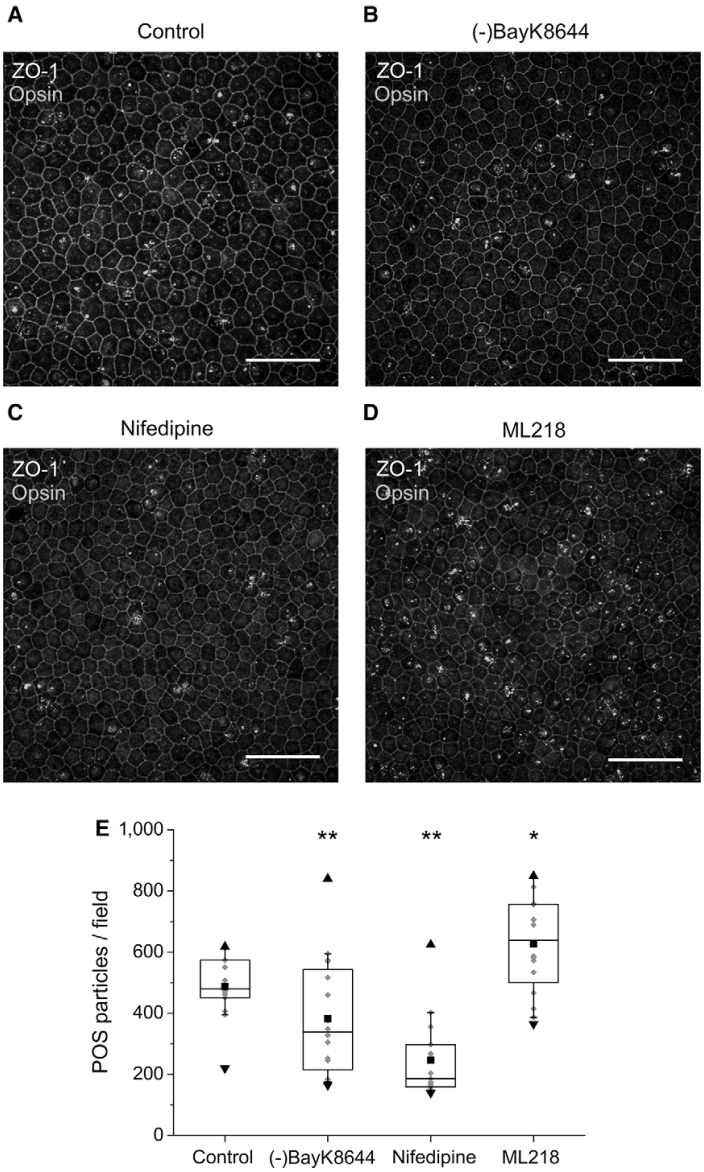

Figure 6. The effect of Ca_V channel modulators on POS phagocytosis in hESC-RPE. Mature hESC-RPE monolayers were incubated with purified porcine POSs in the pulse-chase phagocytosis assay. Xy-maximun intensity projections of the confocal images show both bound and internalized POS particles that were stained with opsin (green) together with the tight junction protein ZO-1 (gray) in **(A)** control conditions, and in the presence of Ca_V channel modulators **(B)** (-)BayK8644, **(C)** nifedipine, or **(D)** ML218. Scale bars 50 μm. **(E):** Quantification of POS particles in control conditions yielded the median value of 485 POS particles/field (n = 16). When modulating the Ca_V channels pharmacologically, the value changed in the presence of (-)BayK8644 to 339 POS particles/field (n = 15), nifedipine to 186 POS particles/field (n = 15), and ML218 to 639 POS particles/field (n = 16). The box limits 25%–75% of the gray data points; the whiskers include 10%–90% of the data; the center line shows the median value; the black square describes the mean; the black triangles present the minimum and the maximum values. Cell line 11/013, days post-confluence 147. Statistically significant differences with $*p < .05$ or $**p < .001$. Abbreviations: POS, photoreceptor outer segment; ZO-1, Zonula occludens.

showed that in mature hESC-RPE, $Ca_V1.3$ localized quite homogeneously on the apical and basolateral cell membranes. Intriguingly, in maturing hESC-RPE, $Ca_V1.3$ appeared as distinct foci that co-localized with PCNT to the base of the primary cilia. A similar punctuated appearance has been previously shown for TRP channel TRPM3 in human fetal RPE [94]. PCNT is

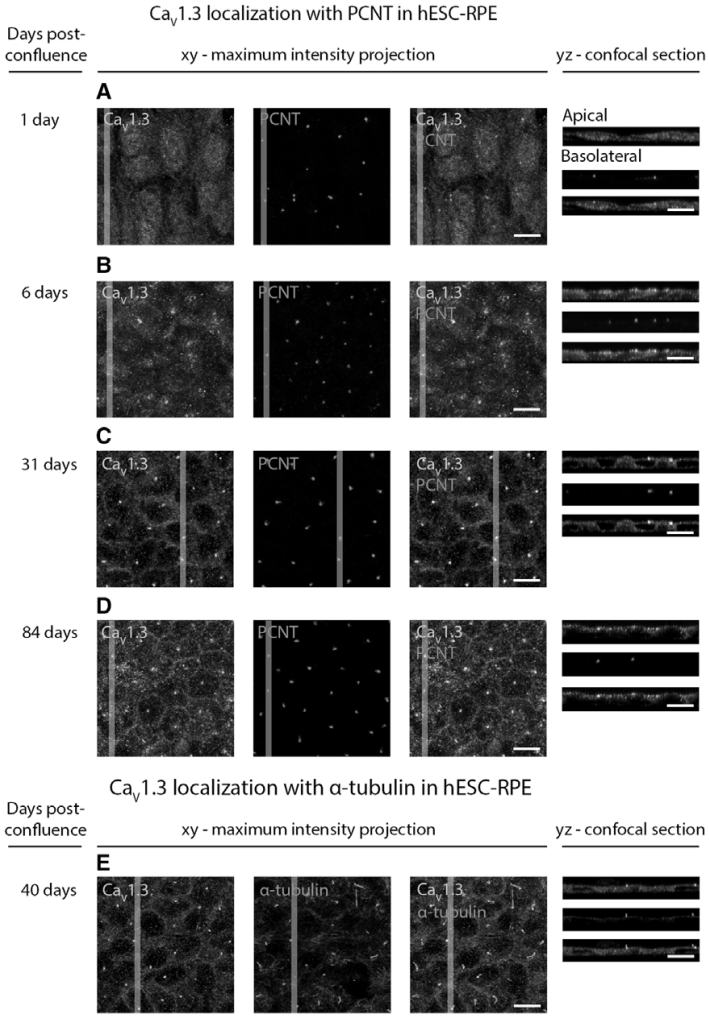

Figure 7. Localization of $Ca_V1.3$ during hESC-RPE maturation. Immunolabeling of $Ca_V1.3$ (green) together with centrosome protein PCNT (red) from post-confluence day 1 to post-confluence day 84 at four time points: **(A)** day 1, **(B)** day 6, **(C)** day 31, and **(D)** day 84 (cell line 08/017). **(E):** Labeling acetylated α-tubulin (red) together with $Ca_V1.3$ (green) shows the localization of $Ca_V1.3$ at the base of the primary cilia during maturation (cell line 08/017, days post-confluence 40). The confocal images are shown as xy-maximum intensity projections and yz-confocal sections (apical side upwards, localization of the section highlighted with a white bar). Scale bars 10 μm. Abbreviations: Ca_V, voltage-gated Ca^{2+} channel; hESC, human embryonic stem cell; RPE, retinal pigment epithelium; PCNT, pericentrin.

critical for the cilia formation, and relevant for our observations, PCNT is suggested to recruit protein complexes involved in cilia assembly and calcium signaling to the base of the primary cilia [66]. On the other hand, primary cilia has been shown to regulate L-type Ca^{2+} channel expression in mouse renal epithelial cells [95]. This occurs through Wnt signaling [95], and interestingly, recent work shows the importance of the regulation of Wnt signaling not only for RPE development [96] but also for RPE maturation [67]. Based on our data and taking into account these observations in the literature, it is possible, that $Ca_V1.3$ participates in ciliogenesis during RPE maturation or that its expression is coupled to the functioning of primary cilia in RPE maturation. This would not be surprising since primary cilia are important Ca^{2+} signaling organelles [97] with the expression of several different types of Ca^{2+} channels [98].

Conclusion

In this article, we demonstrate the presence of a functional machinery of voltage-gated Ca^{2+} channels in hESC-RPE, with L-type Ca^{2+} channel characteristics highly resembling the native RPE. We show a regulatory role for L-type Ca^{2+} channels in VEGF secretion and phagocytosis important for the

hESC-RPE functionality. We also provide novel information regarding the apical localization of $Ca_V1.3$ in RPE as well as its co-localization near the base of the primary cilia during hESC-RPE maturation. Our study represents an initial but significant progress toward a better understanding of Ca_V channels in stem cell-derived RPE, however, further studies are needed to elucidate the specific roles for T-type Ca^{2+} channels in RPE physiology. Overall, the results of the study are promising for the success of stem cell-based RPE transplantation therapies, but highlight the need for sufficient RPE maturation as a prerequisite for its fully functional Ca^{2+} machinery.

Acknowledgments

We thank Viivi Jokinen, Julia Johansson, Elina Hurskainen, Outi Heikkilä, Marja-Leena Koskinen, Outi Melin, Hanna Pekkanen, Outi Paloheimo, and Teemu Ihalainen for their technical assistance. The support from Tampere Imaging Facility and Tampere Facility of Electrophysiological Measurements is also greatly appreciated. This study was financially supported by the Academy of Finland (grant numbers 260375, 287287, 294054, 252225, 218050, 272808, 137801, 304909), the Emil Aaltonen Foundation, the Finnish Cultural Foundation, the Instrumentarium Science Foundation, the TEKES Human Spare Part Project and the Doctoral Programme of the President of Tampere University of Technology.

Author Contributions

I.V.: conception and design, collection and assembly of data, data analysis and interpretation, manuscript writing, final approval of manuscript; T.V.: collection and assembly of data, data analysis and interpretation, provision of study material, manuscript writing, final approval of manuscript; K.J.-U.: conception and design, collection and/or assembly of data, manuscript writing, final approval of manuscript; H.U.-J.: provision of study material, final approval of manuscript; H.S.: provision of study material, manuscript writing, final approval of manuscript; J.H.: financial support, manuscript writing, final approval of manuscript; S.N.: conception and design, financial support, collection and/or assembly of data, data analysis and interpretation, manuscript writing, final approval of manuscript.

Disclosure of Potential Conflicts of Interest

The authors indicated no potential conflicts of interest.

References

1 Strauss O. The retinal pigment epithelium in visual function. Physiol Rev 2005;85:845-881.

2 Wimmers S, Karl MO, Strauss O. Ion channels in the RPE. Prog Retin Eye Res 2007;26:263-301.

3 Ferrington DA, Sinha D, Kaarniranta K. Defects in retinal pigment epithelial cell proteolysis and the pathology associated with age-related macular degeneration. Prog Retin Eye Res 2016;51:69-89.

4 Wong WL, Su X, Li X et al. Global prevalence of age-related macular degeneration and disease burden projection for 2020 and 2040: A systematic review and meta-analysis. Lancet Glob Health 2014;2:e106-e116.

5 Riera M, Fontrodona L, Albert S et al. Comparative study of human embryonic stem cells (hESC) and human induced pluripotent stem cells (hiPSC) as a treatment for retinal dystrophies. Mol Ther Methods Clin Dev 2016;3:1-12.

6 Schwartz SD, Regillo CD, Lam BL et al. Human embryonic stem cell-derived retinal pigment epithelium in patients with age-related macular degeneration and Stargardt's macular dystrophy: Follow-up of two open-label phase 1/2 studies. Lancet 2015;385:509-516.

7 Song WK, Park K, Kim H et al. Treatment of macular degeneration using embryonic stem cell-derived retinal pigment epithelium: Preliminary results in Asian patients. Stem Cell Reports 2015;4:860-872.

8 Schwartz SD, Tan G, Hosseini H et al. Subretinal transplantation of embryonic stem cell–derived retinal pigment epithelium for the treatment of macular degeneration: An assessment at 4 years. Invest Ophthalmol Vis Sci 2016;57:ORSFc1-ORSFc9.

9 Mandai M, Watanabe A, Kurimoto Y et al. Autologous induced stem-cell–derived retinal cells for macular degeneration. N Engl J Med 2017;376:1038-1046.

10 Southwest Hospital, China. Clinical study of subretinal transplantation of human embryo stem cell derived retinal pigment epitheliums in treatment of macular degeneration diseases. Available at https://www.clinicaltrials.gov/ct2/show/NCT02749734. Accessed January 9, 2018.

11 Chinese Academy of Sciences. Subretinal transplantation of retinal pigment epitheliums in treatment of age-related macular degeneration diseases. Available at https://www.clinicaltrials.gov/ct2/show/NCT02755428. Accessed January 9, 2018.

12 Cell Cure Neurosciences Ltd. Safety and efficacy study of OpRegen for treatment of advanced dry-form age-related macular degeneration. Available at https://www.clinicaltrials.gov/ct2/show/NCT02286089. Accessed January 9, 2018.

13 Astellas Institute for Regenerative Medicine. Long term follow up of sub-retinal transplantation of hESC derived RPE cells in Stargardt macular dystrophy patients. Available at https://www.clinicaltrials.gov/ct2/show/NCT02445612. Accessed January 9, 2018.

14 Astellas Institute for Regenerative Medicine. Safety and tolerability of sub-retinal transplantation of hESC derived RPE (MA09-hRPE) cells in patients with advanced dry age related macular degeneration (Dry AMD). Available at https://www.clinicaltrials.gov/ct2/show/NCT01344993. Accessed January 9, 2018.

15 Astellas Institute for Regenerative Medicine. Sub-retinal transplantation of hESC derived RPE(MA09-hRPE)cells in patients with Stargardt's macular dystrophy. Available at https://www.clinicaltrials.gov/ct2/show/NCT01345006. Accessed January 9, 2018.

16 Astellas Institute for Regenerative Medicine. Long term follow up of sub-retinal transplantation of hESC derived RPE cells in patients with AMD. Available at https://www.clinicaltrials.gov/ct2/show/NCT02463344. Accessed January 9, 2018.

17 Pfizer. Retinal pigment epithelium safety study for patients in B4711001. Available at https://www.clinicaltrials.gov/ct2/show/NCT03102138. Accessed January 9, 2018.

18 Federal University of São Paulo. Stem cell therapy for outer retinal degenerations. Available at https://www.clinicaltrials.gov/ct2/show/NCT02903576. Accessed January 9, 2018.

19 Chinese Academy of Sciences. Treatment of dry age related macular degeneration disease with retinal pigment epithelium derived from human embryonic stem cells. Available at https://www.clinicaltrials.gov/ct2/show/NCT03046407. Accessed January 9, 2018.

20 Pfizer. A study of implantation of retinal pigment epithelium in subjects with acute wet age related macular degeneration. Available at https://www.clinicaltrials.gov/ct2/show/NCT01691261. Accessed January 9, 2018.

21 da Cruz L, Fynes K, Georgiadis O et al. Phase 1 clinical study of an embryonic stem cell–derived retinal pigment epithelium patch in age-related macular degeneration. Nat Biotechnol 2018;36:328-337.

22 Li Y, Tsai Y, Hsu C et al. Long-term safety and efficacy of human-induced pluripotent stem cell (iPS) grafts in a preclinical model of retinitis pigmentosa. Mol Med 2012;18:1312-1319.

23 Lu B, Malcuit C, Wang S et al. Long-term safety and function of RPE from human embryonic stem cells in preclinical models of macular degeneration. Stem Cells 2009;27: 2126-2135.

24 Kanemura H, Go MJ, Shikamura M et al. Tumorigenicity studies of induced pluripotent stem cell (iPSC)-derived retinal pigment epithelium (RPE) for the treatment of age-related macular degeneration. PLOS ONE 2014;9(1):e85336.

25 Koss MJ, Falabella P, Stefanini FR et al. Subretinal implantation of a monolayer of human embryonic stem cell-derived retinal pigment epithelium: A feasibility and safety study in Yucatan minipigs. Graefes Arch Clin Exp Ophthalmol 2016;254:1553-1565.

26 Galloway CA, Dalvi S, Hung SSC et al. Drusen in patient-derived hiPSC-RPE models of macular dystrophies. Proc Natl Acad Sci USA 2017;114:E8214-E8223.

27 Thomas BB, Zhu D, Zhang L et al. Survival and functionality of hESC-derived retinal pigment epithelium cells cultured as a monolayer on polymer substrates transplanted in RCS rats. Invest Ophthalmol Vis Sci 2016;57:2877-2887.

28 Carr A, Vugler AA, Hikita ST et al. Protective effects of human iPS-derived retinal pigment epithelium cell transplantation in the retinal dystrophic rat. PLOS ONE 2009;4(12):e8152.

29 Hongisto H, Jylhä A, Nättinen J et al. Comparative proteomic analysis of human embryonic stem cell-derived and primary human retinal pigment epithelium. Sci Rep 2017;7:6016.

30 Subrizi A, Hiidenmaa H, Ilmarinen T et al. Generation of hESC-derived retinal pigment epithelium on biopolymer coated polyimide membranes. Biomaterials 2012;33: 8047-8054.

31 Singh R, Shen W, Kuai D et al. iPS cell modeling of Best disease: Insights into the pathophysiology of an inherited macular degeneration. Hum Mol Genet 2013;22: 593-607.

32 Brandl C, Zimmermann SJ, Milenkovic VM et al. In-depth characterisation of retinal pigment epithelium (RPE) cells derived from human induced pluripotent stem cells (hiPSC). Neuromolecular Med 2014;16:551-564.

33 Kokkinaki M, Sahibzada N, Golestaneh N. Human iPS-derived retinal pigment epithelium (RPE) cells exhibit ion transport, membrane potential, polarized VEGF secretion and gene expression pattern similar to native RPE. Stem Cells 2011;29: 825-835.

34 Blenkinsop TA, Saini JS, Maminishkis A et al. Human adult retinal pigment epithelial stem cell–derived RPE monolayers exhibit key physiological characteristics of native tissue. Invest Ophthalmol Vis Sci 2015;56:7085-7099.

35 Maeda T, Lee MJ, Palczewska G et al. Retinal pigmented epithelial cells obtained from human induced pluripotent stem cells possess functional visual cycle enzymes in vitro and in vivo. J Biol Chem 2013;288:34484-34493.

36 Muñiz A, Greene WA, Plamper ML et al. Retinoid uptake, processing, and secretion in human iPS-RPE support the visual cycle. Invest Ophthalmol Vis Sci 2014;55: 198-209.

37 Peng S, Gan G, Qiu C et al. Engineering a blood-retinal barrier with human embryonic stem cell-derived retinal pigment epithelium: Transcriptome and functional analysis. Stem Cells Translational Medicine 2013;2:534-544.

38 Stanzel BV, Liu Z, Somboonthanakij S et al. Human RPE stem cells grown into polarized RPE monolayers on a polyester matrix are maintained after grafting into rabbit subretinal space. Stem Cell Reports 2014;2: 64-77.

39 Miyagishima KJ, Wan Q, Corneo B et al. In pursuit of authenticity: Induced pluripotent stem cell-derived retinal pigment epithelium for clinical applications. Stem Cells Translational Medicine 2016;5: 1562-1574.

40 Abu Khamidakh AE, Dos Santos FC, Skottman H et al. Semi-automatic method for Ca2+ imaging data analysis of maturing human embryonic stem cells-derived retinal pigment epithelium. Ann Biomed Eng 2016; 44:3408-3420.

41 Müller C, Más Gómez N, Ruth P et al. CaV1.3 L-type channels, maxiK Ca2 +-dependent K+ channels and bestrophin-1 regulate rhythmic photoreceptor outer segment phagocytosis by retinal pigment epithelial cells. Cell Signal 2014;26:968-978.

42 Wimmers S, Halsband C, Seyler S et al. Voltage-dependent Ca2+ channels, not ryanodine receptors, activate Ca2+-dependent BK potassium channels in human retinal pigment epithelial cells. Mol Vis 2008;14: 2340-2348.

43 Rosenthal R, Heimann H, Agostini H et al. Ca^{2+} channels in retinal pigment epithelial cells regulate vascular endothelial growth factor secretion rates in health and disease. Mol Vis 2007;13:443-456.

44 Rosenthal R, Malek G, Salomon N et al. The fibroblast growth factor receptors, FGFR-1 and FGFR-2, mediate two independent signalling pathways in human retinal pigment epithelial cells. Biochem Biophys Res Commun 2005;337:241-247.

45 Mergler S, Steinhausen K, Wiederholt M et al. Altered regulation of L-type channels by protein kinase C and protein tyrosine kinases as a pathophysiologic effect in retinal degeneration. FASEB J 1998; 12:1125-1134.

46 Wimmers S, Coeppicus L, Rosenthal R et al. Expression profile of voltage-dependent Ca2+ channel subunits in the human retinal pigment epithelium. Graefes Arch Clin Exp Ophthalmol 2008;246:685-692.

47 Ueda Y, Steinberg RH. Voltage-operated calcium channels in fresh and cultured rat retinal pigment epithelial cells. Invest Ophthalmol Vis Sci 1993;34: 3408-3418.

48 Ueda Y, Steinberg RH. Dihydropyridine-sensitive calcium currents in freshly isolated human and monkey retinal pigment epithelial cells. Invest Ophthalmol Vis Sci 1995;36:373-380.

49 Strauss O, Mergler S, Wiederholt M. Regulation of L-type calcium channels by protein tyrosine kinase and protein kinase C in cultured rat and human retinal pigment epithelial cells. FASEB J 1997;11:859-867.

50 Strauss O, Buss F, Rosenthal R et al. Activation of neuroendocrine L-type channels (α1D subunits) in retinal pigment epithelial cells and brain neurons by pp60c-src. Biochem Biophys Res Commun 2000;270:806-810.

51 Rosenthal R, Bakall B, Kinnick T et al. Expression of bestrophin-1, the product of the VMD2 gene, modulates voltage-dependent Ca2+ channels in retinal pigment epithelial cells. FASEB J 2006;20: 178-180.

52 Wollmann G, Lenzner S, Berger W et al. Voltage-dependent ion channels in the mouse RPE: Comparison with Norrie disease mice. Vision Res 2006;46:688-698.

53 Rosenthal R, Thieme H, Strauss O. Fibroblast growth factor receptor 2 (FGFR2) in brain neurons and retinal pigment epithelial cells act via stimulation of neuroendocrine L-type channels (Cav1.3). FASEB J 2001;15: 970-977.

54 Reichhart N, Markowski M, Ishiyama S et al. Rab27a GTPase modulates L-type Ca2+ channel function via interaction with the II–III linker of CaV1.3 subunit. Cell Signal 2015;27: 2231-2240.

55 Reichhart N, Milenkovic VM, Halsband C et al. Effect of bestrophin-1 on L-type Ca2+ channel activity depends on the Ca2+ channel beta-subunit. Exp Eye Res 2010;91:630-639.

56 Rohrer B, Kunchithapautham K, Genewsky A et al. Prolonged src kinase activation, a mechanism to turn transient, sublytic complement activation into a sustained pathological condition in retinal pigment epithelium cells. Adv Exp Med Biol 2014;801: 221-227.

57 Skottman H. Derivation and characterization of three new human embryonic stem cell lines in Finland. In Vitro Cell Dev Biol Anim 2010;46:206-209.

58 Vaajasaari H, Ilmarinen T, Juuti-Uusitalo K et al. Toward the defined and xeno-free differentiation of functional human pluripotent stem cell-derived retinal pigment epithelial cells. Mol Vis 2011;17: 558-575.

59 Bodenstein L, Sidman RL. Growth and development of the mouse retinal pigment epithelium: I. Cell and tissue morphometrics and topography of mitotic activity. Dev Biol 1987;121:192-204.

60 Johansson JK, Ihalainen TO, Skottman H et al. Fast voltage sensitivity in retinal pigment epithelium: Sodium channels and their novel role in phagocytosis. bioRxiv 2017;223719.

61 Schneider CA, Rasband WS, Eliceiri KW. NIH Image to ImageJ: 25 years of image analysis. Nat Methods 2012;9:671-675.

62 Mao Y, Finnemann SC. Analysis of photoreceptor outer segment phagocytosis by RPE cells in culture. Methods Mol Biol 2013; 935:285-295.

63 Luo Y, Zhuo Y, Fukuhara M et al. Effects of culture conditions on heterogeneity and the apical junctional complex of

the ARPE-19 cell line. Invest Ophthalmol Vis Sci 2006;47:3644-3655.

64 Karl MO, Kroeger W, Wimmers S et al. Endogenous Gas6 and Ca2+-channel activation modulate phagocytosis by retinal pigment epithelium. Cell Signal 2008;20: 1159-1168.

65 Burke JM. Epithelial phenotype and the RPE: Is the answer blowing in the Wnt? Prog Retin Eye Res 2008;27:579-595.

66 Jurczyk A, Gromley A, Redick S et al. Pericentrin forms a complex with intraflagellar transport proteins and polycystin-2 and is required for primary cilia assembly. J Cell Biol 2004;166:637-643.

67 May-Simera HL, Wan Q, Jha BS et al. Primary cilium-mediated retinal pigment epithelium maturation is disrupted in ciliopathy patient cells. Cell Rep 2018;22: 189-205.

68 Koschak A, Reimer D, Huber I et al. a1D (Cav1.3) subunits can form L-type Ca2+ channels activating at negative voltages. J Biol Chem 2001;276:22100-22106.

69 Singh A, Gebhart M, Fritsch R et al. Modulation of voltage- and Ca2 +-dependent gating of CaV1.3 L-type calcium channels by alternative splicing of a C-terminal regulatory domain. J Biol Chem 2008;283:20733-20744.

70 Striessnig J, Pinggera A, Kaur G et al. L-type Ca2+ channels in heart and brain. Wiley Interdiscip Rev Membr Transp Signal 2014;3:15-38.

71 Cordeiro S, Strauss O. Expression of Orai genes and ICRAC activation in the human retinal pigment epithelium. Graefes Arch Clin Exp Ophthalmol 2011;249:47-54.

72 Martínez-García MC, Martínez T, Pañeda C et al. Differential expression and localization of transient receptor potential vanilloid 1 in rabbit and human eyes. Histol Histopathol 2013;28:1507-1516.

73 Cordeiro S, Seyler S, Stindl J et al. Heat-sensitive TRPV channels in retinal pigment epithelial cells: Regulation of VEGF-A secretion. Invest Ophthalmol Vis Sci 2010;51: 6001-6008.

74 Wimmers S, Strauss O. Basal calcium entry in retinal pigment epithelial cells is mediated by TRPC channels. Invest Ophthalmol Vis Sci 2007;48:5767-5772.

75 Balse E, Steele DF, Abriel H et al. Dynamic of ion channel expression at the plasma membrane of cardiomyocytes. Physiol Rev 2012;92:1317-1358.

76 Perez-Reyes E. Molecular physiology of low-voltage-activated T-type calcium channels. Physiol Rev 2003;83:117-161.

77 Strauss O, Wienrich M. Ca2+−conductances in cultured rat retinal pigment epithelial cells. J Cell Physiol 1994;160:89-96.

78 Kovach JL, Schwartz SG, Flynn HW Jr et al. Anti-VEGF treatment strategies for wet AMD. J Ophthalmol 2012;2012:1-7.

79 Klettner A, Kaya L, Flach J et al. Basal and apical regulation of VEGF-A and placenta growth factor in the RPE/choroid and primary RPE. Mol Vis 2015;21:736-748.

80 Blaauwgeers HGT, Holtkamp GM, Rutten H et al. Polarized vascular endothelial growth factor secretion by human retinal pigment epithelium and localization of vascular endothelial growth factor receptors on the inner choriocapillaris: Evidence for a trophic paracrine relation. Am J Pathol 1999;155: 421-428.

81 Hollborn M, Vogler S, Reichenbach A et al. Regulation of the hyperosmotic induction of aquaporin 5 and VEGF in retinal pigment epithelial cells: Involvement of NFAT5. Mol Vis 2015;21:360-377.

82 Faby H, Hillenkamp J, Roider J et al. Hyperthermia-induced upregulation of vascular endothelial growth factor in retinal pigment epithelial cells is regulated by mitogen-activated protein kinases. Graefes Arch Clin Exp Ophthalmol 2014;252: 1737-1745.

83 Kannan R, Zhang N, Sreekumar PG et al. Stimulation of apical and basolateral vascular endothelial growth factor-A and vascular endothelial growth factor-C secretion by oxidative stress in polarized retinal pigment epithelial cells. Mol Vis 2006;12: 1649-1659.

84 Gal A, Li Y, Thompson DA et al. Mutations in MERTK, the human orthologue of the RCS rat retinal dystrophy gene, cause retinitis pigmentosa. Nat Genet 2000; 26:270-271.

85 Vollrath D, Yasumura D, Benchorin G et al. Tyro3 modulates mertk-associated retinal degeneration. PLoS Genet 2015;11: e1005723.

86 Hall MO, Abrams TA, Mittag TW. ROS ingestion by RPE cells is turned off by increased protein kinase C activity and by increased calcium. Exp Eye Res 1991;52: 591-598.

87 Milenkovic VM, Krejcova S, Reichhart N et al. Interaction of bestrophin-1 and Ca2+ channel β-subunits: Identification of new binding domains on the bestrophin-1 C-terminus. PLoS ONE 2011;6(4):e19364.

88 Szklarczyk D, Franceschini A, Wyder S et al. STRING v10: Protein-protein interaction networks, integrated over the tree of life. Nucleic Acids Res 2015;43:447-452.

89 Mazzoni F, Safa H, Finnemann SC. Understanding photoreceptor outer segment phagocytosis: Use and utility of RPE cells in culture. Exp Eye Res 2014;126:51-60.

90 Sugino IK, Sun Q, Wang J et al. Comparison of FRPE and human embryonic stem cell–derived RPE behavior on aged human Bruch's membrane. Invest Ophthalmol Vis Sci 2011;52:4979-4997.

91 Yang X, Chung JY, Rai U et al. Cadherins in the retinal pigment epithelium (RPE) revisited: P-cadherin is the highly dominant cadherin expressed in human and mouse RPE in vivo. PLoS ONE 2018;13(1):e0191279.

92 Bennis A, Gorgels TG, Ten Brink JB et al. Comparison of mouse and human retinal pigment epithelium gene expression profiles: Potential implications for age-related macular degeneration. PLoS ONE 2015;10(10):e0141597.

93 Bakall B, Marmorstein LY, Hoppe G et al. Expression and localization of bestrophin during normal mouse development. Invest Ophthalmol Vis Sci 2003;44:3622-3628.

94 Zhao PY, Gan G, Peng S et al. TRP channels localize to subdomains of the apical plasma membrane in human fetal retinal pigment epithelium. Invest Ophthalmol Vis Sci 2015;56:1916-1923.

95 Muntean BS, Jin X, Williams FE et al. Primary cilium regulates CaV1.2 expression through Wnt signaling. J Cell Physiol 2014;229:1926-1934.

96 Westenskow P, Piccolo S, Fuhrmann S. Beta-catenin controls differentiation of the retinal pigment epithelium in the mouse optic cup by regulating Mitf and Otx2 expression. Development 2009;136:2505-2510.

97 Delling M, DeCaen PG, Doerner JF et al. Primary cilia are specialized calcium signalling organelles. Nature 2013;504:311-314.

98 Pablo JL, DeCaen PG, Clapham DE. Progress in ciliary ion channel physiology. J Gen Physiol 2017;149:37-47.

See www.StemCellsTM.com for supporting information available online.

PUBLICATION II

Heterogeneity of potassium channels in human embryonic stem cell-derived retinal pigment epithelium

Korkka I, Skottman H, Nymark S

Manuscript
Accepted for publication in Stem Cells Transl Med

PUBLICATION III

Characterization of chloride channels in human embryonic stem cell derived retinal pigment epithelium

Korkka I, Johansson JK, Skottman H, Hyttinen J, Nymark S

EMBEC & NBC 2017. IFMBE Proceedings, 2017, 65:454-457
https://doi.org/10.1007/978-981-10-5122-7_114

Characterization of Chloride Channels in Human Embryonic Stem Cell Derived Retinal Pigment Epithelium

I. Korkka[*1], J.K. Johansson[*1], H. Skottman[2], J. Hyttinen[1] and S. Nymark[1]

[*]Equal contributions
[1]BioMediTech Institute, Faculty of Biomedical Sciences and Engineering, Tampere University of Technology, Tampere, Finland
[2]BioMediTech Institute, Faculty of Medicine and Life Sciences, University of Tampere, Tampere, Finland

Abstract—**Retinal pigment epithelium (RPE) is vital for vision. Its ion channels play important roles in the various functions of RPE that are critical for retinal welfare. These functions are often disrupted in degenerative eye diseases leading to visual impairment and even blindness. New treatments are currently being developed and transplantation of human embryonic stem cell (hESC)-derived RPE is showing great promise. For the success of these therapies, functionality of the transplantable cells needs to be verified. Presence of ion channels in hESC-derived RPE remains poorly known, particularly regarding the various chloride (Cl^-) channels. We addressed this issue by investigating the Cl^- conductivity of hESC-derived RPE by whole-cell patch clamp recordings followed by immunolabeling of the Cl^- channels typical to RPE. Our recordings showed a diverse pattern of slowly inactivating currents characteristic to voltage-dependent Cl^- channels (ClC) previously reported for RPE. Some of the identified currents were modulated by changes in intracellular calcium concentration. This data, together with the immunolabeling, demonstrated the presence of bestrophin-1, cystic fibrosis transmembrane regulator (CFTR) and ClC-2 channels in hESC-derived RPE thus indicating their capability to mimic native Cl^- physiology.**

Keywords—**Retinal pigment epithelium, chloride channels, human embryonic stem cells, patch clamp, immunolabeling**

I. Introduction

The retinal pigment epithelium (RPE) is a pigmented monolayer of polarized cells covering the inner wall of the eye. Located between photoreceptors and choroid, RPE regulates the transport of nutrients and ions between bloodstream and subretinal space. RPE fulfils multiple tasks essential for the visual function such as regeneration of the visual pigment, phagocytosis, secretion, and light absorption [1]. Malfunctions of RPE have been implicated in the pathogenesis of several degenerative eye diseases [2], for which stem cell derived RPE transplantation therapies provide a potential treatment.

Many of the maintenance roles of RPE rely on ion channels. Under physiological conditions, most anion channels conduct chloride (Cl^-) as it is the predominant permeable anion [1]. These channels are involved in the transepithelial transport of water, protection against osmotic cell swelling as well as pH regulation [3, 4]. The Cl^- channels found in the RPE can be broadly classified as volume or voltage dependent, ligand-gated or second messenger activated. These second messengers include calcium (Ca^{2+}) and/or cyclic adenosine monophosphate (cAMP) [1, 5, 6].

The basal Cl^- conductance is provided by a family of voltage-gated Cl^- channels (ClC), mainly by hyperpolarization-activated ClC-2 channel [1, 6, 7]. The disruption of this channel has been suggested to lead to retinal degeneration [1]. The cAMP-activated Cl^- conductance has been linked to cystic fibrosis transmembrane regulator (CFTR) protein [4, 8]. Besides its Cl^- channel function, CFTR might be involved in the regulation of other ion channels, transporters and cellular functions such as release of ATP [8]. Ca^{2+}-dependent Cl^- conductance, on the other hand, has been suggested to result from bestrophin-1. This ubiquitously expressed channel is modulated by cell volume and acts as a regulator of intracellular Ca^{2+} levels. Importantly, the mutations of bestophin-1 have been associated with various forms of macular dystrophy [1, 9].

Despite their importance for RPE physiology, detailed studies regarding Cl^- channels present in human embryonic stem cell (hESC) derived RPE are still missing. The purpose of this study was to characterize the Cl^- channel composition of these cells by electrophysiological recordings and immunolabeling. The expression and functionality of these channels is critical for the success of transplantation therapies.

II. Materials and Methods

A. hESC-derived RPE cells

Previously derived hESC lines Regea08/023 and Regea08/017 were used in this study [10]. The hESC culturing [11] and differentiation [12] were performed as previously described. Briefly, the hESCs were cultured at 37°C in 5% CO_2 on top of feeder cells (CRL-2429TM, ATCC, Manassas, VA, USA) and the hESC colonies were cultured as floating aggregates on low cell bind six-well plates (Nalgene NUNC, Tokyo, Japan). The pigmented areas were dissociated with TrypLE Select (Invitrogen, UK) and subsequently seeded onto Collagen IV (5µg/cm^2, Sigma-Aldrich) coated 24-well

H. Eskola et al. (eds.), *EMBEC & NBC 2017*,
IFMBE Proceedings 65,
DOI: 10.1007/978-981-10-5122-7_114

plates (Corning® CellBIND®; Corning, Inc., Corning, NY) with a density of $5.5x10^5$cells/cm^2. The cells were then passaged onto Collagen IV-treated culture inserts (pore size 1μm, BD Biocoat, BD Biosciences, San Jose, CA) and cultured until mature.

B. Patch clamp measurements

Whole-cell patch clamp recordings were performed at room temperature (RT) on hESC-derived RPE by patching individual cells in the monolayer. In control conditions, patch pipettes (resistance 4-8 MΩ) were filled with internal solution containing (in mM) 130 CsCl, 5.5 EGTA, 0.5 $CaCl_2$, 4 ATP-Mg, 0.1 GTP-Na, 10 HEPES, 5 NaCl and 5 TeaCl. The pH was adjusted to 7.2 with CsOH and osmolarity was adjusted to 290 mOsm with sucrose. In test conditions, the content of intracellular $CaCl_2$ was decreased to 0 mM, which was compensated by increasing CsCl to 131 mM. The RPE was perfused with control external solution containing (in mM): 130 NaCl, 5 TeaCl, 1.1 $CaCl_2$, 1.2 $MgCl_2$, 10 HEPES and 5 glucose. The pH was adjusted to 7.4 with NaOH and the osmolarity was set to 305 mOsm with sucrose. Recordings were made in voltage clamp mode using pClamp10.2 software. Axopatch200B patch clamp amplifier was connected to an acquisition computer via AD/DA Digidata1440 (Molecular Devices, CA, USA). Data was filtered with 2 kHz and sampled with 10000 Hz. Current-voltage (IV)-curves were derived from the peak value of the current against applied membrane potential.

C. Immunofluorescence staining and confocal microscopy

The sample preparation and immunolabeling incubations were carried out at RT. The PBS-washed cells were fixed by 15 min incubation in 4% paraformaldehyde (pH 7.4; Sigma-Aldrich). After three washes with PBS, sample was permeabilized with 0.1% Triton X-100 in PBS (Sigma-Aldrich) for 15min and blocked with 3% BSA in PBS (BSA; Sigma-Aldrich-Aldrich) for 1h.

Primary antibodies against the following proteins were used in this study: Bestrophin-1 1:100 (016-Best1-01, Lagen Laboratories), CFTR 1:50 (MA1-935, Thermo Fisher Scientific), ClC-2 1:200 (ACL-002, Alomone Labs) and Zonula occludens-1 (ZO-1) 1:50 (33-9100, Life Technologies). All primary antibodies were diluted in 3% BSA in PBS and incubated for 1h. The cells were washed with PBS and incubated for 1h with conjugated secondary antibodies; goat anti-rabbit Alexa Fluor 568, donkey anti-rabbit Alexa Fluor 488, donkey anti-mouse Alexa Fluor 568, donkey anti-mouse Alexa Fluor 488 (all from Molecular Probes, Thermo Fisher Scientific) diluted 1:200 in 3% BSA in PBS. Actin was visualized using a direct Phalloidin Atto-633 conjugate 1:50 (68825, Sigma-Aldrich) and the nuclei were stained with 4´,6´-diamidino-2-phenylidole (DAPI) present in the mounting medium (P36935, Thermo Fisher Scientific).

Imaging was performed with Zeiss LSM780 LSCM on inverted Zeiss Cell Observer microscope (Zeiss, Jena, Germany) by using Plan-Apochromat 63x/1.4 oil immersion objective. Voxel size was set to x=y=66nm and z=200nm. Pixels were set to 1024x1024 and stacks of 100-120 slices were obtained with a line average of 2. The dyes were excited with (in nm): 405 diode laser (DAPI); 488 Argon laser (Alexa Fluor 488); 561 DPSS (Alexa Fluor 568); 628 InTune laser (Atto 633). Emission windows were set to (in nm): 410 – 495 (DAPI), 499 – 579 (Alexa Fluor 488), 579 – 642 (Alexa Fluor 568) and 642 – 755 (Atto-633). Data was saved in .czi format and the images were processed with ImageJ [13]. Only linear brightness and contrast adjustments were performed. Figure panel was then assembled using Adobe Photoshop CS6 (Adobe Systems, San Jose, USA).

D. Statement of human and animal rights

We have approval from the National Authority for Medicolegal Affairs Finland (Dnro 1426/32/300/05) and the supportive statement from the local ethics committee of the Pirkanmaa hospital district Finland. These allowed us to derive and expand hESC-lines from surplus embryos excluded from infertility treatments and to use the lines for research purposes (R05116). Novel cell lines were not derived in this study.

III. Results

A. Voltage-dependent chloride currents in hESC-derived RPE

Diverse pattern of Cl^- currents in hESC-derived RPE was detected with patch clamp measurements in whole-cell configuration (Fig. 1) with an average membrane capacitance of 54.5±5.0 pF (mean±SEM, n=11). In all measurements, holding potential was -50mV. Three out of five measured cells showed currents as a response to 400 ms voltage steps from -150 mV to 150 mV after 0 mV depolarization (Fig. 1 A). The corresponding IV-curve demonstrates that negative currents were activated at around -90 mV and positive currents at around 40 mV (Fig. 1 B). From the twelve measured cells, eight responded to stimulation of 400 ms voltage steps from -50 mV holding potential to 150 mV (Fig. 1 C). The IV-curve indicates that positive currents activated at around 50 mV (Fig. 1 D). Three out of seven cells showed currents after a 500 ms depolarizing pre-pulse to 100 mV followed by 500ms voltage steps from -150mV to 0mV (Fig. 1 E). Negative currents activated at around -50mV (Fig. 1 F).

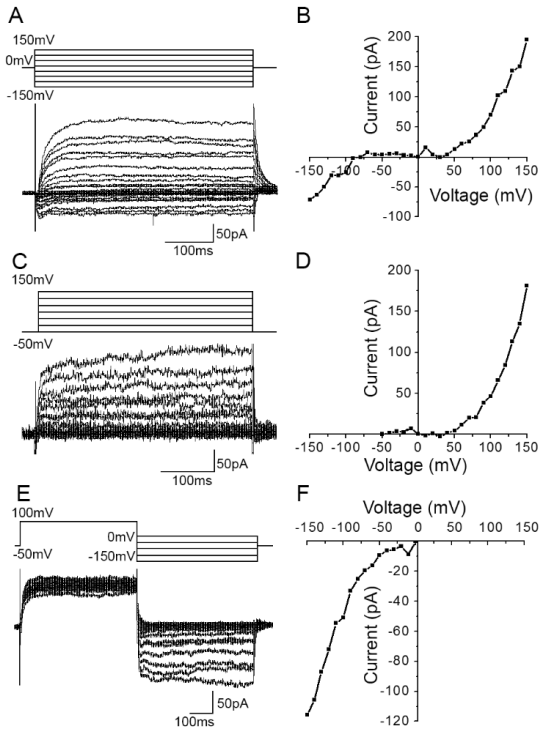

Fig. 1 Cl^- currents in hESC-derived RPE measured in whole-cell configuration. Holding potential was -50 mV in all of the protocols. A) Typical example of the current elicited by 400 ms voltage steps in 10 mV increments following depolarization to 0 mV and B) the corresponding IV-curve. C) Typical response elicited by 400 ms voltage steps in 10 mV increments from the -50 mV holding potential and D) the corresponding IV-curve. E) Current elicited after a 500 ms pre-pulse to 100 mV followed by 10 mV voltage steps from -150mV to 0 mV with 500ms duration and F) the corresponding IV-curve.

B. The effect of intracellular calcium concentration on chloride currents

The depletion of intracellular Ca^{2+} from 0.5mM to 0mM decreased the positive currents (Fig. 2). At the highest depolarizing membrane voltage (150mV), the currents were decreased to half of the values in control Ca^{2+} conditions with both tested protocols (54.3%, Fig. 2 A and 48.4%, Fig. 2 B). The negative half of the IV-curve showed no Ca^{2+} dependency (Fig. 2 A).

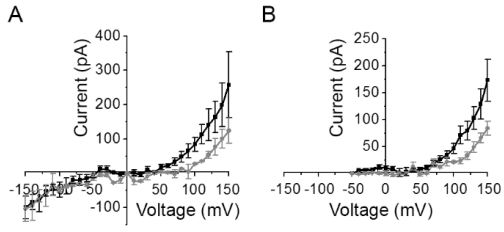

Fig. 2 The effect of intracellular Ca^{2+} on Cl^- currents in hESC-derived RPE. Comparison of currents (mean±sem) recorded in 0.5 mM (black) and 0 mM (grey) intracellular Ca^{2+} A) for the currents shown in Fig. 1 A-B (n=3 in 0.5mM Ca^{2+} and n=3 in 0 mM Ca^{2+}), and B) for the currents shown in Fig. 1 C-D (n=8 in 0.5 mM Ca^{2+} and n=4 in 0 mM Ca^{2+}).

C. Different chloride channels are found in hESC-derived RPE

The Cl^- channel composition of hESC-derived RPE was characterized further by immunolabeling the channel types that have previously been reported in RPE (Fig. 3). Our results showed positive labeling for all tested channel types, but there was variation in the specific labeling pattern. Of the tested markers, bestrophin-1 (Fig. 3 A) showed the most uniform labeling pattern whereas CFTR (Fig. 3 B) was concentrated to ring-type structures in the cells. The labeling of ClC-2 was weaker, but observed in both cell-cell junctions as well as in the cell centers (Fig. 3 C).

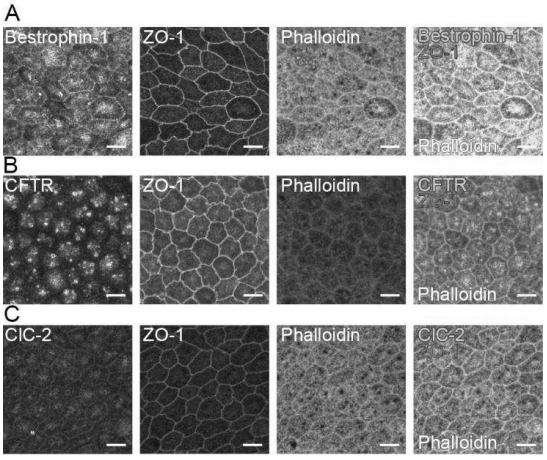

Fig. 3 The localization of different Cl^- channels in mature hESC-derived RPE. Laser scanning confocal microscopy Z-maximum intensity projections of the channels with filamentous actin staining (gray) and ZO-1 (red) together with A) bestrophin-1 (green) B) CFTR (green) and C) ClC-2 (green). Scale bars 10µm.

IV. Discussion

Cl^- channels facilitate several important functions of RPE [1, 3]. Thus, their presence is vital for the success of transplantation therapies to treat degenerative eye diseases. Despite the rich literature regarding Cl^- channel modulation and physiological roles [4], detailed studies of their presence in hESC-derived RPE have been missing.

Our patch clamp measurements revealed a diverse pattern of slowly inactivating voltage-dependent currents, and their electrophysiological characteristics resembled previously reported ClC channels [6, 7, 14]. This finding was supported by our immunostainings that showed the presence of ClC-2 channels in hESC-derived RPE. It is likely that additional channels participate in the Cl^- conductance such as CFTR that was also found by immunolabeling.

Ca^{2+}-dependency of Cl^- currents has so far been connected to changes in intracellular and extracellular Ca^{2+}, calmodulin-dependent protein kinase and cyclic guanosine monophosphate -dependent channels [7]. In this study, we focused on the modulation by intracellular Ca^{2+}. Our results demonstrate some level of Ca^{2+}-dependency of the recorded Cl^- currents and bestrophin-1 was detected by immunolabeling. These findings are consistent with the earlier work on *Xenopus* RPE [6], but further studies are required to confirm the specific channel types. This is important since the identified Ca^{2+}-dependent current could also be carried by the novel anoctamin channels recently described in RPE [15].

Our studies showed the presence of functional Cl^- channels in hESC-derived RPE. However, their performance in Cl^--dependent functions, such as fluid transport or pH regulation in hESC-derived RPE, remains to be investigated.

V. Conclusion

Different Cl^- channels were identified in hESC-derived RPE by immunolabeling and our recordings demonstrate that they carry functional currents. Their presence is promising for the clinical use of hESC-derived RPE and may reflect *in vivo*-like physiology regarding Cl^--dependent processes. Further studies are required to compare them to native RPE.

Acknowledgment

The authors acknowledge the technical assistance of Outi Heikkilä, Outi Melin and Hanna Pekkanen. This study was funded by the Academy of Finland (grant numbers 260375, 287287, 294054, 252225, 218050, 272808), Emil Aaltonen Foundation, TEKES Human Spare Part Project and Doctoral Programme of the President of Tampere University of Technology.

Conflict of Interest

The authors declare that they have no conflict of interest.

References

1. Wimmers S, Karl MO, Strauss O (2007) Ion channels in the RPE. Prog Retin Eye Res 26:263–301. doi: 10.1016/j.preteyeres.2006.12.002
2. Ferrington DA, Sinha D, Kaarniranta K (2016) Defects in retinal pigment epithelial cell proteolysis and the pathology associated with age-related macular degeneration. Prog Retin Eye Res 51:69–89. doi: 10.1016/j.preteyeres.2015.09.002
3. Strauss O (2005) The Retinal Pigment Epithelium in Visual Function. Physiol Rev 85:845–881. doi: 10.1152/physrev.00021.2004
4. Foskett JK (1998) ClC and CFTR chloride channel gating. Annu Rev Physiol 60:689–717. doi: 10.1146/annurev.physiol.60.1.689
5. Wills NK, Weng T, Mo L, et al (2000) Chloride Channel Expression in Cultured Human Fetal RPE Cells: Response to Oxidative Stress. Invest Ophthalmol Vis Sci 41:4247–4255.
6. Hartzell HC, Qu Z (2003) Chloride currents in acutely isolated Xenopus retinal pigment epithelial cells. J Physiol 549:453–69. doi: 10.1113/jphysiol.2003.040428
7. Jentsch TJ, Stein V, Weinreich F, Zdebik AA (2002) Molecular Structure and Physiological Function of Chloride Channels. Physiol Rev 82:503–568.
8. Jiang Q, Mak D, Devidas S, et al (1998) Cystic fibrosis transmembrane conductance regulator-associated ATP release is controlled by a chloride sensor. J Cell Biol 143:645–57.
9. Marmorstein AD, Kinnick TR, Stanton JB, et al (2015) Bestrophin-1 influences transepithelial electrical properties and Ca2+ signaling in human retinal pigment epithelium. Mol Vis 21:347–59.
10. Skottman H (2010) Derivation and characterization of three new human embryonic stem cell lines in Finland. In Vitro Cell Dev Biol Anim 46:206–209. doi: 10.1007/s11626-010-9286-2
11. Vaajasaari H, Ilmarinen T, Juuti-Uusitalo K, et al (2011) Toward the defined and xeno-free differentiation of functional human pluripotent stem cell-derived retinal pigment epithelial cells. Mol Vis 17:558–75.
12. Sorkio A, Hongisto H, Kaarniranta K, et al (2014) Structure and barrier properties of human embryonic stem cell-derived retinal pigment epithelial cells are affected by extracellular matrix protein coating. Tissue Eng Part A 20:622–34. doi: 10.1089/ten.TEA.2013.0049
13. Schneider CA, Rasband WS, Eliceiri KW (2012) NIH Image to ImageJ: 25 years of image analysis. Nat Methods 9:671–675. doi: 10.1038/nmeth.2089
14. Weng TX, Godley BF, Jin GF, et al (2002) Oxidant and antioxidant modulation of chloride channels expressed in human retinal pigment epithelium. AJP Cell Physiol 283:C839–C849. doi: 10.1152/ajpcell.00445.2001
15. Schreiber R, Kunzelmann K (2016) Expression of anoctamins in retinal pigment epithelium (RPE). Pflügers Arch - Eur J Physiol 468:1921–1929. doi: 10.1007/s00424-016-1898-2

Author: Soile Nymark
Institute: BioMediTech Institute, Faculty of Biomedical Sciences and Engineering, Tampere University of Technology
Street: Lääkärinkatu 1
City: Tampere
Country: Finland
Email: soile.nymark@tut.fi

PUBLICATION IV

Computational model of Ca^{2+} wave propagation in human retinal pigment epithelial ARPE-19 cells

Vainio I, Abu Khamidakh A, Paci M, Skottman H, Juuti-Uusitalo K, Hyttinen J, Nymark S

PLoS One. 2015, 10(6):e0128434
https://doi.org/10.1371/journal.pone.0128434

PLOS ONE

RESEARCH ARTICLE

Computational Model of Ca^{2+} Wave Propagation in Human Retinal Pigment Epithelial ARPE-19 Cells

Iina Vainio[1,2]*, Amna Abu Khamidakh[1,2], Michelangelo Paci[1,2], Heli Skottman[3], Kati Juuti-Uusitalo[3], Jari Hyttinen[1,2], Soile Nymark[1,2]

1 Department of Electronics and Communications Engineering, Tampere University of Technology, Tampere, Finland, **2** Institute of Biosciences and Medical Technology, Tampere University of Technology, Tampere, Finland, **3** Institute of Biosciences and Medical Technology, University of Tampere, Tampere, Finland

* iina.vainio@tut.fi

Citation: Vainio I, Abu Khamidakh A, Paci M, Skottman H, Juuti-Uusitalo K, Hyttinen J, et al. (2015) Computational Model of Ca^{2+} Wave Propagation in Human Retinal Pigment Epithelial ARPE-19 Cells. PLoS ONE 10(6): e0128434. doi:10.1371/journal.pone.0128434

Academic Editor: Zsolt Ablonczy, Medical University of South Carolina, UNITED STATES

Received: October 24, 2014

Accepted: April 27, 2015

Published: June 12, 2015

Data Availability Statement: All relevant data are within the paper.

Funding: This study was financially supported by the Academy of Finland (grant numbers 252225, 260375, 218050 and 137801), TEKES- the finnish funding agency for innovation (Human Spare Part Project), and Doctoral Programme of the President of the Tampere University of Technology. The funders had no role in study design, data collection and analysis, decision to publish, or preparation of the manuscript.

Abstract

Objective

Computational models of calcium (Ca^{2+}) signaling have been constructed for several cell types. There are, however, no such models for retinal pigment epithelium (RPE). Our aim was to construct a Ca^{2+} signaling model for RPE based on our experimental data of mechanically induced Ca^{2+} wave in the *in vitro* model of RPE, the ARPE-19 monolayer.

Methods

We combined six essential Ca^{2+} signaling components into a model: stretch-sensitive Ca^{2+} channels (SSCCs), P_2Y_2 receptors, IP_3 receptors, ryanodine receptors, Ca^{2+} pumps, and gap junctions. The cells in our epithelial model are connected to each other to enable transport of signaling molecules. Parameterization was done by tuning the above model components so that the simulated Ca^{2+} waves reproduced our control experimental data and data where gap junctions were blocked.

Results

Our model was able to explain Ca^{2+} signaling in ARPE-19 cells, and the basic mechanism was found to be as follows: 1) Cells near the stimulus site are likely to conduct Ca^{2+} through plasma membrane SSCCs and gap junctions conduct the Ca^{2+} and IP_3 between cells further away. 2) Most likely the stimulated cell secretes ligand to the extracellular space where the ligand diffusion mediates the Ca^{2+} signal so that the ligand concentration decreases with distance. 3) The phosphorylation of the IP_3 receptor defines the cell's sensitivity to the extracellular ligand attenuating the Ca^{2+} signal in the distance.

Competing Interests: The authors have declared that no competing interests exist.

Conclusions

The developed model was able to simulate an array of experimental data including drug effects. Furthermore, our simulations predict that suramin may interfere ligand binding on P_2Y_2 receptors or accelerate P_2Y_2 receptor phosphorylation, which may partially be the reason for Ca^{2+} wave attenuation by suramin. Being the first RPE Ca^{2+} signaling model created based on experimental data on ARPE-19 cell line, the model offers a platform for further modeling of native RPE functions.

Introduction

Epithelial tissue covers and lines all internal and external body surfaces. These cell layers have multiple functions depending on their location, and many of these functions are controlled by Ca^{2+} activity[1]. Retinal pigment epithelium (RPE), a monolayer of pigmented polarized cells, is crucial for the maintenance of visual functions. Located in the back of the eye between photoreceptors and choriocapillaries, RPE forms a vital part of the blood-retinal barrier (BRB)[2]. The physiology of RPE is tightly coupled with the activity of the various ion channels, such as Ca^{2+} channels that are associated with several important RPE functions including transepithelial transport of ions and water, dark adaption of photoreceptor activity, phagocytosis, secretion, and differentiation[3]. In RPE, as well as in other epithelia, local deformation of the cell membrane initiates a significant Ca^{2+} wave [4–6]. Such deformation of the cell membrane can occur in clinically important pathological conditions such as retinal tear resulting from complications after photodynamic therapy[7], intravitreal bevacizumab injection[8], or intravitreal pegaptanib injection[9]. Intercellular Ca^{2+} signaling is also linked to the initial stages of wound repair: excessive mechanical stimulation causes cell death and thus initiates Ca^{2+} waves that create Ca^{2+} gradients which play an important role in cell migration[1]. In addition, Ca^{2+} waves also regulate the local transepithelial ion transport to maintain the spatial ion gradients across the epithelium[1]. We recently demonstrated in RPE that an easily induced and repeatable Ca^{2+} wave could be produced by mechanical stimulation[5]. This provides an experimental way to study Ca^{2+} activity in the epithelial monolayer.

In silico models of various cellular processes are becoming an increasingly important part of biological research, including drug discovery and toxicology studies. The importance of this was recently emphasized in a review of cardiotoxicity testing [10]. Computational models of Ca^{2+} signaling, specifically, have been developed for many cell types including pancreatic and parotid acinar cells[11], astrocytes[12], and hepatocytes[13]. Epithelial Ca^{2+} signaling, however, differs from other cell types because the epithelium forms a highly polarized cell monolayer that comprises organized apical and basal cell membranes. The epithelial cells are tightly connected with tight junctions and gap junctions between the cells[14]. At present, there are only a few epithelial Ca^{2+} signaling models available, for example for the urothelial monolayer[15] and for the airway epithelium[16]. RPE has many unique functions compared to other epithelia as it supports the complex processes of vision. Indeed, in the treatment of many eye diseases, RPE is either the drug target or it hinders drug penetration and provides a barrier between most of the eye and the blood stream. Hence, computational models of the functions of RPE, including Ca^{2+} dynamics, are well warranted.

The aim of this study, therefore, is to provide a deeper understanding of the study of Ca^{2+} activity by introducing a detailed computational model of RPE Ca^{2+} dynamics. The computational model described in this paper is based on our experimental data on a mechanically

induced Ca^{2+} wave in ARPE-19 cells, a commercial immortalized human RPE cell line that is widely used to assess RPE cell functions *in vitro* [17–19], regardless of its limitations in cellular morphology, organization and function [20].

The computational model is mostly based on the experimental data of Abu Khamidakh et al. 2013[5]. In addition, the model comprises our new unpublished α-glycyrrhetinic acid (GA)-suramin-treated data. We constructed the model by combining previously published cell Ca^{2+} dynamics model components of P_2Y_2 receptors [21], inositol 1,4,5-trisphosphate (IP_3) receptors [22], ryanodine receptors [23], Ca^{2+} pumps and gap junctions to a new model component of mechanical stretch. Furthermore, we connected the epithelial cells to each other in the model to enable the diffusion of the molecules and propagation of the stretch. We developed the model based on two experimental data sets: the GA-treated data, where gap junctions (GJs) were blocked by α-glycyrrhetinic acid and untreated control data, where GJs define the connections between the cells. The varying conditions the cells are exposed to due to the mechanical stimulation were modeled by defining three location-specific variables: stretch, extracellular ligand concentration, and IP_3 receptor phosphorylation rate. In addition, we validated the model by simulating the combined blocking effect of GJs and P_2 receptors by GA and suramin. This way, we obtained the first RPE Ca^{2+} signaling model, and we could reveal a deeper understanding of Ca^{2+} activity.

Materials and Methods

Experimental data

In this study, the experimental data of Abu Khamidakh et al. 2013[5] was complemented with new experimental data. Passage numbers for confluent cultures of human RPE immortalized cells (ARPE-19 cell line [ATCC Manassas, VA, U.S.A.]) were p. 23, 24, 30 for GA-treated dataset, p. 23, 24, 28, 30 for control data set and p. 29, 30, 31 for GA-suramin-treated data set. These ARPE-19 cultures were used for Ca^{2+} imaging, by loading them with the Ca^{2+}-sensitive dye fura-2-acetoxymethyl ester. Single cell mechanical stimulation, membrane perforation of one cell, was induced with a glass micropipette. The intracellular Ca^{2+} concentration transient travelled over the ARPE-19 monolayer starting from the mechanically stimulated (MS) cell, and spreading to the neighboring (NB) cells (Fig 1). The NB cells immediately surrounding the MS cell were defined as the first NB cell layer (NB layer 1 = NB_1); cells immediately surrounding the first layer were defined as the second NB layer (NB layer 2 = NB_2) and so on. The ratio of the emitted fluorescence intensities resulting from excitation at 340 and 380 nm (F_{340}/F_{380}) was determined for each cell after background correction. Normalized fluorescence (NF), which reflects the changes in intracellular Ca^{2+} concentration, was then obtained by dividing the fluorescence value by the mean fluorescence value before the mechanical stimulation.[5] The experimental work produced data in NF units. The computational model, however, is presented in absolute calcium concentrations. Due to the lack of absolute reference we consider the model predictions only relative.

Three data sets were simulated with the model. Firstly, in the GA-treated data set the gap junctions (GJs) were blocked by α-glycyrrhetinic acid (GA) (Sigma-Aldrich, St. Louis, MO, USA). Secondly, the model was verified with an untreated control data set that was based on the previous model—only the GJ model component was added. Thirdly, the model was applied to predict a combined blocking effect of GA and P_2 receptor blocker suramin (Sigma-Aldrich) with GA-suramin-treated data set. Each data set was averaged from at least three separate experiments.

The experiments with GA-suramin-treated ARPE-19 cells were not included in the original paper of Abu Khamidakh et al. 2013[5]. The experimental details concerning the ARPE-19 cells as well as the experimental solutions, infrastructure, and protocols are presented in[5] with the following exception: the cells were incubated in a solution containing 30μM GA

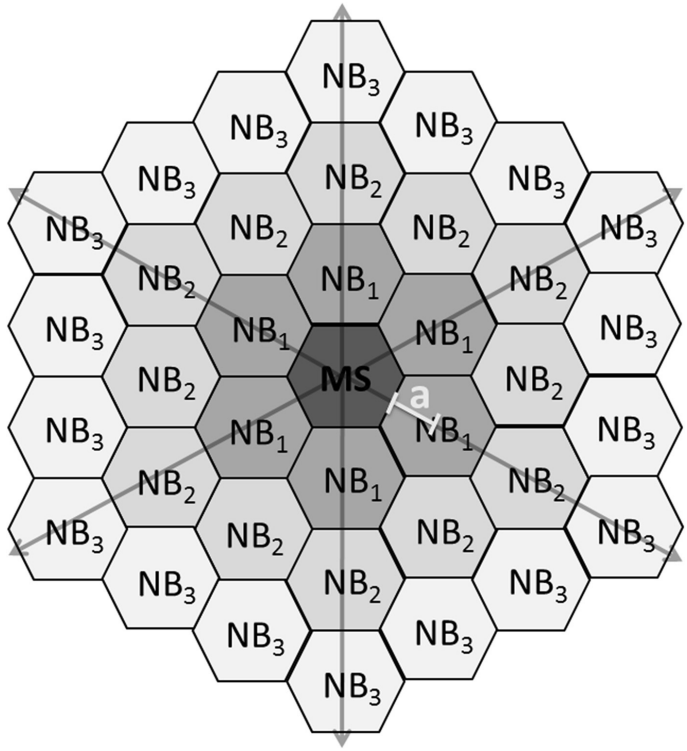

Fig 1. Numbering of the cell layers. Schematic representation of the location of the mechanically stimulated (MS) cell with respect to the neighboring (NB) cell layers: NB_1 is the first layer which is in direct contact with the MS cell; NB_2 is the second layer which is in direct contact with NB_1, and so forth. White line segment marks an apothem (a) of a hexagon.

doi:10.1371/journal.pone.0128434.g001

(incubation time 30 min) and 50μM suramin (incubation time 25 min) prior to mechanical stimulation. To receive representative data for each NB layer, the raw data was averaged so that the NF graphs were aligned by the starting time of mechanical stimulation, and the mean values were calculated for each NB with a one-second sampling rate. This was previously done for the control data set[5], but the averaging was performed also here for the GA-treated and GA-suramin-treated data sets.

Indirect immunofluorescence staining. ARPE-19 cells (p. 24, 27, 44, three cover slips from each passage) were cultured on glass coverslips for two days. For immunofluorescence staining, the samples were washed three times with PBS and fixed for 15 min with 4% paraformaldehyde (pH 7.4; Sigma-Aldrich) at room temperature (RT). After three subsequent washes with PBS, the samples were permeabilizing by a 15 min incubation in 0.1% Triton X-100 in PBS (Sigma-Aldrich) at RT. This was followed again by three PBS washes, after which the samples were incubated with 3% bovine serum albumin (BSA; Sigma-Aldrich) at RT for 1 h. Primary antibody Zonula Occludens (ZO-1) 1:100 (33–9100, Life Technologies) was diluted in 3% BSA PBS and incubated for 1 h at RT. Samples were then washed four times with PBS, and

followed by 1h incubation at RT with secondary antibody donkey anti-mouse Alexa Fluor 568 (A10037, Life Technologies) diluted 1:400 in 3% BSA in PBS. The washes with PBS were repeated again and nuclei were stained with 4′, 6′ diamidino-2-phenylidole (DAPI) included in the mounting medium (P36935, Life Technologies).

Confocal microscopy and image processing. Zeiss LSM780 LSCM on inverted Zeiss Cell Observer microscope (Zeiss, Jena, Germany) with Plan-Apochromat 63x/1.4 oil immersion objective was used for confocal microscopy. Voxel size was set to x = y = 66nm and z = 200nm, pixel stacks were set to 1024x1024, and approximately 50–80 slices were acquired with line average of 2. DAPI and Alexa-568 were excited with 405nm and 561nm lasers and detected with emission windows of 410–495nm and 570–642nm, respectively. The images saved in czi format were processed with ImageJ (Rasband, W.S., ImageJ, U. S. National Institutes of Health, Bethesda, Maryland, USA, http://imagej.nih.gov/ij/, 1997–2014.) and assembled using Adobe Photoshop CS6 (Adobe Systems, San Jose, USA).

Construction of the model

The Ca^{2+} model was constructed by combining six subcellular model components that included the stretch component designed in this study and the P_2Y_2 receptor models of Lemon et al. 2003[21], the IP_3 receptor type 3 (IP_3R_3) of LeBeau et al. 1999[22], and the ryanodine receptor (RyR) of Keizer & Levine 1996[23]. The GJ model component connected the neighboring cells. These model components with corresponding numbering and their rationale, hypothesized Ca^{2+} wave propagation mechanisms as well as model equations (see chapter Detailed model equations) that were used for the NB layers and data sets are summarized in Table 1. The basis for the mathematical implementation is presented in Fig 2 as a schematic model.

Parameters and parameterization

The model parameters are represented in Table 2 and the parameters specific for each NB layer in Table 3. Most of the parameters were adopted from the models of Lemon et al. 2003[21], LeBeau et al. 1999[22], and Keizer & Levine 1996[23]. Typically, the volumes of ARPE-19 cells [5,24,25] and RPE cells[26,27] are variable. The cell width was approximated to be 14μm from the corner-to-corner of a hexagon and the height was 12μm[5].The cytoplasmic volume was approximated to be about 70% of the total cell volume[28]. Thus, a cytoplasmic volume (v) of $1.07\ 10^{-15}\ m^3$ was used in the simulations. The initial values, the values at time of mechanical stimulation, were taken mostly from the model of Lemon et al. 2003[21]. The initial value 0.12μM for intracellular Ca^{2+} concentration ($[Ca^{2+}]_i$) is an arbitrary value approximating the baseline Ca^{2+} concentration determined from GA-treated data set for NB_5-NB_{10} layers using Matlab SimBiology Toolbox.

The rest of the parameters were fitted with Matlab SimBiology Parameter Fit Task: First, the parameter values, excluding SSCC and GJ model components, were fitted with GA-treated data set in NB5 layer. This layer has in general the largest Ca^{2+} response from those NB layers that do not experience any stretch due to mechanical stimulation, according to our assumption. Secondly, the SSCC model component parameters, excluding the location-specific stretch (θ) parameter (see below), were fitted with the same GA-treated data set in NB1 layer that is assumed to have the largest stretch. These values were then used in all simulations for all data sets and NB layers. For the control data set with gap junctions, all other parameters were kept unchanged but the GJ related diffusion parameters, $D_{Ca^{2+}}$, D_{IP_3}, $In_{Ca^{2+}}$ and In_{IP_3}, were fitted using NB1 layer. As a boundary condition we assumed that there is no outflow of IP_3 and Ca^{2+} outside the epithelium, thus Out_{IP_3} and $Out_{Ca^{2+}}$ were assigned to be zero.

Table 1. Model design.

Mechanism	Number	Component	Rationale	Equations	NB layer	Data set
Mechanical stimulus applied to MS cell may stretch ARPE-19 cells near the site of stimulation [5] resulting in the opening of SSCCs that conduct Ca^{2+} from the extracellular space to the cytoplasm. It is shown that ARPE-19 cells can secrete ligand to the extracellular space as a response to stimuli [38].	I	Stretch-sensitive Ca^{2+} channel (SSCC)	Cultured rat RPE expresses SSCCs on plasma membrane [4,53]. In ARPE-19 $[Ca^{2+}]_i$ wave was seen in NB_1-NB_4 layers even when the ER was depleted[5], indicating a Ca^{2+} influx mechanism independent of the ER, possibly the SSCCs.	7–9[a]	1–4	GA-treated, Control, GA-suramin-treated
The ligand, likely ATP or UTP [3,30,38,54], interacts with G-protein coupled purinergic receptor type P_2Y_2 on the cell membrane leading to the production of inositol 1,4,5-trisphosphate (IP_3) to the cytoplasm in a ligand concentration dependent manner.	II	Purinergic P_2Y_2 receptor (P_2Y_2)	The presence of P_2Y_2 receptors has been shown in cultured human RPE[30], bovine and human fetal RPE as well as in Long-Evans rats[55]	10–16[b]	1–10	GA-treated, Control, GA-suramin-treated[e]
IP_3 diffuses across the cytoplasm to the endoplasmic reticulum (ER), where it interacts with IP_3R_3 resulting in a release of Ca^{2+} from the ER[22].	III	IP_3 receptor type 3 (IP_3R_3)	Currently there is no direct evidence about the subtype of IP_3R expressed in ARPE-19. Hence, the data from other epithelia [56], [57], and[58] and an epithelial model [16] was utilized to choose the subtype 3 (IP_3R_3).	17–21[c]	1–10	GA-treated, Control, GA-suramin-treated
As the cytoplasmic Ca^{2+} concentration increases, RyRs become activated releasing more Ca^{2+} to the cytoplasm from the ER[23].	IV	Ryanodine receptor (RyR)	RyRs, locating on the membrane of ER participate in Ca^{2+} signaling in rat RPE[4], and ARPE-19[51].	22–24[d]	1–10	GA-treated, Control, GA-suramin-treated
The cytoplasmic Ca^{2+} concentration is decreased by the pumping activities of SERCA and PMCA. IP_3 is degraded in the cytoplasm. Ca^{2+} leak currents maintain the cytoplasmic Ca^{2+} baseline level.	V	Sarco/endoplasmic reticulum ATPase (SERCA), plasma membrane Ca^{2+} ATPase (PMCA), Leak	The presence of SERCA has been shown by blocking it to deplete the ER from Ca^{2+} in ARPE-19 cells[5] and rat RPE [53]. PMCA has been identified on the plasma membrane of cultured human RPE[59].	25	1–10	GA-treated, Control, GA-suramin-treated
GJs form intercellular connections between neighboring cells allowing diffusion of Ca^{2+} and IP_3 between the NB layers.	VI	Gap junction (GJ)	GJs form intercellular connections in ARPE-19[5], and rat RPE[4,60] enabling Ca^{2+} wave to spread over the monolayer.	26–28	1–10	Control

[a]Designed in this study

[b]Lemon et al. 2003[21]

[c]LeBeau et al. 1999[22]

[d]Keizer & Levine 1996[23]

[e]Parameter values of k_p modified

Hypothesized mechanisms and model components for Ca^{2+} wave propagation after mechanical stimulation with corresponding equations, NB layers, and data sets.

doi:10.1371/journal.pone.0128434.t001

Location-dependent parameters

Three parameters were assumed to vary according to the location of the cell with respect to the MS cell: stretch (θ) activating the stretch-sensitive Ca^{2+} channels (SSCCs), the extracellular ligand concentration ([L])[6,16,29,30], and the phosphorylation rate of IP_3R_3 (α_4)[22]. Ca^{2+}

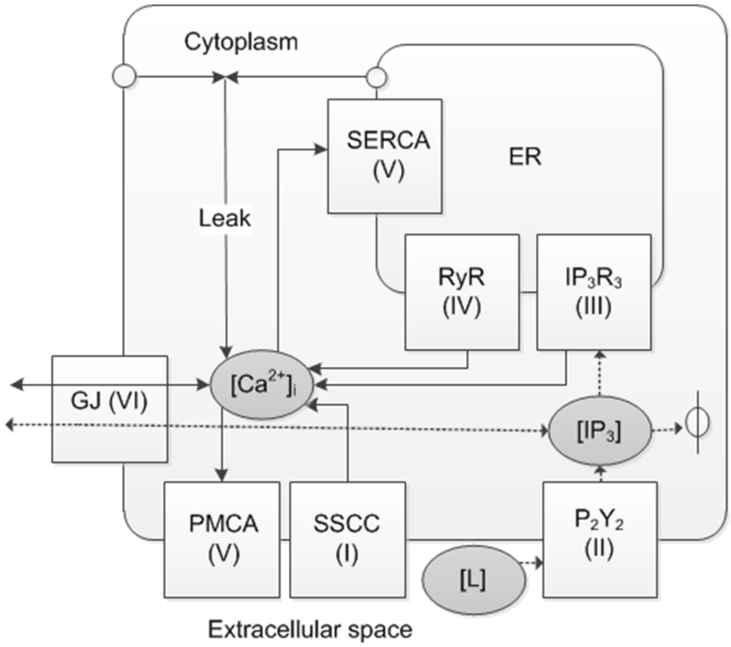

Fig 2. Schematic diagram of the Ca^{2+} signaling model. Solid arrows represent Ca^{2+} fluxes and dashed arrows IP_3 dynamics. Roman numerals denote the model components I-VI. Abbreviations: $[Ca^{2+}]_i$ = cytoplasmic Ca^{2+} concentration, [L] = extracellular ligand concentration, $[IP_3]$ = cytoplasmic IP_3 concentration, SSCC = stretch-sensitive Ca^{2+} channel, P_2Y_2 = purinergic receptor type P_2Y_2, IP_3R_3 = IP_3 receptor type 3, RyR = ryanodine receptor, SERCA = sarco/endoplasmic reticulum Ca^{2+} ATPase, PMCA = plasma membrane Ca^{2+} ATPase, Leak = combinatory Ca^{2+} leak from the extracellular space and the endoplasmic reticulum (ER), GJ = gap junction, ϕ = degradation.

doi:10.1371/journal.pone.0128434.g002

concentration was modeled separately in each NB layer. The distance (x) defines the distance of the NB layer from the MS cell centre that was calculated using the idealized hexacon RPE cell architecture (Fig 1) as

$$x = a2n = \frac{s}{2\tan\left(\frac{180}{6}\right)}2n, \quad (1)$$

where a is an apothem of the hexagon, 6 is the number of corners in the hexagon, s = 7μm is the length of the hexagon side and n = 1, 2, 3. . .10 according to the NB layer numbering.

The stretch component was present in cell layers NB1-NB4. Stretch (θ) was parameterized in the GA-treated data set separately for each NB layer. The obtained parameters resulted in an exponentially decaying function corresponding to the decay of an amplitude envelope of a damped wave in a membrane [31]. This function was then used for modeling the stretch

$$\theta = 0.3426e^{-0.105x}, \quad (2)$$

where x is the distance from the MS cell (R^2 = 0.9878).

Table 2. Constant parameters and initial conditions.

Parameter	Description	Value	Reference
I Stretch-sensitive Ca^{2+} channels (SSCCs)			
k_{SSCC}	Maximal SSCC flux rate	1.025 μM s^{-1}	fitted
k_f	SSCC forward rate constant	0.1382 s^{-1}	fitted
k_b	SSCC backward rate constant	0.04027 s^{-1}	fitted
k_θ	Stretch-relaxation parameter	0.08105 s^{-1}	fitted
II Metabotropic receptor P_2Y_2			
L_0	Bolus extracellular ligand concentration at x = 0μm	1310 μM	fitted
D_{ATP}	Diffusion coefficient of A	236 μm^2 s^{-1}	[61]
$[R_T]$	Total number of P_2Y_2 receptors	$2 \cdot 10^4$	[62]
K_1	Unphosphorylated receptor dissociation constant	5 μM	[21]
K_2	Phosphorylated receptor dissociation constant	100 μM	[21]
k_r	Receptor recycling rate	$1.75 \cdot 10^{-4}$ s^{-1}	[21]
k_p	Receptor phosphorylation rate	0.03 s^{-1}	[21]
k_e	Receptor endocytosis rate	$6 \cdot 10^{-3}$ s^{-1}	[21]
ξ	Fraction of mobile receptors	0.85	[21]
$[G_T]$	Total number of G-protein molecules	$1 \cdot 10^5$	[63]
k_{deg}	IP_3 degradation rate	1.25 s^{-1}	[64]
k_a	G-protein activation rate	0.017 s^{-1}	[21]
k_d	G-protein deactivation rate	0.15 s^{-1}	[21]
$[(PIP_2)_T]$	Total number of PIP_2 molecules	$5.0 \cdot 10^4$	[21]
r_r	PIP_2 replenishment rate	0.015 s^{-1}	[21]
δ	G-protein intrinsic activity parameter	$1.238 \cdot 10^{-3}$	[21]
K_3	Dissociation constant for Ca^{2+} binding to PLC	0.4 μM	[21]
α	Effective signal gain parameter	$2.781 \cdot 10^{-5}$ s^{-1}	[21]
N_a	Avogadro's constant	$6.02252 \cdot 10^{23}$	
v	Volume of the cytoplasmic space	$1.07 \cdot 10^{-15}$ m^3	see text
III IP_3 receptor type 3 (IP_3R_3)			
α_1	Maximum rate of k_1	40 μM s^{-1}	[22]
β_1	$[Ca^{2+}]_i$ for half-maximal k_1	0.8 μM	[22]
k_{-1}	Rate of O to S transition	0.88 s^{-1}	[22]
k_2	Rate of O to I_1 transition	0.5 s^{-1}	[22]
k_3	Rate of I_1 to S transition	0.5 s^{-1}	[22]
β_4	$[IP_3]$ for half-maximal k_4	0.01 μM	[22]
k_5	Rate of I_2 to S transition	0.02 s^{-1}	[22]
$k_{IP_3R_3}$	Maximum IP_3R_3 flux rate	155.8 μM s^{-1}	fitted
IV Ryanodine receptor (RyR)			
K_a	Keizer & Levine dissociation constant	0.37224 μM	[23]
K_b	Keizer & Levine dissociation constant	0.63601 μM	[23]
K_c	Keizer & Levine dissociation constant	0.05714 μM	[23]
k_{RyR}	Maximum RyR flux rate	16.04 μM s^{-1}	fitted
V Ca^{2+} pumps and leak current			
V_{Pump}	Maximal pump rate	5.341 μM s^{-1}	fitted
K_{Pump}	$[Ca^{2+}]_i$ for half-maximal V_{Pump}	0.5030 μM	fitted
J_{Leak}	Ca^{2+} leak current	0.1450 μM s^{-1}	fitted
VI Gap junctions (GJ)			
$D_{Ca^{2+}}$	Diffusion coefficient of Ca^{2+} through GJs	512.7 μm^2 s^{-1}	fitted
D_{IP_3}	Diffusion coefficient of IP_3 through GJs	913.9 μm^2 s^{-1}	fitted

(*Continued*)

Table 2. (*Continued*)

Parameter	Description	Value	Reference
$In_{Ca^{2+}}$	Ca^{2+} input to NB1	-0.003320 μM s^{-1}	fitted
In_{IP_3}	IP_3 input to NB1	0.5771 μM s^{-1}	fitted
$Out_{Ca^{2+}}$	Ca^{2+} output from NB10	0 μM s^{-1}	see text
Out_{IP_3}	IP_3 output from NB10	0 μM s^{-1}	see text
Initial conditions (time 0s)			
$[R^S]$	Total number of unphosphorylated surface receptors	17000	[21]
$[R^S_p]$	Total number of phosphorylated surface receptors	0	[21]
[G]	Basal number of G-protein molecules	14	[21]
$[IP_3]$	Basal IP_3 concentration	0.01 μM	[21]
$[PIP_2]$	Basal number of PIP_2 molecules	49997	[21]
$[Ca^{2+}]_i$	Basal cytoplasmic Ca^{2+} concentration	0.12 μM	see text

Most of the parameters were taken from the models of Lemon et al. 2003[21] for P_2Y_2 receptor, LeBeau et al. 1999[22] for IP_3R_3, and Keizer & Levine 1996[23] for RyR. Reference 'fitted' means that the parameter was optimized in this study.

doi:10.1371/journal.pone.0128434.t002

Ligand diffusion in the extracellular space is modelled according to thin film solution to Fick's diffusion law [32] as follows describing the ligand concentration (L) as a function of time (t)

$$L(x,t) = \frac{L_0}{\sqrt{4\pi D_{ATP} t}} e^{-x^2/(4Dt)}, \quad (3)$$

where L_0 is the initial bolus ligand concentration above the MS cell (at x = 0), D_{ATP} is the diffusion coefficient for ATP, and x describes the NB layer distance from the central MS cell.

IP_3R_3 phosphorylation rate (α_4) used in Eq 21 was fitted separately for each NB layer in GA-treated and control data sets, which resulted in shallowly rising exponential functions with respect to the distance of the cell from the MS cell (x). The equation for GA-treated data

Table 3. Location-dependent parameters with respect to the MS cell.

Parameter	Description	Equation	Range
x	Distance from the MS cell centre	1	From 12.12 μm (NB1) to 121.24 μm (NB10)
θ	Stretch	2 (exponential decay)	From 0.096 (NB1) to 1.014 10^{-6} (NB10)
L	Extracellular ligand concentration	3 (exponential decay)	From 26.14 μM (NB1) to 2.61 μM (NB10)
α_4	IP_3R_3 phosphorylation rate	4 (exponential rise)	From 0.0413 s^{-1} (NB1) to 0.1548 s^{-1} (NB10)
		5 (exponential rise)	From 0.0333 (NB1) to 0.1503 (NB10)
$J_{GJ,Ca^{2+}}$	Ca^{2+} flux through GJs	26	From 0.049 μM s^{-1} (NB1→NB2) to 1.8 10^{-6} μM s^{-1} (NB9→NB10)
J_{GJ,IP_3}	IP_3 flux through GJs	27	From 0.407 μM s^{-1} (NB1→NB2) to 0.022 μM s^{-1} (NB9→NB10)
A	Area of the cell membranes connecting NB layers	28	From 1512 μm^2 (NB1) to 10584 μm^2 (NB10)

doi:10.1371/journal.pone.0128434.t003

set ($R^2 = 0.9740$) is

$$\alpha_4 = 0.0357e^{0.0121x} \quad (4)$$

and for control data set ($R^2 = 0.9798$)

$$\alpha_4 = 0.0282e^{0.0138x}. \quad (5)$$

Similarly to θ and L, these functions were then used in simulations instead of values from separate fits.

Model simulations

The parameters were fitted with Matlab SimBiology (R2012a, The MathWorks, Natick, MA) to the experimental data using Parameter Fit task, where the maximum iterations was 100. The solver type was ode45 (Dormand-Prince) and the error model was constant error model. The time step in the simulations was set to $\Delta t = 0.1$ seconds.

Sensitivity analysis

Sensitivity analysis was performed to evaluate the uncertainty of selected parameters that were fitted in this study (parameters $k_{IP_3R_3}$, k_{RyR}, V_{Pump}, K_{Pump}, J_{Leak}, In_{IP_3}, $In_{Ca^{2+}}$, D_{IP_3} and D_{IP_3} from Table 2) or behaved as location-specific parameters (parameters θ, L and α_4 from Table 3). Values of these parameters were changed -25%, -10%, 0%, +10% and +25% in the model including all the model components I-VI for the control data set. The influence of these parameter were studied for NB layers NB1, NB5 and NB10 concentrating on the following features of the Ca^{2+} wave: peak amplitude, time to peak, Ca^{2+} wave width at half maximum, and Ca^{2+} concentration at the end of the Ca^{2+} wave (at 90 seconds' time point).

Model prediction of drug effect: suramin

With the model, we investigated the mechanism by which suramin influences the Ca^{2+} waves in ARPE-19 cells. First, we compared the peak amplitude, time to peak, Ca^{2+} wave width at half maximum, and Ca^{2+} concentration in the end of the Ca^{2+} wave at 90 seconds' time point between two experimental data sets: GA-treated and GA-suramin-treated data sets. Second, we made sensitivity analysis about the behaviour of P_2Y_2 receptor regulation parameters (K_1, K_2, k_r, k_p, k_e, ξ), since suramin is a known unspecific antagonist of P_2 receptors. Suramin has also been suggested to disrupt the coupling between the receptor in the cell membrane and the G-protein by blocking the association of the G-protein α and βγ subunits[33]. Hence, the G-protein cascade parameters k_a, k_d and δ were also evaluated. The sensitivity analysis was done in the model for GA-treated data set (including model components I-V) in NB1, NB5 and NB10 layers. The parameter values were changed in the model by -25% and +25% in order to compare the effects of parameter modifications to the observed differences in the experimental data between GA-treated and GA-suramin-treated data sets. All other parameters were kept unchanged. Third, based on the results of this approach, the model was fitted to the GA-suramin-treated data set by refitting those P_2Y_2 receptor and G-protein cascade parameters that were observed to change the Ca^{2+} curve similarly to the differences seen in the experimental data between GA-treated and GA-suramin-treated data sets. This was done with Matlab SimBiology Parameter Fit task for each NB layer.

Detailed model equations

Time dependent changes in intracellular Ca^{2+} concentration $[Ca^{2+}]_i$ are presented in the model as a combination of Ca^{2+} fluxes

$$\frac{d[Ca^{2+}]_i}{dt} = J_{SSCC} + J_{IP_3R_3} + J_{RyR} - J_{Pump} + J_{Leak} + J_{GJ,Ca^{2+}}, \quad (6)$$

where the subscripts indicate the source of the flux: stretch-sensitive Ca^{2+} channels (J_{SSCC}), inositol 1,4,5-trisphosphate (IP_3) receptor type 3 ($J_{IP_3R_3}$), and ryanodine receptor (J_{RyR}). J_{Pump} combines the Ca^{2+} pumping functions of sarco/endoplasmic reticulum ATPase (SERCA) and the plasma membrane Ca^{2+} ATPase (PMCA). Leak Ca^{2+} current (J_{Leak}) describes the total leakage from the extracellular space and the endoplasmic reticulum (ER) to the cytoplasm. $J_{GJ,Ca^{2+}}$ is the Ca^{2+} flux through gap junctions.

I Stretch-sensitive Ca^{2+} channels (SSCCs). Stretch-sensitive Ca^{2+} channels (SSCCs) on the cell membrane are activated, when exposed to mechanical stimulation. Their closure is caused either by relaxation in the mechanical force or by their adaption to that mechanical force[34]. The SSCC model is described with Eqs 7–9. In this study, a model for SSCCs was developed according to the kinetic diagram shown in Fig 3, where C_{SSCC} describes the proportion of the channels in the closed state. O_{SSCC} is the proportion of SSCCs in the open state defined as

$$\frac{dO_{SSCC}}{dt} = \theta k_f - (\theta k_f + k_b) O_{SSCC}, \quad (7)$$

where k_f is the forward rate constant and k_b is the backward rate constant. Ca^{2+} flux via SSCCs (J_{SSCC}) is expressed as

$$J_{SSCC} = k_{SSCC} O_{SSCC}, \quad (8)$$

where k_{SSCC} is the maximum Ca^{2+} flux rate via SSCCs. Parameter θ is dimensionless, and describes the quantity of stretch induced at the time of mechanical stimulation, which then decreases with time

$$\frac{d\theta}{dt} = -k_\theta \theta, \quad (9)$$

according to a stretch-relaxation parameter k_θ.

II Purinergic receptor P_2Y_2. The agonist-induced activation of the second messenger system, here P_2Y_2, is represented by Eqs 10–16[21].The kinetic diagram for the P_2Y_2 receptor is presented in Fig 3. Some of the ligand-bound P_2Y_2 receptors on the cell surface are phosphorylated irreversibly at rate k_p, which causes desensitization of the receptors. Phosphorylated receptors are internalized at a rate k_e, and these internalized receptors are then dephosphorylated and recycled back to the surface at rate k_r. G-proteins can only be activated by the unphosphorylated P_2Y_2 receptors $[R^S]$ defined by

$$\frac{d[R^S]}{dt} = k_r[R_T] - \left(k_r + \frac{k_p[L]}{K_1 + [L]}\right)[R^S] - k_r[R_p^S], \quad (10)$$

where $[R_T]$ denotes the total number of surface receptors, K_1 is the dissociation constant for unphosphorylated receptors, and [L] is the extracellular ligand concentration. The total

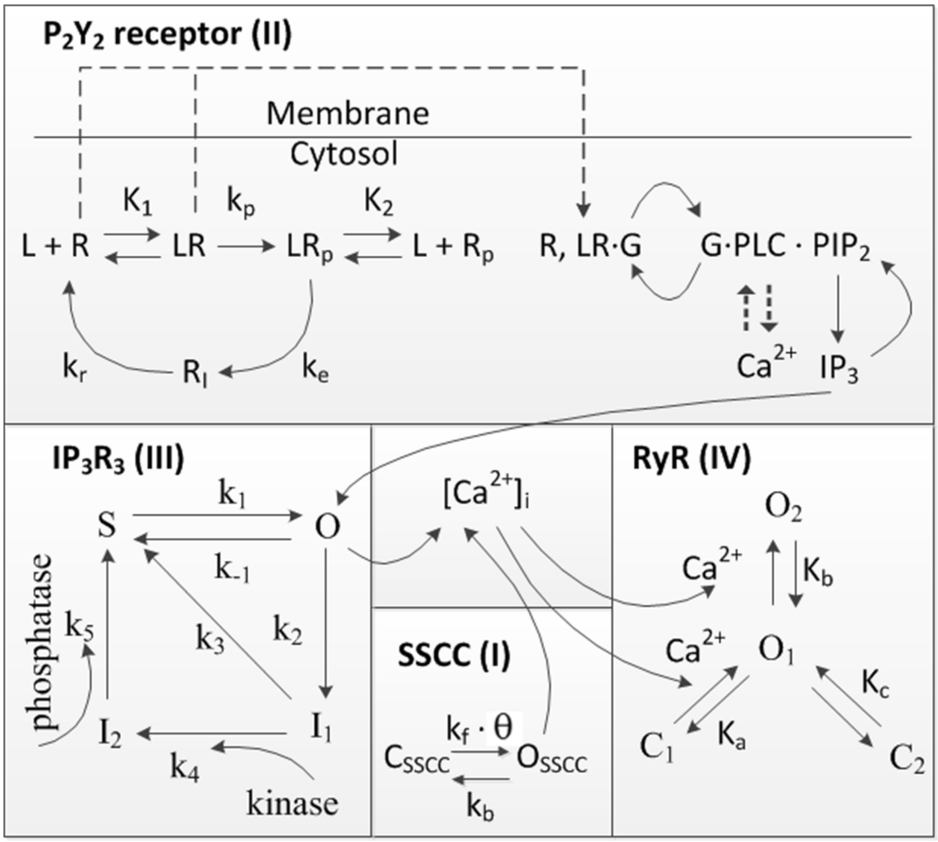

Fig 3. Kinetic diagram. Kinetics of the model component I (SSCC) were combined with the kinetics of model components II-IV from the original models of the P_2Y_2 receptor[21], IP_3R_3[22], and RyR[23].

doi:10.1371/journal.pone.0128434.g003

number of phosphorylated surface receptors $[R_p^S]$ is

$$\frac{d[R_p^S]}{dt} = [L]\left(\frac{k_p[R^S]}{K_1 + [L]} - \frac{k_e[R_p^S]}{K_2 + [L]}\right), \tag{11}$$

where K_2 is the dissociation constant for phosphorylated receptors. The binding of the ligand to the G-protein coupled receptor P_2Y_2 results in a cascade of events leading to the activation of enzyme phospholipase C (PLC). This enzyme then hydrolyses the phosphatidylinositol 4,5-bisphosphate (PIP_2) to IP_3. The activation rate (k_a) of the G-protein is proportional to two ratios: the ratio of the activities of the ligand unbound and bound receptor species (δ), and the ratio of the number of ligand bound receptors and the total number of receptors (p_r). Denoting the deactivation of G-protein to occur at a deactivation rate of k_d, the equations for the amount

of Gα · GTP labeled as [G] as well as for the ratio p_r can be expressed as

$$\frac{d[G]}{dt} = k_a(\delta + p_r)([G_T] - [G]) - k_d[G], \tag{12}$$

and

$$p_r = \frac{[L][R^S]}{\xi[R_T](K_1 + [L]).} \tag{13}$$

Equation for the concentration of IP_3 is

$$\frac{d[IP_3]}{dt} = r_h N_a^{-1} v^{-1}[PIP_2] - k_{\deg}[IP_3] + J_{GJ,IP_3}, \tag{14}$$

where k_{deg} is the degradation rate of IP_3 and J_{GJ,IP_3} is the IP_3 flux through gap junctions. The rate coefficient for PIP_2 hydrolysis (r_h) includes the effective signal gain parameter (α) and the dissociation constant for Ca^{2+} binding to PLC (K_3) that can be expressed as

$$r_h = \alpha\left(\frac{[Ca^{2+}]_i}{K_3 + [Ca^{2+}]_i}\right)[G]. \tag{15}$$

Replenishment of PIP_2 is required for IP_3 production to be maintained over sustained periods of agonist stimulation. The equation for the number of PIP_2 molecules $[PIP_2]$ is

$$\frac{d[PIP_2]}{dt} = -(r_h + r_r)[PIP_2] - r_r N_a v[IP_3] + r_r[(PIP_2)_T], \tag{16}$$

where r_r represents the PIP_2 replenishment rate and $[(PIP_2)_T]$ the total number of PIP_2 molecules.[21]

III IP_3 receptor type 3 (IP_3R_3). The IP_3 receptor type 3 (IP_3R_3) function is represented by the Eqs 17–21[22]. The kinetic diagram for IP_3R_3 is shown in Fig 3. The IP_3-induced release of Ca^{2+} from the ER through IP_3R_3 ($J_{IP_3R_3}$) is

$$J_{IP_3R_3} = k_{IP_3R_3} O^4, \tag{17}$$

where $k_{IP_3R_3}$ is the maximum rate of Ca^{2+} release, and IP_3R_3 comprises four subunits that all must be in the open state (O) for the receptor to conduct. The steady-state proportion of open receptors (O) is

$$O = \frac{\phi[IP_3]}{\frac{k_{-1}+k_2}{k_1}\phi + [IP_3]}, \tag{18}$$

Where ϕ function controls the sensitivity of IP_3R_3 to $[IP_3]$, and it can be expressed as

$$\phi = \frac{1}{1 + \frac{k_2}{k_3+k_4}\left(1 + \frac{k_4}{k_5}\right)}, \tag{19}$$

with rate coefficients k_{-1}, k_2, k_3, and k_5 being constants. Coefficient k_1 describes a rate for IP_3R_3 transition from shut state (S) to open state (O)

$$k_1 = \frac{\alpha_1[Ca^{2+}]_i^{\,3}}{\beta_1^{\,3} + [Ca^{2+}]_i^{\,3}}, \tag{20}$$

where constant α_1 is the maximum rate of S to O transition, and β_1 is the $[Ca^{2+}]_i$ at which the rate is half of its maximum. Coefficient k_4 expresses the rate for IP_3R_3 from the first inactivated

state (I_1) to the second inactivated state (I_2). It can be expressed as

$$k_4 = \frac{\alpha_4[IP_3]}{\beta_4 + [IP_3]}, \tag{21}$$

where the I_1 to I_2 transition is agonist specific and involves a phosphorylation of IP_3R_3 by kinase activity. This is defined by parameter α_4 that denotes the maximum rate of I_1 to I_2 transition, while β_4 denotes the value of $[IP_3]$ at which the rate is half maximal.[22]

IV Ryanodine receptor (RyR). The ryanodine receptor (RyR) dynamics were modeled by Keizer & Levine 1996[23] with Eqs 22–24. In Fig 3 the kinetic diagram for RyR is illustrated. The Ca^{2+} release from the ER through RyR (J_{RyR}) is defined by the maximum RyR flux rate (k_{RyR}) multiplied by the open probability (P_{RyR}) as

$$J_{RyR} = k_{RyR} P_{RyR} \tag{22}$$

where

$$P_{RyR} = \left(\frac{w^{\infty}\left(1+\left(\frac{[Ca^{2+}]_i}{K_b}\right)^3\right)}{1+\left(\frac{K_a}{[Ca^{2+}]_i}\right)^4+\left(\frac{[Ca^{2+}]_i}{K_b}\right)^3} \right), \tag{23}$$

and where w^{∞} is the RyR sensitivity function

$$w^{\infty} = \left(\frac{1+\left(\frac{K_a}{[Ca^{2+}]_i}\right)^4+\left(\frac{[Ca^{2+}]_i}{K_b}\right)^3}{1+\frac{1}{K_c}+\left(\frac{K_a}{[Ca^{2+}]_i}\right)^4+\left(\frac{[Ca^{2+}]_i}{K_b}\right)^3} \right), \tag{24}$$

and K_a, K_b, and K_c are dissociation constants. [23]

V Sarco/endoplasmic reticulum Ca^{2+} ATPase (SERCA) and plasma membrane Ca^{2+} ATPase (PMCA). J_{Pump} combines the pumping functions of sarco/endoplasmic reticulum Ca^{2+} ATPase (SERCA) and plasma membrane Ca^{2+} ATPase (PMCA)

$$J_{Pump} = \frac{V_{Pump}[Ca^{2+}]_i^2}{K_{Pump}^2 + [Ca^{2+}]_i^2}, \tag{25}$$

where V_{Pump} indicates the maximum flux rate of the pumps and K_{Pump} states the $[Ca^{2+}]_i$ for half-maximal pumping rate.

VI Gap junctions (GJs). Gap junctions (GJs) and the Ca^{2+} flux via GJs ($J_{GJ,Ca^{2+}}$) are modeled as

$$J_{GJ,Ca^{2+}} = \frac{D_{Ca^{2+}}}{A_{n-1,n}}([Ca^{2+}]_{in-1} - [Ca^{2+}]_{in}) - \frac{D_{Ca^{2+}}}{A_{n,n+1}}([Ca^{2+}]_{in} - [Ca^{2+}]_{in+1}), \tag{26}$$

where n is the number of the NB layer. The NB layer n receives Ca^{2+} from the previous NB layer $n-1$ and delivers Ca^{2+} to the next NB layer $n+1$ according to the concentration gradient. Similarly, IP_3 flux through GJs (J_{GJ,IP_3}) is modelled as

$$J_{GJ,IP_3} = \frac{D_{IP_3}}{A_{n-1,n}}([IP_3]_{n-1} - [IP_3]_n) - \frac{D_{IP_3}}{A_{n,n+1}}([IP_3]_n - [IP_3]_{n+1}), \tag{27}$$

where n is the number of the NB layer. $D_{Ca^{2+}}$ is the diffusion coefficient for Ca^{2+} and D_{IP_3} is the diffusion coefficient for IP_3. These diffusion coefficients do not take into account the open probability, regulation, or density of the GJs as they describe the actual movement of Ca^{2+} and

IP_3 from one NB layer to the next NB layer. As an exception to other NB layers, the fluxes from MS cell to NB_1 layer are modelled by parameters $In_{Ca^{2+}}$ and In_{IP_3} for Ca^{2+} and IP_3, respectively. Similarly, the fluxes from NB_{10} layer to distant cell layers are modelled with parameters $Out_{Ca^{2+}}$ and Out_{IP_3}.

Parameter A describes the area of the cell membranes connecting the neighbouring NB layers in the monolayer. The value for A is received by multiplying the area of one hexagon side, that is the length of the hexagon side (l = 7μm) times the height of the cell (h = 12μm), by the number of hexagon edges between the two NB layers as

$$A_{n\to n+1} = ((3 + 2(n - 1))6)lh, \tag{28}$$

where n is the number of the NB layer (n = 1, 2, 3. . ..10). Each NB layer has six cells with three connecting sides and (n-1) 6 cells with two connecting sides (see Fig 1). In other words, the area (A) increases with distance from the central MS cell.

Results

Polarization of the ARPE-19 monolayer

Polarization of the ARPE-19 monolayer was demonstrated by immunolabeling the tight junctions in the monolayer. Confocal microscopy image (Fig 4) shows that within 2 days the ARPE-19 cells have formed a monolayer where ZO-1 is localised continuously in the junctions of the cells, forming a homogeneous network. This can be taken as an indication of the polarization of the epithelial cell culture [35].

Ca^{2+} signal propagation mechanisms

The fittings of the model to the experimental data in the NB1-NB10 layers are illustrated in Fig 5A for the GA-treated data set and in Fig 5B for the control data set. The model simulations managed to catch very well the features of the experimental data in both data sets. In GA-treated data set (Fig 5A), the simulations closely followed the data in peak amplitude, time to peak, Ca^{2+} wave width at half maximum and end Ca^{2+} concentration in NB1-NB9 layers. In NB10 layer, however, time to peak was longer in the simulation results than in the data. In the control data set (Fig 5B), the Ca^{2+} wave features differed slightly between the model and the data, but overall the curve shape of the model followed the data reasonably well. R^2 values describing the goodness of fit are presented in Table 4. In GA-treated data set and control data set R^2 values were higher than 0.8 in NB1-NB9 and lower than 0.8 in NB10. Hence, 90% of the fits in GA-treated data set and control data set resulted in $R^2 > 0.8$.

The model includes the model components of SSCCs, P_2Y_2 receptors, IP_3R_3s, RyRs, Ca^{2+} pumps and GJs, and the parameters were either obtained from previous studies or defined in this study for ARPE-19. The basic fit was done in GA-treated data set for NB5, but the SSCC model component was fitted in NB1 (Table 2). Three location-specific parameters were defined in this study: stretch (θ), extracellular ligand concentration (L) and phosphorylation rate of IP_3R_3 (α4) (Table 3). The stretch (θ) and extracellular ligand concentration (L) decayed exponentially from NB1 towards the distant NB cell layers. The IP_3R_3 phosphorylation rate regulated by the kinase activity (α_4) increased following a shallow exponential, almost linear function, from NB1 to NB10. The corresponding values of α_4 with the distance were lower in the control data set (Eq 5) than in the GA-treated data set (Eq 4) indicating a possible role of IP_3 receptor phosphorylation rate as a regulator of Ca^{2+} signaling. The GJ model component was parameterized in control data set for NB1. GJs mediated the Ca^{2+} signal by allowing the diffusion of Ca^{2+} and IP_3 between adjacent cell layers so that the fluxes of these species decreased with

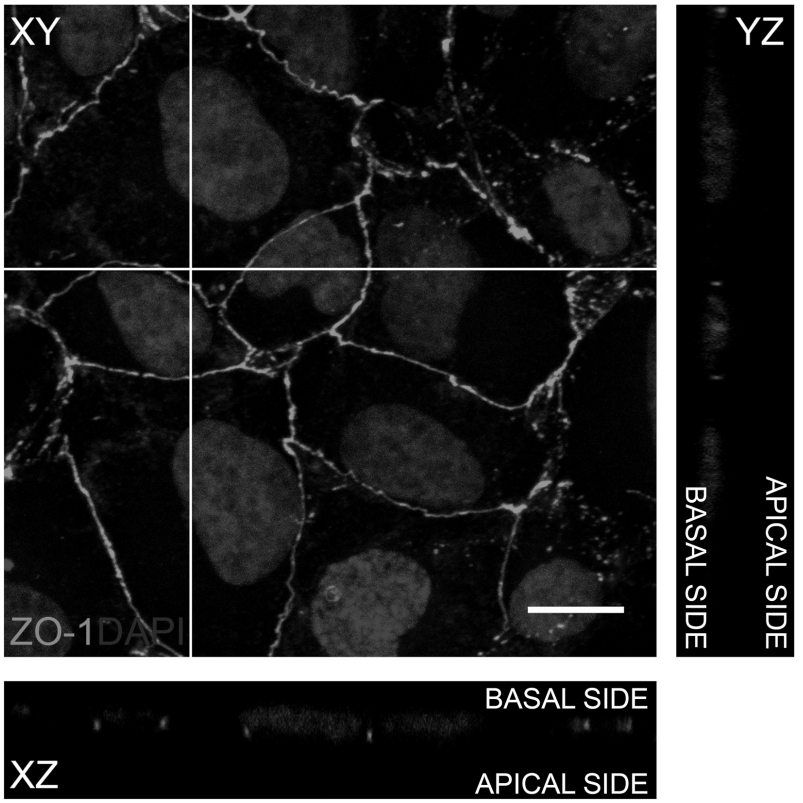

Fig 4. Polarization of the ARPE-19 monolayer. Z-projections (XZ and YZ) from apical side to basal side and maximum intensity projection of the XY plane in the ARPE-19 monolayer represent the localization of Zonula Occludens (ZO-1, red) in the confocal micrograph after immunofluorescence labeling with the nuclear label 4',6-diamidino-2-phenylindole (DAPI, blue). Scale bar is 10μm.

doi:10.1371/journal.pone.0128434.g004

distance from the MS cell due to the increasing area of the cell membranes connecting the NB layers (Table 3).

The resulting model of mechanical stimulus induced Ca^{2+} dynamics is: 1) Cells near the stimulus site conduct Ca^{2+} through plasma membrane SSCCs, and gap junctions conduct the Ca^{2+} and IP_3 between cells further away from stimulated cell. 2) The MS cell secretes one or several types of ligand to the extracellular space where the ligand diffusion mediates the Ca^{2+} signal so that the ligand concentration decreases with distance. 3) The phosphorylation of the IP_3 receptor defines the cell's sensitivity to the extracellular ligand attenuating the Ca^{2+} signal in the distance.

Results of the sensitivity analysis

The sensitivity of the four Ca^{2+} wave features described in Materials and Methods was studied for a set of parameters that were fitted in this study for NB1, NB5 and NB10 layers (Fig 6).

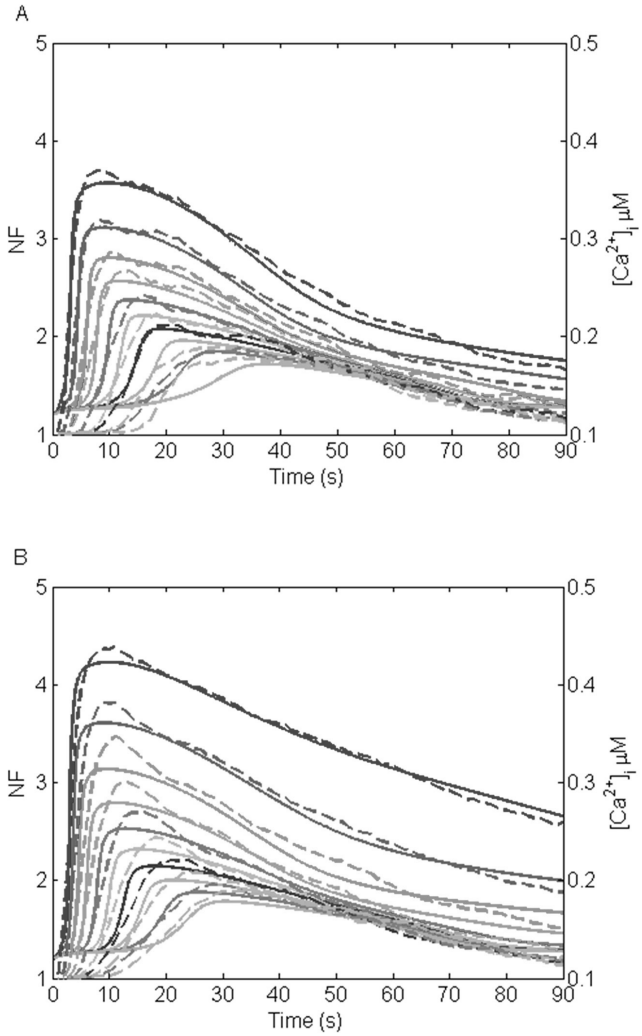

Fig 5. Fittings of the model to the experimental data. (A) GA-treated, and (B) control data sets with dashed lines representing the data in dimensionless NF units and solid lines representing the model simulations with arbitrary units representing $[Ca^{2+}]_i$ in μM concentrations. The uppermost curve pair (blue) represents NB1, the second uppermost NB2 (green), followed by NB3 (red), NB4 (light blue), NB5 (purple), NB6 (yellow), NB7 (black), NB8 (light red), NB9 (grey), and NB10 (orange).

doi:10.1371/journal.pone.0128434.g005

From the location-dependent parameters, θ, L and α_4, Ca^{2+} wave features were most sensitive to modifications in α_4 and the least sensitive to modifications in θ. Overall, decreasing the stretch parameter (θ) resulted in faster Ca^{2+} waves in NB1 (Fig 6B). Increasing the extracellular

Table 4. R^2 values indicating the goodness of fit between the model and the data.

Data set	NB1	NB2	NB3	NB4	NB5	NB6	NB7	NB8	NB9	NB10
GA-treated	0.9839	0.9815	0.9811	0.9651	0.9716	0.9627	0.9677	0.9326	0.8837	0.4561
Control	0.9665	0.9613	0.9454	0.9653	0.9686	0.9558	0.9508	0.9419	0.9108	0.6259
GA-suramin-treated	0.8633	0.8543	0.9344	0.9323	0.9414	0.9156	0.9253	0.7812	0.6110	0.2297

R^2 values are listed separately for each data set and NB layer.

doi:10.1371/journal.pone.0128434.t004

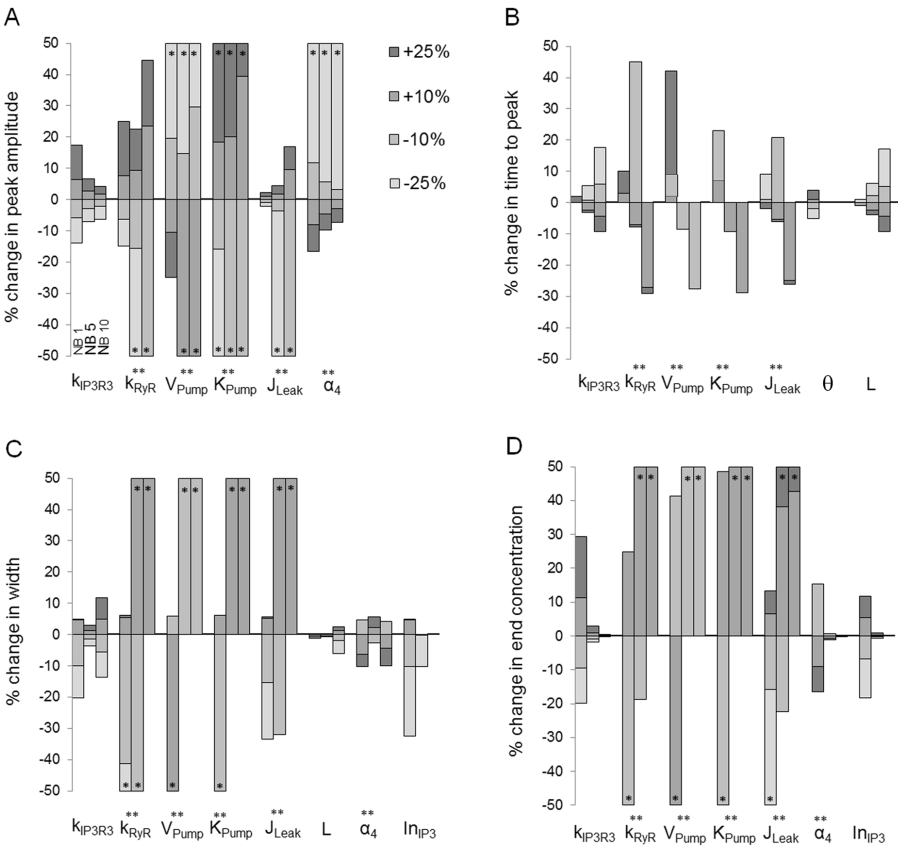

Fig 6. Sensitivity analysis of the model parameters. Percentage changes in Ca^{2+} wave (A) peak amplitude, (B) time to peak, (C) Ca^{2+} wave width at half maximum, and (D) end Ca^{2+} concentration at 90 seconds' time point due to changes in model parameters $k_{IP_3R_3}$, k_{RyR}, V_{Pump}, K_{Pump}, J_{Leak}, θ, L, α_4, In_{IP_3}, $In_{Ca^{2+}}$, D_{IP_3}, and $D_{Ca^{2+}}$ as marked in the x-axis. The analysis was carried out in NB layers NB1, NB5 and NB10 as denoted in (A) for parameter $k_{IP_3R_3}$. The amount of modification (-25%, -10%, +10% or +25%) is shown in the grayscale of the histogram. The histogram bar is marked with asterisk (*) if the change was greater than 50%, and with double asterisk (**) if parameter modification did not result typical Ca^{2+} waveform. Regarding each Ca^{2+} wave feature, the parameter is illustrated only if the change was more than 5%.

doi:10.1371/journal.pone.0128434.g006

ligand concentration (L) in turn decreased the time to peak (Fig 6B) and increased the Ca^{2+} wave width at half maximum (Fig 6C). The effects of the changes in IP_3 receptor phosphorylation rate (α_4) on Ca^{2+} wave features were complex: with decreasing α_4 Ca^{2+} wave peak amplitude increased (Fig 6A), time to peak decreased (Fig 6B), the Ca^{2+} wave width at half maximum increased or decreased depending on the NB layer (Fig 6C), and the end concentration increased (Fig 6D). The Ca^{2+} wave features were insensitive to gap junction related parameters $In_{Ca^{2+}}$, D_{IP_3} and $D_{Ca^{2+}}$ so that the tested modifications in their values resulted in less than 5% change in the features from the original conditions. Thus, they are not illustrated in Fig 6. However, increasing IP_3 input to NB1 via GJs (In_{IP_3}) increased the Ca^{2+} wave width at half maximum (Fig 6C) and end concentration (Fig 6D), and the sensitivity was significantly higher in NB1 layer than in the more distant NB layers. In general, the sensitivity of the model to the changes in tested parameters depended on the NB layer and thus on the distance to the MS cell. Few parameters, however, were independent of the location (parameters $k_{IP_3R_3}$, k_{RyR}, V_{Pump}, K_{Pump}, J_{Leak}), but changes in their values affected significantly the investigated Ca^{2+} wave features.

Possible suramin effect on attenuation of Ca^{2+} waves

Similarly to the general sensitivity analysis, the four Ca^{2+} wave features were compared between the experimental GA-treated and GA-suramin-treated data sets as well in NB1, NB5 and NB10 layers (Fig 7A). In the GA-suramin-treated data set, differences in peak amplitude were less than 10% compared to the GA-treated data set. However, time to peak decreased for NB1 and increased for NB5 and NB10 layers in the GA-suramin-treated data set. Furthermore, in this data set the Ca^{2+} wave width at half maximum and the end Ca^{2+} concentration were lower than in the GA-treated data set.

Since suramin is a known P_2 receptor blocker, we studied the sensitivity of the model to P_2Y_2 receptor parameters for the GA-treated data set (including model components I-V) by changing their values by ±25%. Similarly, G-protein cascade parameters were studied as well to consider the possible effect of suramin to disrupt the coupling between the receptor in the cell membrane and the G-protein. Our aim was to investigate the degree to which the observed differences in the Ca^{2+} wave features between GA-treated and GA-suramin-treated data sets could be accounted for by the changes in these parameters. The sensitivity analysis revealed that the modifications in P_2Y_2 unphosphorylated receptor dissociation constant (K_1) and P_2Y_2 receptor phosphorylation rate (k_p) indeed induced changes that were similar to the experimental observations (see Fig 7A): increase in K_1 modified the time to peak (Fig 7B) and increase in k_p narrowed the Ca^{2+} wave width at half maximum (Fig 7C). This would indicate disrupted ligand binding to the receptor or a higher phosphorylation rate of P_2Y_2 receptors as well as a faster desensitization of the receptors after ligand binding. P_2Y_2 receptor parameters K_2, k_r, k_e, ξ, on the contrary, had a negligible influence on Ca^{2+} wave behaviour: the modifications of these parameters by ±25% resulted only in less than 3% change on Ca^{2+} wave features, as was the case also for G-protein cascade parameter δ. G-protein cascade parameters G-protein activation rate (k_a) (Fig 7D) and G-protein deactivation rate (k_d) (Fig 7E) had diverse effects on the Ca^{2+} wave features: for example decreasing k_a and increasing k_d narrowed the Ca^{2+} wave width at half maximum in NB1 and NB5, but widened it in NB10. Thus, their behaviour did not follow the observations from the experimental data and therefore these factors were not considered to be responsible for the effects of suramin on the Ca^{2+} wave.

Fig 7F illustrates the fit of the model to the GA-suramin-treated data set after refitting the model parameters K_1 and k_p. The values of these parameters ranged as follows: K_1 values decreased from 8.83μM in NB1 to 5.15μM in NB10 and k_p values decreased from $0.19s^{-1}$ in NB1

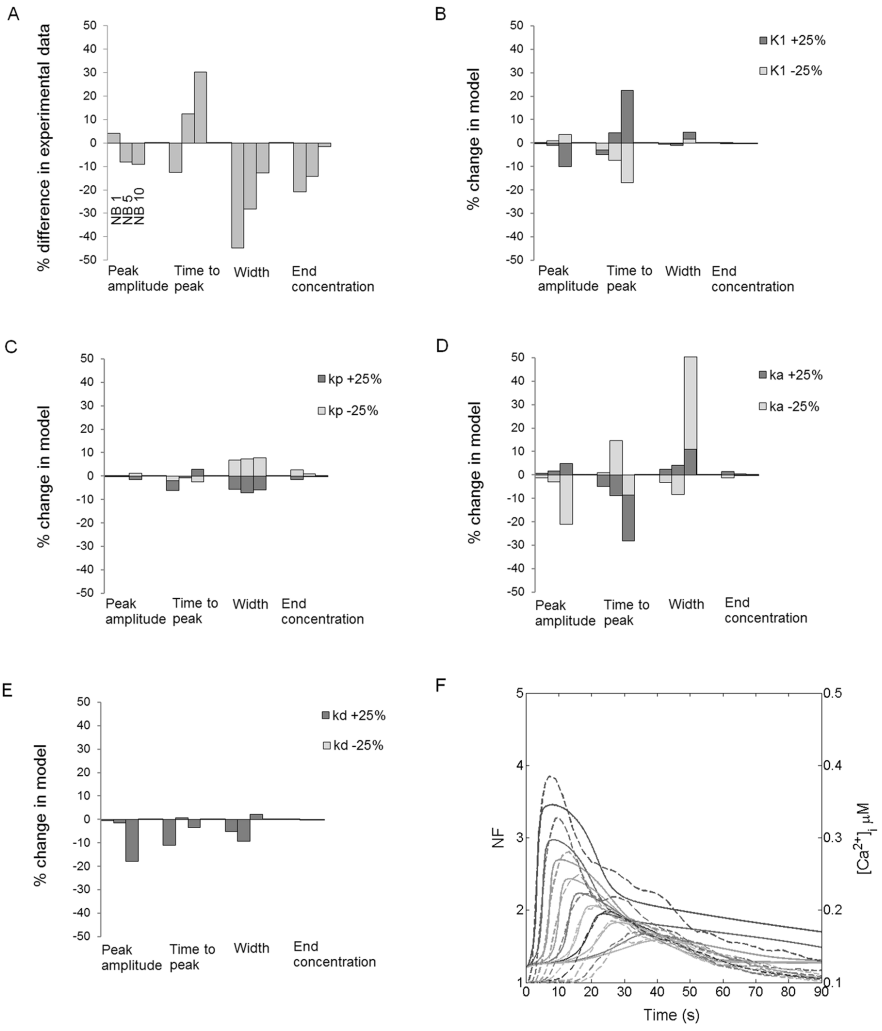

Fig 7. Suramin effects on Ca^{2+} wave. (A) Comparison of the peak amplitude, time to peak, Ca^{2+} wave width at half maximum, and end Ca^{2+} concentration at 90 seconds' time point in cell layers NB1, NB5 and NB10 between the experimental GA-treated and GA-suramin-treated data sets. The deviations of each Ca^{2+} wave feature in GA-suramin-treated data set from GA-treated data set are expressed as percentages. (B) Unphosphorylated P_2Y_2 receptor dissociation constant (K_1), (C) P_2Y_2 receptor phosphorylation rate (k_p), (D) G-protein activation rate (k_a), and (E) G-protein deactivation rate (k_d) were changed in the model for GA-treated data set either -25% or +25%, as denoted in the grayscale of the histogram, and the percentage change in each Ca^{2+} wave feature is illustrated. (F) Fitting of the model to the GA-suramin-treated data set. Dashed lines represent the data in dimensionless NF units, whereas solid lines represent the model simulations with arbitrary units representing $[Ca^{2+}]_i$ in µM concentrations. The uppermost curve pair (blue) represents NB1, the second uppermost NB2 (green), followed by NB3 (red), NB4 (light blue), NB5 (purple), NB6 (yellow), NB7 (black), NB8 (light red), NB9 (grey), and NB10 (orange).

doi:10.1371/journal.pone.0128434.g007

to $0.05s^{-1}$ in NB10. Overall, the values of K_1 and k_p were higher in the GA-suramin-treated data set than in the GA-treated data set. The simulated curves seem to fit well to the experimental data, except in NB1 layer at the end of the Ca^{2+} wave. In GA-suramin-treated data set, R^2 values were higher than 0.8 in NB1-NB7 and lower than 0.8 in NB8-NB10 (Table 4). 70% of the fits in GA-suramin-treated data set resulted in $R^2 > 0.8$ indicating that the model explains only partially the combined effect of GA and suramin on Ca^{2+} waves especially in the distant NB layers.

Discussion

The ARPE-19 cell line is an important biological model of human RPE despite its certain limitations [20]. This paper presents the first computational RPE model of Ca^{2+} signaling using the experimental data measured from the ARPE-19 monolayer after mechanical stimulation. We aimed to create a model that combines the most important Ca^{2+} signaling mechanisms in ARPE-19 cells so that the model can be used later in the development of more complicated RPE and epithelial models. Furthermore, the model was used to simulate and explain the Ca^{2+} signaling of epithelia, especially RPE, taking into account the following factors: 1) cells are on the monolayer; 2) they are connected to each other by GJs permeating Ca^{2+} and IP_3, and 3) the cells are most probably experiencing different stretching and chemical conditions depending on their distance from the mechanical stimulation site. To the best of our knowledge, this is the first time as Ca^{2+} signaling model has been implemented for the ARPE-19 monolayer. The model uses a set of location specific parameters including stretch, extracellular ligand concentration, and IP_3R_3 phosphorylation rate as well as the Ca^{2+} and IP_3 fluxes through GJs.

The identity of the extracellular ligand

The airway epithelium secretes the signal carriers ATP or UTP to the extracellular space in response to mechanical stimulation[16,36]. The connection of these ligands to Ca^{2+} signaling as extracellular signal mediators has been mathematically modeled[16]. It is likely that a similar function can be linked to ARPE-19 or RPE, where the ligand interacts with the cell membrane P_2Y_2 receptors. In our model, the ligand carried the signal in the extracellular space from the MS cell towards the distant NB cell layers after mechanical stimulation. According to our model, the extracellular ligand concentration decreased exponentially from NB1 towards NB10. We suggest, based on our modeling results, that the MS cell secretes ligand to the extracellular space. Epithelial cells such as ARPE-19 have been shown to secrete ATP under different stimuli[37,38]. On the other hand, the ligand degradation by ectonucleotidase activity[39] decrease the ligand concentration. The model predicts that the magnitude of the extracellular ligand concentration partly defines the nature of the cell response: higher and faster Ca^{2+} waves were observed with higher ligand concentrations. The ligand concentration was derived from diffusion equation, and the obtained exponential decay function fitted well to the experimental data. Experimental studies show that the Ca^{2+} wave peak amplitude value increases with increased ligand concentration in cultured human RPE[30] and in human airway epithelium[6]. Also, in the mathematical model of Warren et al. 2010[16], it was observed that the time to peak for human airway epithelium decreased as the ligand concentration increased. These observations are in good agreement with our model.

The role of IP_3 receptor phosphorylation rate

The phosphorylation of the IP_3 receptor represents an important regulatory mechanism for Ca^{2+} release[40–42]. It has been shown that the production of cyclic AMP (cAMP) through the

activation of the adenylyl cyclase pathway leads to the activation of protein kinase A that phosphorylates IP_3 receptors[43].

Our simulation results show that the maximal phosphorylation rate of IP_3R_3 (α_4) followed a shallow exponential, almost linear, increase from NB1 to NB10 in all three data sets. The parameter α_4 has previously been modeled as agonist specific only [22]. It is of note, however, that in addition to ATP or UTP and their interaction with P_2Y_2 receptors, also other types of ligand-receptor interactions may occur. One plausible explanation could be that MS cell secretes different types of ligands, because its cell membrane was broken in mechanical stimulation. This would further lead to complex biological interactions at the cellular level, which is seen as a chance of this parameter with cell location.

The need to model α_4 separately for the GA-treated data set and the control data set may be related to the functioning of the GJs, especially to their ability to alter ligand secretion in different cell types. Previous studies show that GJs participate in the regulation of the release of signaling molecules to the extracellular medium [44]. In astrocytes, as an example, GJs have been proposed to regulate the release of glutamate[45], an excitatory neurotransmitter and an important regulator of astrocyte Ca^{2+} oscillations[46].

Overall, α_4 parameter may reflect a number of ligands and cell mechanisms not modelled in this nor other epithelial Ca^{2+} models. The low α_4 values near the MS cell enable higher and faster Ca^{2+} waves at corresponding ligand concentrations compared to the distal cell layers, where higher levels of kinase activity attenuate and slow down the signal. This aligns well with the literature. In RPE, the addition of 8-Br-cAMP counteracted the elevation of $[Ca^{2+}]_i$ induced by connective tissue growth factor (CTGF)[47], and the cell migration inhibitor adrenomedullin increased intracellular cAMP and decreased $[Ca^{2+}]_i$[48]. The effect of the adenylyl cyclase pathway on IP_3R kinetics has been ignored in most of the previously published Ca^{2+} models e.g.[16,21,29], possibly because the kinase activity may not have been activated in those cell types or experimental conditions.

Gap junctions in Ca^{2+} wave propagation

GJs connect the adjacent cells together and allow the diffusion of signaling molecules between them. The diffusion through GJs has previously been modeled, for example, in airway epithelium[16]. In our model, GJs carried the Ca^{2+} signaling molecules between the NB layers based on the Ca^{2+} and IP_3 concentration gradients, and permeated Ca^{2+} and IP_3 selectively. As expected, NB layers near the MS cell were more sensitive to IP_3 input than the distant NB layers, and this was seen especially in the end Ca^{2+} concentration at 90 seconds' time point.

Possible Ca^{2+} wave attenuation mechanisms of suramin

In the GA-suramin-treated data set, the experimental data was reproduced in our model by increasing the unposphorylated receptor dissociation constant, which likely reflects disrupted ligand binding, and by increasing the phosphorylation rate of the P_2Y_2 receptors to enhance their desensitization. This may indicate that suramin targets on P_2Y_2 receptors as an unspecific P_2 receptor antagonist attenuating the Ca^{2+} wave. This intriguing model hypothesis driven from the model results needs to be confirmed experimentally. It is worth noting, however, that suramin has also been considered to disrupt the coupling between the receptor in the cell membrane and the G-protein by blocking the association of the G-protein α and $\beta\gamma$ subunits[33]. In our model, modifications in G-protein cascade parameters influenced the peak amplitude, time to peak and Ca^{2+} wave width at half maximum. Despite the observed diversity in their effects between the NB layers, it is possible that suramin targets the G-protein cascade as well, by acting as an attenuator of the Ca^{2+} wave.

Limitations of the model

Our work presents a computational model of epithelial Ca^{2+} signaling based on experimental work on the ARPE-19 cell line. This cell line is used extensively as a model of RPE, although it differs from it to some extent. The limitations of ARPE-19 compared to native human RPE arise, for example, from cell organization and metabolism[20]. Importantly for our study, ARPE-19 cell line in our experimental setup lacked pigmentation which resulted in a lack of the large Ca^{2+} stores, melanosomes, and needs to be taken into account when expanding our model to describe native RPE. In addition, we confirmed the polarity of the ARPE-19 monolayer with confocal microscopy. Trans-epithelial resistance (TER) that is a general measure of epithelial integrity was not measured due to technical challenges to perform the measurements on glass cover slips with our present equipment [49]. Nevertheless, the computational model created in this study describes the most important components of epithelial and ARPE-19 Ca^{2+} activity. Thus it provides a good basis to address the native RPE in the future, even though it, being based on an *in vitro* model of RPE, needs to be considered only as a model. To improve the model further, experimental data and model implementations on certain additional Ca^{2+} related mechanisms, such as P_2X receptors[50], voltage-sensitive Ca^{2+} channels[51] and Na^+/Ca^{2+} exchangers[52] would be well warranted. Finally, it is worth noting that the experimental work of Abu Khamidakh et al. 2013[5] did not produce absolute Ca^{2+} concentrations, and therefore our model also features only relative Ca^{2+} activity.

Conclusions

A full mathematical understanding of RPE and epithelial Ca^{2+} signaling would allow one to simulate cellular Ca^{2+} responses under several physiological, pathological, and experimental conditions. Our present model represents significant progress towards this goal since it is able to reproduce the experimental data from an RPE type epithelium, ARPE-19 cell line, in different conditions, simulate several epithelial Ca^{2+} signaling mechanisms, and predict drug responses in the epithelia. Our future work will include further development of the model especially focusing on the role of the voltage sensitive Ca^{2+} channels in the RPE.

Author Contributions

Conceived and designed the experiments: IV AA KJ SN JH. Performed the experiments: IV AA. Analyzed the data: IV AA SN. Contributed reagents/materials/analysis tools: IV AA HS JH. Wrote the paper: IV AA MP HS KJ JH SN.

References

1. Sanderson MJ, Charles AC, Boitano S, Dirksen ER. Mechanisms and function of intercellular calcium signaling. Mol Cell Endocrinol. 1994; 98: 173–187. PMID: 8143927
2. Konari K, Sawada N, Zhong Y, Isomura H, Nakagawa T, Mori M. Development of the blood-retinal barrier in vitro: Formation of tight junctions as revealed by occludin and ZO-1 correlates with the barrier function of chick retinal pigment epithelial cells. Exp Eye Res. 1995; 61: 99–108. PMID: 7556475
3. Wimmers S, Karl MO, Strauss O. Ion channels in the RPE. Prog Retin Eye Res. 2007; 26: 263–301. PMID: 17258931
4. Himpens B, Stalmans P, Gomez P, Malfait M, Vereecke J. Intra- and intercellular Ca2+ signaling in retinal pigment epithelial cells during mechanical stimulation. The FASEB Journal. 1999; 13: 63–68. PMID: 9872930
5. Abu Khamidakh AE, Juuti-Uusitalo K, Larsson K, Skottman H, Hyttinen J. Intercellular Ca2+ wave propagation in human retinal pigment epithelium cells induced by mechanical stimulation. Exp Eye Res. 2013; 108: 129–139. doi: 10.1016/j.exer.2013.01.009 PMID: 23352832

6. Hansen M, Boitano S, Dirksen ER, Sanderson MJ. Intercellular calcium signaling induced by extracellular adenosine 5′-triphosphate and mechanical stimulation in airway epithelial cells. Journal of Cell Science. 1993; 106: 995–1004. PMID: 8126116
7. Gelisken F, Inhoffen W, Partsch M, Schneider U, Kreissig I. Retinal pigment epithelial tear after photodynamic therapy for choroidal neovascularization. Am J Ophthalmol. 2001; 131: 518–520. PMID: 11292425
8. Garg S, Brod R, Kim D, Lane RG, Maguire J, Fischer D. Retinal pigment epithelial tears after intravitreal bevacizumab injection for exudative age-related macular degeneration. Clin Experiment Ophthalmol. 2008; 36: 252–256. doi: 10.1111/j.1442-9071.2008.01710.x PMID: 18412594
9. Singh RP, Sears JE. Retinal pigment epithelial tears after pegaptanib injection for exudative age-related macular degeneration. Am J Ophthalmol. 2006; 142: 160–162. PMID: 16815269
10. Rae Shi K. Revolution dawning in cardiotoxicity testing. Nature Reviews Drug Discovery. 2013; 12: 565–567. doi: 10.1038/nrd4083 PMID: 23903208
11. Sneyd J, Tsaneva-Atanasova K, Bruce JIE, Straub SV, Giovannucci DR, Yule DI. A model of calcium waves in pancreatic and parotid acinar cells. Biophys J. 2003; 85: 1392–1405. PMID: 12944257
12. Höfer T, Venance L, Giaume C. Control and plasticity of intercellular calcium waves in astrocytes: A modeling approach. The Journal of Neuroscience. 2002; 22: 4850–4859. PMID: 12077182
13. Wu D, Jia Y, Zhan X, Yang L, Liu Q. Effects of gap junction to Ca2+ and to IP3 on the synchronization of intercellular calcium oscillations in hepatocytes. Biophys Chem. 2005; 113: 145–154. PMID: 15617821
14. Rizzolo LJ. Development and role of tight junctions in the retinal pigment epithelium. Int Rev Cytol. 2007; 258: 195–234. PMID: 17338922
15. Appleby PA, Shabir S, Southgate J, Walker D. Cell-type-specific modelling of intracellular calcium signalling: A urothelial cell model. Journal of The Royal Society Interface. 2013; 10.
16. Warren NJ, Tawhai MH, Crampin EJ. Mathematical modelling of calcium wave propagation in mammalian airway epithelium: Evidence for regenerative ATP release. Experimental Physiology. 2010; 95: 232–249. doi: 10.1113/expphysiol.2009.049585 PMID: 19700517
17. Dunn KC, Marmorstein AD, Bonilha VL, Rodriguez-Boulan E, Giordano F, Hjelmeland LM. Use of the ARPE-19 cell line as a model of RPE polarity: Basolateral secretion of FGF5. Investigative Ophthalmology & Visual Science. 1998; 39: 2744–2749.
18. Glotin A, Debacq-Chainiaux F, Brossas J, Faussat A, Tréton J, Zubielewicz A, et al. Prematurely senescent ARPE-19 cells display features of age-related macular degeneration. Free Radical Biology and Medicine. 2008; 44: 1348–1361. doi: 10.1016/j.freeradbiomed.2007.12.023 PMID: 18226607
19. Yamamoto A, Akanuma S, Tachikawa M, Hosoya K. Involvement of LAT1 and LAT2 in the high- and low-affinity transport of L-leucine in human retinal pigment epithelial cells (ARPE-19 cells). J Pharm Sci. 2010; 99: 2475–2482. doi: 10.1002/jps.21991 PMID: 19890975
20. Ablonczy Z, Dahrouj M, Tang PH, Liu Y, Sambamurti K, Marmorstein AD, et al. Human retinal pigment epithelium cells as functional models for the RPE in vivo. Investigative Ophthalmology & Visual Science. 2011; 52: 8614–8620.
21. Lemon G, Gibson WG, Bennett MR. Metabotropic receptor activation, desensitization and sequestration—I: Modelling calcium and inositol 1,4,5-trisphosphate dynamics following receptor activation. J Theor Biol. 2003; 223: 93–111. PMID: 12782119
22. LeBeau AP, Yule DI, Groblewski GE, Sneyd J. Agonist-dependent phosphorylation of the inositol 1,4,5-trisphosphate receptor. The Journal of General Physiology. 1999; 113: 851–872. PMID: 10352035
23. Keizer J, Levine L. Ryanodine receptor adaptation and Ca2+(-)induced Ca2+ release-dependent Ca2+ oscillations. Biophys J. 1996; 71: 3477–3487. PMID: 8968617
24. Ahmado A, Carr A, Vugler AA, Semo M, Gias C, Lawrence JM, et al. Induction of differentiation by pyruvate and DMEM in the human retinal pigment epithelium cell line ARPE-19. Investigative Ophthalmology & Visual Science. 2011; 52: 7148–7159.
25. Dunn KC, Aotaki-Keen AE, Putkey FR, Hjelmeland LM. ARPE-19, a human retinal pigment epithelial cell line with differentiated properties. Exp Eye Res. 1996; 62: 155–170. PMID: 8698076
26. Peng S, Rahner C, Rizzolo LJ. Apical and basal regulation of the permeability of the retinal pigment epithelium. Investigative Ophthalmology & Visual Science. 2003; 44: 808–817.
27. Ross MH, Romrell LJ, Kaye GI. Histology a text and atlas. Baltimore: Lippincott Williams & Wilkins; 1995.
28. Feeney-Burns L, Hilderbrand ES, Eldridge S. Aging human RPE: Morphometric analysis of macular, equatorial, and peripheral cells. Investigative Ophthalmology & Visual Science. 1984; 25: 195–200.

29. Wang J, Huang X, Huang W. A quantitative kinetic model for ATP-induced intracellular oscillations. J Theor Biol. 2007; 245: 510–519. PMID: 17188305

30. Sullivan DM, Erb L, Anglade E, Weisman GA, Turner JT, Csaky KG. Identification and characterization of P2Y2 nucleotide receptors in human retinal pigment epithelial cells. J Neurosci Res. 1997; 49: 43–52. PMID: 9211988

31. Giancoli DC. Physics for scientists and engineers with modern physics (3rd edition): Prentice Hall; 2000.

32. Fall CP, Marland ES, Wager JM, Tyson JJ. Computational cell biology. New York: Springer; 2002.

33. Chung W, Kermode JC. Suramin disrupts receptor-G protein coupling by blocking association of G protein α and βγ subunits. Journal of Pharmacology and Experimental Therapeutics. 2005; 313: 191–198. PMID: 15626724

34. Hamill OP. Twenty odd years of stretch-sensitive channels. Pflugers Arch—Eur J Physiol. 2006; 453: 333–351.

35. Luo Y, Zhuo Y, Fukuhara M, Rizzolo LJ. Effects of culture conditions on heterogeneity and the apical junctional complex of the ARPE-19 cell line. Investigative Ophthalmology & Visual Science. 2006; 47: 3644–3655.

36. Homolya L, Steinberg TH, Boucher RC. Cell to cell communication in response to mechanical stress via bilateral release of atp and utp in polarized epithelia. The Journal of Cell Biology. 2000; 150: 1349–1360. PMID: 10995440

37. Reigada D, Mitchell CH. Release of ATP from retinal pigment epithelial cells involves both CFTR and vesicular transport. American Journal of Physiology—Cell Physiology. 2005; 288: C132–C140.

38. Mitchell CH. Release of ATP by a human retinal pigment epithelial cell line: Potential for autocrine stimulation through subretinal space. The Journal of Physiology. 2001; 534: 193–202. PMID: 11433002

39. Reigada D, Lu W, Zhang X, Friedman C, Pendrak K, McGlinn A, et al. Degradation of extracellular ATP by the retinal pigment epithelium. American Journal of Physiology—Cell Physiology. 2005; 289: C617–C624.

40. Chaloux B, Caron AZ, Guillemette G. Protein kinase A increases the binding affinity and the Ca2+ release activity of the inositol 1,4,5-trisphosphate receptor type 3 in RINm5F cells. Biology of the Cell. 2007; 99: 379–388. PMID: 17373911

41. Betzenhauser MJ, Fike JL, Wagner LE, Yule DI. Protein kinase A increases type-2 inositol 1,4,5-trisphosphate receptor activity by phosphorylation of serine 937. Journal of Biological Chemistry. 2009; 284: 25116–25125. doi: 10.1074/jbc.M109.010132 PMID: 19608738

42. Caron AZ, Chaloux B, Arguin G, Guillemette G. Protein kinase C decreases the apparent affinity of the inositol 1,4,5-trisphosphate receptor type 3 in RINm5F cells. Cell Calcium. 2007; 42: 323–331. PMID: 17320950

43. Wojcikiewicz RJH, Luo SG. Phosphorylation of inositol 1,4,5-trisphosphate receptors by cAMP-dependent protein kinase. Journal of Biological Chemistry. 1998; 273: 5670–5677. PMID: 9488697

44. Nielsen MS, Nygaard Axelsen L, Sorgen PL, Verma V, Delmar M, Holstein-Rathlou N. Gap junctions. 2012;Jul; 2(3): 1981–2035. doi: 10.1002/cphy.c110051 PMID: 23723031

45. Ye Z, Wyeth M, Baltan-Tekkok S, Ransom B. Functional hemichannels in astrocytes: A novel mechanism of glutamate release. J Neurosci. 2003;May 1; 23(9): 3588–3596. PMID: 12736329

46. De Pittà M, Goldberg M, Volman V, Berry H, Ben-Jacob E. Glutamate regulation of calcium and IP3 oscillating and pulsating dynamics in astrocytes. J Biol Phys. 2009; 35(4): 383–411. doi: 10.1007/s10867-009-9155-y PMID: 19669422

47. Guo C, Wang Y, Hu D, Han Q, Wang J, Hou X, et al. Modulation of migration and Ca2+ signaling in retinal pigment epithelium cells by recombinant human CTGF. Current Eye Research. 2009; 34:10: 852–862. doi: 10.3109/02713680903128935 PMID: 19895313

48. Huang W, Wang L, Yuan M, Ma J, Hui Y. Adrenomedullin affects two signal transduction pathways and the migration in retinal pigment epithelial cells. Investigative Ophthalmology & Visual Science. 2004; 45: 1507–1513.

49. Savolainen V, Juuti-Uusitalo K, Onnela N, Vaajasaari H, Narkilahti S, Suuronen R, et al. Impedance spectroscopy in monitoring the maturation of stem cell-derived retinal pigment epithelium. Annals of Biomedical Engineering. 2011; 39: 3055–3069. doi: 10.1007/s10439-011-0387-1 PMID: 21904797

50. Yang D, Elner SG, Clark AJ, Hughes BA, Petty HR, Elner VM. Activation of P2X receptors induces apoptosis in human retinal pigment epithelium. Investigative Ophthalmology & Visual Science. 2011; 52: 1522–1530.

51. Wimmers S, Halsband C, Seyler S, Milenkovic V, Strauss O. Voltage-dependent Ca2+ channels, not ryanodine receptors, activate Ca2+-dependent BK potassium channels in human retinal pigment epithelial cells. Mol Vis. 2008; 14: 2340–2348. PMID: 19096717

52. Loeffler KU, Mangini NJ. Immunohistochemical localization of na+/Ca2+ exchanger in human retina and retinal pigment epithelium. Graefe's Arch Clin Exp Ophthalmol. 1998; 236: 929–933. PMID: 9865624

53. Stalmans P, Himpens B. A decreased Ca2+-wave propagation is found among cultured RPE cells from dystrophic RCS rats. Investigative Ophthalmology & Visual Science. 1998; 39: 1493–1502.

54. Peterson WM, Meggyesy C, Yu K, Miller SS. Extracellular ATP activates calcium signaling, ion, and fluid transport in retinal pigment epithelium. The Journal of Neuroscience. 1997; 17: 2324–2337. PMID: 9065493

55. Maminishkis A, Jalickee S, Blaug SA, Rymer J, Yerxa BR, Peterson WM, et al. The P2Y2 receptor agonist INS37217 stimulates RPE fluid transport in vitro and retinal reattachment in rat. Investigative Ophthalmology & Visual Science. 2002; 43: 3555–3566.

56. Siefjediers A, Hardt M, Prinz G, Diener M. Characterization of inositol 1,4,5-trisphosphate (IP3) receptor subtypes at rat colonic epithelium. Cell Calcium. 2007; 41: 303–315. PMID: 16950509

57. Maranto AR. Primary structure, ligand binding, and localization of the human type 3 inositol 1,4,5-trisphosphate receptor expressed in intestinal epithelium. Journal of Biological Chemistry. 1994; 269: 1222–1230. PMID: 8288584

58. Sugiyama T, Yamamoto-Hino M, Wasano K, Mikoshiba K, Hasegawa M. Subtype-specific expression patterns of inositol 1,4,5-trisphosphate receptors in rat airway epithelial cells. Journal of Histochemistry & Cytochemistry. 1996; 44: 1237–1242.

59. Kennedy BG, Mangini NJ. Plasma membrane calcium-ATPase in cultured human retinal pigment epithelium. Exp Eye Res. 1996; 63: 547–556. PMID: 8994358

60. Stalmans P, Himpens B. Confocal imaging of Ca2+ signaling in cultured rat retinal pigment epithelial cells during mechanical and pharmacologic stimulation. Investigative Ophthalmology & Visual Science. 1997; 38: 176–187.

61. Shen J, Gimbrone MA Jr, Luscinskas FW, Dewey CF Jr. Regulation of adenine nucleotide concentration at endothelium-fluid interface by viscous shear flow. Biophys J. 1993; 64: 1323–1330. PMID: 8494987

62. Garrad RC, Otero MA, Erb L, Theiss PM, Clarke LL, Gonzalez FA, et al. Structural basis of agonist-induced desensitization and sequestration of the P2Y2 nucleotide receptor. Journal of Biological Chemistry. 1998; 273: 29437–29444. PMID: 9792648

63. Mahama PA, Linderman JJ. A monte carlo study of the dynamics of G-protein activation. Biophys J. 1994; 67: 1345–1357. PMID: 7811949

64. Fink CC, Slepchenko B, Loew LM. Determination of time-dependent inositol-1,4,5-trisphosphate concentrations during calcium release in a smooth muscle cell. Biophys J. 1999; 77: 617–628. PMID: 10388786